

# SMIP98

## SMIP98 SEMINAR ON UTILIZATION OF STRONG-MOTION DATA

Oakland, California  
September 15, 1998

### PROCEEDINGS

Sponsored by

California Strong Motion Instrumentation Program  
Division of Mines and Geology  
California Department of Conservation

Supported in Part by

California Seismic Safety Commission  
Federal Emergency Management Agency



DEPARTMENT OF  
CONSERVATION

Division of  
Mines and Geology

The California Strong Motion Instrumentation Program (CSMIP) is a program within the Division of Mines and Geology of the California Department of Conservation and is advised by the Strong Motion Instrumentation Advisory Committee (SMIAC), a committee of the California Seismic Safety Commission. Current program funding is provided by an assessment on construction costs for building permits issued by cities and counties in California, with additional funding from the California Department of Transportation, the Office of Statewide Health Planning and Development, and the California Department of Water Resources.

In January 1997, a joint project, TriNet, between CDMG, Caltech and USGS was funded by the Federal Emergency Management Agency (FEMA) through the California Office of Emergency Services (OES). The goals of the project are to record and rapidly communicate ground shaking information in southern California, and to analyze the data for the improvement of seismic codes and standards.

#### **DISCLAIMER**

Neither the sponsoring nor supporting agencies assume responsibility for the accuracy of the information presented in this report or for the opinions expressed herein. The material presented in this publication should not be used or relied upon for any specific application without competent examination and verification of its accuracy, suitability, and applicability by qualified professionals. Users of information from this publication assume all liability arising from such use.

# SMIP98

## SMIP98 SEMINAR ON UTILIZATION OF STRONG-MOTION DATA

Oakland, California  
September 15, 1998

### PROCEEDINGS

Edited by

Moh Huang

Sponsored by

California Strong Motion Instrumentation Program  
Division of Mines and Geology  
California Department of Conservation

Supported in Part by

California Seismic Safety Commission  
Federal Emergency Management Agency



**PREFACE**

The California Strong Motion Instrumentation Program (CSMIP) in the Division of Mines and Geology of the California Department of Conservation promotes and facilitates the improvement of seismic codes through the Data Interpretation Project. The objective of this project is to increase the understanding of earthquake strong ground shaking and its effects on structures through interpretation and analysis studies of CSMIP and other applicable strong-motion data. The ultimate goal is to accelerate the process by which lessons learned from earthquake data are incorporated into seismic code provisions and seismic design practices.

Since the establishment of CSMIP in the early 1970s, over 650 stations, including 430 ground-response stations, 150 buildings, 20 dams and 54 bridges, have been installed. Significant strong-motion records have been obtained from many of these stations. One of the most important sets of strong-motion records is from the 1994 Northridge earthquake. During this earthquake strong-motion records were obtained from 116 ground-response stations and 77 extensively-instrumented structures. In addition to these records, CSMIP in cooperation with the City of Los Angeles and other agencies, collected and archived accelerograms recorded at over 300 high-rise buildings during the Northridge earthquake. These buildings were instrumented by the building owners as required by the City's Building Code. The strong-motion records from the Northridge earthquake have been and will be the subject of CSMIP data interpretation projects.

The SMIP98 Seminar is the ninth in a series of annual events designed to transfer recent interpretation findings on strong-motion data to practicing seismic design professionals and earth scientists. The purpose of the Seminar is to increase the utilization of strong-motion data in improving seismic design and practices. In the presentations, investigators of the CSMIP-funded data interpretation projects will present the results from their studies on the near fault ground motions and on four concrete moment frame buildings. In addition, five invited experts who have utilized strong-motion data in specific studies will discuss the applications of strong-motion data to a variety of areas including rapid earthquake response by utilities, prediction of earthquake impacts, seismic building code improvements, development of TriNet shaking maps, bridge instrumentation and post-earthquake evaluations of bridges. Professor Hiroo Kanamori of Caltech and Chris Poland, President of Degenkolb Engineers will present a luncheon address on the seismological and engineering perspectives on the TriNet project.

The papers in this Proceedings volume presented by the investigators of the CSMIP-funded data interpretation projects represent interim results. Following this seminar the investigators will be preparing final reports with their final conclusions. These reports will be more detailed and will update the results presented here. CSMIP will make these reports available after the completion of the studies.

Anthony F. Shakal  
CSMIP Program Manager

Moh J. Huang  
Data Interpretation Project Manager



**TABLE OF CONTENTS**

**Seminar Program**

**Development of An Improved Representation of Near Fault Ground Motions . . . . . 1**  
Paul Somerville

**Development of Improved Design Procedures for Near Fault Ground Motions . . . . . 21**  
H. Krawinkler and B. Alavi

**Utilization of Rapid Post-Earthquake Data by Utilities . . . . . 43**  
William Savage

**Bridge Instrumentation and Post-Earthquake Evaluation of Bridges . . . . . 53**  
Patrick Hipley, Moh Huang and Anthony Shakal

**Response Evaluation of a 20-story Concrete Frame Building to the Northridge  
and Other Earthquakes . . . . . 73**  
G. Hart, M. Skokan and H. Martin

**Response Evaluation of Three Concrete Frame Buildings to the January 17, 1994  
Northridge Earthquake . . . . . 91**  
Farzad Naeim, Roy Lobo, Julia Li, Tom Sabol and Roger Li

**New Tools for Predicting and Mitigating Earthquake Impacts Based on  
Ground Motion Data . . . . . 119**  
Charles Kircher

**Seismic Code Improvements Based on Recorded Motions of Buildings During  
Earthquakes. . . . . 135**  
Anil K. Chopra, Rakesh K. Goel, and Juan Carlos De la Llera

**TriNet "ShakeMaps": Rapid Generation of Peak Ground Motion and Intensity Maps  
for Earthquakes in Southern California . . . . . 155**  
David J. Wald, V. Quitoriano, T.H. Heaton, H. Kanamori and C. W. Scrivner





**SMIP98 SEMINAR ON  
UTILIZATION OF STRONG-MOTION DATA**

Marriott Hotel, Oakland, California  
September 15, 1998

**PROGRAM**

- 8:00 - 9:00      **Registration**
- 9:00 - 9:10      **Welcoming Remarks**  
*Donald Wolfe*, LA County Dept. of Public Works, Seismic Safety  
Commission, and Chair, Strong Motion Instrumentation  
Advisory Committee (SMIAC)  
*James Davis*, State Geologist, Division of Mines and Geology
- 9:10 - 9:20      **Introductory Remarks**  
*Anthony Shakal* and *Moh Huang*, Strong Motion Instrumentation Program

**SESSION I      NEAR FAULT GROUND MOTIONS**  
**Moderator:** *Bruce Bolt*, UC Berkeley  
Chair, SMIAC Ground-Response Subcommittee

- 9:20 - 9:50      **Development of an Improved Representation for Near Fault Ground Motions**  
*Paul Somerville*, Woodward-Clyde, Pasadena
- 9:50 - 10:20      **Development of Improved Design Procedures for Near Fault Ground Motions**  
*Helmut Krawinkler*, and B. Alavi, Stanford University
- 10:20 - 10:30      **Questions and Answers for Session I**
- 10:30 - 10:50      Break

**SESSION II      UTILIZATION OF DATA IN RAPID EARTHQUAKE RESPONSE**  
**Moderator:** *Vern Persson*, Division of Safety of Dams, DWR  
Chair, SMIAC Lifelines Subcommittee

- 10:50 - 11:20      **Utilization of Rapid Post-Earthquake Data by Utilities**  
*Woody Savage*, PG&E, San Francisco
- 11:20 - 11:50      **Bridge Instrumentation and Post-Earthquake Evaluation of Bridges**  
*Patrick Hipley*, Caltrans and *Moh Huang*, SMIP, Sacramento
- 11:50 - 12:00      **Questions and Answers for Session II**

## SMIP98 Seminar Proceedings

12:00 - 1:20      **Luncheon**  
Introduction *James Davis*, State Geologist, Division of Mines and Geology  
Topic: **Seismological and Engineering Perspectives on the TriNet Project**  
Speakers: *Hiroo Kanamori*, John E. and Hazel S. Smits Professor, Caltech  
*Chris Poland*, President, Degenkolb Engineers

### SESSION III      **RESPONSE OF CONCRETE FRAME BUILDINGS**

Moderator: *Chris Poland*, Degenkolb Engineers

Chair, SMIAC Buildings Subcommittee

1:20 - 1:50      **Response Evaluation of a 20-Story Concrete Frame Building to the Northridge and Other Earthquakes**  
*G. Hart*, *Matthew Skokan* and *H. Martin*, University of California, Los Angeles

1:50 - 2:20      **Response Evaluation of Three Concrete Frame Buildings to the Northridge Earthquake**  
*Farzad Naeim*, and *Roy Lobo*, J.A. Martin & Associates, *Julia Li*, UCLA,  
*Tom Sabol* and *Roger Li*, Englekirk & Sabol, Los Angeles

2:20 - 2:30      **Questions and Answers for Session III**

2:30 - 2:50      Break

### SESSION IV      **POST-EARTHQUAKE UTILIZATION OF DATA**

Moderator: *Woody Savage*, PG&E

Member, SMIAC Ground Response Subcommittee

2:50 - 3:20      **New Tools for Predicting and Mitigating Earthquake Impacts Based on Ground Motion Data**  
*Charles Kircher*, Kircher and Associates, Mountain View

3:20 - 3:50      **Seismic Code Improvements Based on Recorded Motions of Buildings During Earthquakes**  
*Anil Chopra*, University of California, Berkeley, *Rakesh Goel*, California Polytechnic State University, San Luis Obispo, *Juan Carlos De la Llera*, Pontificia Universidad Catolica de Chile

3:50 - 4:20      **TriNet "ShakeMaps": Rapid Generation of Peak Ground Motion and Intensity Maps for Earthquakes in Southern California.**  
*David Wald*, U.S. Geological Survey, *V. Quitoriano*, *T. Heaton*, *H. Kanamori*, Caltech, and *C. Scrivner*, SMIP

4:20 - 4:30      **Questions and Answers for Session IV**

4:30              **Closing Remarks**

**DEVELOPMENT OF AN IMPROVED REPRESENTATION OF NEAR-FAULT  
GROUND MOTIONS**

Paul Somerville

Woodward-Clyde, Pasadena, CA

**ABSTRACT**

The principal objective of this study is to develop an improved parameterization for the engineering specification of near-fault ground motions. In addition to the response spectrum, we would like to include time domain parameters that describe the near-fault pulse, such as its period, amplitude, and number of half-cycles. We have developed a preliminary model that relates time domain parameters of the near-fault ground motion pulse to the earthquake magnitude and distance. The model is for forward rupture directivity conditions, which produce a strong pulse of motion in the fault-normal direction. The pulse parameters that we have modeled are the period and peak amplitude of the largest cycle of motion of the velocity pulse. The records analyzed include 15 time histories recorded in the distance range of 0 to 10 km from earthquakes in the magnitude range of 6.2 to 7.3, augmented by 12 simulated time histories that span the distance range of 3 to 10 km and the magnitude range of 6.5 to 7.5.

**INTRODUCTION**

The objective of this study is to develop an improved representation of near-fault ground motions for use in building codes. The effects of rupture directivity on near-fault ground motions have been recognized by strong-motion seismologists for several decades. The propagation of fault rupture toward a site at a velocity close to the shear wave velocity causes most of the seismic energy from the rupture to arrive in a single large long-period pulse of motion that occurs at the beginning of the record (Somerville et al., 1997a). This pulse of motion, sometimes referred to as "fling," represents the cumulative effect of almost all of the seismic radiation from the fault. The radiation pattern of the shear dislocation on the fault causes this large pulse of motion to be oriented in the direction perpendicular to the fault, causing the strike-normal peak velocity to be larger than the strike-parallel peak velocity. Figure 1 shows these effects of rupture directivity in the time history of the Olive View recording of the 1994 Northridge earthquake.

Currently, all seismic design guidelines and codes specify design ground motions using the response spectrum. The effect of forward rupture directivity on the response spectrum is to increase the level of the response spectrum of the horizontal component normal to the fault strike at periods longer than 0.5 seconds (Somerville, 1996; Somerville et al., 1997a), as shown in Figure 2. This causes the peak response spectral acceleration of the strike-normal component to shift to longer periods, for example from 0.25 seconds to as much as 0.75 seconds. Near fault effects cannot be adequately described by uniform scaling of a fixed response spectral shape; instead the shape of the spectrum becomes richer in long periods as the level of the spectrum increases. A detailed model describing the amplitude and duration effects of rupture directivity

on near-fault ground motions was developed by Somerville et al. (1997a).

Current guideline and code documents that address near fault ground motions include SEAOC Vision 2000, the SEAOC Blue Book, the 1997 UBC, the 1997 NEHRP Seismic Provisions, and the FEMA-273 Rehabilitation Guidelines. These guideline and code documents recognize the importance of near-fault effect to varying degrees, but in most cases attempt to account for near-fault effects by increasing the design shear force. Two basic approaches are presently adopted. In the 1997 NEHRP provisions, mapped values of spectral ordinates at 1.0 second (obtained from the lesser of deterministic maps and probabilistic 2/50 maps) are used as the basis for determining the importance of near-fault effects. These mapped values are then multiplied by 2/3 to arrive at design spectral values from which the base shear is derived. In the 1997 UBC (and Appendix C of the 1996 SEAOC Blue Book), tables of near-source factors  $N_a$  and  $N_v$  are provided to amplify the design spectrum at distances less than 10 to 15 km from the seismic source. These near-source factors constitute the consensus of a SEAOC Seismology Subcommittee. Both approaches contain sound engineering judgment but result in somewhat different design values. Also, both approaches disregard the effect of pulse-like ground motions on the dynamic response of structures.

The quantification of the near-source factor in the SEAOC Blue Book and the 1997 UBC was based in part on the response spectral model developed by Somerville (1996) using strong motion recordings of the 1989 Loma Prieta, 1994 Northridge, and 1995 Kobe earthquakes. Specifically, the observations by Somerville (1996) concerning the dependence of the near-fault response spectral shape on magnitude and distance led to the incorporation of separate near-source factors for the acceleration and velocity parts of the response spectrum. As shown in Figure 2, the near-source spectrum in the 1997 UBC is compatible with the average of the two horizontal components of motion derived from the model of Somerville (1996) for both the design basis (10% in 50 years) and maximum capable (5% in 50 years) levels. However, the 1997 UBC does not specifically address the larger ground motion in the strike-normal component than in the strike-parallel component, which becomes especially significant for the maximum capable (5% in 50 years) level. The ground motion attenuation relations used in generating the NEHRP design values maps do not include any specific provision for the near-fault ground motion characteristics described above (Somerville et al., 1997a).

Although the response spectrum provides the basis for the specification of design ground motions in all current design guidelines and code provisions, there is a growing recognition that the response spectrum alone does not provide an adequate characterization of near-fault ground motions. For example, a broad consensus was reached at the NCEER Workshop on National Representation of Seismic Ground Motion for New and Existing Highway Facilities, held in San Francisco on May 29-30, 1997, that the response spectrum alone does not provide an appropriate characterization of near-fault ground motions for the design of bridges. This is because near fault ground motions are characterized by a relatively simple long period pulse of strong motion having relatively brief duration, rather than by a stochastic process having relatively long duration that characterizes more distant ground motion. Unlike the case for more distant ground motion, the resonance phenomenon that the response spectrum is designed to represent has insufficient time to build up when the input is a near-fault pulse. The response spectrum is thus not capable of adequately describing the seismic demands presented by a near-fault pulse.

The inadequacy of the response spectrum as a sole design criterion becomes readily apparent when time histories are selected to represent a design response spectrum. It is well known that a suite of different ground motion time histories which all match the same response spectrum produce variations in the response of a structure subjected to non-linear time history analysis. However, when the input time history is a near-fault pulse, this effect is accentuated to the point where small modifications of a near-fault time history that have no significant effect on the response spectrum can have a major effect on the response of a structure when subjected to non-linear time history analysis. This demonstrates that the current standard of practice does not provide a reliable basis for providing near-fault ground motion time histories that are specified solely on the basis of a design response spectrum.

Current trends in the development of future building codes have all embraced the concept of performance based design, and conceptual frameworks of that approach have been developed by SEAOC Vision 2000 and FEMA-273. Since the goal of performance based design depends heavily on realistic specification of ground motion inputs and realistic models of building response, it is clear that some alternative approach needs to be developed for specifying near-fault ground motions for seismic design. The new approach that we have developed has the goal of supplementing the response spectrum with time domain parameters such as the period and amplitude of the near-fault pulse. These ground motion parameters have been identified as being important for predicting damage to structures.

### SELECTION OF NEAR-FAULT TIME HISTORIES

A set of near fault time histories was selected to systematically sample three variables: the magnitude range of 6.0 to 7.5, the distance range of 0 to 10 km, and directivity conditions ranging from forward to backward, in sets of both recorded and simulated time histories for soil conditions. Figure 3 displays the distribution of the selected soil time histories for magnitude vs. distance; directivity condition vs. magnitude, and directivity condition vs. distance for three sets: recorded data; simulations; and the combined recorded data and simulations.

Additional time histories for rock and soft soil conditions were included. However, except for the set of rock simulations, these do not systematically span the magnitude, distance and directivity condition ranges of interest. The recorded data set includes time histories from a variety of earthquake focal mechanisms, but does not systematically sample them, and the simulated time histories are all for strike-slip.

Tables 1 and 2 list the recorded and simulated time histories that were developed. Table 1 lists 29 recorded time histories. It includes all ten recorded time histories in the SAC Phase 2 near fault set (Somerville et al., 1997b), which were all for soil site conditions (either recorded on those conditions, or modified for those conditions). Ten soil site recordings have been added to produce a set of 20 time histories that span the magnitude range of 6.0 to 7.5, the distance range of 0 to 10 km, and a range of directivity conditions from forward to backward. Three soft soil recordings, and six rock recordings which also appear in the soil set after modification from rock to soil conditions, have also been added.

Table 2 lists 54 simulated time histories. It contains 27 time histories that were generated for rock conditions, and 27 time histories for soil conditions that were derived from the 27 simulations for rock. The 27 simulations span the magnitude range of 6.5 to 7.5, the distance range of 3 to 10 km, and a range of directivity conditions from forward to backward. The set of simulated time histories does not include those in the SAC Phase 2 Near Fault set, because they did not systematically sample the ranges of magnitude, distance and directivity condition. The time histories were generated using the procedure described by Somerville et al. (1996).

Forward directivity effects are manifested in the time histories as large velocity pulses on the strike normal component of ground motion, as shown in the Olive View recording of the 1994 Northridge earthquake (Figure 1). In Figure 4, the velocity response spectra of near fault recordings of three earthquakes show the dependence of the response spectral shape and level on earthquake magnitude and rupture directivity conditions. Forward rupture directivity effects are manifested in the response spectra by large long period ordinates on the strike-normal component.

#### IMPROVED PARAMETERIZATION OF NEAR-FAULT DESIGN GROUND MOTIONS

The principal objective of this study is to develop an improved parameterization for the engineering specification of near-fault ground motions. In addition to the response spectrum, the ground motion parameters include time domain parameters that describe the near-fault pulse, such as its period, amplitude, and number of half-cycles. Our goal is to select a set of parameters for representing near-fault ground motion that is optimally effective in predicting structural response.

We have developed a preliminary model that relates time domain parameters of the near-fault ground motion pulse to the earthquake magnitude. The model is for forward rupture directivity conditions, which produce a strong pulse of motion in the fault-normal direction. The pulse parameters that we have modeled are the period and amplitude of the largest cycle of motion of the velocity pulse. The records analyzed include 15 time histories recorded in the distance range of 0 to 10 km from earthquakes in the magnitude range of 6.2 to 7.3. Simple peak and trough representations of these time histories are shown in Figure 5 for comparison with the simple pulse models P1, P2 and P3 analyzed by Professor Krawinkler, as described later. These recorded pulses are augmented by 12 simulated time histories that span the distance range of 3 to 10 km and the magnitude range of 6.5 to 7.5, whose simple peak and trough representations are shown in Figure 6. All of the time histories are for soil site conditions, although in some cases rock time histories were spectrally modified to reproduce soil site conditions.

The preliminary relationship between the period  $T$  of the near-fault fault-normal forward directivity pulse recorded on soil and the moment magnitude  $M_w$ , assuming the period to be independent of distance, is:

$$\log_{10} T = -2.5 + 0.425 M_w$$

Constraining the relation between pulse period and magnitude to be self-similar, i.e. to

grow in proportion to the fault dimension, we obtain the relation shown in Figure 7:

$$\log_{10} T = -3.0 + 0.5 M_w$$

This relationship was also examined for separate sets of recorded and simulated time histories. It was found that the period of the recorded time histories grows more rapidly with magnitude than that of the simulated time histories. However, when the recorded and simulated time histories were combined, the resulting relationship was very similar to that of the recorded time histories.

An approximate relationship between the peak velocity PGV on soil of the near-fault fault-normal forward directivity pulse and the moment magnitude  $M_w$  and closest distance R is:

$$\log_{10} PGV = -1.0 + 0.5 M_w - 0.5 \log_{10} R$$

This model assumes a linear relationship between PGV and R which may not be realistic at very close distances; data recorded at distances of less than 3 km were not used in developing this relationship. This relationship was also examined for separate sets of recorded and simulated time histories. It was found that the peak velocity of the recorded time histories grows more rapidly with magnitude than for the simulated time histories, and decreases more gradually with distance than for simulated time histories. The approximate model given above is based on the recorded time histories and a subset of the simulated time histories that is most compatible with the recorded time histories. This subset consists of simulations for the magnitude range of 6.5 to 7.0 containing strong forward rupture directivity effects.

#### COMPARISON OF THE PULSE MODEL AND RECORDED PULSES WITH THE KRAWINKLER PULSE MODELS

The preliminary model of the pulse that we have developed addresses only the largest cycle of motion of the near-fault fault-normal forward directivity pulse. The model of the pulse is a symmetrical cycle of motion characterized by a peak, a trough and three zero crossings. To generate a more realistic time history from this simplified model, a continuous curve can be fit through these points using spline interpolation.

Our preliminary pulse model has one whole cycle of motion. Professor Krawinkler analyzed the response of structures to three different pulses, P1, P2 and P3, which are shown in Figure 6. These pulses have 0.5, 1 and 2.5 cycles of motion respectively. In our model, we have used the largest cycle of motion in the record, regardless of how many cycles it has, so our model is not quite the same as the P1 model of Professor Krawinkler.

In Table 3, we summarize how the 15 recorded pulses fit the three pulse models analyzed by Professor Krawinkler. Of the 15 near-fault pulses selected for analysis and provided to Professor Krawinkler, none provide a good fit to his P1 model, although 3 pulses are moderately well fit by that model. Of the 15 pulses, 9 fit his P2 model to the extent that the first peak and the following trough have larger peak velocity than the following peaks and troughs. Of these,

the first peak is larger in 6 and smaller in 3 than the following trough (the pulses are rectified so they all start upward with a peak). The remaining 6 time histories fit Professor Krawinkler's P3 model to the extent that subsequent peaks (or troughs) are larger than at least one of the first two peaks. In addition to these 6 time histories that fit P3, 5 of the 9 P2 pulses have subsequent peaks that are comparable to the first peak or trough, making a total of 11 time histories that are fit to some extent by the P3 model. This indicates the need to extend the preliminary pulse model presented here to include more half cycles, which in some cases come before the largest cycle (as in model P3) and in other cases come after.

#### RELATIONSHIP BETWEEN PULSE PERIOD AND RISE TIME

It is expected that the period of the pulse is most strongly influenced by the rise time  $T_R$  of slip on the fault, which measures the duration of slip at a single point on the fault. Somerville et al. (1998) found a self-similar relation between rise time and magnitude from an empirical analysis of 15 crustal earthquakes:

$$\log_{10} T_R = -3.34 + 0.5 M_w$$

The self-similar relation between pulse period and magnitude obtained above is:

$$\log_{10} T = -3.0 + 0.5 M_w$$

Eliminating  $M_w$  from these two equations, we find that the period  $T$  of the pulse is related to the rise time  $T_R$  by the relation:

$$T = 2.2 T_R$$

The period of the pulse is thus equal to about twice the rise time of slip on the fault. This is consistent with the fact that the rise time is a lower bound on the period of the pulse. If the fault were a point source, then the only source parameter that would contribute to the period of the pulse would be the rise time, and the period of the pulse would equal the rise time if wave propagation effects such as  $Q$  are ignored. Since the fault is actually finite, and the rupture velocity is less than the shear wave velocity, the finite apparent duration of the rupture as observed at recording stations also contributes to the widening of the pulse, as described in the Appendix. For stations that experience forward rupture directivity, this apparent duration is much shorter than the actual duration of rupture.

#### DEPENDENCE OF RISE TIME (AND PULSE PERIOD) ON STYLE OF FAULTING

Analyses performed by Professor Krawinkler using pulse models P1, P2 and P3 demonstrate that the period of the near-fault pulse has a strong influence on the demands on the structure. We have just shown that the period of the pulse is directly related to the rise time. We have also found a correlation between rise time and faulting mechanism that may explain the style-of-faulting factor. For a given seismic moment, the rise times for reverse earthquakes are



on average about half as long as those for strike-slip earthquakes, as shown in Figure 8. Strong motion simulations show that halving the rise time causes an increase of about a factor of 1.4 in ground motion amplitudes. This increase is consistent with the style of faulting factor in empirical strong motion attenuation relations, in which ground motions for reverse earthquakes typically exceed those for strike-slip earthquakes by a factor ranging from about 1.3 to 1.4. Thus the larger ground motion levels in thrust faulting may be due to a shorter rise time. The shorter rise times of the reverse faulting events are manifested in the velocity response spectrum by a peak or plateau occurring at a shorter period than for strike-slip faults.

### IMPORTANCE OF MULTIPLE PULSES

Structural response analyses by Professor Krawinkler using simple input pulses show that the response grows rapidly with the number of half-cycles of input motion. The presence of multiple pulses in the velocity time history can thus dramatically increase the damage potential of the ground motions. For example, the destructiveness of the ground motions from the 1995 Kobe earthquake was accentuated by the presence of two consecutive pulses in the recorded velocity waveforms, as shown in Figure 5. Some recordings of the 1994 Northridge and 1989 Loma Prieta earthquakes also contained velocity pulses having more than the 1 to 1½ cycles that characterize the simplest pulses recorded in other earthquakes. This indicates the need to identify the conditions that give rise to multiple pulses in near-fault ground motions. A preliminary review indicates that they may be due to multiple asperities on the fault rupture plane, and that their occurrence depends on the relative location of the hypocenter, of asperities on the fault, and of the recording site.

### APPENDIX

#### CONTRIBUTION OF RISE TIME AND RUPTURE DURATION TO PULSE PERIOD

From the analysis of the data described above, we found that the period  $T$  of the pulse is related to the rise time  $T_R$  by the relation:

$$T = 2.2 T_R$$

The period of the pulse is thus equal to about twice the rise time of slip on the fault. This is consistent with the fact that the rise time is a lower bound on the period of the pulse. In this appendix we use a simple analytical model to assess more quantitatively whether this relationship is compatible with fault rupture models. If the fault were a point source, then the only source parameter that would contribute to the period of the pulse would be the rise time, and the period of the pulse would equal the rise time if wave propagation effects such as  $Q$  are ignored. Since the fault is actually finite, and the rupture velocity is less than the shear wave velocity, the finite apparent duration of the rupture as observed at recording stations, defined to be the difference between the pulse duration and the rise time

$$t_a = T - T_R$$

also contributes to the widening of the pulse. From the relation between  $T$  and  $T_R$  given above,

$$t_a = 1.2 T_R$$

For stations that experience forward rupture directivity, this apparent rupture duration is shorter than the actual duration of rupture, as shown in the analysis that follows.

The relation between fault rupture area A and magnitude for crustal earthquakes in tectonically active regions is given by (Somerville et al., 1998):

$$\log_{10} A = M_w - 3.95$$

For a square fault of dimension L, this gives

$$\log_{10} L = 0.5 M_w - 1.975$$

The relation between rise time and magnitude from Somerville et al. (1998) is

$$\log_{10} T_R = 0.5 M_w - 3.34$$

Eliminating  $M_w$ , the relation between fault area A and rise time  $T_R$  is:

$$\log_{10} L = 1.365 \log_{10} T_R$$

or fault dimension L in km = 23.2 x rise time  $T_R$  in seconds.

Somerville et al. (1997) analyzed ground motions recorded within 10 km of the fault. For forward rupture directivity, the fraction of the fault dimension that lies between the hypocenter and the recording site (parameter X for strike-slip, parameter Y for dip-slip) is 0.64, averaged over 44 recordings. The X and Y values are listed in Somerville et al. (1997), Table 8, and the identification of forward rupture directivity sites is listed in Somerville (1997), Table 1. Using the term F to represent the length of the fault between the hypocenter and the station, we then have

$$F = 0.64 L \text{ and hence}$$

$$F = 14.83 T_R$$

The time t for rupture to propagate across distance F, assuming a rupture velocity  $V_r$  of 2.75 km/sec (i.e. 0.8 times the shear wave velocity of 3.5 km/sec), is

$$t = 5.4 T_R$$

The apparent duration  $t_a$  of the rupture across distance F as seen at a station is related to the actual duration t by the equation

$$t_a = t (1 - (V_s/V_r) \cos \theta)$$

where  $\theta$  is the angle between the fault plane and the direction to the station. This relation strictly holds only at large distances from the fault where the angle  $\theta$  is constant for all points on the fault. Somerville et al. (1997) analyzed ground motions recorded within 10 km of the fault. For forward rupture directivity, the angle between the fault plane and the recording site measured from the hypocenter (parameter  $\theta$  for strike-slip, parameter  $\phi$  for dip-slip) is 13 degrees, averaged over 44 recordings. The theta and phi values are listed in Somerville et al. (1997), Table 8, and the identification of forward rupture directivity sites is listed in Somerville (1997), Table 1. This gives

$$t_a = 0.22 t$$

and

$$t_a = 1.2 T_R$$

This relation between the apparent rupture time  $t_a$  and the rise time  $T_R$ , derived from a simple analytical model of fault rupture is the same as the result obtained above from analyzing the period of the pulse in the recorded data. Thus both the data and the simple analytical model indicate that the duration of the pulse  $T$  is related to the rise time  $T_R$  by the relation

$$T = 2.2 T_R$$

#### REFERENCES

- Somerville, P.G., K. Irikura, R. Graves, S. Sawada, D. Wald, N. Abrahamson, Y. Iwasaki, T. Kagawa, N. Smith and A. Kowada (1998). Characterizing earthquake slip models for the prediction of strong ground motion. *Seismological Research Letters*, submitted.
- Somerville, P.G. (1997). Engineering characteristics of near fault ground motion, Proceedings, SMIP97 Seminar on Utilization of Strong Ground Motion Data, Los Angeles, May 8.
- Somerville, P.G., N.F. Smith, R.W. Graves, and N.A. Abrahamson (1997a). Modification of empirical strong ground motion attenuation relations to include the amplitude and duration effects of rupture directivity, *Seismological Research Letters*, 68, 180-203.
- Somerville, P., N. Smith, S. Punyamurthula, and J. Sun (1997b). Development of ground motion time histories for Phase 2 of the FEMA/SAC Steel Project, Report No. SAC/BD-97-04
- Somerville, P.G. (1996). Strong ground motions of the Kobe, Japan earthquake of Jan. 17, 1995, and development of a model of forward rupture directivity effects applicable in California, *Proceedings of the Western Regional Technical Seminar on Earthquake Engineering for Dams*, Association of State Dam Safety Officials, Sacramento, April 11-12.
- Somerville, P., C.K. Saikia, D. Wald, and R. Graves (1996). Implications of the Northridge earthquake for strong ground motions from thrust faults, *Bull. Seism. Soc. Am.*, 86, S115-S125.

SMIP98 Seminar Proceedings

Table 1. Recorded Near-Fault Time Histories

| Earthquake  | Station      | M   | R    | Directivity | Site              |      |
|-------------|--------------|-----|------|-------------|-------------------|------|
| Tabas       | Tabas        | 7.4 | 1.2  | backward    | soil              |      |
| Landers     | Lucerne      | 7.3 | 1.1  | forward     | mod to soil       | rock |
|             | Joshua Tree  |     | 7.4  | backward    | soil              |      |
| Mendocino   | Petrolia     | 7.1 | 8.5  | backward    | soil              |      |
| Loma Prieta | LGPC         | 7.0 | 3.5  | forward     | mod to soil       | rock |
|             | Lexington    |     | 6.3  | forward     | mod to soil       | rock |
|             | Corralitos   |     | 3.4  | backward    | mod to soil       | rock |
| Kobe        | JMA          | 6.9 | 3.4  | forward     | mod to soil       | rock |
|             | Takatori     |     | 4.3  | forward     | soft soil         |      |
|             | Port Island  |     | 6.6  | forward     | soft soil         |      |
| I.V. 1940   | El Centro    | 6.9 | 10.0 | backward    | mod to soft soil* |      |
| Northridge  | Rinaldi      | 6.7 | 7.5  | forward     | soil              |      |
|             | Olive View   |     | 6.4  | forward     | soil              |      |
|             | Newhall      |     | 7.1  | forward     | soil              |      |
|             | Sepulveda    |     | 8.9  | forward     | soil              |      |
|             | Arleta       |     | 9.2  | backward    | soil              |      |
| Erzincan    | Erzincan     | 6.7 | 2.0  | forward     | soil              |      |
| I.V. 1979   | Array 5      | 6.5 | 4.1  | forward     | soil              |      |
|             | Array 6      |     | 1.2  | forward     | soil              |      |
|             | Bond's Corn  |     | 2.4  | backward    | soil              |      |
| Morgan Hill | Anderson D   | 6.2 | 4.5  | forward     | soil              |      |
|             | Coyote L D   |     | 0.1  | forward     | mod to soil       | rock |
|             | Halls Valley |     | 2.4  | backward    | soil              |      |

\* scaled to LA 10%in 50, then modified for soft soil response using SAC S1 model, 150 feet.

SMIP98 Seminar Proceedings

Table 2. Simulated Near-Fault Time Histories

| Earthquake | Station | M   | R  | Directivity | Site         |      |
|------------|---------|-----|----|-------------|--------------|------|
| 7.5H4S2    | 4       | 7.5 | 3  | backward    | mod. to soil | rock |
|            | 6       |     | 3  | forward     | mod. to soil | rock |
|            | 8       |     | 3  | forward     | mod. to soil | rock |
|            | 4       |     | 5  | backward    | mod. to soil | rock |
|            | 6       |     | 5  | forward     | mod. to soil | rock |
|            | 8       |     | 5  | forward     | mod. to soil | rock |
|            | 4       |     | 10 | backward    | mod. to soil | rock |
|            | 6       |     | 10 | forward     | mod. to soil | rock |
|            | 8       |     | 10 | forward     | mod. to soil | rock |
| 7.0H4S2    | 4       | 7.0 | 3  | backward    | mod. to soil | rock |
|            | 6       |     | 3  | forward     | mod. to soil | rock |
|            | 8       |     | 3  | forward     | mod. to soil | rock |
|            | 4       |     | 5  | backward    | mod. to soil | rock |
|            | 6       |     | 5  | forward     | mod. to soil | rock |
|            | 8       |     | 5  | forward     | mod. to soil | rock |
|            | 4       |     | 10 | backward    | mod. to soil | rock |
|            | 6       |     | 10 | forward     | mod. to soil | rock |
|            | 8       |     | 10 | forward     | mod. to soil | rock |
| 6.5H4S2    | 4       | 6.5 | 3  | backward    | mod. to soil | rock |
|            | 6       |     | 3  | forward     | mod. to soil | rock |
|            | 8       |     | 3  | forward     | mod. to soil | rock |
|            | 4       |     | 5  | backward    | mod. to soil | rock |
|            | 6       |     | 5  | forward     | mod. to soil | rock |
|            | 8       |     | 5  | forward     | mod. to soil | rock |
|            | 4       |     | 10 | backward    | mod. to soil | rock |
|            | 6       |     | 10 | forward     | mod. to soil | rock |
|            | 8       |     | 10 | forward     | mod. to soil | rock |

SMIP98 Seminar Proceedings

Table 3. Fit of 15 Recorded Near-Fault Pulses to the Krawinkler Pulse Models.

| EARTHQUAKE          | SITE            | Fit to P1 | Fit to P2 | Fit to P3 |
|---------------------|-----------------|-----------|-----------|-----------|
| Landers             | Lucerne         | x         | x         |           |
| Loma Prieta         | Los Gatos P. C. |           |           | x         |
|                     | Lexington Dam   |           | x         | x         |
| Kobe                | JMA             |           |           | x         |
|                     | Takatori        |           |           | x         |
|                     | Port Island     |           |           | x         |
| Northridge          | Sylmar          |           | x         | x         |
|                     | Newhall         |           |           | x         |
|                     | Rinaldi         | x         | x         |           |
|                     | Sepulveda       |           | x         | x         |
| Erzincan            | Erzincan        | x         | x         |           |
| Imperial Valley '79 | Array 6         |           | x         |           |
|                     | Meloland        |           | x         | x         |
| Morgan Hill         | Anderson Dam    |           |           | x         |
|                     | Coyote Lake Dam |           | x         | x         |

CSMIP Near Fault Project - Recorded Time Histories  
1994 Northridge Recorded at Sylmar

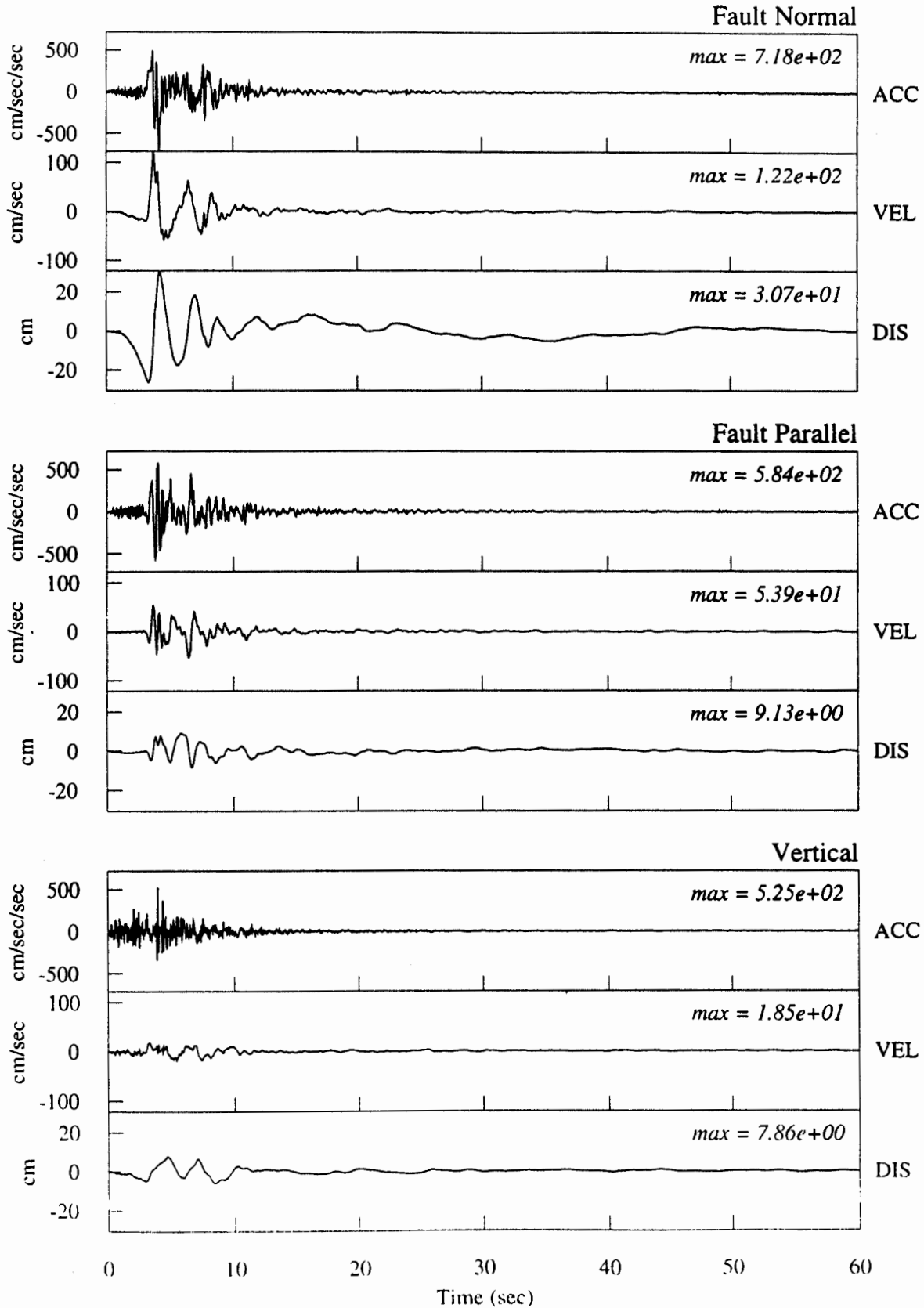


Figure 1. Olive View recording of the 1994 Northridge earthquake, containing a large velocity pulse.

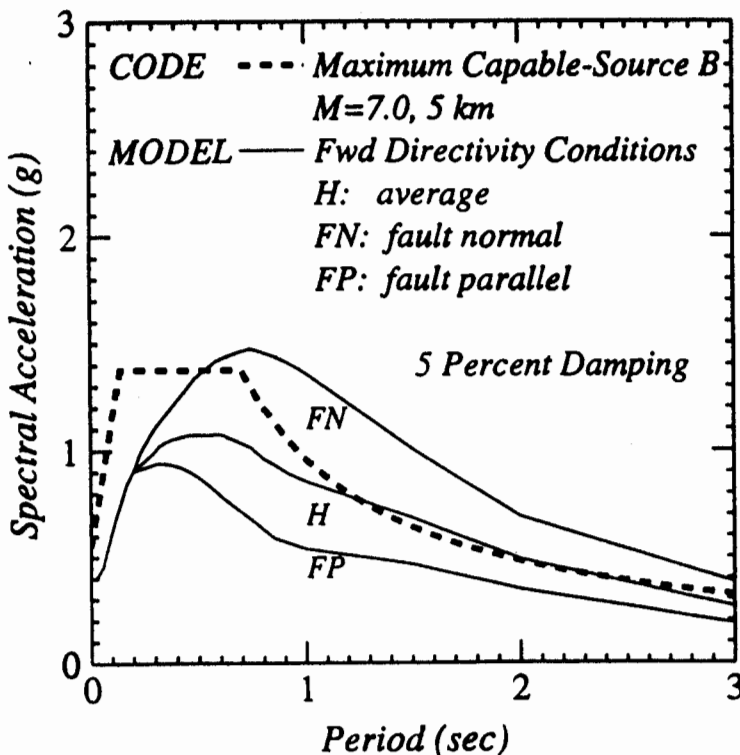
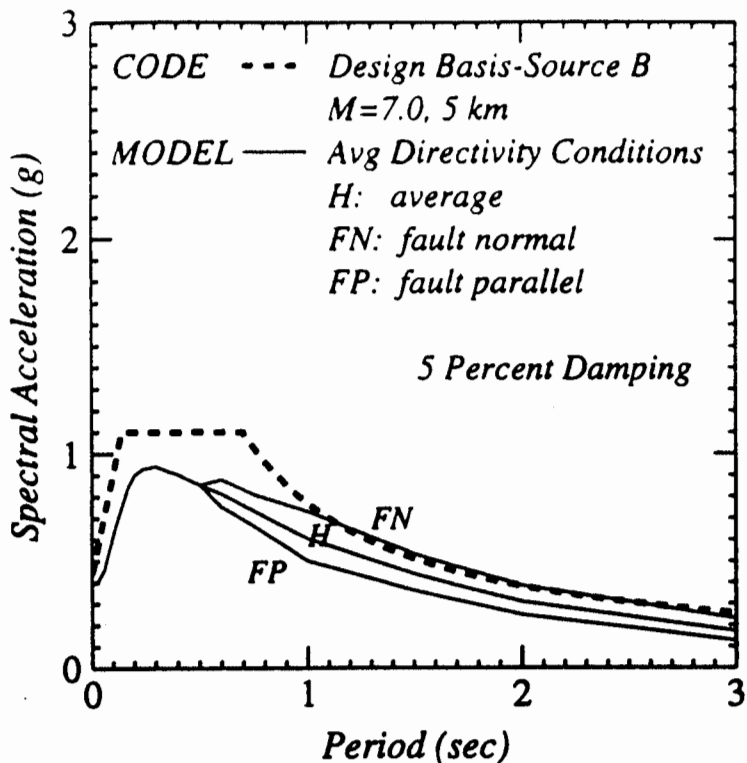


Figure 2. Response spectra for (top) average rupture directivity conditions and (bottom) forward rupture directivity conditions for a magnitude 7 earthquake at a distance of 5 km on soil. The response spectra are shown for the strike-normal, strike-parallel, and average horizontal components. Also shown for comparison are UBC spectra including the near-fault factor for design basis (top) and maximum capable (bottom) events.



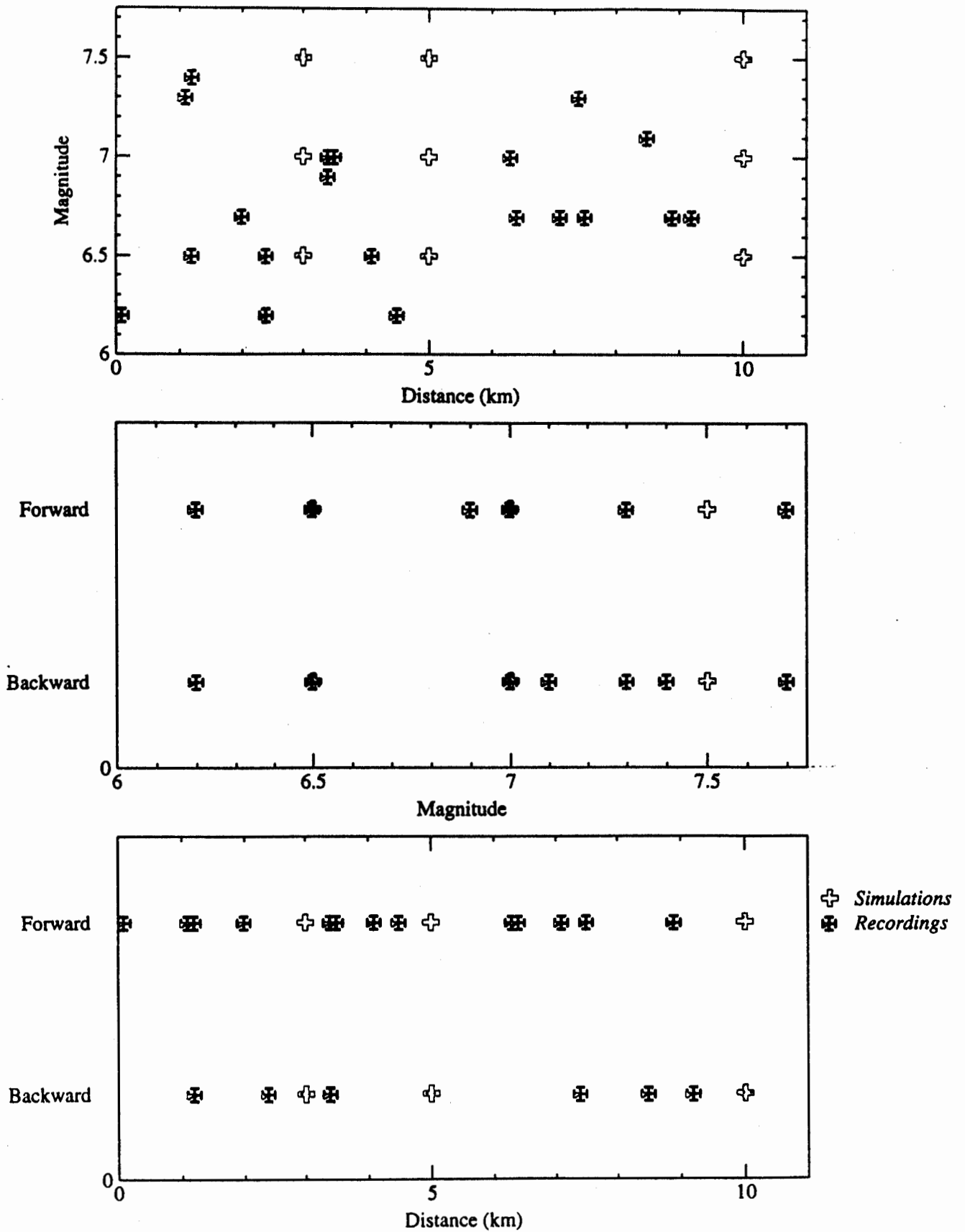


Figure 3. Distribution of recorded and simulated time histories. Top: magnitude vs distance; Center: directivity condition (forward or backward) vs. magnitude; Bottom: directivity condition (forward or backward) vs. distance.

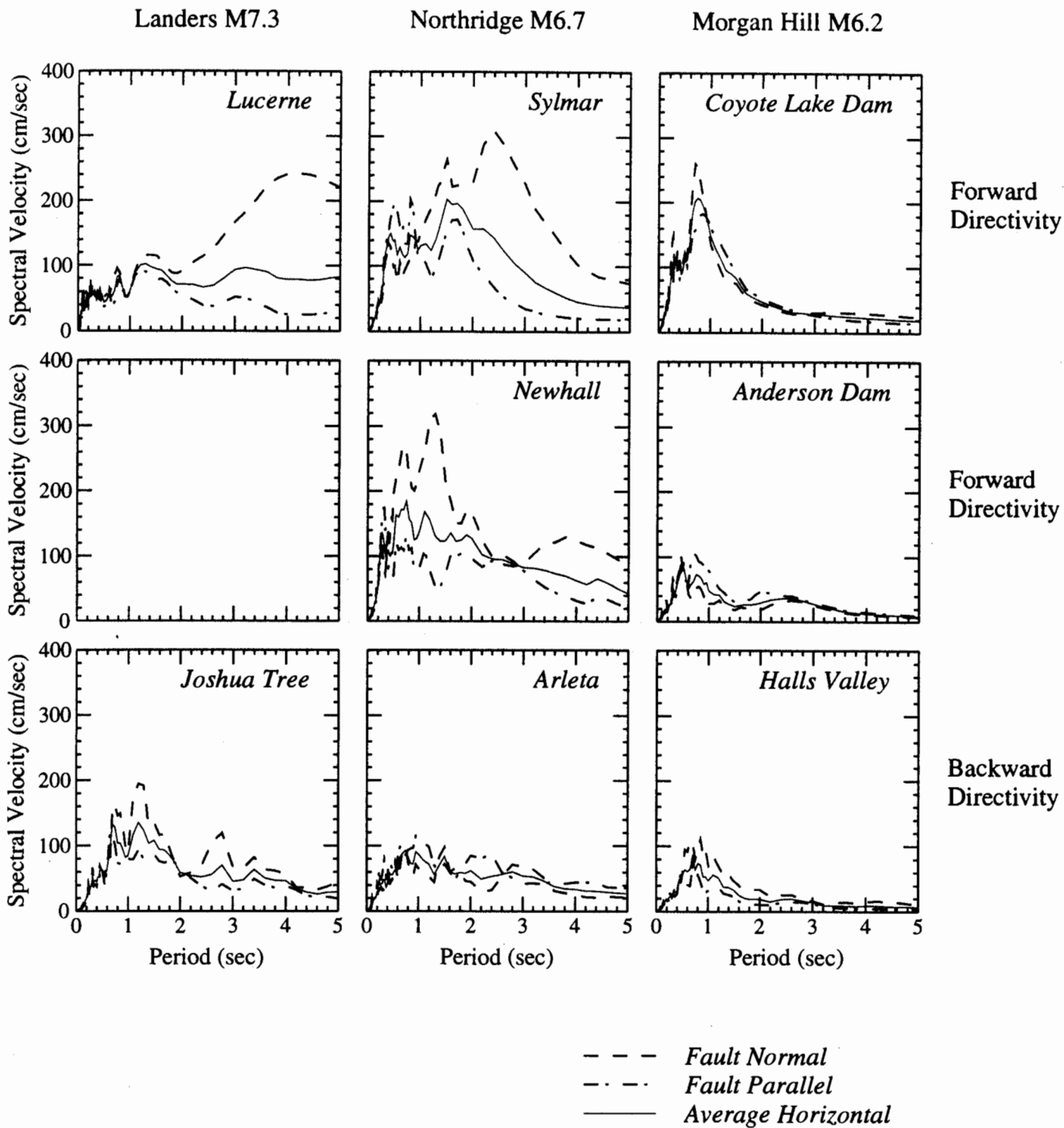
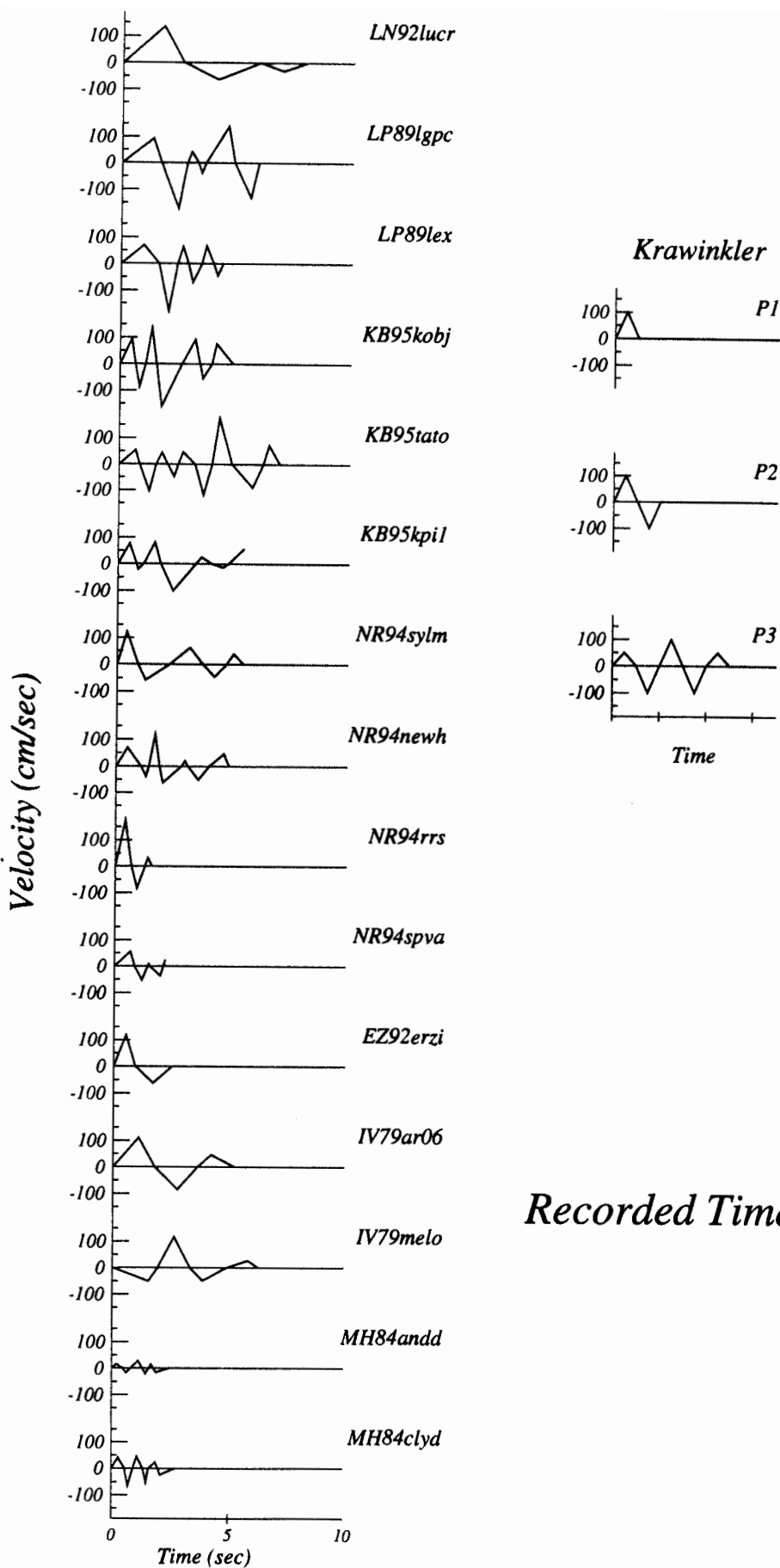


Figure 4. Response spectra of recorded time histories from 3 earthquakes showing dependence of spectrum on magnitude and directivity conditions.



## Recorded Time Histories

Figure 5. Left: Simplified representation of near fault velocity pulses in recorded ground motion. Right: Three representative pulses P1, P2 and P3 used in dynamic non-linear analyses by Krawinkler (1998).

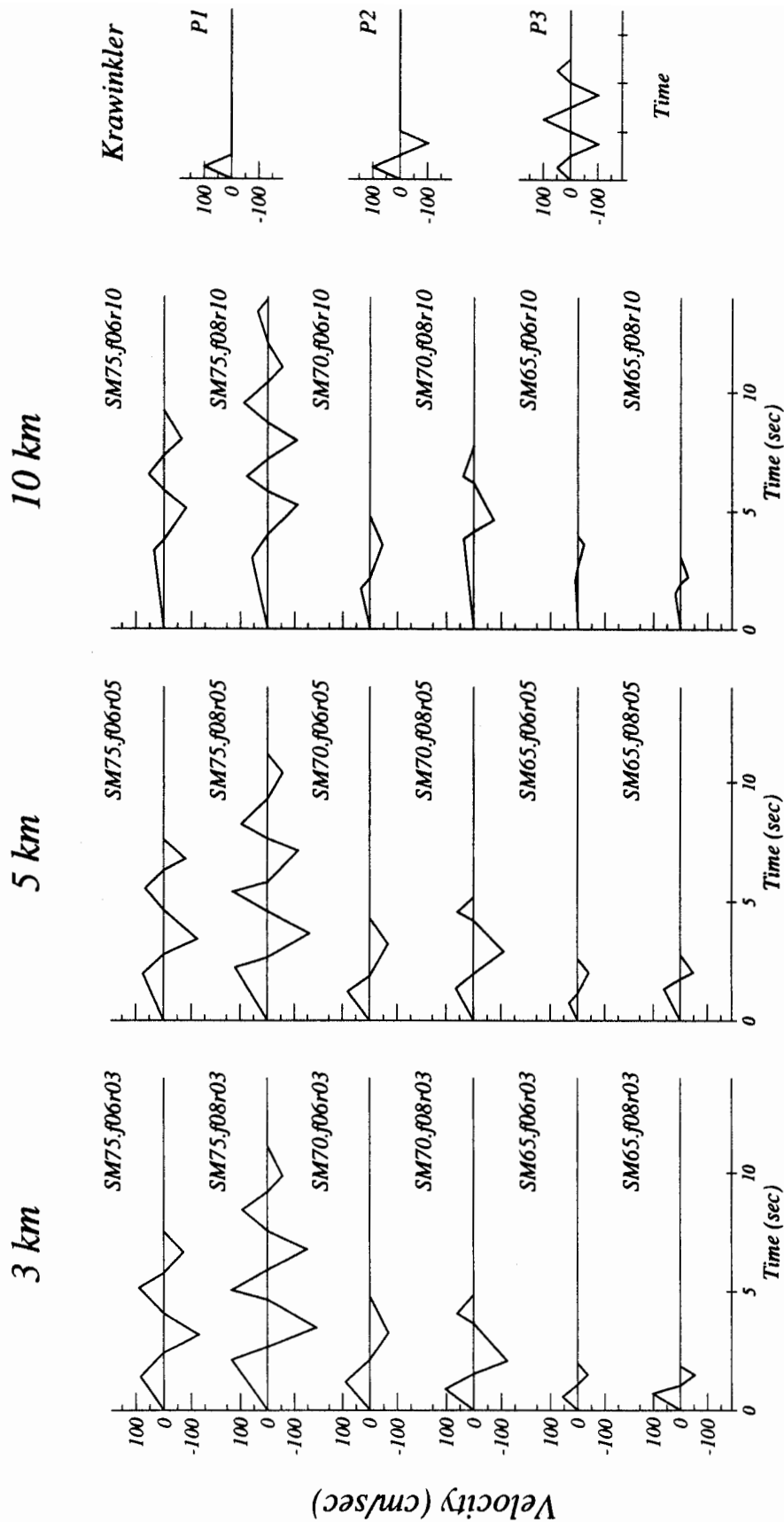


Figure 6. Left: Simplified representation of near fault velocity pulses in simulated ground motion. Right: Three representative pulses P1, P2 and P3 used in dynamic non-linear analyses by Krawinkler (1998).

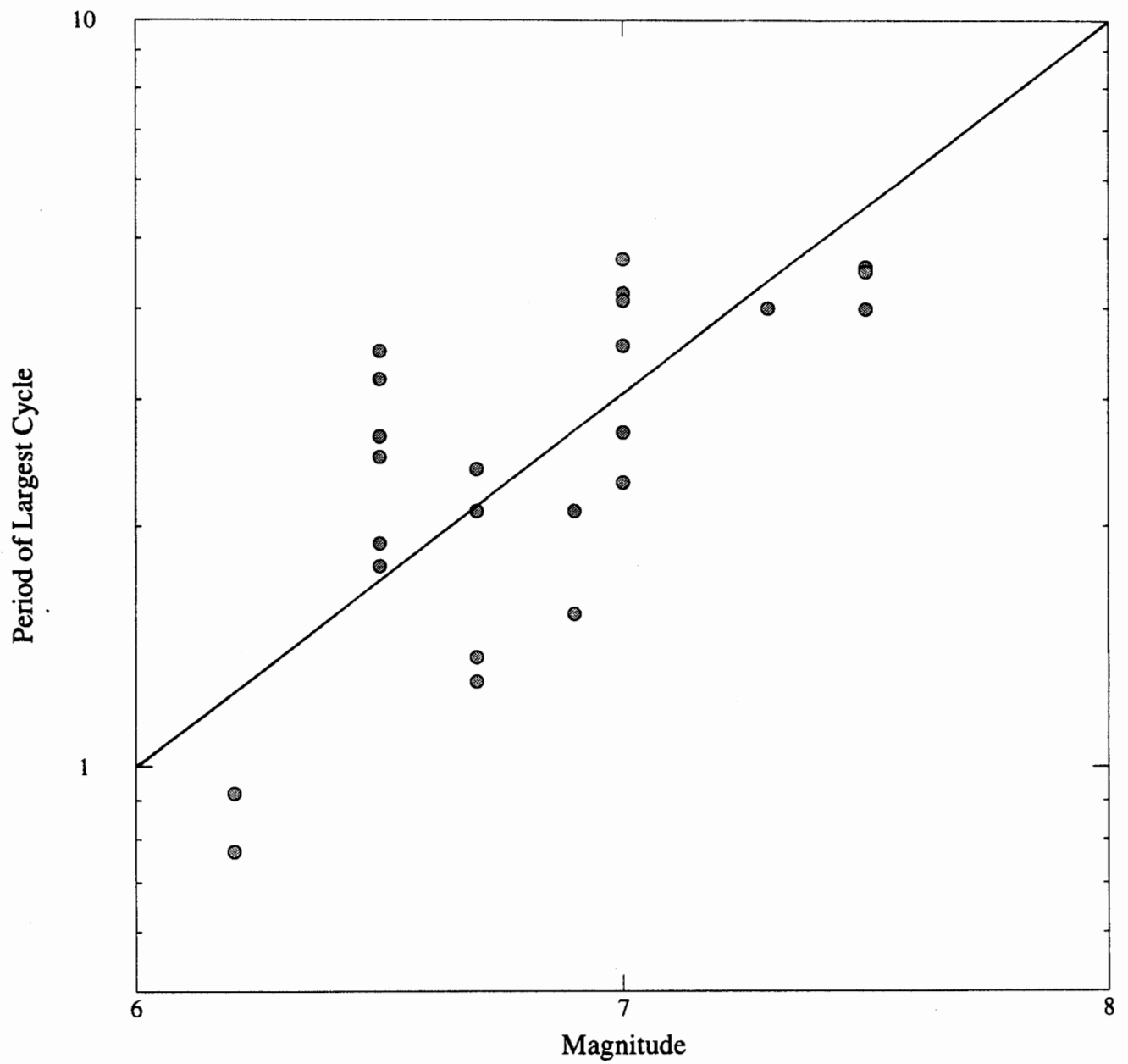


Figure 7. Relationship between the period of the largest cycle and magnitude.

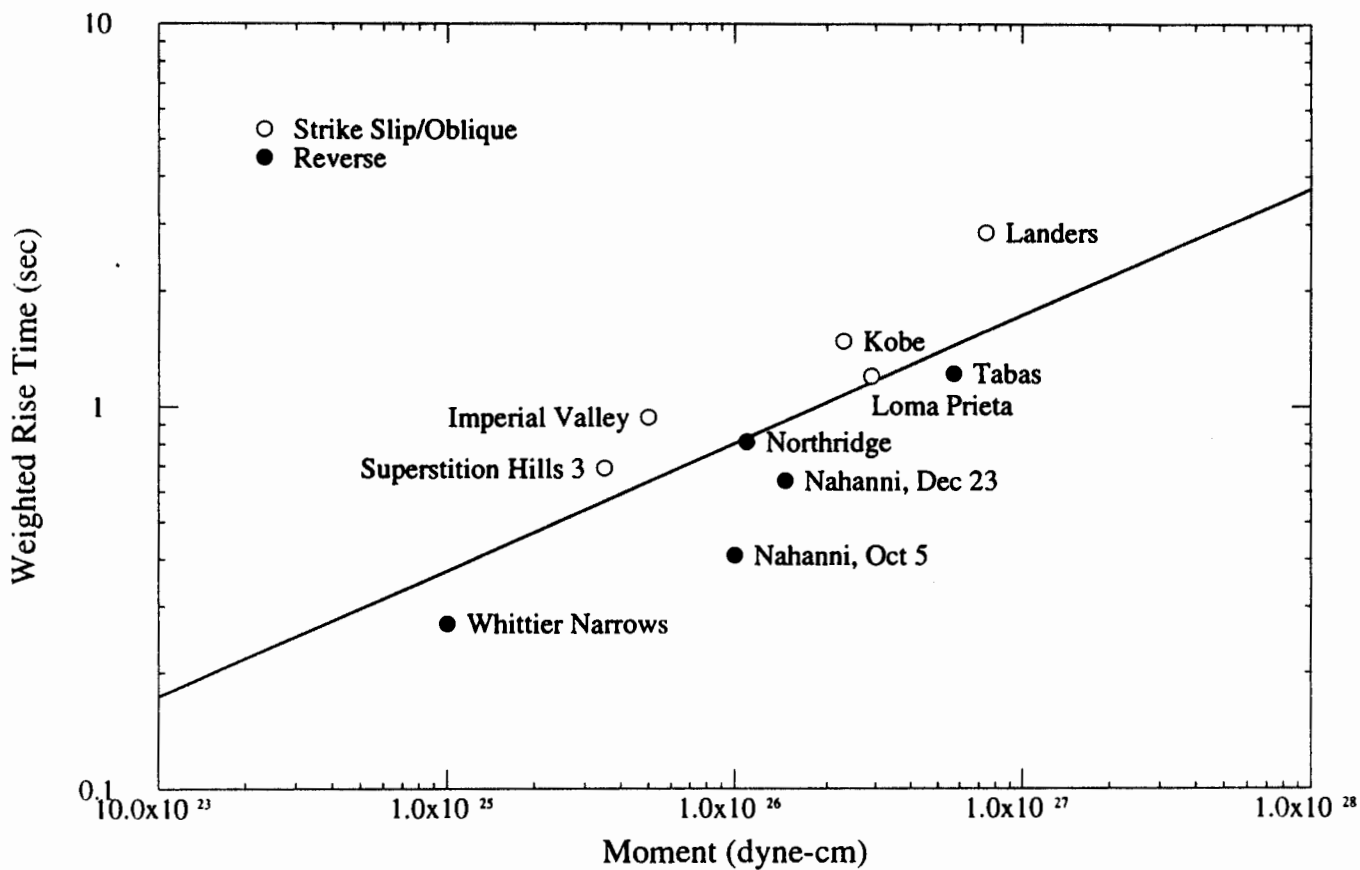


Figure 8. Relationship between rise time and seismic moment for crustal earthquakes. The rise times of reverse faulting earthquakes all fall below the self-similar relation derived from the data set as a whole, and those for strike-slip earthquakes fall above the relation.

**DEVELOPMENT OF IMPROVED DESIGN PROCEDURES FOR  
NEAR FAULT GROUND MOTIONS**

H. Krawinkler and B. Alavi

Department of Civil and Environmental Engineering  
Stanford University

**ABSTRACT**

The results of the study summarized here are intended to shed light on some of the important issues that affect the response of structures to near fault ground motions. Attempts are presented to identify salient response characteristics, to describe near fault ground motions by properties of equivalent pulses, and to utilize the pulse response characteristics to define behavior attributes of structures when subjected to near fault ground motions. The ultimate objective is to develop improved design procedures. Preliminary recommendations are made in this respect, but it must be understood that much more work needs to be done before comprehensive answers will be found.

**INTRODUCTION**

Recordings from recent earthquakes have provided much evidence that ground shaking near a fault rupture is characterized by a small number of pulses (often only one) with very high energy input. This holds true particularly in the "forward" direction, where the propagation of the fault rupture towards a site at a velocity close to the shear wave velocity causes most of the seismic energy from the rupture to arrive in a single large long-period pulse of motion that occurs at the beginning of the record (Somerville et al., 1997). The radiation pattern of the shear dislocation on the fault causes this large pulse of motion to be oriented in the direction perpendicular to the fault, causing the strike-normal peak velocity to be larger than the strike-parallel peak velocity (Somerville, 1998). This phenomenon requires consideration in the design process for structures that are located in the "near-fault" region, which is usually assumed to extend 10 to 15 km from the seismic source (1996 SEAOC Bluebook). Recent guidelines and codes have recognized the existence of the problem by providing magnitude and distance dependent "near source factors" that are applied directly to the design spectrum (or base shear) values.

The near source factors recommended presently may be considered as a stopgap measure that gives recognition to the problem but does not necessarily provide a final answer. The measure of increasing the design base shear without modifying the design shear force distribution over the height of the structure may not solve the problem. Moreover, the recent emphasis on performance-based seismic design makes it necessary to explicitly assess performance at different levels, ranging from immediate occupancy to collapse prevention, i.e., from nearly elastic behavior to near-collapse behavior. Much research is needed to identify and quantify the magnitude and distance dependent characteristics of near fault ground motions and address all the issues concerned with the response of different types of structures subjected to different types of near fault ground motions. This paper addresses only small parts of a big

problem, but the authors hope that the presented ideas and concepts will help in forming a foundation on which to base further research and development and, ultimately, a design procedure that will provide adequate and consistent protection of structures and their contents in near fault regions.

The results of the study summarized here are intended to shed light on some of the important issues that affect the response of structures to near fault ground motions. Attempts are presented to identify salient response characteristics, to describe near fault ground motions by properties of equivalent pulses, and to utilize the pulse response characteristics to define behavior attributes of structures when subjected to near fault ground motions. The ultimate objective is to develop improved design procedures. Preliminary recommendations are made in this respect, but it must be understood that much more work needs to be done before comprehensive answers will be found.

The conclusions drawn later have to be interpreted in the context of the assumptions that had to be made in order to arrive at preliminary answers to a complex problem. Some of the assumptions are summarized here:

- It is assumed that the two sets of near fault records used in this study cover the range of characteristics contained in typical near fault ground motions.
- Only ground motions in soil (NEHRP soil type D) are considered.
- Only the worst-case scenario is investigated; i.e., only forward directivity is considered, and the response evaluation is performed for the fault-normal component of the ground motion.
- This study is concerned only with the response of two-dimensional generic frames whose design and response behavior follow certain patterns that are described later.
- It is assumed that inelastic seismic response is controlled by the shear strength provided in each story, and that the story ductility ratio is the basic performance parameter.
- The emphasis is on long period frame structures whose fundamental period is longer than the period of the pulse that characterizes the near fault ground motion.
- Structures whose response is controlled by overturning moments (such as most wall-type structures) are not considered.

### NEAR FAULT GROUND MOTION RECORDS USED IN THIS STUDY

The records used in this study are discussed in more detail in Somerville (1998). Recorded and simulated motions are available for dynamic analysis. The designation and basic properties of the recorded soil motions are listed in Table 1. These motions cover a magnitude range from 6.2 to 7.4 and a distance range from 0.0 to 10.0 km, without a systematic pattern. The simulated motions represent two stations (f6 and f8) and cover systematic ranges of magnitude (6.5, 7.0, and 7.5) and distance (3, 5, and 10 km). For the analytical study summarized in this paper, only the fault-normal components of soil records with forward directivity are utilized. A total of 15 recorded motions and 18 simulated motions are available for this purpose.



Typical acceleration (elastic strength demand), velocity, and displacement spectra for two recorded time history pairs (both the fault-normal and fault-parallel components of a record) are presented in Fig. 1. The figure shows clearly the large difference between the fault-normal and fault-parallel components, and indicates in the velocity spectra a dominant peak at a well defined period (at 1.0 sec. for LP89lex, and 2.4 sec. for NR94sylv). As will be shown later, this period can be designated as the period of an equivalent pulse. Typical spectra for simulated ground motions are presented in Fig. 2. A predominant period is again evident in the velocity spectra. The figure illustrates the magnitude and distance dependence of the spectra.

A reference set of 15 “standard” records is utilized for comparison purposes. These records were used in past studies (Seneviratna and Krawinkler (1997) and are scaled in a manner so that the spectrum of each individual record matches the NEHRP soil type D spectrum with a minimum error, using discrete periods in the range of 0.6 to 4.0 seconds (constant velocity range). The mean acceleration spectrum of the 15 scaled records, referred to as 15-D\* (mean), is shown in Fig. 3 together with the NEHRP soil type D spectrum. Thus, in average, these 15-D\* time histories are reasonable representations of presently employed design ground motions.

Figure 4 shows the mean velocity spectrum of the 15-D\* records superimposed on the velocity spectra of several of the recorded near fault time histories. This figure is presented for two reasons. First, to illustrate the great variability in the response spectra that have to be expected from near fault ground motions, and second, to put the severity of near fault ground motions in perspective with present design ground motions. Maximum values of spectral velocities of the near fault records are several times those of the means of the design ground motions. Even though this figure presents an unduly negative picture (only fault-normal components of the near fault records are used, and individual records of the 15-D\* set have also relatively large peaks), it points out that near fault records can impose very large demands that need to be considered in the design process. The response of structures to the ground motions represented by these spectra is discussed later.

## SDOF AND MDOF SYSTEMS USED IN THIS STUDY

In the dynamic studies the structural systems are assumed to have 2% damping ( $\xi = 2\%$ ) rather than the customary 5%. The reason is that long period flexible structures are often steel frame structures for which 5% damping is difficult to justify. For SDOF response studies bilinear nondegrading load-deformation characteristics are used, usually with 3% strain hardening ( $\alpha = 3\%$ ).

MDOF structural systems are represented by a generic 2-dimensional single-bay frame whose strength and stiffness properties are tuned to specific requirements. The fundamental elastic period  $T$  is considered as a variable, but the number of stories is kept constant at 20. Story masses and story heights are assumed uniform over the height of the structure. The beam and column stiffnesses are tuned such that a straight line deflected shape results under a shear force pattern that corresponds to the SRSS combination of modal shear forces under a  $1/T$ -type response spectrum. For strength design the same SRSS shear force pattern is used to tune the member bending strengths in a manner that results in simultaneous yielding at all plastic hinge locations. Inelastic deformations are permitted only at plastic hinge locations at the column base and at beam ends, resulting in a mechanism that involves the full structure, see Fig. 5. In this

manner structures are generated whose story shear strengths are tuned to the widely used SRSS load pattern for a standard design spectrum. The base shear that causes yielding in the structure is denoted as  $V_y$ , and the lateral strength of the structure is defined in a dimensionless form by the parameter  $\gamma = V_y / W$ .

At all plastic hinge locations a bilinear nondegrading moment-rotation model with 3% strain hardening is used. This member hardening rule results in a story hardening stiffness of 3.6% for structures in which P-delta effects are neglected. Designs with P-delta effects are also performed. In these designs the magnitude of the gravity loads is tuned such that the elastic second order effect in the first story amounts to 10% (in present codes such a second order effect does not require design modifications). This P-delta effect results in a negative story stiffness of -2.8% of the elastic stiffness in the first story of the structure. The lateral load (base shear) vs. first story drift relationships with and without P-delta effect, obtained from a pushover analysis, are shown in Fig. 6. Even though the negative stiffness is rather small, the effects of P-delta were found to vary from negligible to dominant, depending on the case studied. This paper focuses only on behavior of structures without P-delta effects. However, it must be emphasized that the results of this study have demonstrated that P-delta effects may have a dominant effect on structural response and, in general, deserve serious consideration.

## RESPONSE OF SDOF AND MDOF SYSTEMS TO PULSE INPUT

In order to acquire a basic understanding of the response of structures to pulse loading of the type represented by near fault ground motions, elastic and inelastic dynamic analyses are performed on SDOF and MDOF systems using pulses as input motions. Various pulses are investigated, with the most basic ones being denoted as half pulse (P1), full pulse (P2) and multiple pulse (P3). The acceleration, velocity, and displacement time histories of pulses P2 and P3 are shown in Fig. 7. Pulse P1 consists of half of pulse P2. The pulses are fully defined by the pulse period  $T_p$  and the peak ground acceleration  $a_{g,max}$ . Other pulses with linear acceleration wave forms and with different configurations have also been studied, but it was found that their response characteristics do not differ by much from those of the three basic pulses.

Elastic spectral properties of the three basic pulses are presented in Fig. 8. The period axis is normalized to the pulse period  $T_p$  and the spectral values are normalized to the peak time history values. Peaks in the velocity spectra at  $T/T_p = 1.0$  are clearly evident for pulses P2 and P3. In the interpretation it must be considered that the peak displacement  $u_{g,max}$  of Pulse P3 is only half the value of the peak displacement of Pulses P1 and P2 (this explains the very large normalized spectral displacement values for P3). The inelastic strength demand spectra for specific ductility values, presented in Fig. 9, show large fluctuations for  $T/T_p$  values smaller than 1.0 but consistent and well established patterns (e.g., large strength reduction factors at the periods at which the elastic spectra have a peak) for  $T/T_p$  values of 1.0 or larger.

Story shear demand patterns over the height of the structure for elastic MDOF systems with various  $T/T_p$  ratios subjected to pulse P3 are shown in Fig. 10. Results are obtained from time history analysis (Fig. 10(a)) and SRSS modal combinations obtained from the pulse spectrum (Fig. 10(b)). Shown on both figures is also the SRSS pattern from the  $1/T$ -type spectrum that is used for strength design. The important observations are that for  $T/T_p$  values greater than 1.0 the shear force patterns exhibit a traveling wave effect that results in very high

story shears in upper stories, and that the SRSS modal combination is not a good surrogate for dynamic story shear forces, particularly if  $T/T_p > 1.0$ . This observation provides a hint that spectral analysis may not capture all important response characteristics of structures subjected to pulse-type ground motions. This is likely true for structures responding elastically and certainly true for structures responding inelastically.

The inelastic response of MDOF systems to pulse-type inputs shows special and peculiar characteristics, which later will be confirmed also for the response to near fault ground motions. The inelastic response is described here by maximum story ductility ratios,  $\mu$ , which become greater than 1.0 when the shear strength in any story is smaller than that causing elastic response. The base shear strength of MDOF systems subjected to pulse-type inputs is defined by the ratio  $\eta = V_y/ma_{g,max}$ . Distributions of ductility demands over the height of the structure for pulses P2 and P3 and ratios of  $T/T_p = 1.0$  and 2.0 are shown in Figs. 11 and 12 for various  $\eta$  values.

Since the MDOF structures are designed for a story shear force pattern corresponding to the SRSS modal combination for a  $1/T$ -type spectrum ("SRSS Pattern" in Fig. 10), it is expected that yielding will start in those stories in which the elastic story shear demand pattern exceeds the "SRSS Pattern" by the largest amount. As Fig. 10(a) indicates, for pulse P3 and  $T/T_p = 2.0$  this occurs about  $2/3^{\text{rd}}$  up the height of the structure. Figure 12(a) shows that the ductility demands are highest at this location, for relatively strong structures (large  $\eta$  values). However, for weak structures (small  $\eta$  values) a clear migration occurs of maximum ductility demands to the bottom of the structure. At the  $2/3^{\text{rd}}$  level the ductility demands stabilize around 3 and grow no further, whereas at the lower stories the ductility demands increase rapidly. The same phenomenon is observed for pulse P2 and  $T/T_p = 2.0$  (Fig. 11(a)).

The consistency of this phenomenon is surprising and deserves much scrutiny because it is one of the basic phenomena of pulse-type and near fault ground motion response. Clearly it has to do with the traveling wave effect that occurs primarily for  $T/T_p > 1.0$ . At  $T/T_p = 1.0$  this phenomenon starts to occur but is not yet very pronounced (see Figs. 11(b) and 12(b)).

A comprehensive picture of the maximum story ductility demand for pulse-type input, regardless of location in the structure, can be obtained from the  $\eta - \mu_{max}$  diagrams presented for various  $T/T_p$  ratios in Figs. 13 and 14. Figure 13, which is for pulse P2, shows a distinct stabilization range at a maximum ductility ratio of about 3 for  $T/T_p$  values larger than 1.0. In this range the base shear strength can be reduced by a factor larger than 2 without causing much, if any, increase in ductility demand. However, once a threshold of strength is reached, the ductility demand increases rapidly for a small reduction in strength. This is the threshold when the critical story has migrated from the upper portion to the bottom of the structure.

The strong statement made about stabilization of ductility demands has to be put in perspective. The results presented here are obtained for structures whose relative story shear strength follows the SRSS shear force distribution for a  $1/T$ -type design spectrum. Thus, the results are useful for performance evaluation of structures designed according to present practice. This is not to say that a strength design according to this shear force distribution is desirable. Desirable shear strength distributions are discussed later. Also, the results presented here for pulse-type inputs are relevant only if actual near fault ground motions can be represented by equivalent pulses. This issue is also discussed later.

## RESPONSE OF MDOF SYSTEMS TO NEAR FAULT GROUND MOTIONS

The fundamental observations made on response characteristics of MDOF systems to pulse inputs apply also to near fault ground motions. For elastic systems a traveling wave effect for long-period structures is evident in the story shear distribution over the height. This traveling wave effect is partially but not fully captured by an SRSS modal analysis; see Figure 15, which can be compared to Fig. 10. This wave effect has similar consequences on the inelastic response as were discussed for pulse inputs.

Figure 16 shows the distribution of story ductility demands over the height of the structure for the near fault records whose velocity spectra are shown in Fig. 4, for MDOF systems with a fundamental period  $T = 2.0$  sec. and a base shear strength defined by  $\gamma = V_y/W = 0.15$ . For records for which the ductility demands are small the demands are about the same over the height, but for records for which the demands are large there is a concentration of demands near the base of the structure. In the upper story the ductility demands do not exceed a value of about 5. Thus, a migration of demands towards the base is evident as the ground motion becomes more severe (or the structure becomes weaker). For comparison, the mean story ductility demands for the reference set of 15-D\* records are also shown. The graph indicates that, in the mean, an SRSS based strength design results in a uniform ductility distribution – for standard ground motions. However, the same design results in great variations of ductility demands over the height when a structure is subjected to near fault ground motions.

A comprehensive assessment of maximum story ductility demands for the same records and MDOF systems with  $T = 2.0$  sec. can be obtained from the  $\gamma - \mu_{\max}$  curves presented in Fig. 17. Many of the curves exhibit a kink (rapid change in slope) around a maximum ductility demand of about 3 to 4, which is the range in which the maximum story ductility demand migrates from the upper portion of the structure to the base. Again, a comparison of ductility demands between near fault records and the mean of the 15-D\* records looks alarming, but it must be kept in mind that all near fault records are fault-normal components and that the curve for the 15-D\* records shows only mean values but no peak values.

The story ductility migration phenomenon can be observed also in the story ductility demand graphs for individual records shown in Fig. 18. Distributions of demands over the height are shown for different  $\gamma$  values covering the range from elastic behavior to large ductility demands. In both cases the period is selected to be clearly larger than the period of the equivalent pulse (1.0 sec. for LP89lex and 2.4 sec. for NR94sylv). These results and others have demonstrated that important similarities exist between near fault responses and pulse responses. The issue of representing near fault records by equivalent pulses is pursued next.

## REPRESENTATION OF NEAR FAULT GROUND MOTIONS BY EQUIVALENT PULSES

Figure 4 shows that near fault ground motions come in great variations. Any attempt to evaluate performance and/or develop design criteria would have to be extremely complex unless such ground motions can be represented by simplified motions that reasonably replicate the most important response characteristics of the near field motions. Based on (1) visual inspection of time history records, (2) inspection and evaluation of velocity and displacement response spectra,

and (3) evaluation of elastic and inelastic MDOF response characteristics it is concluded that within certain limitations near fault records can be represented by equivalent pulses of the type discussed previously.

It is unreasonable to expect that this equivalence can be established for the full period range of interest. In particular in the short period range the near fault time history trace is likely contaminated by many ancillary waves that have little to do with the characteristics of the long-period high-energy pulse generated by the propagation of fault rupture. It is also likely that in the very long period range other phenomena (e.g., basin effects) contaminate the record. But it is postulated that in the range of periods from about one to three times the pulse period an equivalence between a near fault ground motion and a pulse can be established with reasonable confidence. In the following discussion it is assumed that an equivalence can be established for the range of  $T/T_p$  from 0.75 to 3.0, where  $T$  is the fundamental period of the structure and  $T_p$  is the period of the equivalent pulse.

Much effort has been devoted to establishing such an equivalence through a consistent procedure. The writers do not claim that the issue has been resolved to full satisfaction. There are many successes, but not all near fault records used in this study have become part of this success. The present status is that promising results have been obtained, but it must be emphasized that many more records need to be evaluated and more work needs to be done before a full equivalence can be established with confidence.

Three parameters are needed to establish a record to pulse equivalence; the pulse type (P1, P2, or P3), the pulse period  $T_p$ , and the pulse severity. The peak acceleration of the square wave acceleration history,  $a_{g,max}$ , shown in Fig. 7 is used for the latter purpose. In the following discussion the  $a_{g,max}$  of the equivalent pulse is referred to as the effective acceleration,  $a_{eff}$ . If these parameters are known, all other time history, spectral, and other response properties can be derived.

Engineering rather than seismological considerations are used in this study to deduce these parameters. Mostly judgment is employed to decide on the pulse type, based on an inspection of the time history trace and on a comparison between ground motion and pulse spectral shapes (primarily velocity and displacement spectra). A sensitivity study that supports these judgmental decisions still needs to be performed. The pulse period  $T_p$  is determined from the peaks of the velocity spectra. Typical examples are illustrated in Fig. 19, which shows the velocity spectra of the three basic pulses superimposed on the velocity spectra of two near fault records. In most cases a narrow range for  $T_p$  could be established rigorously, but at the end judgment had to be employed to decide on a final value.

Various procedures were investigated to determine the effective pulse acceleration  $a_{eff}$ ; the simplest one being the estimation of  $a_{eff}$  from the elastic displacement spectra (equating pulse and ground motion spectral displacement at  $T = T_p$ ). Inconsistent results were obtained when the so estimated values were used to compute ductility demands for MDOF systems. The reason is that no consideration is given to inelastic response characteristics when the determination of  $a_{eff}$  is based on elastic spectra only. Ultimately, a rigorous process was employed with the objective being the minimization of the differences between the maximum story ductility demands obtained from the near fault ground motion and the equivalent pulse. The following steps are used in this procedure:

1. Compute the  $\eta-\mu_{\max}$  curves for the selected pulse type for  $T/T_p = 0.75, 1.0, 1.5, 2.0, \& 3.0$ .
2. Compute the  $\gamma-\mu_{\max}$  curves for the near fault record for  $T/T_p = 0.75, 1.0, 1.5, 2.0, \text{ and } 3.0$ .
3. For each  $T/T_p$  value convert the  $\eta-\mu_{\max}$  curve of the pulse into a  $\gamma-\mu_{\max}$  curve [ $\gamma = (a_{\text{eff}}/g)\eta$ ] and find best-fit values for  $a_{\text{eff}}$  by minimizing the relative differences between the two  $\gamma-\mu_{\max}$  curves for the following three ranges of  $\mu_{\max}$ :  $\mu_{\max} = 1$  to 10 (full range of interest),  $\mu_{\max} = 4$  to 10 (low performance levels), and  $\mu_{\max} = 1.0$  (high performance level). The least-squares method is used to minimize the differences between the two curves.
4. Obtain final values for  $a_{\text{eff}}$  by averaging the best-fit values for the five period ratios. At this time this is done separately for the three ranges of  $\mu_{\max}$ .

The results of this procedure for the recorded and simulated near fault records are summarized in Tables 2 and 3, respectively. The tables list pulse type and period, as well as effective acceleration and peak velocity and displacement of the equivalent pulse for the three ductility ranges. The results are preliminary because a sensitivity study still needs to be performed. Even though the effective acceleration is used as the basic pulse parameter, the more relevant parameters for structural response evaluation are the peak velocity and displacement values (peak velocity =  $a_{\text{eff}}T_p/4$ ).

The results for the simulated records are rather consistent and show clear patterns with magnitude and distance (for peak velocity and displacement, but not for  $a_{\text{eff}}$ ). As expected, the values differ somewhat but not by a large amount between the three ductility ranges. Patterns for the recorded motions are not that evident, which may not be surprising when it is considered that these records come from several different events. The Landers (Lucerne) record (LN92lucr) has been omitted from Table 2 because it has a pulse period of greater than 4 seconds, which eliminates this record from consideration.

Figure 20 illustrates examples of “best” matches between the converted pulse  $\gamma-\mu_{\max}$  curves and the  $\gamma-\mu_{\max}$  curves for two ground motions, using the full ductility range of 1 to 10 for matching. Examples of story ductility demands obtained from a near fault record and the equivalent pulse are shown in Fig. 21 for cases of large and small ductility demands. It is observed that the important response characteristics are captured by the equivalent pulse.

The conclusion is that within the range of  $0.75 < T/T_p < 3.0$  it appears to be reasonable to represent near fault ground motions by an equivalent pulse. The accuracy of such a representation is good in many cases and questionable in some. More records need to be investigated to test this hypothesis and to establish “reliable” relationships between soil type dependent pulse parameters and magnitude, distance, and fault mechanism. If this can be done, the monumental task of developing design procedures and assessing performance of structures under near fault ground motions boils down to a thorough investigation of the elastic and inelastic response of MDOF systems to a small number of pulses. A few preliminary results are summarized in the next section.

## DESIGN CONSIDERATIONS FOR NEAR FAULT GROUND MOTIONS

The final goal of the work summarized here is the development of design recommendations. Such recommendations depend on the current state of knowledge and on the

design objectives, both of which are in a state of transition. The current state of knowledge on near fault ground motion effects is inadequate but growing rapidly, and design objectives are in a state of change because of the emergence of performance-based engineering. For instance, it would be inappropriate to focus only on one performance level, such as collapse prevention, because the results presented here have demonstrated that ductility demands are very sensitive not only to base shear strength but also to the story shear strength distribution over the height of the structure. On the other hand, at this time it would be inappropriate to make strong design recommendations because much more knowledge still needs to be acquired on the site dependent characteristics of near fault ground motions and on their effect on MDOF systems. Thus, only suggestions that deserve considerations in the design against near fault ground motion effects are presented here.

The results of this study indicate that it is reasonable to represent near fault ground motions by equivalent pulses, at least in the period range of  $0.75 < T/T_p < 3.0$ . Such pulses are defined by a pulse type, a pulse period  $T_p$ , and an effective acceleration  $a_{eff}$ . The square pulses (in the acceleration domain) shown in Fig. 7 appear to be adequate for this purpose. The type of pulse depends on the rupture mechanism and on the geologic medium between the source and the site.

Critical parameters are the pulse period  $T_p$  and a measure of pulse severity. The pulse period can be estimated with reasonable confidence from the peaks of the velocity response spectrum of the ground motion. For design purposes, the effective acceleration  $a_{eff}$  may be the most useful measure of severity, but from a ground motion perspective the effective velocity is a much more consistent parameter. It is important to note that in almost all cases the effective pulse velocity, computed as  $v_{eff} = a_{eff} (T_p/4)$ , is within 20% of the peak velocity (PGV) of the recorded near fault ground motions used in this study. It is tempting to recommend the use of the recorded peak velocity as  $v_{eff}$ , and to compute  $a_{eff}$  from this recorded parameter.

The parameters of the equivalent pulses are dependent on earthquake magnitude and closest distance to the fault, and also on the rupture mechanism. The data presented in Tables 2 and 3 provide some information on these parameters. A different approach for the determination of these parameters is proposed by Somerville, who presents preliminary relationships between pulse parameters ( $T_p$  and PGV) and seismological parameters ( $M_w$  and  $R$ ) in Somerville (1998). In many cases Somerville's closed-form predictions match well with the results obtained in this study, but in some cases the match is poor. This has to be expected since the recordings come from earthquakes with different rupture mechanisms and geological source to site conditions.

Provided that the equivalent pulse parameters can be predicted as a function of  $M_w$  and  $R$ , the design process can, for a large period range, be based on pulse response studies. This does not apply to the short period range (approximately  $T/T_p < 0.75$ ), where ground motions do not have discernable pulse characteristics. In this period range it may be appropriate to employ "standard design procedures" based on a spectrum that contains near fault modification factors. In the range of  $0.75 < T/T_p < 3.0$  advantage can be taken of information of the type discussed in this paper. It should be feasible to describe the seismic demand by pulse parameters that capture the range of  $T_p$  and  $a_{eff}$  making up the seismic hazard at the site. This process needs to pay attention to expected variations in  $T_p$  and  $a_{eff}$ , and to the fact that few structures are oriented precisely in the fault-normal direction. If the latter were the case, protection against near fault ground motions would be a challenging task. This is illustrated in Fig. 22, which shows

equivalent pulse spectra for three recorded ground motions superimposed on the NEHRP soil type D spectrum. The spectral amplification would be very large over a wide range of periods.

Presuming that the hazard is given in terms of pulse type,  $T_p$ ,  $a_{eff}$ , and associated pulse spectra, the task is to determine base shear demands and the shear strength distribution over the height of the structure. If the design objective is protection against damage, and elastic response is desired, the elastic spectra shown in Fig. 8 provide a good starting point for design. The base shear demand for elastic MDOF systems is related to the first mode SDOF strength demand as shown in Fig. 23. As can be seen, the MDOF/SDOF strength demand ratio is sensitive to the pulse type and the ratio  $T/T_p$ , and easily may exceed 1.0 for larger  $T/T_p$  ratios. Moreover, for  $T/T_p$  ratios greater than 1.0 the shear demand over the height of the structure is very different than for smooth  $1/T$ -type spectra, see Fig. 10. To achieve elastic response, either the base shear strength needs to be increased further, or the story shear strength needs to be tuned to the patterns illustrated in Fig. 10. This would be a significant departure from present design practice.

A new design approach is also needed to control story ductility demands for inelastic MDOF systems. For designs that follow a standard SRSS story shear strength pattern, the story ductility demands follow the trends illustrated in Figs. 11 to 14. Since such SRSS strength designs lead to very large variations of ductility demands over the height (Figs. 11 and 12), such designs may be undesirable for protection against near fault ground motions. It can be postulated that an ideal design should produce uniform ductility demands over the height in order to utilize equally the energy dissipation capacity available in all members. The story shear strength patterns that induce uniform ductility over the height can be found through an iterative process in which story shear strengths are varied until a desirable uniform story ductility is achieved. Patterns that result in uniform target ductilities from 1 (elastic behavior) to 8 are shown in Fig. 24 for pulse P2 and  $T/T_p = 2.0$ . The  $\mu = 1$  pattern corresponds to the elastic shear force distribution. The SRSS shear strength pattern based on a  $1/T$ -type spectrum is also shown.

The trends are clear and consistent. For close to elastic behavior ( $\mu = 1$  and 2) the story shear strength demands are high about  $2/3^{rd}$  up the structure, whereas for a uniform ductility of 3 or larger the demands are high at the base and decrease rapidly with height. Thus, the design shear force pattern for uniform ductility changes radically with the target ductility ratio, but the change takes place within a narrowly confined ductility range from 2 to 3.

The implications of this observation become clearer with the inspection of Fig. 25, which shows the base shear strength that is needed to limit the story ductility to a prescribed target value, for two story shear strength patterns. The solid line is for the case of the shear strength pattern causing uniform story ductility, and the dotted line is for the case of the SRSS shear force pattern. Up to a maximum story ductility of 3+ the two curves are radically different, whereas they are identical for larger ductilities. Thus, ductility control is a matter of base shear strength and story shear strength pattern, except for low strength structures ( $\mu > 3.5$ ) in which the first story is the critical one and the story shear strength pattern no longer matters. It appears to be prudent to design a structure for a base shear strength parameter  $\eta$  [ $\eta = (V/W)(g/a_{eff})$ ] of at least 0.25, because for smaller values of  $\eta$  the maximum ductility demand increases at a rapid rate. Limiting values of  $\eta$  for other  $T/T_p$  ratios can be obtained from the kinks in the  $\eta-\mu_{max}$  curves



shown in Figs. 13 and 14. Once  $\eta$  is determined, the base shear strength parameter  $\gamma = V/W$  can be obtained as  $\gamma = \eta(a_{\text{eff}}/g)$ .

A design for a minimum base shear strength as discussed in the previous paragraph should provide adequate protection against excessive ductility demands for a low performance level such as collapse prevention. It pays, however, little attention to damage control under more frequent earthquakes (smaller  $a_{\text{eff}}$ ). Damage control, represented by low ductility demands, is very sensitive to the distribution of story shear strength over the height of the structure. Figure 25 delivers a clear message in this regard, as illustrated in the following example. If the design is based on a standard SRSS shear strength distribution over the height (dotted line), the maximum ductility demand remains around three for a range of  $\eta$  from 0.25 to 0.75, the latter corresponding to an  $a_{\text{eff}}$  that is  $1/3^{\text{rd}}$  of  $a_{\text{eff}}$  for  $\eta = 0.25$ . Thus, significant damage has to be expected in upper stories under more frequent events (presuming that more frequent events still exhibit pulse-like near fault ground motion characteristics). However, the picture changes radically if the story shear strength distribution is tailored more towards the pattern shown in Fig. 24 for  $\mu = 1$  or 2. If this is done, the maximum ductility demand for smaller  $a_{\text{eff}}$  (larger  $\eta$  values) decreases rapidly. This can be seen from the solid line in Fig. 25.

Thus, the two important preliminary design conclusions to be drawn are as follows. First, in order to prevent excessive ductility demands under severe earthquakes, it is important to design long period structures ( $T/T_p > 1$ ) for a minimum strength parameter  $\eta$  that can be determined from kinks in the  $\eta$ - $\mu_{\text{max}}$  diagrams of equivalent pulses. Second, in order to provide damage control under smaller earthquakes, it is prudent to provide a story shear strength distribution over the height that is closer to the pattern for  $\mu = 1$  to 2 in Fig. 24. This could be achieved through careful tuning of story shear strengths, or in the simplest case through a bilinear shear strength patterns (for instance, constant shear strength to about  $2/3^{\text{rd}}$  of the structure height and linearly decreasing strength thereafter). It is a matter of economic consequences to what extent the second recommendation deserves consideration. It would be a significant departure from present practice.

## CONCLUSIONS

The analytical study with near fault records and elastic and inelastic SDOF and MDOF systems has led to the following preliminary conclusions:

- SRSS modal combinations do not fully capture the traveling wave effects for elastic MDOF systems with  $T/T_p > 1.0$ .
- Inelastic response leads to a significant redistribution of story ductility demands that cannot be captured from an elastic spectral or dynamic analysis.
- The fault-normal component of near fault ground motions with forward directivity is very severe and has pulse-like characteristics, which in the approximate period range of  $0.75 < T/T_p < 3.0$  can be represented by equivalent pulses.
- In this period range, design can be based on response characteristics of equivalent pulses, which are defined by the pulse type, the pulse period, and an effective acceleration (or velocity).

## SMIP98 Seminar Proceedings

- More work needs to be done to define the site seismic hazard in terms of these pulse parameters.
- The required base shear strength for ductility control under severe earthquakes can be determined from  $\eta-\mu_{max}$  curves of equivalent pulses, utilizing the aforementioned pulse parameters.
- Effective damage control for less severe near fault earthquakes necessitates a design that is based on a strength distribution over the height that is very different from the one employed in present practice.

### ACKNOWLEDGEMENTS

Most of the work summarized here was carried out under a subcontract with Woodward-Clyde and was funded by the California Department of Conservation as a SMIP 1997 Data Interpretation Project. Some of the results on pulse responses were obtained in a study sponsored by Kajima Corporation as part of the CUREe/Kajima Research Program. The financial support provided by the sponsors is gratefully acknowledged. The opinions expressed in this paper are those of the authors. The contents of the paper do not necessarily represent the policy of the sponsoring agency, and no endorsement by the State Government should be assumed. The constructive collaboration of Dr. P. Somerville of Woodward-Clyde on all aspects of this research is much appreciated.

### REFERENCES

- Seneviratna, G.D.P.K., and Krawinkler, H., 1997. "Evaluation of Inelastic MDOF Effects for Seismic Design," *John A. Blume Earthquake Engineering Center Report No. 120*, Department of Civil Engineering, Stanford University, June 1997.
- Somerville, P.G., Smith, N.F., Graves, R.W., and Abrahamson, N.A., 1997. "Modification of Empirical Strong Ground Motion Attenuation Relations to Include the Amplitude and Duration Effects of Rupture Directivity," *Seismological Research Letters*.68, 180-203.
- Somerville, P.G., 1998. "Development of an Improved Ground Motion Representation for Near Fault Ground Motions," *SMIP98 Seminar on Utilization of Strong-Motion Data*, Oakland, CA, Sept. 1998.

Table 1. Designation and Properties of Recorded Fault-Normal Components

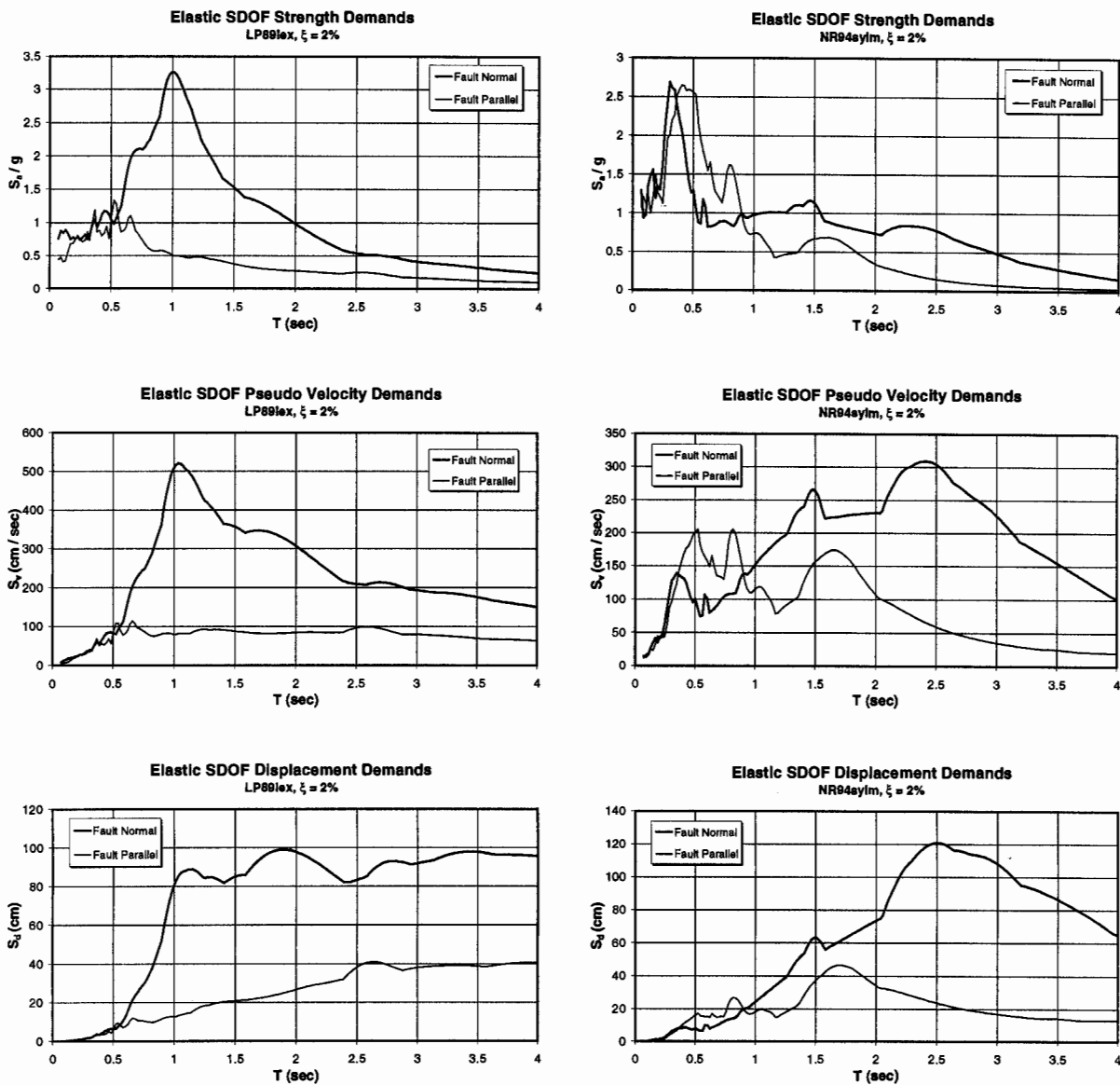
| Designation | Earthquake            | Station      | Directivity | Magnitude | Distance |
|-------------|-----------------------|--------------|-------------|-----------|----------|
| TB78tab     | Tabas, 1978           | Tabas        | backward    | 7.4       | 1.2      |
| LP89lgpc    | Loma Prieta, 1989     | Los Gatos    | forward     | 7.0       | 3.5      |
| LP89lex     | Loma Prieta, 1989     | Lexington    | forward     | 7.0       | 6.3      |
| CM92petr    | Mendocino, 1992       | Petrolia     | backward    | 7.1       | 8.5      |
| EZ92erzi    | Erzincan, 1992        | Erzincan     | forward     | 6.7       | 2.0      |
| LN92lucr    | Landers, 1992         | Lucerne      | forward     | 7.3       | 1.1      |
| NR94rrs     | Nothridge, 1994       | Rinaldi      | forward     | 6.7       | 7.5      |
| NR94sylv    | Nothridge, 1994       | Olive View   | forward     | 6.7       | 6.4      |
| KB95kobj    | Kobe, 1995            | JMA          | forward     | 6.9       | 3.4      |
| KB95tato    | Kobe, 1995            | Takatori     | forward     | 6.9       | 4.3      |
| IV40iviri   | Imperial Valley, 1940 | El Centro    | backward    | 6.9       | 10.0     |
| IV79ar06    | Imperial Valley, 1979 | Array 6      | forward     | 6.5       | 1.2      |
| IV79bond    | Imperial Valley, 1979 | Bond's Corn  | backward    | 6.5       | 2.4      |
| IV79melo    | Imperial Valley, 1979 | Meloland     | forward     | 6.5       | 0.0      |
| KB95kpi1    | Kobe, 1995            | Port Island  | forward     | 6.9       | 6.6      |
| LN92josh    | Landers, 1992         | Joshua Tree  | backward    | 7.3       | 7.4      |
| LP89corr    | Loma Prieta, 1989     | Corralitos   | backward    | 7.0       | 3.4      |
| MH84andd    | Morgan Hill, 1984     | Anderson D   | forward     | 6.2       | 4.5      |
| MH84clyd    | Morgan Hill, 1984     | Coyote L D   | forward     | 6.2       | 0.1      |
| MH84hall    | Morgan Hill, 1984     | Halls Valley | backward    | 6.2       | 2.4      |
| NR94newh    | Nothridge, 1994       | Newhall      | forward     | 6.7       | 7.1      |
| NR94nord    | Nothridge, 1994       | Arlita       | backward    | 6.7       | 9.2      |
| NR94spva    | Nothridge, 1994       | Sepulveda    | forward     | 6.7       | 8.9      |

Table 2. Equivalent Pulses for Recorded Near Fault Ground Motions (Forward Directivity)

| Record Name | M <sub>w</sub> | R (km) | Pulse Type | T <sub>p</sub> (sec) | μ = 1                  |                           |                       | μ = (1-10)             |                           |                       | μ = (4-10)             |                           |                       |
|-------------|----------------|--------|------------|----------------------|------------------------|---------------------------|-----------------------|------------------------|---------------------------|-----------------------|------------------------|---------------------------|-----------------------|
|             |                |        |            |                      | a <sub>eff</sub> (g's) | v <sub>eff</sub> (cm/sec) | u <sub>eff</sub> (cm) | a <sub>eff</sub> (g's) | v <sub>eff</sub> (cm/sec) | u <sub>eff</sub> (cm) | a <sub>eff</sub> (g's) | v <sub>eff</sub> (cm/sec) | u <sub>eff</sub> (cm) |
| LP89lgpc    | 7.0            | 3.5    | P3         | 3.0                  | 0.24                   | 176.6                     | 66.2                  | 0.23                   | 169.2                     | 63.5                  | 0.24                   | 176.6                     | 66.2                  |
| LP89lex     | 7.0            | 6.3    | P2         | 1.0                  | 0.71                   | 174.1                     | 43.5                  | 0.81                   | 198.7                     | 49.7                  | 1.04                   | 255.1                     | 63.8                  |
| EZ92erzi    | 6.7            | 2.0    | P2         | 2.3                  | 0.38                   | 214.3                     | 123.3                 | 0.46                   | 259.5                     | 149.2                 | 0.58                   | 327.2                     | 188.1                 |
| NR94rrs     | 6.7            | 7.5    | P2         | 1.0                  | 0.62                   | 152.1                     | 38.0                  | 0.74                   | 181.5                     | 45.4                  | 0.80                   | 196.2                     | 49.1                  |
| NR94sylv    | 6.7            | 6.4    | P3         | 2.4                  | 0.18                   | 105.9                     | 31.8                  | 0.17                   | 100.1                     | 30.0                  | 0.19                   | 111.8                     | 33.6                  |
| KB95kobj    | 6.9            | 3.4    | P2         | 0.9                  | 0.95                   | 209.7                     | 47.2                  | 0.88                   | 194.2                     | 43.7                  | 0.94                   | 207.5                     | 46.7                  |
| KB95tato    | 6.9            | 4.3    | P3         | 2.0                  | 0.38                   | 186.4                     | 46.6                  | 0.33                   | 161.9                     | 40.5                  | 0.31                   | 152.1                     | 38.0                  |
| IV79ar06    | 6.5            | 1.2    | P2         | 3.4                  | 0.13                   | 108.4                     | 92.1                  | 0.13                   | 108.4                     | 92.1                  | 0.16                   | 133.4                     | 113.4                 |
| IV79melo    | 6.5            | 0.0    | P2         | 2.8                  | 0.15                   | 103.0                     | 72.1                  | 0.15                   | 103.0                     | 72.1                  | 0.19                   | 130.5                     | 91.3                  |
| KB95kpi1    | 6.9            | 6.6    | P2         | 1.8                  | 0.28                   | 123.6                     | 55.6                  | 0.24                   | 105.9                     | 47.7                  | 0.27                   | 119.2                     | 53.6                  |
| MH84andd    | 6.2            | 4.5    | P2         | 0.8                  | 0.18                   | 35.3                      | 7.1                   | 0.16                   | 31.4                      | 6.3                   | 0.17                   | 33.4                      | 6.7                   |
| MH84clyd    | 6.2            | 0.1    | P3         | 0.8                  | 0.41                   | 80.4                      | 8.0                   | 0.49                   | 96.1                      | 9.6                   | 0.55                   | 107.9                     | 10.8                  |
| NR94newh    | 6.7            | 7.1    | P2         | 1.3                  | 0.39                   | 124.3                     | 40.4                  | 0.34                   | 108.4                     | 35.2                  | 0.40                   | 127.5                     | 41.4                  |
| NR94spva    | 6.7            | 8.9    | P3         | 2.7                  | 0.10                   | 66.2                      | 22.3                  | 0.08                   | 53.0                      | 17.9                  | 0.08                   | 53.0                      | 17.9                  |

Table 3. Equivalent Pulses for Simulated Near Fault Ground Motions(Forward Directivity)

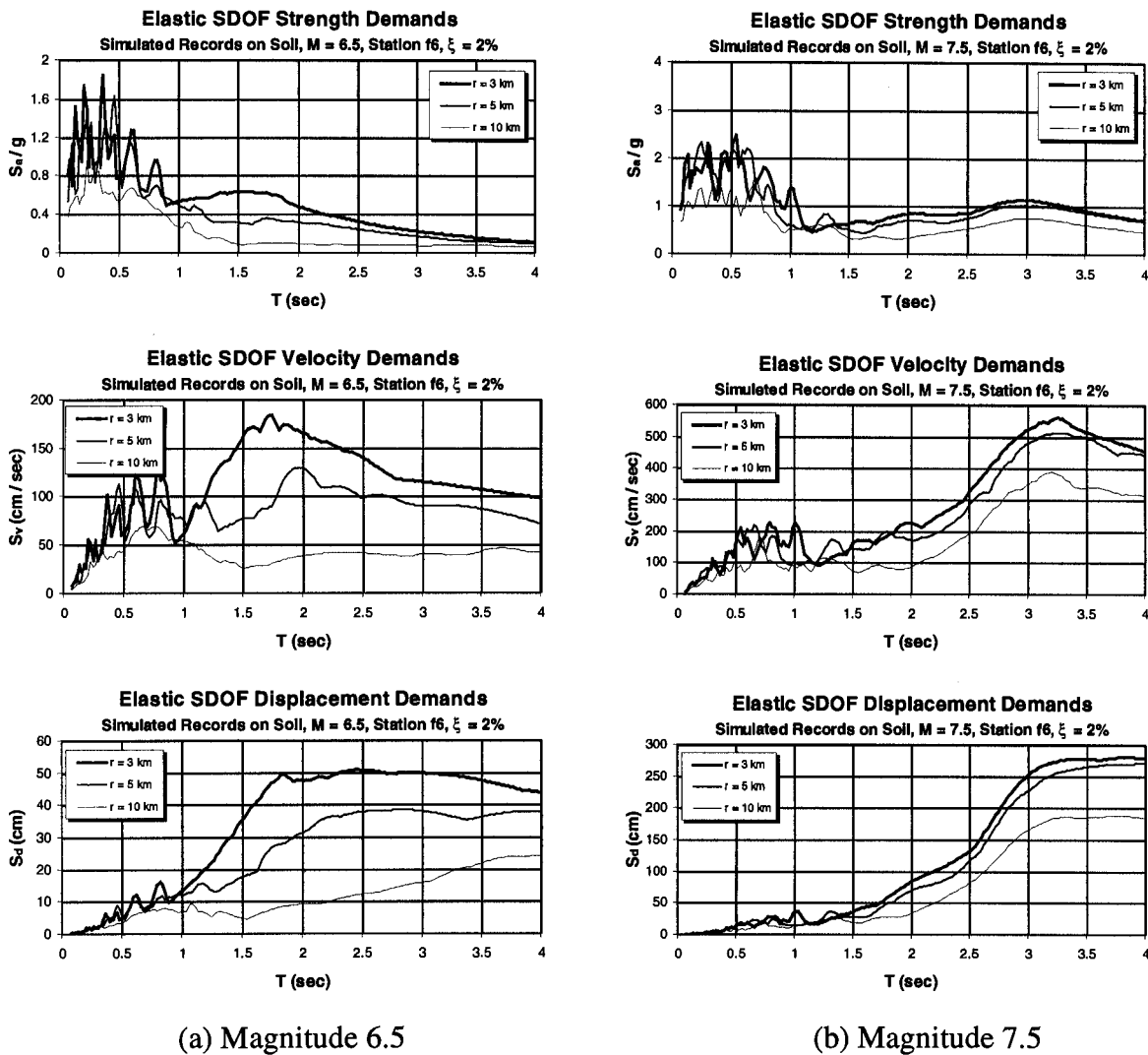
| Ststion | M <sub>w</sub> | R (km) | Pulse Type | T <sub>p</sub> (sec) | μ = 1                  |                           |                       | μ = (1-10)             |                           |                       | μ = (4-10)             |                           |                       |
|---------|----------------|--------|------------|----------------------|------------------------|---------------------------|-----------------------|------------------------|---------------------------|-----------------------|------------------------|---------------------------|-----------------------|
|         |                |        |            |                      | a <sub>eff</sub> (g's) | v <sub>eff</sub> (cm/sec) | u <sub>eff</sub> (cm) | a <sub>eff</sub> (g's) | v <sub>eff</sub> (cm/sec) | u <sub>eff</sub> (cm) | a <sub>eff</sub> (g's) | v <sub>eff</sub> (cm/sec) | u <sub>eff</sub> (cm) |
| f6      | 6.5            | 3      | P2         | 1.7                  | 0.17                   | 70.9                      | 30.1                  | 0.18                   | 75.05                     | 31.9                  | 0.21                   | 87.6                      | 37.2                  |
| f8      | 6.5            | 3      | P2         | 1.2                  | 0.35                   | 103.0                     | 30.9                  | 0.45                   | 132.44                    | 39.7                  | 0.51                   | 150.1                     | 45.0                  |
| f6      | 6.5            | 5      | P2         | 2.0                  | 0.10                   | 49.1                      | 24.5                  | 0.10                   | 49.05                     | 24.5                  | 0.11                   | 54.0                      | 27.0                  |
| f8      | 6.5            | 5      | P2         | 2.1                  | 0.17                   | 87.6                      | 46.0                  | 0.19                   | 97.85                     | 51.4                  | 0.20                   | 103.0                     | 54.1                  |
| f6      | 6.5            | 10     | P2         | 2.6                  | 0.04                   | 25.5                      | 16.6                  | 0.03                   | 19.13                     | 12.4                  | 0.04                   | 25.5                      | 16.6                  |
| f8      | 6.5            | 10     | P2         | 3.0                  | 0.05                   | 36.8                      | 27.6                  | 0.04                   | 29.43                     | 22.1                  | 0.05                   | 36.8                      | 27.6                  |
| f6      | 7.0            | 3      | P2         | 3.2                  | 0.13                   | 102.0                     | 81.6                  | 0.12                   | 94.18                     | 75.3                  | 0.15                   | 117.7                     | 94.2                  |
| f8      | 7.0            | 3      | P2         | 3.4                  | 0.20                   | 166.8                     | 141.8                 | 0.20                   | 166.77                    | 141.8                 | 0.20                   | 166.8                     | 141.8                 |
| f6      | 7.0            | 5      | P2         | 3.5                  | 0.11                   | 94.4                      | 82.6                  | 0.10                   | 85.84                     | 75.1                  | 0.12                   | 103.0                     | 90.1                  |
| f8      | 7.0            | 5      | P2         | 3.6                  | 0.16                   | 141.3                     | 127.1                 | 0.16                   | 141.26                    | 127.1                 | 0.17                   | 150.1                     | 135.1                 |
| f6      | 7.0            | 10     | P2         | 5.0                  | 0.04                   | 49.1                      | 61.3                  | 0.03                   | 36.79                     | 46.0                  | 0.03                   | 36.8                      | 46.0                  |
| f8      | 7.0            | 10     | P2         | 3.3                  | 0.11                   | 89.0                      | 73.4                  | 0.10                   | 80.93                     | 66.8                  | 0.11                   | 89.0                      | 73.4                  |
| f6      | 7.5            | 3      | P3         | 3.2                  | 0.19                   | 149.1                     | 59.6                  | 0.22                   | 172.66                    | 69.1                  | 0.23                   | 180.5                     | 72.2                  |
| f8      | 7.5            | 3      | P3         | 3.2                  | 0.28                   | 219.7                     | 87.9                  | 0.27                   | 211.90                    | 84.8                  | 0.28                   | 219.7                     | 87.9                  |
| f6      | 7.5            | 5      | P3         | 3.2                  | 0.17                   | 133.4                     | 53.4                  | 0.19                   | 149.11                    | 59.6                  | 0.21                   | 164.8                     | 65.9                  |
| f8      | 7.5            | 5      | P3         | 3.2                  | 0.25                   | 196.2                     | 78.5                  | 0.24                   | 188.35                    | 75.3                  | 0.25                   | 196.2                     | 78.5                  |
| f6      | 7.5            | 10     | P3         | 3.2                  | 0.12                   | 94.2                      | 37.7                  | 0.14                   | 109.87                    | 43.9                  | 0.14                   | 109.9                     | 43.9                  |
| f8      | 7.5            | 10     | P3         | 3.2                  | 0.19                   | 149.1                     | 59.6                  | 0.18                   | 141.26                    | 56.5                  | 0.19                   | 149.1                     | 59.6                  |



(a) Lexington Dam (LP89lex)

(b) Sylmar (NR94sylv)

Figure 1. Acceleration (Elastic Strength Demand), Velocity, and Displacement Spectra of Two Recorded Ground Motions (Fault-Normal and Fault-Parallel Components)



(a) Magnitude 6.5 (b) Magnitude 7.5  
 Figure 2. Acceleration (Elastic Strength Demand), Velocity, and Displacement Spectra of Simulated Ground Motions at Station f6 (Fault-Normal Components Only)

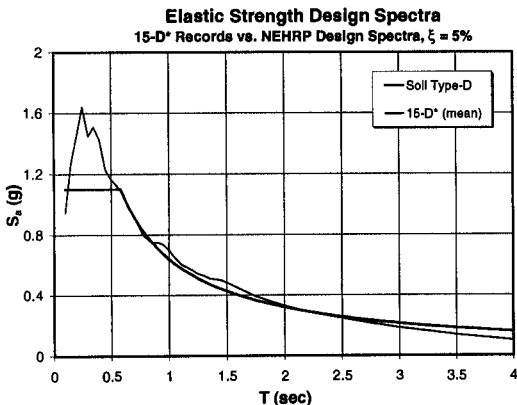


Figure 3. Mean Acceleration (Strength Demand) Spectrum of Reference Set of Records, 15-D\*

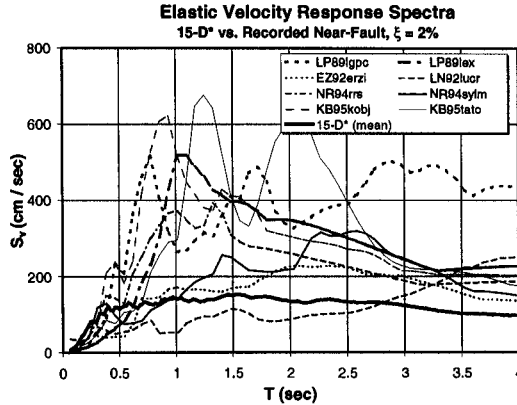


Figure 4. Velocity Response Spectra of Near Fault and Reference Ground Motions

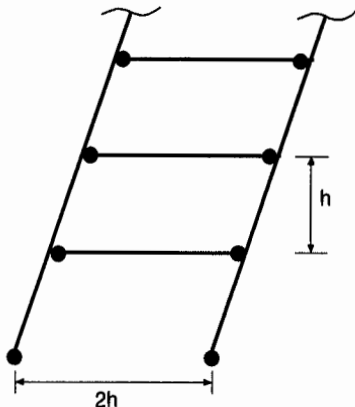


Figure 5. Global Mechanism for Generic Structure (Beam Hinge Model)

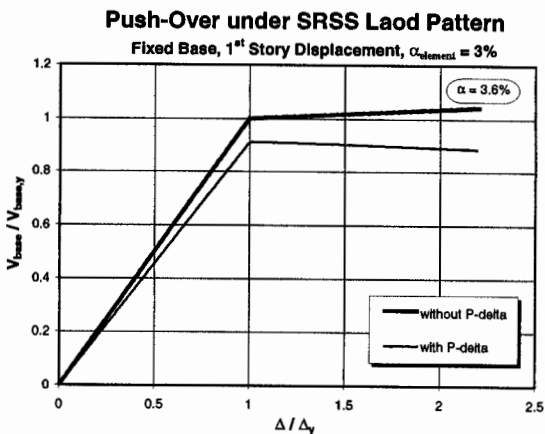


Figure 6. Pushover Response of First Story of Generic Structure with and without P-Delta

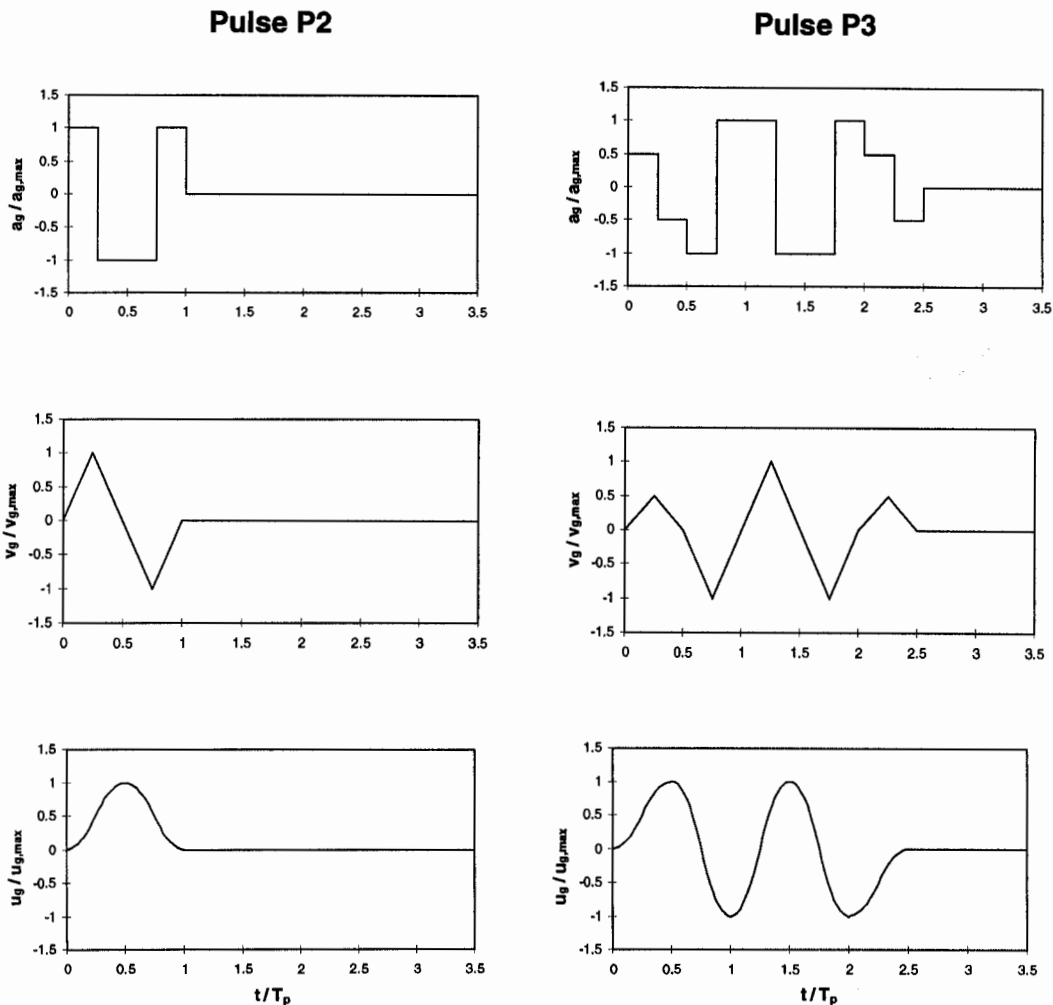


Figure 7. Acceleration, Velocity, and Displacement Time Histories of Pulses P2 and P3

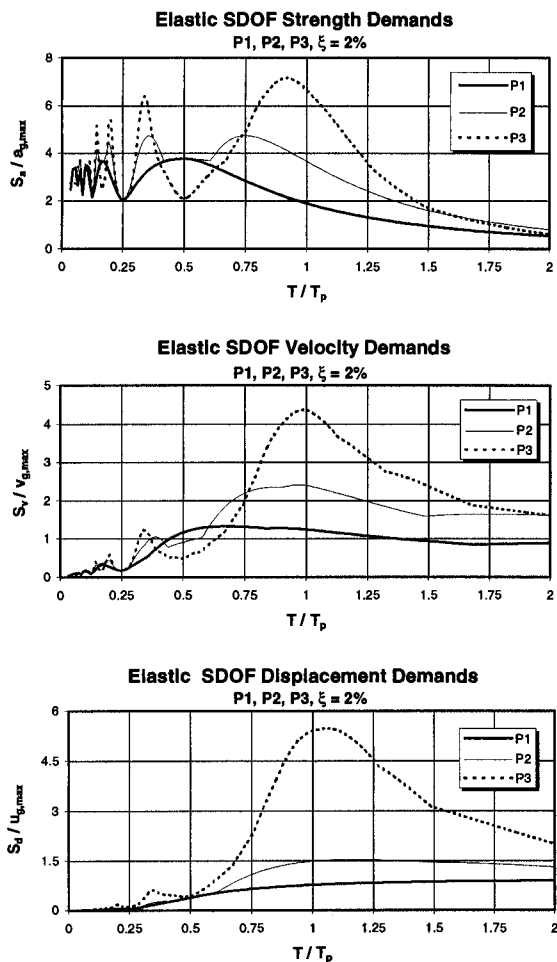


Figure 8. Elastic Strength Demand, Velocity, and Displ. Spectra for Pulses P1, P2, and P3

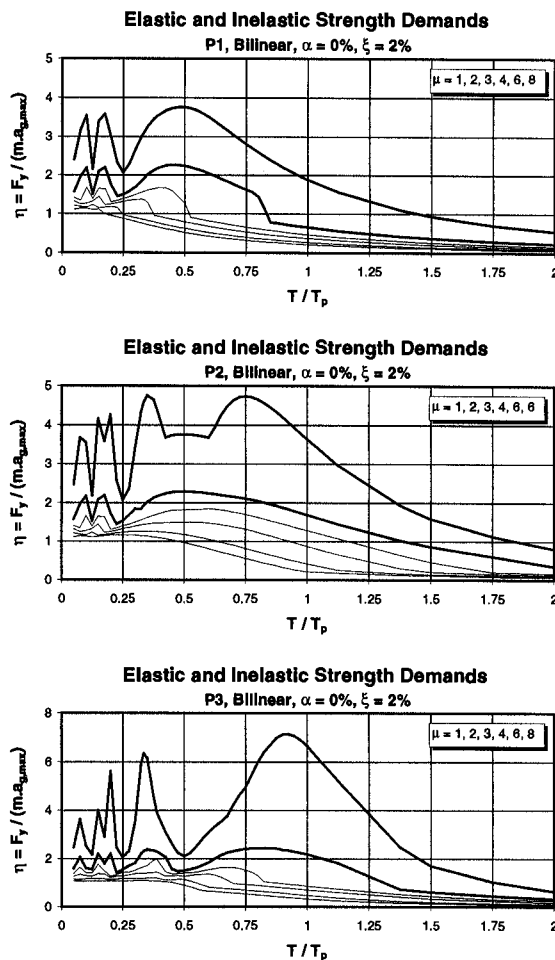
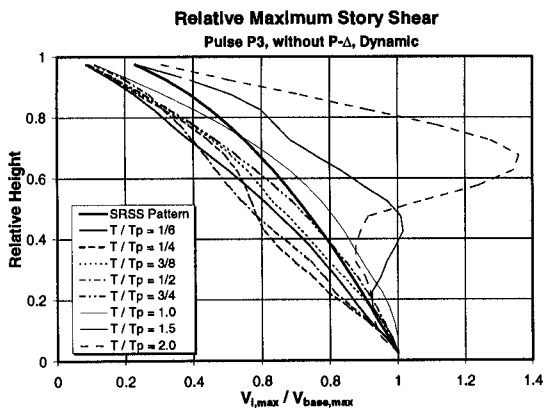
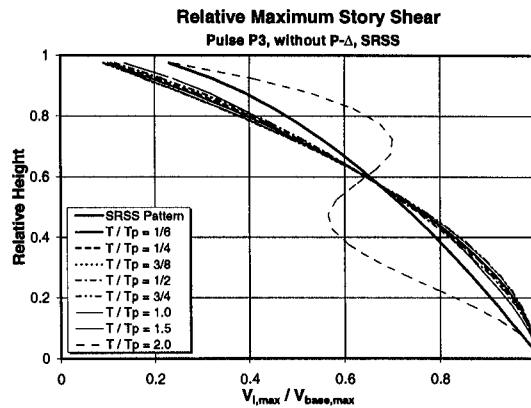


Figure 9. Elastic and Inelastic Strength Demand Spectra for Pulses P1, P2, and P3

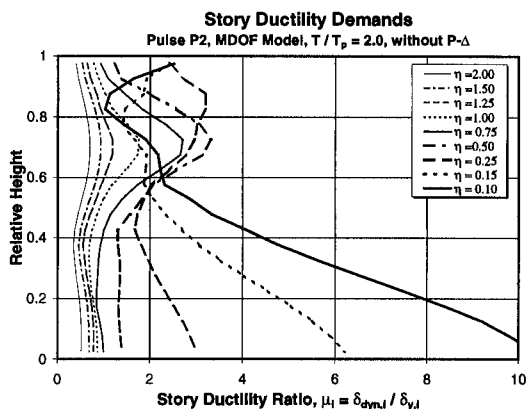


(a) From Time History Analysis

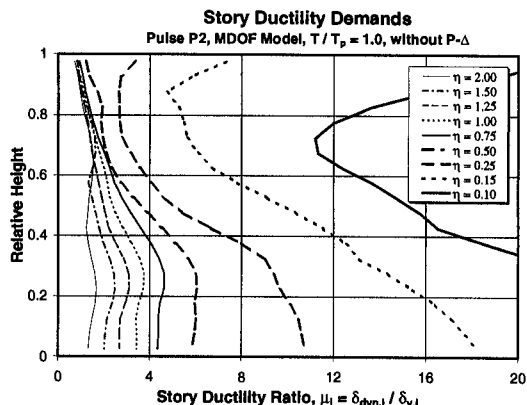


(b) From SRSS Modal Combination

Figure 10. Normalized Elastic Story Shear Demands for Pulse P3, Various Values of  $T/T_p$

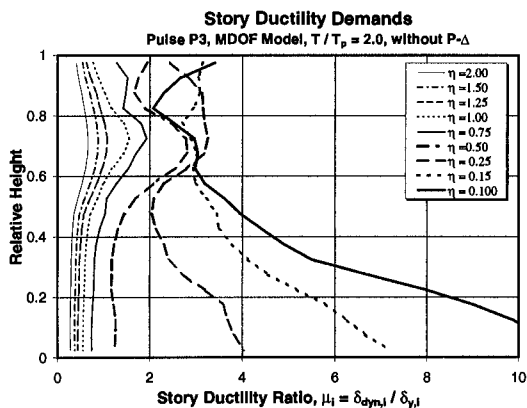


(a)  $T/T_p = 2.0$

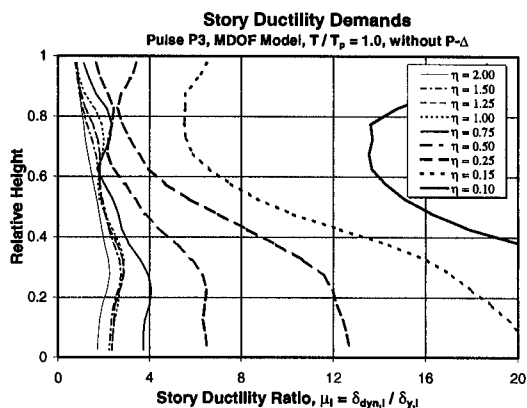


(b)  $T/T_p = 1.0$

Figure 11. Story Ductility Demands for Pulse P2, Various Values of  $\eta$



(a)  $T/T_p = 2.0$



(b)  $T/T_p = 1.0$

Figure 12. Story Ductility Demands for Pulse P3, Various Values of  $\eta$

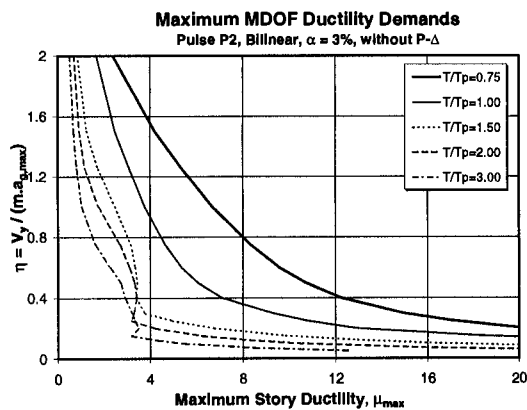


Figure 13. Base Shear Strength vs. Maximum Story Ductility Demands for Various  $T/T_p$  Values, Pulse P2

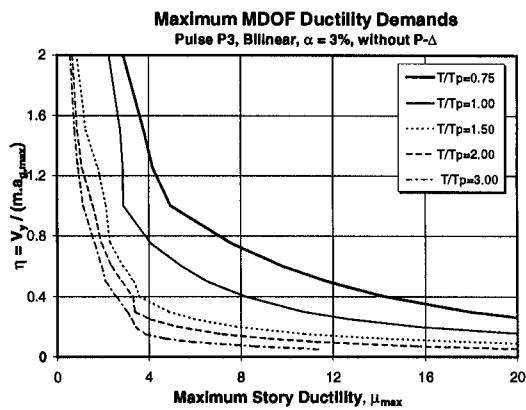
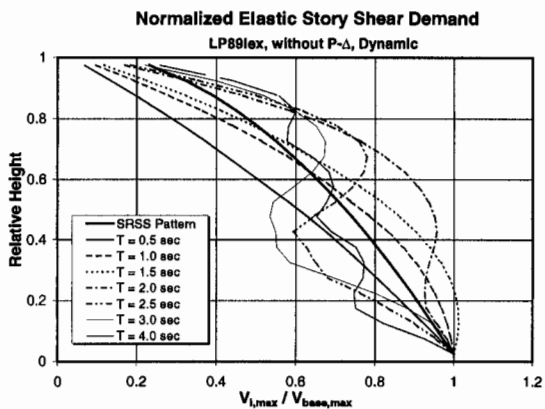
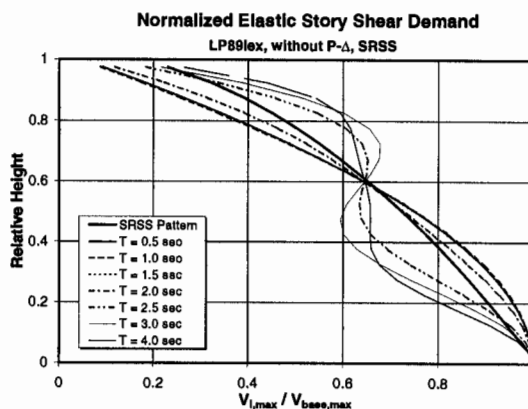


Figure 14. Base Shear Strength vs. Maximum Story Ductility Demands for Various  $T/T_p$  Values, Pulse P3





(a) From Time History Analysis



(b) From SRSS Modal Combination

Figure 15. Normalized Elastic Story Shear Demands for Record LP89lex, Various Values of T

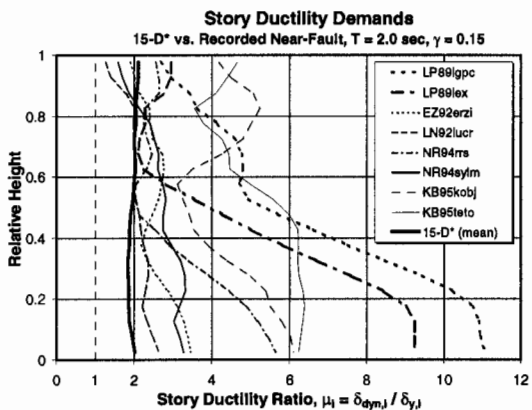


Figure 16. Story Ductility Demands for Several Near Fault Records, T = 2.0 sec., γ = 0.15

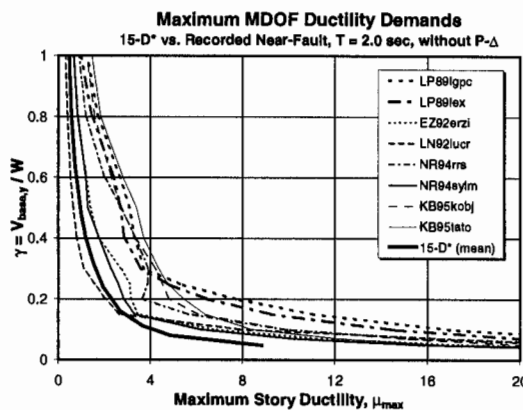
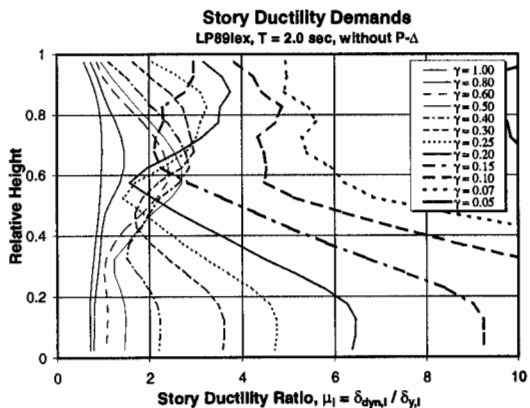
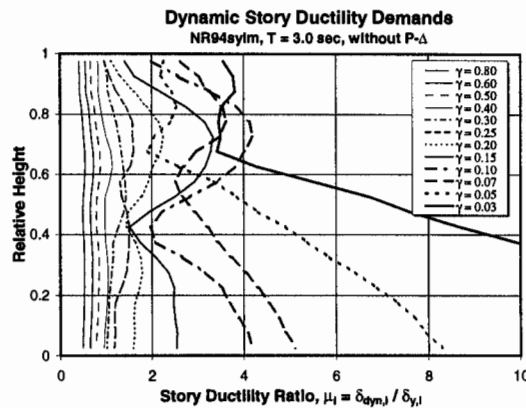


Figure 17. Base Shear Strength vs. Maximum Ductility Demand for Several Near Fault Records, T = 2.0 sec.

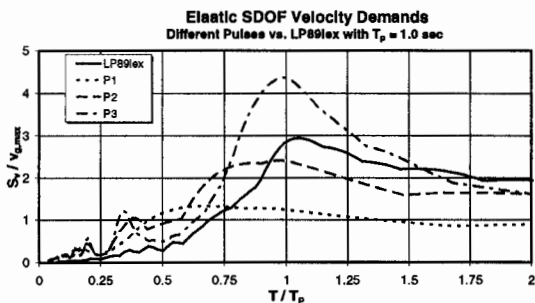


(a) Record LP89lex, T = 2.0 sec.

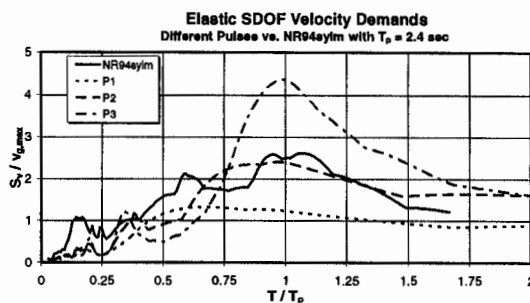


(b) Record NR94sytm, T = 3.0 sec.

Figure 18. Dependence of Story Ductility Demands on Base Shear Strength

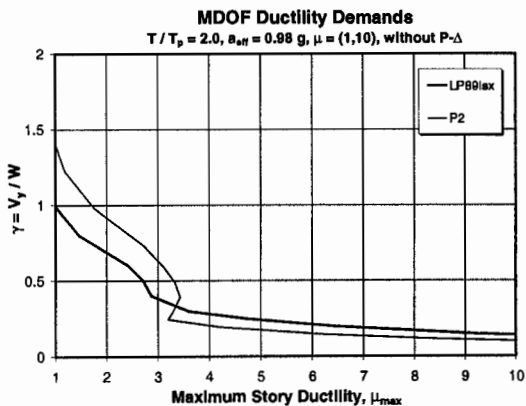


(a) Record LP89lex

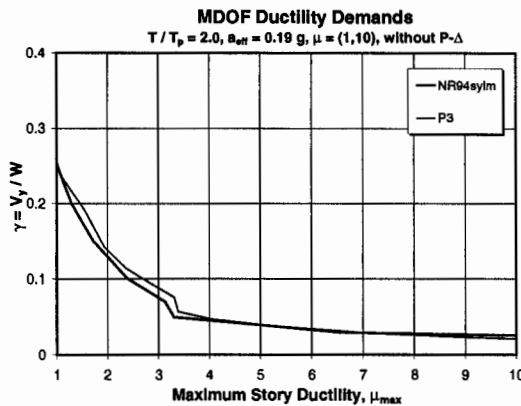


(b) Record NR94sylv

Figure 19. Determination of Pulse Period (and Pulse Type) from Velocity Spectra

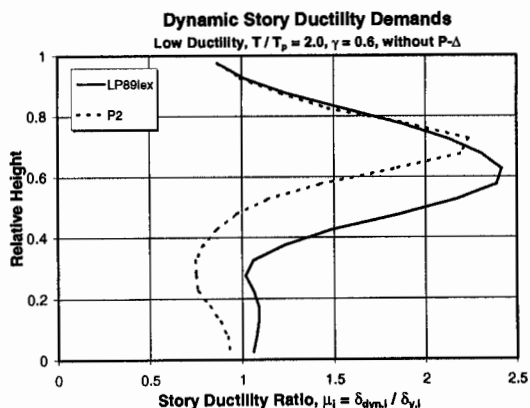


(a) Record LP89lex,  $T/T_p = 2.0$

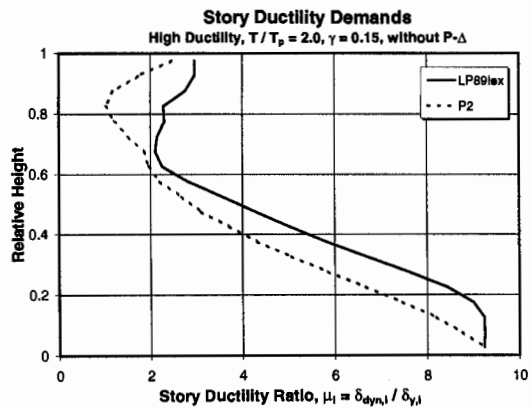


(b) Record NR94sylv,  $T/T_p = 2.0$

Figure 20. Matching of  $\gamma-\mu$  Curves for Identification of Best-Fit  $a_{eff}$



(a) High Strength, Low Ductility



(b) Low Strength, High Ductility

Figure 21. Story Ductility Demands Obtained from a Near Fault Record and its Equivalent Pulse

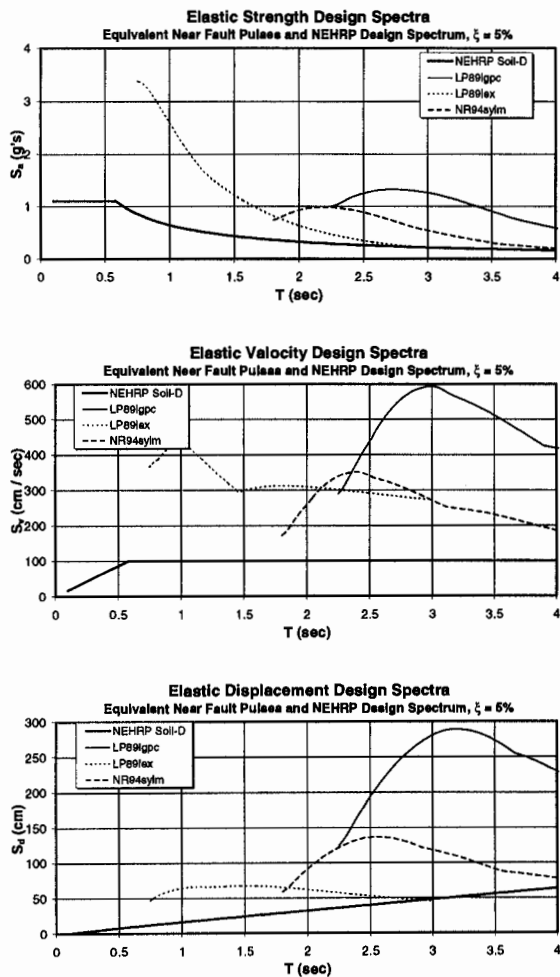


Figure 22. Examples of Near Fault Equivalent Pulse Spectra Superimposed on NEHRP Design Spectra

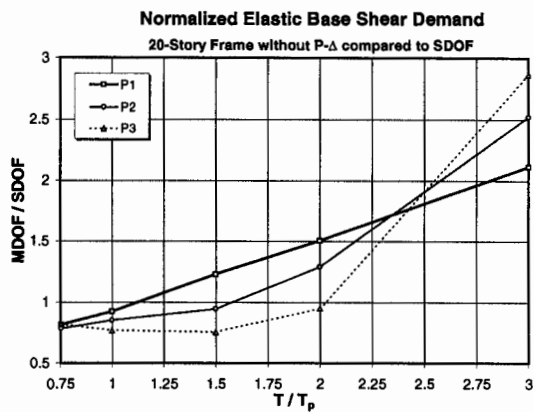


Figure 23. Ratio of MDOF Base Shear to SDOF Strength Demand for Elastic Systems

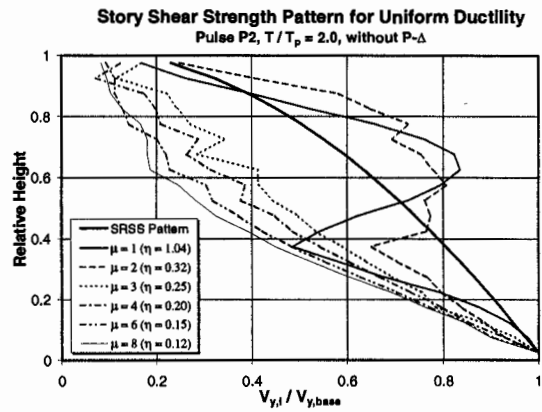


Figure 24. Story Shear Strength Patterns for Target "Uniform Ductilities" Over Height; Pulse P2,  $T/T_p = 2.0$

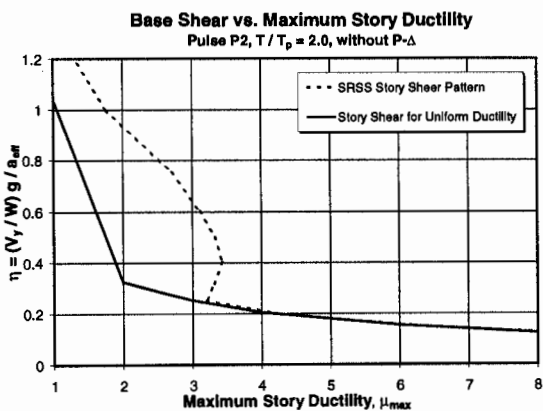


Figure 25. Base Shear Demands for Specific Target Ductilities; SRSS and "Uniform Ductility" Shear Strength Patterns; Pulse P2,  $T/T_p = 2.0$



UTILIZATION OF RAPID POST-EARTHQUAKE DATA BY UTILITIES

William U. Savage

Geosciences Department  
Pacific Gas and Electric Company  
San Francisco, CA

ABSTRACT

When a potentially damaging earthquake occurs, utilities (electricity, gas, water, and telecommunications) have an urgent need for information about the effects of the event so that they can make optimal decisions regarding safety and maintaining and restoring utility functionality. Modern earthquake instrumentation systems, including strong-motion recorders and regional seismic networks, can collect data and provide information products that can greatly improve this decision-making and action-taking process. Four areas of utility response to earthquakes illustrate the utilization of these data: (1) Rapidly available network and strong-motion data can provide an earthquake alert that will make utility personnel aware that an earthquake is occurring, what area of the utility's service territory is affected, and the likely extent of damaging ground motions. This alert will focus the earthquake response attention of the utility and may permit quick operational and life-safety actions. (2) Within 10 to 30 minutes after the earthquake, analysis of strong-motion data from key utility sites will provide assessments of the likelihood of damage that can be used to prioritize deployment of field personnel and guide the initial operational control and recovery plans. (3) In the same time frame, similar strong-motion-based damage assessments of transportation routes (e. g. freeways, bridges, and overpasses) along with reported damage and disruption will help the utilities plan how to get inspection and repair crews to key facilities. In addition, damage likelihood assessments of commercial, industrial, and residential buildings will indicate where utility service connections may need rapid responses to safety and secondary damage threats. (4) Within a few hours of the earthquake, pre-arranged building inspectors can use building response strong-motion measurements to help evaluate the safety of continued occupancy of structures housing critical post-earthquake response functions.

INTRODUCTION

Modern society is increasingly dependent on safe and reliable services provided by the utility industries, including electric power, natural gas, telecommunications, and water and waste-water. The utilities consist of networks of transportation conduits (primarily pipelines, conductors, and fiber-optic cables) and myriad ancillary facilities that connect the sources and destinations of utility products. Significant earthquakes in recent years have demonstrated that seismic vulnerabilities in utility networks can lead to interruptions in customer service that are dangerous to life and property, disruptive and costly to commercial enterprises, and produce

long-term hardships on affected communities and people. While such long-term measures as improved seismic design practices and seismic retrofit programs can reduce the likelihood of damage, many utilities systems contain older components that are more vulnerable than their modern versions. Thus, in the coming years, utility system damage and service disruptions need to be anticipated, and utilities need to prepare for effective responses.

Accompanying the increased dependence on utility services in the Information Age have come major new developments in earthquake data acquisition, analysis and data processing, and communication of data and resultant information products (Kanamori and others, 1997). Digital strong-motion recorders, broadband seismometers and digital data loggers, high-speed and reliable telecommunications, and powerful computers and user-friendly software combine to make possible the rapid notification of earthquake occurrence and effects to emergency responders. This paper focuses on the increasingly important role that modern strong-motion data, along with other earthquake data, can play in effective and rapid earthquake response by utilities.

### WHAT UTILITIES NEED

When a potentially damaging earthquake occurs, personnel in a utility who are responsible for operations, maintenance, and emergency response want to know:

- What happened: Was it an earthquake, an explosion, a plane crash? In a large utility, key personnel may be too far away from the earthquake to feel it, yet they still need to know what has happened.
- Where is the affected area: The locality affected is critical information to start the response process.
- How much damage and disruption is there: This is the most important information to utility personnel. The level of damage not only affects their response effort, but may have personal impact because of potential threats to their families and homes.

Utility personnel are practiced in gathering this emergency response information from such traditional sources as fire and police reports, field reports from utility personnel and customers, and media announcements. But the utility response can be significantly improved by additional rapidly provided data and information to speed up the decision-making processes of utilities (and other emergency responders). What is needed is to use modern scientific and engineering information based on real-time and near-real-time earthquake data to rapidly develop an accurate description of the likely state of damage of utility facilities, and other structures of interest such as transportation corridors and customer buildings. From this knowledge, utility decision-makers can take optimal action to address the damage conditions their organization is facing.

Basic earthquake data (such as recordings of strong ground shaking and of regional and broadband seismographic networks) are used to derive earthquake information such as location coordinates, focal depth, local magnitude, focal mechanism, moment tensor and moment magnitude, aftershock locations and rates, tectonic association, and others. Strong-motion data

analysis adds peak acceleration, velocity, and displacement and response spectral ordinates at each instrument site; contour maps of ground motion parameters; event-specific attenuation, and others. These information products can be directly used or transformed into additional products that directly address what the earthquake did to utility facilities and other parts of the build environment. Figure 1 illustrates the relationship between earthquake data and information products and the sequence of utility responses that will be discussed in the next section.

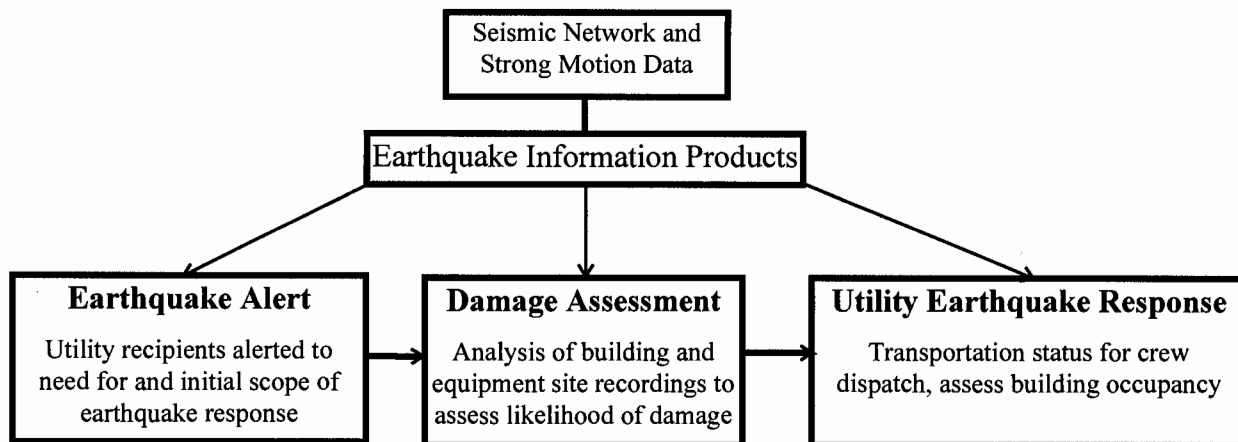


Figure 1. Rapid earthquake data used in earthquake response sequence by utility decision-makers.

## RAPID DATA UTILIZATION BY UTILITIES

### Earthquake Alert

In a modern-instrumented urban region, as the Los Angeles basin or the San Francisco Bay Area are becoming, an alert that an earthquake is occurring and information about its location (geographic coordinates) and size (magnitude) can be provided to utility recipients in a minute or two. This notification has immediate value to the recipients:

- Utility personnel know that an earthquake has just happened, rather than some other kind of disruptive or damaging event.
- The region affected by the earthquake is known. Current systems incorporate paged or e-mailed notification information into utility computers or GIS map servers, and distribute the combined earthquake and facilities location information within the utility via its intranet. This provides a vivid picture of where the earthquake occurred with respect to utility facilities. Figure 2 shows an example of a recent earthquake

near San Juan Bautista east of Monterey Bay plotted on a map along with locations of gas and electric power facilities, faults, and highways.

- From the earthquake location and magnitude, computations using attenuation relations can give an initial map of the areal distribution and severity of ground shaking. The utility personnel can gain a graphic understanding of the extent of the region affected by the earthquake.

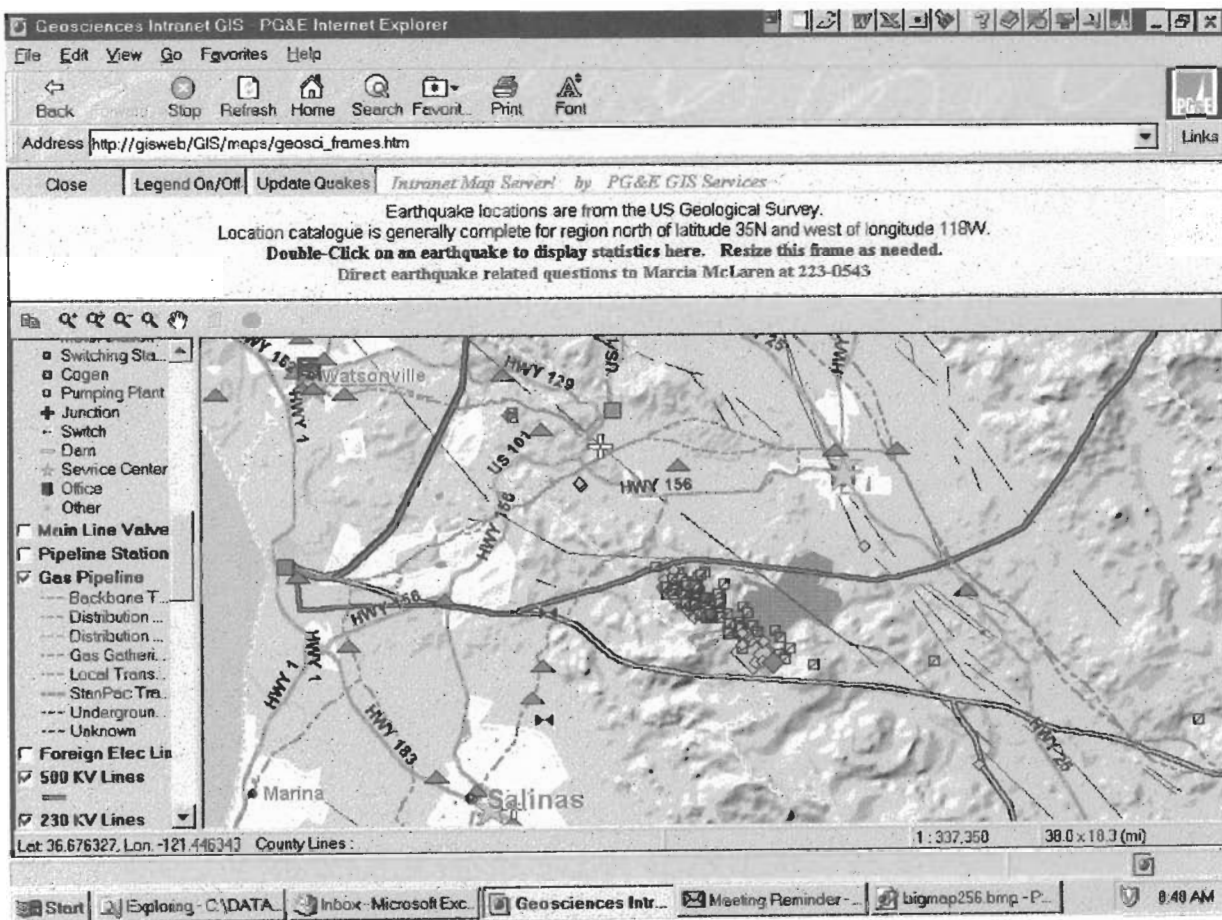


Figure 2. Map of August 12, 1998, M5.4 earthquake near San Juan Bautista plotted on map of PG&E gas and electric facilities. Light lines are faults (note that the earthquake sequence is systematically located about 2 miles southwest of the San Andreas fault zone due to local seismic velocity effects; the earthquakes actually occurred along the San Andreas zone).

The initial rapid notification information serves to immediately initiate the utility organization's response to the consequences of the event. The CUBE and USGS/UC Berkeley notification systems are excellent examples of providing increasingly rapid information.



Because the utility response is people- and decision-intensive, the faster they know the area within which a serious event has taken place, the more accurate their response can be.

It is desirable from the utility perspective to have faster initial information made available on earthquake location and size, instead of delaying while getting highly accurate values. A quick location that is accurate within 5 miles is close enough for the initial utility response to begin. It is particularly important to quickly distinguish between earthquakes with significant damage potential ( $M6\frac{1}{2}+$ ) and those that may be locally damaging but that are not large enough to affect a widespread area ( $M5\frac{1}{2}$  to  $6\frac{1}{2}$ ). It would be useful to develop a fast, approximate measure of earthquake size, even if the size were described by words (e.g. "moderate, big, very big") or magnitude ranges (e.g.  $M5\pm$ ,  $M6\pm$ , or  $M5\frac{1}{2}$  to  $M6\frac{1}{2}$ ).

If the earthquake alert is prepared and distributed sufficiently quickly, it becomes an early warning of strong earthquake shaking for locations relatively far from large earthquakes. Possible benefits of such early warnings are enabling employees to get out of potentially dangerous working situations, or alerting remote backup operational facilities to take over for possibly threatened primary facilities. However, utilities need to practice receiving earthquake alerts, and to gain experience and confidence in using such information before the implementation of substantial early warning actions will be acceptable. Utility operators are reluctant to take significant preemptive operational actions that result in customer services being interrupted. There are likely to be major liability issues if electric power is cut off in a region that is threatened by strong shaking, for example. In general, any responsive actions taken as a result of receipt of an earthquake early warning will need to be preceded by extensive training and practice by employees, and the benefits of such actions will need to be clearly established.

### **Rapid Damage Likelihood Assessment for Facilities**

As noted previously, the information that utility personnel want to have immediately after an earthquake is the state of damage of utility equipment (substations, pump facilities, etc.) and of office buildings and buildings housing repair equipment and spare parts. Since many facilities and buildings are not routinely occupied, particularly at night or on weekends, on-site personnel may not be available to conduct immediate inspections. If personnel are on-site, they may be initially occupied with injuries or other immediate safety matters. Strong-motion instruments located at the facilities and buildings provide a means to perform a remote damage likelihood assessment. Using a free-field recording taken at the facility, the ground motion can be compared with previously determined fragility curves for the equipment and structures at a site. The comparison would take about 15 minutes after the earthquake begins, allowing time for data transmission from 10 or so key sites in the affected region. The fragility curves indicate probability of damage as a function of ground motion parameter for specified damage states (e.g., porcelain break for a transformer, limited entry for a building). Figure 3 illustrates this comparison for a high-voltage transformer shaken at 0.5g. While this is presently an approximate procedure due to the uncertainties in available fragility curves, it is a useful first assessment of what the damage is at a utility site, prior to conducting field inspections, which may occur several hours later.

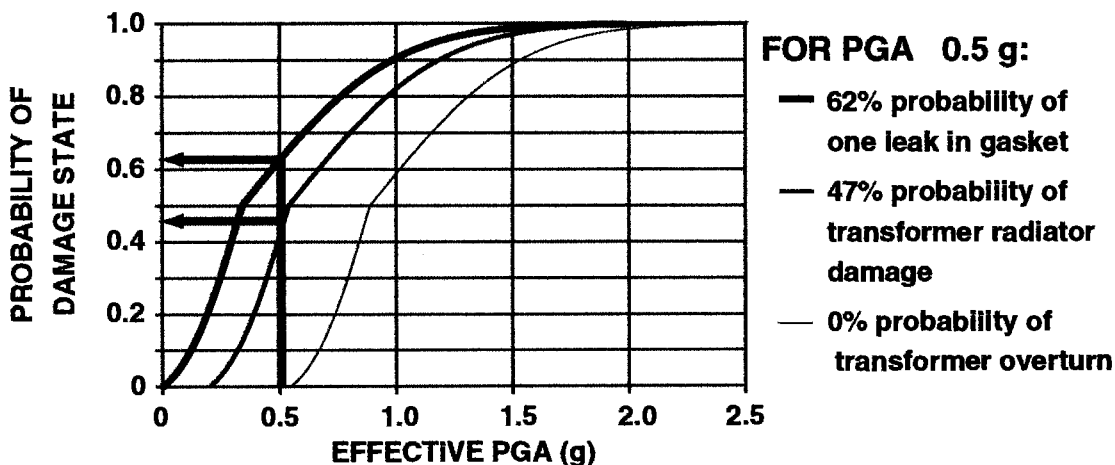


Figure 3. Illustrative fragility curves for three damage states of a 500 kV transformer. The effective PGA value includes the effects of magnitude and site period.

Detailed contoured ground shaking maps can be constructed that include strong-motion data provided by many public and private sources, including utilities. For utility sites that do not have strong-motion instruments, ground motion estimates can be obtained from these maps. These estimates can then be used in fragility comparisons to assess likely damage. This approach depends upon having maps with sufficient input ground-motion observations to provide a reasonably accurate estimate of site ground shaking.

Installation of strong-motion instruments at utility facilities provides a valuable additional benefit in that ground-motion data from earthquakes can be used to refine the fragility functions for the equipment and buildings exposed to strong shaking from future earthquakes. Along with the site ground-motion recording, it is critical to accurately compile characteristics of the facility or equipment damage that occurs along with the lack of damage.

**Damage Likelihood Assessment of Transportation System and Customer Building Classes**

The response of a utility to a damaging earthquake is also dependent upon the utility having information about the status of other parts of the built environment. Of particular importance is the operational status of the freeways, roads, and streets in the earthquake-affected area immediately after the event. Emergency access is needed to shut off downed power lines, or shut in leaking gas lines or water mains. The California Department of Transportation has instrumented a number of bridges and overpasses; as for utility facilities, rapid analysis of these data can result in remote assessments of the likely damage to the structures and the prudence of continuing to use them or not. When combined with on-site reports of damage, useful early information about traffic access can be provided to utilities.

It is also valuable information for the initial utility response effort to have a preliminary picture of the localities in the earthquake-affected area where there are concentrations of building

damage. These are places where there is likely to be extensive damage to customer utility connections, threatening life and property, and requiring immediate utility attention.

### **Post-Earthquake Building Inspection for Occupancy**

Utilities, medical providers, and other organizations with critical post-earthquake emergency response functions have recognized that certain occupied buildings or buildings containing vital information or equipment may be closed by authorized building inspectors, or may be evacuated by frightened employees, some of who have critical post-earthquake response roles. To address this problem, some organizations have established Post-Earthquake Inspection Programs to facilitate the access to and use of essential buildings. Qualified engineers are contracted by the owner and pre-assigned to automatically inspect key facilities given certain earthquake location and magnitude criteria. They will have the benefit of pre-earthquake evaluations and post-earthquake inspection manuals, and will be able to tag the facilities regarding occupancy (red/yellow/green) under authorization from the local jurisdiction.

To assist the inspecting engineers, certain buildings can be instrumented to provide time history and response spectral data on the actual behavior of the building. The engineer can thus assess the potential for concealed structural damage that may make the building too dangerous for further occupancy, or that may be sufficiently minor to permit necessary emergency access or even full normal occupancy. The data will be available in the same time frame that the inspector arrives at the facility, within an hour after the earthquake.

## ADDITIONAL COMMENTS

### **False Alarms**

The providers of rapid earthquake information are sincerely concerned about the occurrence of false alarms—issuing an announcement of a large earthquake that has not occurred—or failing to report the occurrence of a large event. For the foreseeable future, utilities will most likely rely on their practical experience with their own status and information notification systems, and expect occasional problems and errors coming from the earthquake notifiers. It is simply not prudent for a utility to initiate aggressive or expensive initial response efforts on the basis of an earthquake alert that is not consistent with or verified by other available information. It is incumbent on the organizations issuing rapid notifications to have in place reasonable systems to detect false alarms and to rapidly correct them.

The problem of not issuing an accurate rapid report for a major damaging event that actually occurs has been the case for the 1989, 1992, and 1994 events in California. Recognizing this unfortunate history, the various seismological organizations have taken extensive efforts to build “earthquake-proof” systems. While these efforts are commendable, it is still possible for failures to occur. As the current notification systems continue to be installed and operated, additional opportunities to improve their reliability will no doubt be found and instituted. It should be the responsibility of the utilities and other recipients of rapid earthquake information to continue to

use the notifications to gain experience in how to best apply them, and to let reliance on notifications grow with that experience.

### **Rapid Earthquake Information as a Service**

Rapid earthquake information capabilities have been largely developed in the research seismology community. For some years, these capabilities have been provided to a limited number of recipients on a somewhat experimental basis. These arrangements have been helpful in learning how to improve essentially all aspects of the notification systems. With the development of the FEMA-supported TriNet project in Southern California, it is time to begin to view the provision of rapid earthquake information, from initial alerts, to shake maps and site-specific ground motions, to final archived data sets, as a public service, not an add-on to a research program. Instituting this distinction will clarify many of the uncertainties that currently exist in defining the responsibilities of the issuers and the recipients of information, in determining the sources of financial support for the service versus related research, and other issues. Shifting to a service-oriented perspective should result in a more professional and customer-oriented relationship between issuers and recipients. Federal/state agency partnerships with research/educational organizations appears to be developing into a good model for establishing an "earthquake service" that draws on the best of both academic and agency capabilities.

### **Utility Responsibilities**

Users of earthquake information must take responsibility for effectively understanding and applying the data and information they receive. This includes training and exercises in simulating the use of the rapid notification and damage likelihood assessments. The more frequent occurrence of small events help keep both the notification providers and notification users practiced.

## **CONCLUSIONS**

Utilities and the communities they serve are at the dawn of a new era in earthquake response, as they begin to use the earthquake information products from modern seismic instrumentation. Through the application of such key technologies as digital strong-motion instruments, alternative reliable telecommunication pathways, powerful computers and software, and digital maps for displaying earthquake information, utility personnel will receive faster and more accurate information on earthquake occurrence and damage to be used for improved utility decision-making. This new capability is consistent with the increasing societal value placed on utility safety and reliability.

## **ACKNOWLEDGMENTS**

Discussions and critical reviews by Marcia McLaren and Norm Abrahamson are gratefully appreciated. This paper is based on numerous and ongoing interactions with many colleagues in both the seismological and utility communities regarding utility applications of earthquake information products. In particular, enthusiasm and support from the Geosciences Department

members, key leaders in the operating utility groups, and the management of PG&E are acknowledged.

#### REFERENCES

Kanamori, H., E. Hauksson, and T. Heaton (1997). Real-time seismology and earthquake hazard mitigation, *Nature*, Vol. 390, p. 461-464.

Matsuda, E., L. Cluff, C. Poland, and W. Savage (1995). Post-earthquake inspection of utility buildings, in *Lifeline Earthquake Engineering, Proceedings of the Fourth U. S. Conference*, M. J. O'Rourke, ed., Technical Council on Lifeline Earthquake Engineering Monograph No. 6, American Society of Civil Engineers, New York, p. 787-794.



**BRIDGE INSTRUMENTATION AND POST-EARTHQUAKE  
EVALUATION OF BRIDGES**

Patrick Hipley, P.E.  
Seismic Technology Section  
Office of Earthquake Engineering  
California Department of Transportation

and

Moh Huang, Ph.D., P.E. and Anthony Shakal, Ph.D.  
California Strong Motion Instrumentation Program  
Division of Mines and Geology  
California Department of Conservation

**ABSTRACT**

As the number of large civil structures instrumented for strong motion is increasing, efforts towards utilizing the earthquake data collected from these structures is also increasing. The studies are geared towards verifying seismic engineering design assumptions by comparing the theoretical models to the actual readings. Efforts to utilize the data ranging from simple comparison of the estimated structural period of vibration with the recorded free vibration, to complex comparisons of non-linear time-history models are underway. Many more studies are needed to take full advantage of this valuable data.

Accurately monitoring bridge movements during a large earthquake is necessary to advance our understanding of how these massive structures are affected by seismic input. Bridges of different structure types react differently to the same seismic wave patterns. Dynamic soil-structure interaction can be studied and theories can be verified or disproved based on the actual readings. Before strong motion sensors were placed at ground sites or on civil structures, theories were based on very little data. Therefore, the data collected from large earthquakes with these sensors are invaluable to the seismic engineering community.

The California Department of Transportation (Caltrans) and the California Strong Motion Instrumentation Program (CSMIP) of the California Department of Conservation's Division of Mines and Geology have instrumented more than 50 Caltrans bridges throughout the State since the 1989 Loma Prieta earthquake. In addition, CSMIP and Caltrans are installing more near-real-time stations at selected bridge sites in the State. Consequently, more near-real-time strong-motion data will be available quickly after an earthquake. These data provide information on ground shaking and response of the bridge structure, and are useful not only for improving seismic design practices but for post-earthquake damage evaluation of bridges. This paper describes the current status and future plan of the Caltrans/CSMIP bridge instrumentation project, and discusses quick application of strong-motion data to post-earthquake evaluations of bridges.

Cases of quick application of near-real-time data are presented and criteria for determining post-earthquake inspection of bridges are discussed.

## INTRODUCTION

Since the 1989 Loma Prieta earthquake, a comprehensive program was initiated by the Department of Transportation (Caltrans) and the California Strong Motion Instrumentation Program (CSMIP) of the California Department of Conservation's Division of Mines and Geology to instrument more Caltrans bridges throughout the State. This bridge strong motion instrumentation program was in response to recommendations by the Governor's Board of Inquiry (Housner, 1990) that Caltrans implement comprehensive program of seismic instrumentation to provide measurements of the excitation and response of transportation structures during earthquakes. Caltrans accelerated this effort in 1993 and has instrumented about 10 bridge structures per year since that time.

Since the 1994 Northridge earthquake, CSMIP has developed a near-real-time strong motion monitoring system in which the strong-motion records are recovered and processed automatically right after an earthquake. This system has been installed for CSMIP stations in southern California under the TriNet project and at new and upgraded stations in other parts of the State. In total, TriNet, a joint project between CDMG/CSMIP, Caltech and USGS, funded by the Federal Emergency Management Agency (FEMA) through the California Office of Emergency Services (OES), will install 670 stations in southern California. In the event of potentially damaging earthquakes, TriNet will produce a map, called "ShakeMap", of ground motion distribution within minutes. The first prototype model of a ShakeMap product is discussed by Wald, et al. (1998) in this proceedings volume. These maps will include peak ground acceleration, peak ground velocity, spectral acceleration at 0.3, 1, and 3 seconds, and other ground motion parameters. The ground motion information will be useful for Caltrans to quickly determine where bridge inspection is needed and which areas may have bridge structures damaged.

The current status and future plan of the bridge instrumentation program is presented herein. Quick interpretation of the strong-motion data and the application of near-real-time data to post-earthquake evaluation of bridges are discussed. The near-real-time data plus the existing database of the bridges will lead to development of new tools for post-earthquake response which will eventually be incorporated into Caltrans post-earthquake investigation team procedure.

## BRIDGE INSTRUMENTATION

The California Department of Transportation to date has 54 bridges instrumented for strong motion with the number of sensors per structure ranging from as few as 4 to as many as 38 sensors. This work is a cooperative effort between Caltrans and the California Division of Mines and Geology. The bridge structures chosen for instrumentation vary in size and type, and are located throughout California. The locations of these bridges are shown in Figure 1. They are listed in Table 1 which includes bridge name, station number, bridge number, post-mile, construction date, number of sensors installed and the instrumentation completion date. Most of



# SMIP98 Seminar Proceedings

**Table 1. CSMIP/Caltrans Bridge Strong Motion Instrumentation  
Installed as of 4/30/98**

|                             | Station Name                                   | Station No. | Bridge No. | Post Mile           | Const. Date | No. of Sensor | Instr. Date |
|-----------------------------|--|-------------|------------|---------------------|-------------|---------------|-------------|
| <b>Bridges:</b>             |  |             |            |                     |             |               |             |
| 1                           | Alblon - Hwy 1/Salmon Creek Bridge             | 79683       | 10-134     | 01-MEM-1-43.00      | 1951        | 6             | 3/17/94     |
| 2                           | Arcata - Hwy 101/Murray Road Bridge            | 89708       | 04-170     | 01-HUM-101-R92.99   | 1964        | 12(9+FF)      | 4/6/95      |
| 3                           | Beaumont - I10/60 Interchange Bridge           | 12649       | 56-452F    | 08-RIV-10-6.67      | 1961        | 6             | 12/16/92    |
| 4                           | Belmont - I280 Pedestrian Bridge               | 58678       | 35-285     | 04-SM-280-10.56     | 1973        | 6             | 11/19/93    |
| 5                           | Benicia - Martinez Bridge                      | 88682       | 28-153     | 04-CC-680-25.04     | 1962        | 9             | 3/2/94      |
| 6                           | Big Sur - Hwy 1/Pfeiffer Canyon Bridge         | 47729       | 44-60      | 05-MON-1-45.5       | 1968        | 18(15+FF)     | 4/3/96      |
| 7                           | Corona - I15/Hwy 91 Interchange Bridge         | 13705       | 56-586G    | 08-RIV-15-R41.57    | 1989        | 9             | 9/29/94     |
| 8                           | Cuyama - Hwy 166/Cuyama Rver Bridge            | 25758       | 51-66      | 05-SB-166-R69.94    | 1980        | 12(9+FF)      | 4/8/97      |
| 9                           | Devore - I15/215 Interchange Bridge            | 23650       | 54-783R    | 08-SBD-15-16.35     | 1969        | 6             | 12/18/92    |
| 10                          | El Centro - Hwy 8/Meloland Overpass            | 01336       | 58-215     | 11-IMP-8-43.6       | 1971        | 32(29+FF)     | 4/26/78     |
| 11                          | Eureka - Eureka Channel Bridge                 | 89736       | 04-230     | 01-HUM-255-0.2      | 1971        | 12(9+FF)      | 4/9/96      |
| 12                          | Eureka - Middle Channel Bridge                 | 89735       | 04-229     | 01-HUM-255-0.7      | 1971        | 9(6+FF)       | 4/12/96     |
| 13                          | Eureka - Samoa Channel Bridge                  | 89686       | 04-228     | 01-HUM-255-1.2      | 1971        | 27(24+FF)     | 4/12/96     |
| 14                          | Half Moon Bay - Hwy 1/Tunitas Cr. Bridge       | 58754       | 35-31      | 04-SM-1-20.82       | 1962        | 9(6+FF)       | 5/22/97     |
| 15                          | Hayward - BART Elevated Section                | 58501       | N/A        | BART                | 1967        | 19(16+FF)     | 4/3/86      |
| 16                          | Hayward - Hwy 580/238 Interchange Bridge       | 58658       | 33-214L    | 04-ALA-580-30.80    | 1988        | 10(7+FF)      | 6/11/93     |
| 17                          | Hopland - Hwy 101/Railroad Bridge              | 69760       | 10-81      | 01-MEM-101-R9.53    | 1966        | 16(13+FF)     | 5/22/87     |
| 18                          | Jenner - Hwy 1/Russian River Bridge            | 69671       | 20-195     | 04-SON-1-19.72      | 1984        | 6             | 9/29/93     |
| 19                          | Klamath - Hwy 101/Klamath Rver Bridge          | 99710       | 01-28      | 01-DN-101-R4.04     | 1965        | 6             | 4/13/95     |
| 20                          | Lake Crowley - Hwy 395 Bridge                  | 54730       | 47-48      | 09-MNO-395-13.9     | 1969        | 9(6+FF)       | 8/30/95     |
| 21                          | Los Angeles - I10/405 Interchange Bridge       | 24670       | 53-1630G   | 07-LA-405-29.43     | 1963        | 7             | 9/13/93     |
| 22                          | Los Angeles - I10/La Cienega Bridge            | 24704       | 53-2791    | 07-LA-10-8.8        | 1994        | 15            | 11/2/94     |
| 23                          | Los Angeles - I405/San Gabriel River Bridge    | 14690       | 53-1185    | 07-LA-405-0.02      | 1964        | 6             | 4/27/94     |
| 24                          | Los Angeles - Vincent Thomas Bridge            | 14406       | 53-1471    | 07-LA-47-0.86       | 1964        | 26            | 10/22/81    |
| 25                          | Mojave - Hwy 14/Railroad Bridge                | 34715       | 50-402R    | 09-KER-14-15.32     | 1973        | 12            | 3/22/95     |
| 26                          | Moorpark - Hwy 23/118 Bridge (Arroyo Simi)     | 24738       | 52-331L    | 07-VEN-023/118-21.0 | 1993        | 12(9+FF)      | 5/8/96      |
| 27                          | North Palm Springs - I10/62 Interchange Bridge | 12666       | 56-474F    | 08-RIV-62-0.00      | 1962        | 7             | 6/30/93     |
| 28                          | Oakland - Hwy 580/13 Interchange Bridge        | 58656       | 33-347S    | 04-ALA-580-R39.15   | 1965        | 6             | 5/26/93     |
| 29                          | Oakland - Hwy 580/24 Interchange Bridge        | 58657       | 33-302H    | 04-ALA-580-45.23    | 1970        | 6             | 5/20/93     |
| 30                          | Palmdale - Hwy 14/Barrel Springs Bridge        | 24706       | 53-1794    | 07-LA-14-R57.37     | 1965        | 12(9+FF)      | 12/8/94     |
| 31                          | Parkfield - Hwy 46/Cholame Creek Bridge        | 36668       | 49-36      | 05-SLO-46-54.77     | 1979        | 6             | 8/4/93      |
| 32                          | Pasadena - Hwy 134/210 Interchange Bridge      | 24689       | 53-2318G   | 07-LA-134-R13.25    | 1974        | 9(6+FF)       | 4/21/94     |
| 33                          | Ridgecrest - Hwy 395/Brown Road Bridge         | 33742       | 50-340     | 09-KER-395-R25.08   | 1966        | 9(6+FF)       | 2/22/96     |
| 34                          | Rio Dell - Hwy 101/Painter Street Overpass     | 89324       | 04-236     | 01-HUM-101-R52.89   | 1976        | 20(17+FF)     | 9/29/77     |
| 35                          | Rohnert Park - Hwy 101 Bridge                  | 68717       | 20-235     | 04-SON-101-13.88    | 1973        | 12(9+FF)      | 5/3/95      |
| 36                          | San Bernardino - I10/215 Interchange           | 23631       | 54-823G    | 08-SBD-215-4.05     | 1966        | 37(34+FF)     | 1/10/92     |
| 37                          | San Diego - Coronado Bridge                    | 03679       | 57-857     | 11-SD-75-R20.49     | 1969        | 9             | 11/17/93    |
| 38                          | San Diego - I5/Hwy 52 Interchange Bridge       | 03731       | 57-520L    | 11-SD-5-25.91       | 1966        | 24(21+FF)     | 5/18/95     |
| 39                          | San Fernando - I210/Hwy 118 Bridge             | 24714       | 53-2102    | 07-LA-118/210-6.0   | 1973        | 36(33+FF)     | 4/17/96     |
| 40                          | San Francisco - Bay Bridge/ East               | 58633       | 33-25      | 04-ALA-80-0.0       | 1936        | 9             | 2/28/93     |
| 41                          | San Francisco - Bay Bridge/West                | 58632       | 34-3       | 04-SF-80-5.6        | 1936        | 6             | 2/28/93     |
| 42                          | San Francisco Bay - Dumbarton Bridge           | 58596       | 35-38      | 04-SM-84-29.0       | 1982        | 32(26+2FF)    | 6/10/87     |
| 43                          | San Francisco Bay - San Mateo Bridge           | 58677       | 35-54      | 04-SM-92-14.44      | 1967        | 6             | 10/29/93    |
| 44                          | San Juan Bautista - Hwy 101/156 Overpass       | 47315       | 43-31      | 05-SBT-156-3.02     | 1958        | 12            | 5/24/77     |
| 45                          | San Simeon - Hwy 1/San Simeon Creek Bridg      | 37728       | 49-46      | 05-SLO-1-52.92      | 1984        | 12(9+FF)      | 9/6/95      |
| 46                          | Santa Barbara - San Roque Canyon Brigde        | 25749       | 51-104     | 05-SB-192-1.77      | 1984        | 9(6+FF)       | 10/24/96    |
| 47                          | Santa Clara - Hwy 237/Alviso Overpass          | 57748       | 34-470K    | 04-SCL-237-6.10     | 1994        | 12(9+FF)      | 10/25/95    |
| 48                          | Santa Clara - Hwy 237/Alviso Overpass          | 57748       | 34-470L    | 04-SCL-237-6.10     | 1994        | 9             | 10/25/95    |
| 49                          | South San Francisco - Sierra Point Overpass    | 58536       | 35-130     | 04-SM-101-23.7      | 1957        | 16(13+FF)     | 12/5/85     |
| 50                          | Sylmar - I5/14 Interchange Bridge              | 24694       | 53-2795F   | 07-LA-5-24.5        | 1994        | 38(35+FF)     | 12/20/95    |
| 51                          | Sylmar - I5/14 Interchange Bridge              | 24694       | 53-2797F   | 07-LA-5-24.5        | 1994        | 4             | 12/20/95    |
| 52                          | Truckee - I80/Truckee River Bridge             | 76741       | 17-58L     | 03-NEV-80-20.23     | 1989        | 8(5+FF)       | 10/24/95    |
| 53                          | Ventura - Hwy 101/Telephone Rd Bridge          | 25725       | 52-214L    | 07-VEN-101-R26      | 1961        | 12(9+FF)      | 5/5/95      |
| 54                          | Watsonville - Hwy 1/Struve Slough Bridge       | 47707       | 36-88R     | 04-SCR-1-R1.59      | 1990        | 9(6+FF)       | 11/23/94    |
| <b>Geotechnical Arrays:</b> |  |             |            |                     |             |               |             |
| 1                           | Los Angeles - I10/La Cienega Geotechnical Ar   | 24703       | N/A        | 07-LA-10-8.8        | 1994        | 9(2Dwns)      | 12/15/94    |
| 2                           | Eureka - Geotechnical Array                    | 89734       | N/A        | 01-HUM-255-1.2      | 1997        | 15(4Dwns)     | 5/16/97     |

the efforts are concentrated in the two large urban areas of Los Angeles and the San Francisco Bay Area.

Parallel geotechnical studies are underway to place deep downhole sensor arrays at various depths. Geotechnical downhole arrays are needed to analyze the soil column movement from a deep source and to better predict the surface movement from earthquakes. The ground motion varies from site to site and a large database of site conditions is needed before we can correlate soil and structural models. The downhole arrays are in the early stages but will be located throughout the State. Since geotechnical engineers will predict the site specific ground motions, the bridge engineers will need to work closely with the geotechnical engineers to fully understand all the assumptions and probabilities associated with the predictions. The actual downhole sensor readings will better our understanding of complex geologic vibrations.

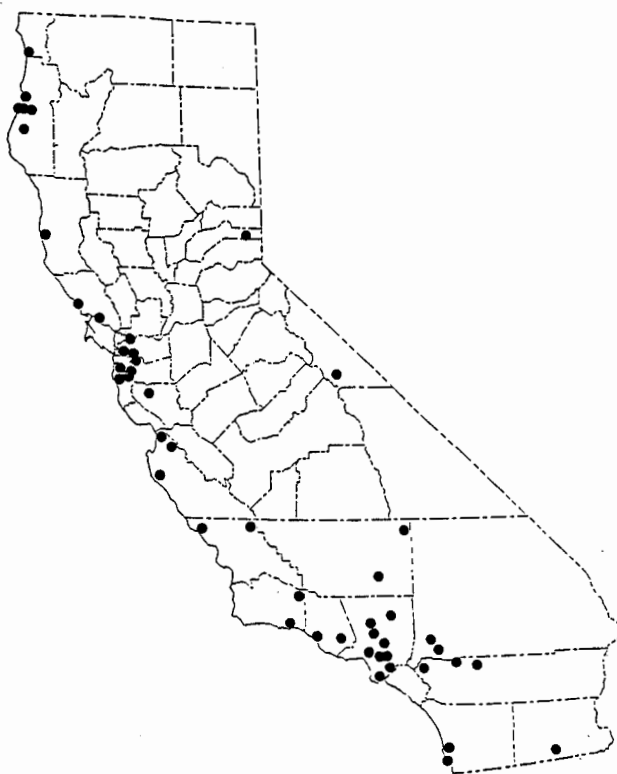


Figure 1. Locations of bridges instrumented with strong-motion sensors under the Caltrans/CSMIP Bridge Instrumentation Project.

Objectives of Bridge Instrumentation

The long-term goals of the bridge instrumentation are to record strong-motion data to (a) improve engineering design codes and practices, and (b) assess and mitigate the hazards posed by existing bridges. Strong-motion data from instrumented bridges are needed because the data

provide critically needed information on the behavior of bridges at damaging levels of ground motion, and on the soil-structure interaction effects on the response of these structures. Due to the complexity of the response of bridges, which are affected by numerous structural elements with great nonlinearity, (e.g., abutments, hinges, soil and foundation pile interactions) nonlinear bridge response to damaging levels of ground shaking may not be reliably predicted using available analytical modeling techniques. Recorded data can be analyzed to verify these techniques and to advance state-of-the-art knowledge on the seismic performance of bridges.

The bridge strong motion instrumentation utilizes force-balance accelerometers that are designed to give readings up to 4g. The dynamic range of the recorders is also wide enough to measure low level vibrations from light shaking, which may be used to predict the movement that will occur when there is strong shaking. The sensors are placed on the bridges to measure seismic movements as they relate to the structural dynamic models. Enough sensors are placed to record the transverse mode shapes of the structure and the longitudinal motion of selected superstructure frame. A free-field tri-axial sensor package is placed at each site to measure the input motion to the structure. The free-field instrument is placed as far as practical away from the influence of any structure such as the bridge, a building, the approach embankment, etc., to avoid anomalous inputs. The free-field is placed on a rock outcrop if one is available.

There are basically three types of instrumentation plans: (a) light, (b) moderate, and (c) full. Typically, light instrumentation has six to nine sensors, moderate instrumentation has 10 to 24 sensors, and full instrumentation has 25 or more sensors. In general, the locations of sensors are planned primarily based on past experience in instrumenting bridges and recommendations from researchers who studied strong-motion data from instrumented bridges. The guidelines for instrumentation of highway bridges developed by Rojahn and Raggett (1981) are also considered. The overall goal of the instrumentation plan is to measure the seismic input motion and the response of the bridge structure. Specific measurements for each instrumentation plan are described as follows:

- (a) light instrumentation. One of abutments and one of the columns are instrumented. Free-field sensors are included if it is feasible. An example is shown in Figure 2.
- (b) moderate instrumentation. Several locations on the deck (to allow determination of the first transverse mode shape), the abutment, and a reference free-field site are instrumented. Special features of the bridge structure such as skewed, short columns, hinges, and soft sites are considered in the instrumentation plan.
- (c) full instrumentation. This plan includes sensors to measure motions at both abutments, and at the base and the top of columns. In addition, a full instrumentation plan will measure lateral, vertical and torsional motions of the deck, relative motions across the hinges and the free-field motion. An example is shown in Figure 3. For major structures, like toll bridges in California, in which the structure spans different geologic conditions and much of the structure's mass is in the substructure, as many sensors as practical are installed at the foundations, and at locations as deep as possible such as at the pile tip in

Oakland - Hwy 580/13 Interchange Bridge  
 Caltrans Bridge No. 33-347S (04-ALA-580-R39.15)  
 CSMIP Station No. 58656

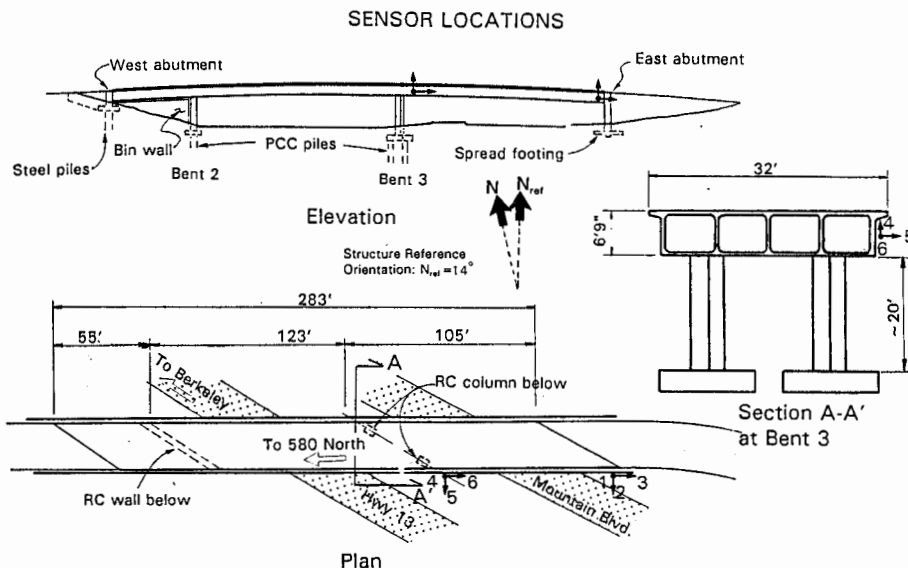


Figure 2. Sensor locations on Highway 580/13 Interchange Bridge in Oakland, which is an example of a light instrumentation plan.

Sylmar - I5/14 Interchange Bridge  
 Caltrans Bridge No. 53-2795F (07-LA-5-24.5)  
 CSMIP Station No. 24694

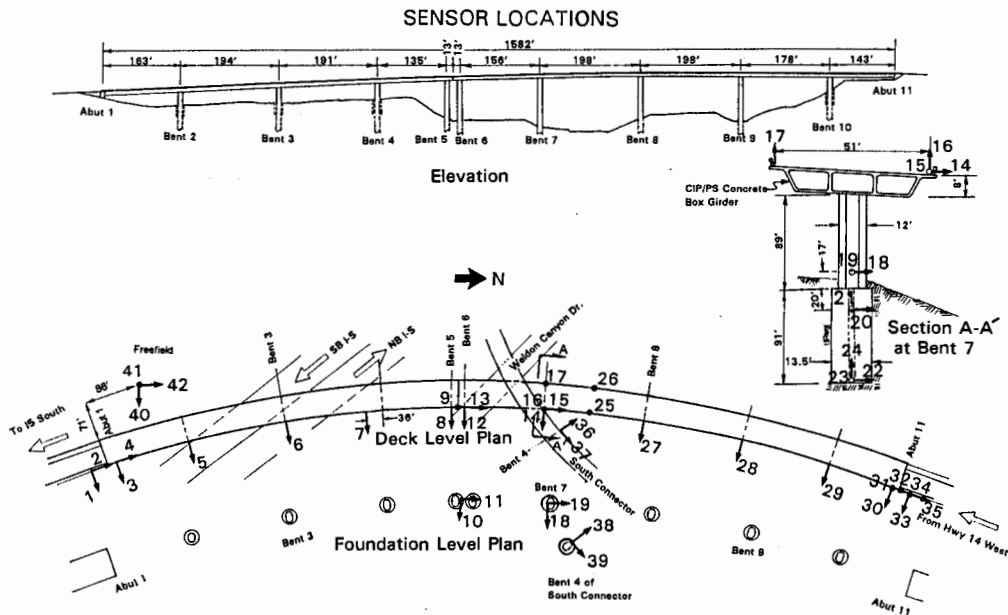


Figure 3. Sensor locations on Interstate 5/14 Interchange Bridge in Sylmar, which is an example of a full instrumentation plan.

the rock. The objectives are to measure differential ground input motions to the bridge and the soil-foundation-structure interaction effects.

Although it is always the case that only a limited number of sensors are available, the final sensor locations are selected optimally to achieve the above specific objectives and to allow determination of important dynamic characteristics of the bridge from strong-motion records.

#### Selection of Bridges for Instrumentation

The California Department of Transportation has over 12,000 bridges under its jurisdiction and it is not possible to instrument every bridge for strong motion. The bridge sites chosen are located throughout California to take advantage of the probability of having a structure close to an epicentral region. Many of the recent strong earthquakes are on newly discovered faults, so knowing where the next earthquake will be quite a challenge. The greater the coverage is the greater the chances are for recording the near source shaking.

Many of the selected Caltrans sites are in the large metropolitan areas. These areas happen to be in some of the highest seismic regions. A large percentage of the population lives in these metropolitan areas, thus a majority of large interchanges and other overcrossings are in big cities. Since life safety is the primary goal of bridge design and seismic retrofit, a great effort is placed on understanding of bridge response to large earthquakes in these areas. An examination of the Caltrans bridge sites having strong motion sensors will reflect these two philosophies, displaying a widely spread network with concentrations in the large urban regions.

Another tool used to determine the most prudent locations in California for bridge instrumentation is the earthquake probabilistic studies by the California Division of Mines and Geology and the U.S. Geological Survey that include mapping of known earthquake epicenters and faults. From these studies it is estimated that certain locations have a higher probability of experiencing strong shaking. These "hot spots" are where most of Caltrans instrumented structures are located.

A variety of bridge structure types are chosen for instrumentation to learn about the seismic responses of different bridge structures. It is hoped that lessons learned from an instrumented bridge can be applied to other bridges of similar type. The most common bridge type in California is the concrete box girder structure. Most of the bridges instrumented are of this type. Other types of bridges such as steel girder, truss structures, orthotropic girder, and pre-cast concrete are also instrumented. A variety of bridges that have multi-column, single-column or pier wall bents have been instrumented. In Santa Clara, two bridges at the same interchange, one with single-column and the other with multi-column bents, were instrumented to study the response of different structures to the same input ground motions.

Along with trying to understand the structure vibration mode shapes in an earthquake, components studies are in place to study individual aspects of bridge dynamics. These studies include the opening and closing of in-span hinges, the movement of superstructure over the

abutments, the top and bottom relative deflection of a column, pile tip and pile cap relative motions, and so on.

The bridge instrumentation process begins with the study of the as-built plans to understand the key seismic response issues for the bridge structure. The most effective instrumentation layout is developed given the number of sensors allotted for the bridge. The instrumentation plan is often developed cooperatively by CSMIP and Caltrans. For toll bridges, the proposed sensor locations are also reviewed by Caltrans engineering consultants who performed the seismic vulnerability study of that bridge. CSMIP engineers and technical operations staff accompany Caltrans engineers and District field staff to the bridge site to finalize details of the actual installation. Finally, the bridge is instrumented by CSMIP field operation staff with logistical support of Caltrans District staff. For toll bridges, a slightly different process is used. For these bridges, the instrumentation plan with cabling runs and equipment enclosures was developed by Caltrans and CSMIP staff, and is incorporated as part of the retrofit work. After the installation, CSMIP staff then maintain the instrumentation, and recover and process the records after an earthquake.

Currently, the bridge instrumentation program has several elements. They include instrumentations of regular highway bridges, downhole arrays, toll bridges and other transportation facilities.

(1) Bridge Instrumentation. This element includes light, moderate and full instrumentation of regular highway bridges. Under this project, various types of bridges located near the major faults have been instrumented. These bridges range from a straight 2-span bridge to a multi-span curved bridge. Some are newly-constructed, e.g., the Interstate 5/Highway 14 Interchange bridge, and some have been retrofitted, e.g., the Interstate 210/118 Interchange bridge.

(2) Downhole Instrumentation. Caltrans is placing geotechnical downhole arrays in various locations throughout the State to study the soil column motion and amplification caused by input from the deep "rock-like" material. Two geotechnical downhole arrays, i.e., La Cienega Array and Eureka Array, have been installed and have recorded several small earthquakes. In addition to these two arrays, this project will install downhole array sensors at sites near major retrofit bridges. Some of the arrays may have only one downhole tri-axial sensor package and one ground surface package; some will have up to ten downhole units at various depths. At these downhole sites, the soil has been characterized very extensively by using P-S suspension logs, soil sampling, E-logs, cross-hole or downhole velocity measurements, etc. The recorded data will allow better understanding of site responses at different levels of shaking and the ground motion at deep material on which the bridge piles are founded.

(3) Toll Bridge Instrumentation. Work is currently underway to instrument all of California's toll bridges for strong motion. Some of the toll bridges are currently lightly instrumented and more sensors will be added. Instrumentation plans have been developed so that the instrumentation can be incorporated as part of the retrofit work. The six existing toll bridges in Table 2 and three planned toll bridges, i.e., new Bay Bridge, new Carquinez Bridge and new Benicia Bridge, will be extensively instrumented. As many as 115 sensors will be installed on and near the bridge to

measure the bedrock motions, free-field ground motions, substructure and superstructure responses in future earthquakes. The records will be used to verify the complex analytical models used in the seismic retrofit analyses of these bridges.

**Table 2. Caltrans/CSMIP Instrumentation of Existing Toll Bridges**

| Name of Bridge                               | Type/Length of Main Structure         | Total Length | Year of Completion | No. of Sensors Planned |
|--|---------------------------------------|--------------|--------------------|------------------------|
| Benicia -<br>Martinez Bridge                 | steel truss, 4,884'                   | 1.2 miles    | 1962               | 90                     |
| Vallejo -<br>Carquinez Bridge (East)         | steel truss, 3,350'                   | 1.0 mile     | 1958               | 72                     |
| Richmond -<br>San Rafael Bridge              | steel truss and plate girder, 18,483' | 4.0 miles    | 1956               | 90                     |
| San Francisco -<br>Oakland Bay Bridge (West) | steel suspension, 10,051'             | 2.0 miles    | 1936               | 75                     |
| San Mateo -<br>Hayward Bridge and Trestle    | steel box girder, 9,650'              | 6.8 miles    | 1967               | 115                    |
| San Diego -<br>Coronado Bridge               | steel girder and box girder, 7,423'   | 1.6 miles    | 1969               | 96                     |

(4) Instrumentation of Other Transportation Facilities The Posey and Webster Street underground tubes in Oakland will be instrumented as part of the retrofit effort. The tubes provide access from Oakland to Alameda and travel under the harbor waterway. The tubes were constructed by sinking the sections into the water and then placing enough soil on top of them to overcome the buoyancy forces. The retrofit will include stone column installations and soil densification to prevent liquefaction. A downhole geotechnical array is also planned at this site to study liquefaction. The strong-motion sensors will also be used to trigger warning signs that will close the tubes after a big event. In another effort, seismic gates similar to railroad crossing gates are placed in very remote locations in northern California to close the bridge after a large earthquake. When the ground motion exceeds a certain level, the instrumentation system activates the closure of the gate. The bridges will remain closed until structural integrity assessment by the local maintenance personnel are completed. Sensors are also placed on these bridges to help with the study on the bridge structure health monitoring.

**POST-EARTHQUAKE EVALUATION OF BRIDGES**

Many of the instrumented bridges have a recording system from which the recorded data can be recovered via the phone lines and processed in Sacramento immediately after an event. The data can be used by the Caltrans engineers to quickly assess the structural integrity of that individual bridge. However, for the bridges that are not instrumented the engineers can utilize the near-real-time data recorded at free-field sites in the area. From the characteristics of that bridge and the ground motion information, the earthquake force experienced by that bridge can be

estimated. Based on the design information and the experience from past earthquakes, Caltrans post-earthquake response team can then determine whether inspection of that bridge is needed.

#### Near-Real-Time Strong-Motion Data

Developments in accelerographic instruments and communication technology have made possible significant advances in the monitoring and reporting of earthquake strong motion. Since 1995 CSMIP has developed and implemented a system for near-real-time data recovery from strong-motion stations (Shakal, et al., 1995 and Shakal, et al., 1997). The data recovered are automatically processed to produce the ground motion parameters that are most useful for engineering assessment of the earthquake impact. As an example of the near-real-time data, Figures 4 and 5 show the record recovered from the Mammoth Lakes station, approximately 8 km west of the epicenter of a magnitude 3.6 earthquake that occurred on January 3, 1998. Three components of band-passed acceleration, velocity and displacement, and the acceleration response spectra were automatically calculated and plotted after the event.

The TriNet project will produce quick maps "ShakeMap" of potentially damaging ground shaking within minutes of a damaging earthquake. By year 2002, there will be 670 stations in southern California that records the ground motions. The "ShakeMap" will give contoured maps of the ground shaking parameters for the affected areas and the heavily impacted areas can be determined from these maps. The parameters for the ground shaking include peak ground acceleration, velocity, and spectral acceleration at 0.3, 1 and 3 seconds. The maps are still under development to meet a variety of needs, however, experimental maps are now available on the Worldwide Web <http://www.trinet.org> after an event. Details on the early development of these maps are presented in a paper in this proceeding volume (Wald, et al., 1998).

The TriNet ShakeMap will be useful for quickly determination of which areas experienced damaging ground shakings. In addition, the ground motion records in those areas affected can be quickly studied and compared with the design spectra to determine whether inspection of the bridges in the area is needed. For those bridges that are instrumented, the recorded response can be quickly interpreted without complex analyses to facilitate the determination.

#### Post-Earthquake Response

In California and Nevada, locations and magnitudes of recent earthquakes are available on Worldwide Web <http://quake.wr.usgs.gov> right after the event. Response personnel can also receive the information from paging systems. Generally, earthquakes smaller than 5 do not cause damages to engineering structures. Therefore, the response personnel will only need to proceed further for earthquakes larger than 5.

Currently, Caltrans has a post-earthquake investigation team procedure. In the procedure, the team coordinator will determine the area of damage and a list of bridges to be investigated based on the magnitude and location of the earthquake. A GIS-based software and the database of bridges are used to create the map and the list. This procedure can be expanded to include the ground shaking information produced by TriNet. Depending on the year of design, design



SMIP98 Seminar Proceedings

Earthquake of Sat Jan 3, 1998 22:19 PST  
 Mammoth Lakes - Sheriffs Substation Sta No. 54685  
 Frequency Band Processed: 5.0 secs to 46.0 Hz  
 - CSMIP AUTOMATED STRONG MOTION PROCESSING (PRELIMINARY) -

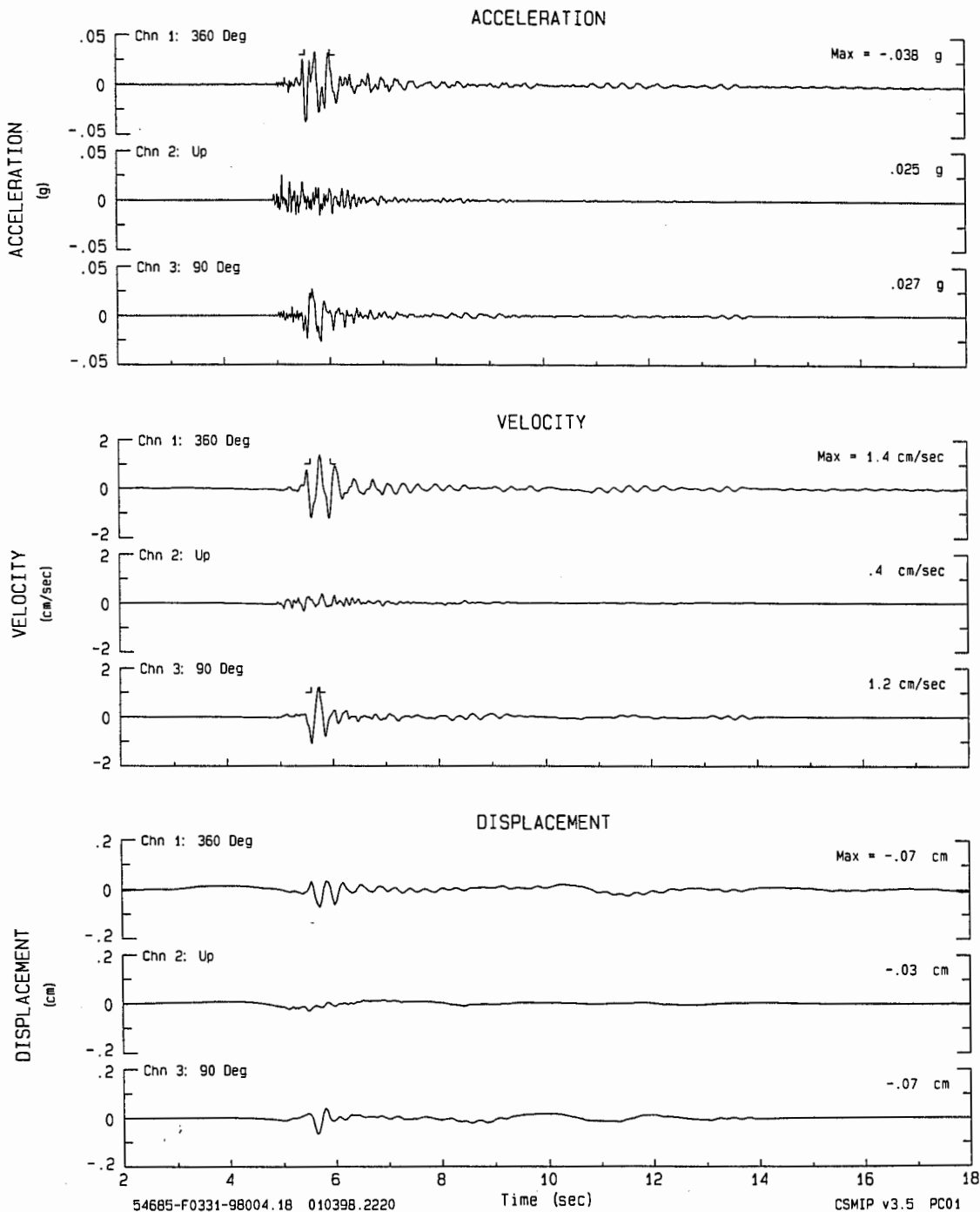


Figure 4. Near-real-time data - three components of band-passes acceleration, velocity and displacement at Mammoth Lakes from the magnitude 3.6 earthquake of January 3, 1998.

Earthquake of Sat Jan 3, 1998 22:19 PS  
 Mammoth Lakes - Sheriffs Substation Sta No. 54685  
 Frequency Band Processed: 5.0 secs to 46.0 Hz

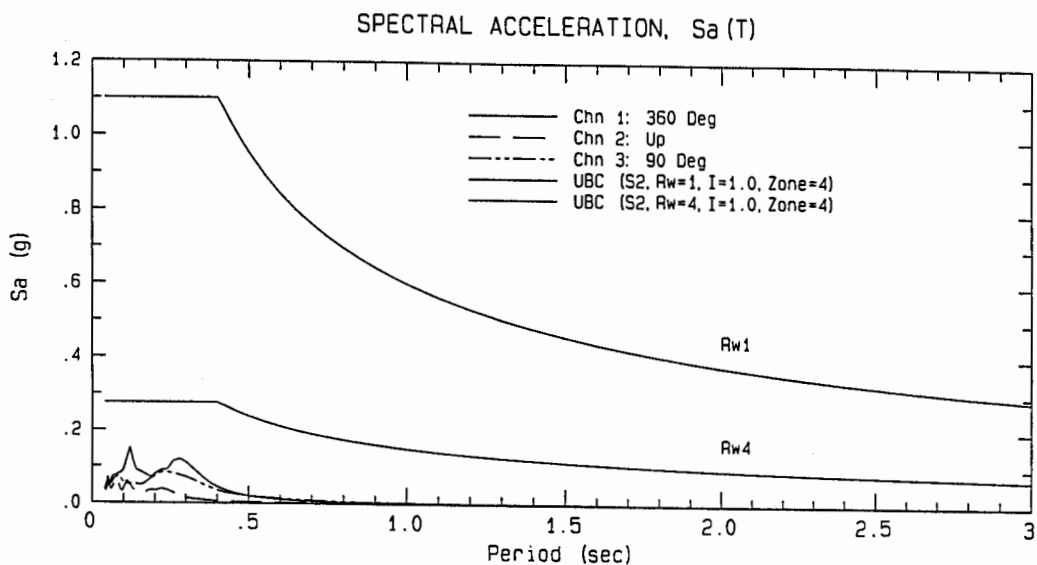


Figure 5. Near-real-time data - three components of spectral acceleration (5% damping) at Mammoth Lakes from the Magnitude 3.6 earthquake of January 3, 1998. The design spectra from the 1994 UBC are plotted for convenient comparison.

forces (ARS curve used in design) and the characteristics of each bridge, Caltrans engineers can determine whether the earthquake force is larger than the design force for each bridge.

One example of post-earthquake evaluation using near-time-data is the Highway 395 near Lake Crowley. The bridge, designed in 1965, is a 2-span, 203 feet long concrete box girder bridge (Figure 6). The substructure consists of a two-column bent and diaphragm abutments supported on spread footings. The bridge was instrumented moderately in 1995 with 9 accelerometers. The locations of these sensors, including 3 at a free-field site and 6 on the bridge structure are shown in Figure 7. The magnitude 5.1 earthquake occurred on June 8, 1998 approximately 5 km west of the bridge. The maximum recorded acceleration was 0.20 g at the free-field and 0.24 g on the bridge (Figure 8).

One can quickly study the acceleration (Figure 8), velocity and displacement (Figure 9) time histories and determine that the bridge has a period of about 0.2 second in the transverse direction and the relative displacement between the top and bottom of column at the central bent is very small. The spectral acceleration of the ground motion at the free-field site level is shown in Figure 10. The force level at 0.2 second is about 0.4 g, which is about one-fourth of the force level, 1.6 g ( $A=0.5g$ ), from the ARS curve in Figure 11 (Caltrans, 1990). One can conclude that the earthquake force was not large enough to damage the bridge.

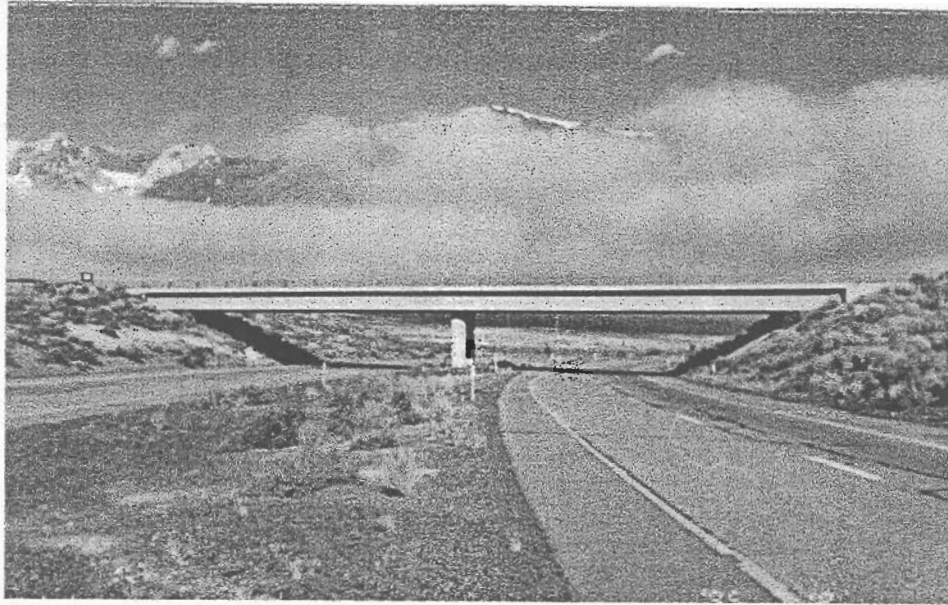


Figure 6. Picture of the Highway 395 Bridge near Lake Crowley. The bridge is a two-span, 203 feet long concrete box girder structure with a two-column bent.

Lake Crowley - Hwy 395 Bridge  
 Caltrans Bridge No. 47-48 (09-MNO-395-13.9)  
 CSMIP Station No. 54730

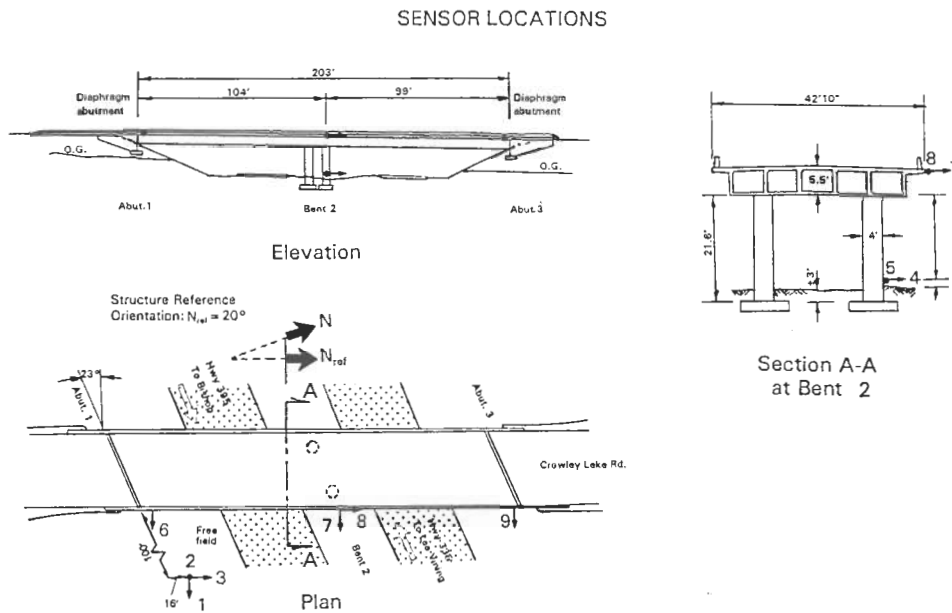
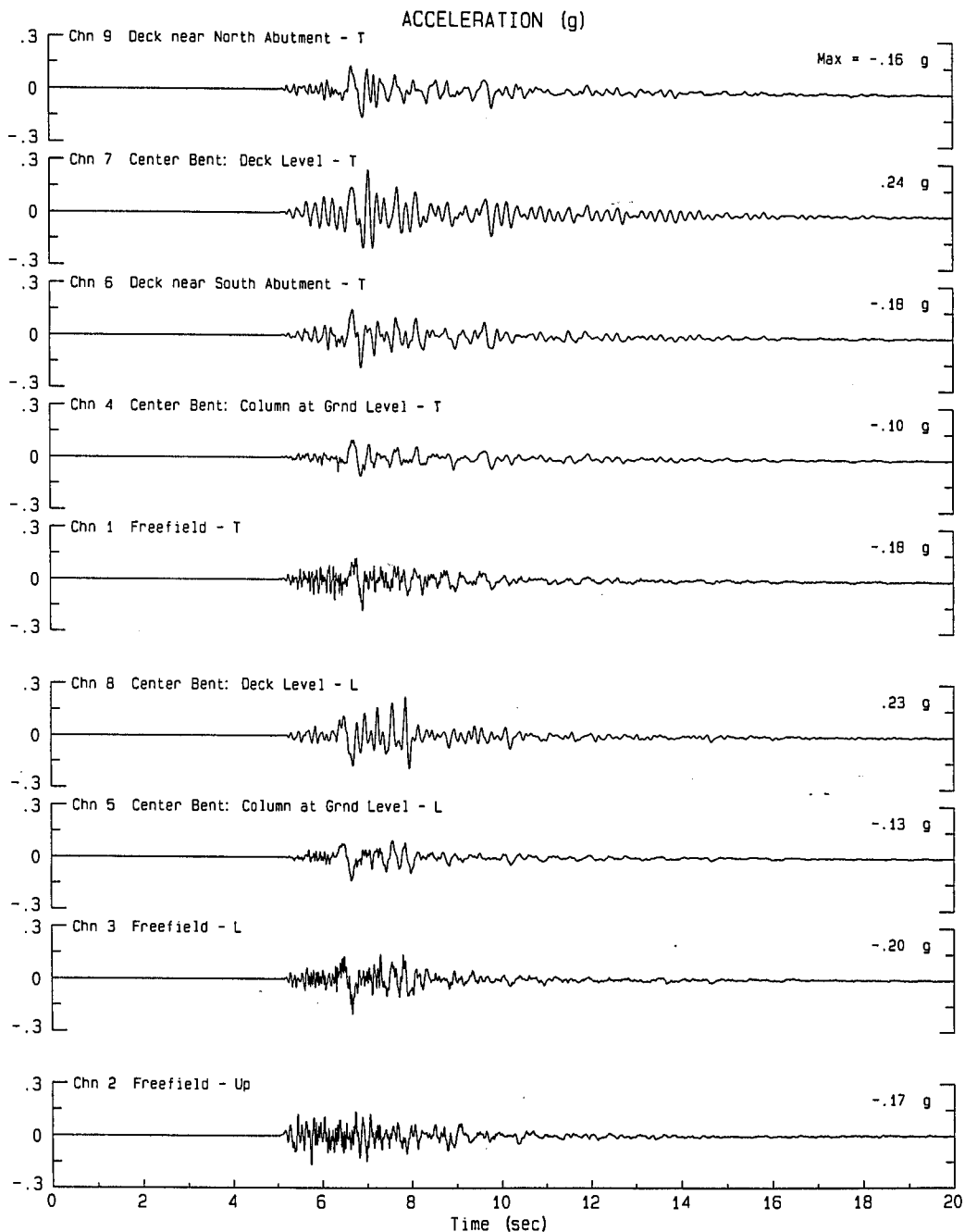


Figure 7. Sensor locations on the Highway 395 Bridge near Lake Crowley. The instrumentation consists of 6 sensors on the bridge and 3 sensors at a reference free-field site.

# SMIP98 Seminar Proceedings

Earthquake of Mon Jun 8, 1998 22:24 PDT  
Lake Crowley - Hwy 395 Bridge Sta No. 54730  
Frequency Band Processed: 5.0 secs to 46.0 Hz  
- CSMIP AUTOMATED STRONG MOTION PROCESSING (PRELIMINARY) -



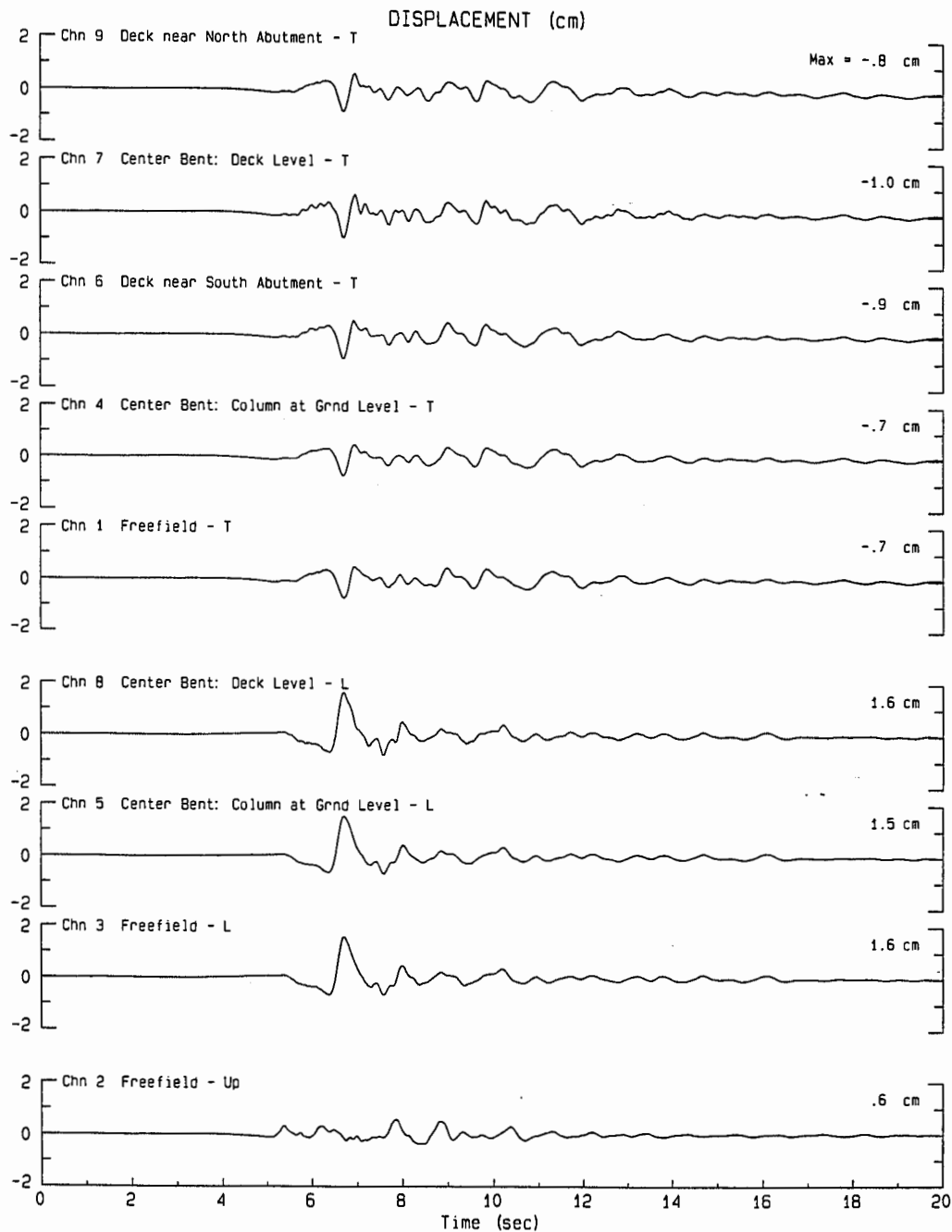
54730-F1275-98159.04 060998.0949

CSMIP v1.0

Figure 8. Acceleration records obtained at the Highway 395 Bridge near Lake Crowley from the magnitude 5.1 earthquake of June 8, 1998, about 5 km west of the bridge.

# SMIP98 Seminar Proceedings

Earthquake of Mon Jun 8, 1998 22:24 PDT  
Lake Crowley - Hwy 395 Bridge Sta No. 54730  
Frequency Band Processed: 5.0 secs to 46.0 Hz  
- CSMIP AUTOMATED STRONG MOTION PROCESSING (PRELIMINARY) -



54730-F1275-98159.04 060998.0949

CSMIP v1.0

Figure 9. Computed displacement (absolute) from acceleration records obtained at the Highway 395 Bridge near Lake Crowley from the magnitude 5.1 earthquake of June 8, 1998, about 5 km west of the bridge.

Earthquake of Mon Jun 8, 1998 22:24 PD  
 Lake Crowley - Hwy 395 Bridge Sta No. 54730  
 Frequency Band Processed: 5.0 secs to 46.0 Hz  
 SPECTRAL ACCELERATION, Sa (T)

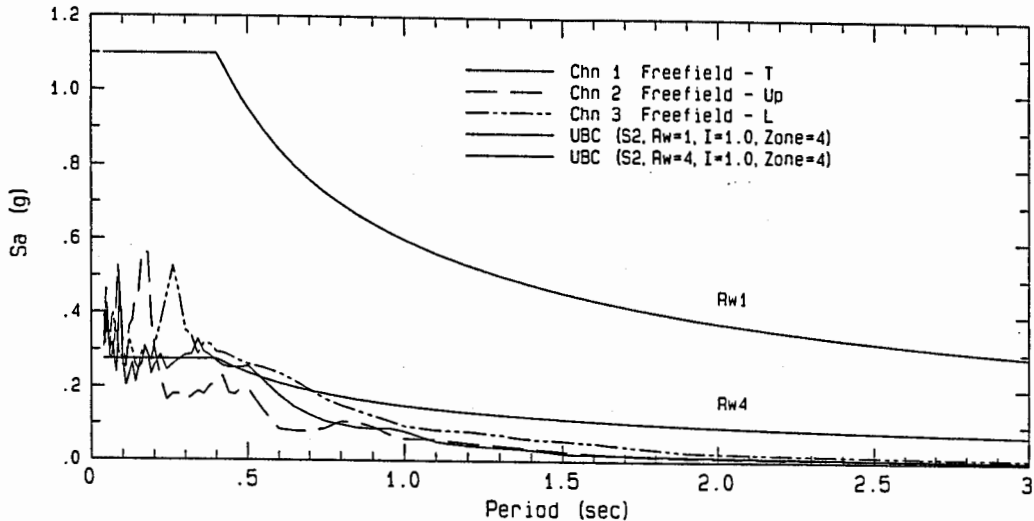


Figure 10. Spectral acceleration (5% damping) for the three-components of ground motion at the free-field site for the Highway 395 Bridge near Lake Crowley from the Magnitude 5.1 earthquake of June 8, 1998.

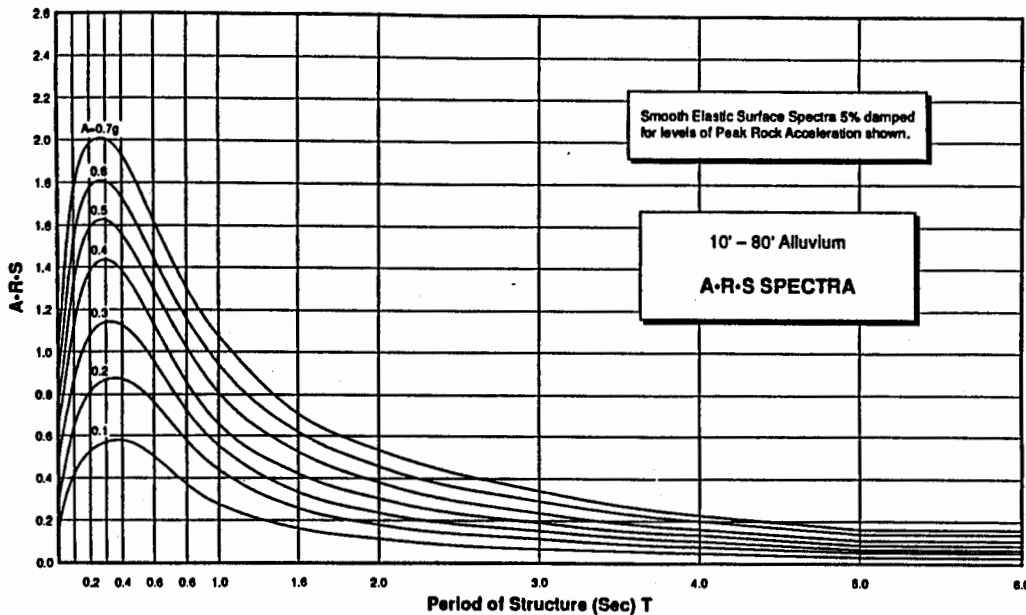


Figure 11. Design spectra (ARS curves) for sites with 10 to 80 feet of alluvium used by Caltrans in design of new bridges and retrofit of existing bridges.

Offshore Eureka Earthquake of 1994

Another example is the magnitude 7.2 earthquake that occurred offshore of Eureka on September 1, 1994, which is the first event for which the near-real-time data were applied for post-earthquake response. Although the earthquake was located 145 km offshore of Eureka, California, a large magnitude earthquake like this is expected to generate a lot of energy at long periods, which may have effects on long-period bridges like the Humboldt Bay Bridge. This earthquake was recorded by the near-real-time instruments installed at the Humboldt Bay Bridge. Peak motions at the bridge abutment was 0.03 g in acceleration and 4 cm/sec in velocity(CSMIP, 1994). The near-real-time data from the bridge and other stations were distributed to Caltrans post-earthquake response team after the earthquake. The information allowed Caltrans engineers to rapidly decide not to send inspectors to the Eureka area, 500 miles from Sacramento, to inspect their bridges in the area, despite the occurrence of an earthquake as large as magnitude 7.2.

Criteria for Post-Earthquake Inspection of Bridges

After a damaging earthquake occurs, TriNet ShakeMaps will provide ground shaking information within minutes of the event. For bridges that collapse during the earthquake, that information will probably be reported by the California Highway Patrol or the local newscasters. However, for the bridges that are damaged and need to be inspected to determine the extent of damage, TriNet ground shaking information will help Caltrans engineers in determining where and which bridges need to be inspected. To facilitate the inspection efforts, it is essential that there is a correlation between the ground shaking and the performance of different types of bridges. The 1994 Northridge earthquake provided an opportunity for studying the relationship between bridge performance and ground motion. The bridges can be grouped into various types of structures bridges, and their performances can be correlated with the ground motion. Fragility curves for each type of bridge structure can be derived in a statistical sense. However, more data are needed from different earthquakes to obtain more reliable empirical fragility curves, and the spectral acceleration values at 0.3, 1 and 3.0 seconds seem to be better parameters than the peak ground acceleration in indicating the effects of ground motion on structures.

One of the simple screening criteria for bridge inspection can be based on the ratio of the earthquake forces inferred from the ground motion data and the design forces used in the working stress design. In designing new bridges and retrofit of existing bridge, the design forces are used to be obtained by dividing the expected seismic forces from the ARS curves by the appropriate factor, Z, as shown in Figure 12 (Caltrans, 1990). One can expect that individual structural members would yield when the earthquake forces exceed the design forces used for those members. The members would have cracked if they yield and therefore need to be inspected. Since most of the Caltrans bridges in the State have been studied for retrofit and some have been retrofitted, the ARS values used in design of various elements in each bridge are known. For recorded earthquake shaking, when  $S_a(T)$  is greater than  $ARS(T)/Z$ , then bridge inspection is warranted.

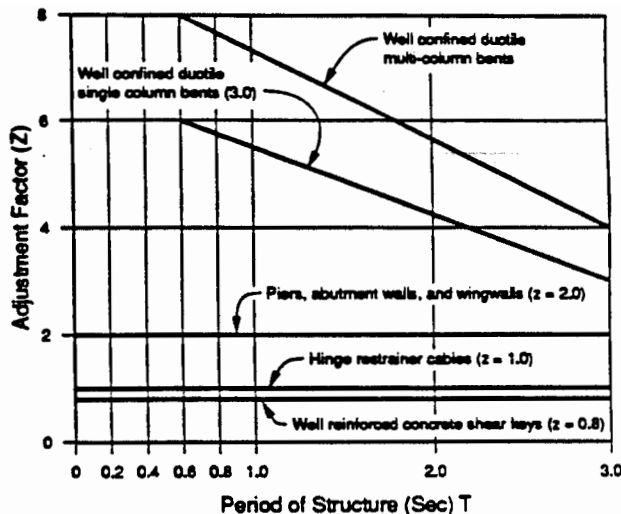


Figure 12. Factor, Z, for adjustment of seismic forces from the ARS curves, used is seismic designs of bridges (Caltrans, 1990).

Another screening criteria may be based on the displacements estimated from the recorded data. Dynamic models of these structures can tabulate the threshold displacements for a particular member prior to an event. This list of threshold deflections can be quickly compared with the near-real-time data recorded from these structures. These fragility lists can be developed for all the toll bridges and for important interchange bridges in the large urban areas. After only a few minutes of review the inspection efforts can be coordinated to concentrate on the areas of greatest concern. This is especially valuable for the large toll bridges which in some cases are many miles long.

It is extremely important to obtain the relative deflection of the large piers of the major toll bridges from the data right after an event. The piers with the most worrisome deflections will be assigned to the first inspection team. A large amount of analytical efforts will need to be put into these threshold lists because the capacity of shorter piers can be vastly different from the capacity of taller piers. The sooner a structure can be opened to the traffic the sooner emergency vehicles can utilize the route. A threshold-exceeded warning system can be set up in the toll plaza to give early bridge closure information to the toll captains after a large earthquake.

## SUMMARY

The California Department of Transportation and the Department of Conservation continue to instrument bridges for strong motion to measure the ground motion and the response of the bridge structure to these motions. The strong-motion data recorded at these bridges provide valuable information for understanding the seismic response of the bridge and for improving seismic design and analysis procedures for bridges. In addition to these long-term



objectives, the near-real-time recovery and processing of the recorded data is useful for post-earthquake evaluation of the bridges. The strong-motion data will be shared with other states and countries to improve seismic safety of bridge structures throughout the world. Bridge and soil-foundation-structure modeling techniques will be improved to reflect the actual measurements from the bridge structures. Continued efforts towards utilizing the near-real-time data for post-earthquake response and structural integrity assessments of the bridge must be ongoing and expanding.

### REFERENCES

CSMIP, (1994). CSMIP Strong-Motion Data from the Offshore Eureka Earthquake of 1 September 1994, Report OSMS 94-18, September 2, 1994.

Caltrans, (1990). Seismic Design References, State of California, Department of Transportation, Division of Structures, June.

Housner, G., chairman (1990). Competing Against Time, Report to Governor George Deukmejian from the Governor's Board of Inquiry on the 1989 Loma Prieta Earthquake, State of California, Office of Planning and Research, May.

Rojahn, C. and Raggett, J. (1981). Guidelines for Strong-Motion Instrumentation of Highway Bridges, U.S. Department of Transportation, Federal Highway Administration, Report No. FHWA/RD-82/016, December.

Shakal, A., Petersen, C., Cramlet, A. and Darragh, R. (1995). CSMIP Near-Real-Time Strong Motion Monitoring System: Rapid Recovery and Processing for Event Response, in SMIP95 Seminar Proceedings, California Strong Motion Instrumentation Program, May.

Shakal, A., Graizer, V., Petersen, C., and Darragh, R. (1997). Near-Real-Time Strong Motion, TriNet Data and Data Dissemination through the Internet, in SMIP97 Seminar Proceedings, California Strong Motion Instrumentation Program, May.

Zelinski, R. (1990) California Highway Bridge Retrofit Strategy and Details, in Proceedings of the SEAOC Annual Meeting, September.

Wald, D., Quitoriano, V., Heaton, T., Kanamori, H., and Scrivner, C. (1998) TriNet ShakeMaps: Rapid Generations of Peak Ground Motion and Intensity Maps for Earthquakes in Southern California, in SMIP98 Seminar Proceedings, California Strong Motion Instrumentation Program, September.



**RESPONSE EVALUATION OF A 20-STORY CONCRETE FRAME  
BUILDING TO THE NORTHRIDGE AND OTHER EARTHQUAKES**

G. Hart, M. Skokan, and H. Martin

Department of Civil and Environmental Engineering  
University of California, Los Angeles

**ABSTRACT**

The response of an instrumented reinforced concrete moment-resisting frame (RCMRF) building, located in Southern California, was investigated in this research and compared to the response of linear elastic analytical models of the building. RCMRF buildings are particularly difficult to model when the objective is to predict the performance of the building. Therefore, nine models of the case study building were created by making three assumptions for the stiffness of the beams and columns and three assumptions for the stiffness of the beam-column joints. Fundamental periods for the models were compared to the fundamental periods calculated directly from the building response recorded during the 1987 Whittier and 1994 Northridge earthquakes. In addition, the analytical models were subjected to the ground accelerations recorded during the Whittier and Northridge earthquakes in a time history analysis and the maximum floor displacements compared to the recorded floor displacements.

**INTRODUCTION**

The design goal of any structural engineer for a new building or seismic rehabilitation project must be the development of a building design whose performance during a range of earthquakes can be accurately estimated. This concept is known as Performance-Based Design (PBD) and is currently the subject of building code developments. The goal of performance prediction can only be achieved when the design is based on a proper analytical model of the building system and the earthquake ground motion that the building can be expected to experience during its design life.

The SEAOC Vision 2000 report (OES, 1995) outlines a framework for implementing the PBD concept. One of the first steps in PBD is the selection of performance objectives, each of which requires the selection of a seismic hazard level and performance level. The seismic hazard level is defined by the selection of a return period for the earthquake motion and the performance level specifies a level of structural and non-structural damage by both qualitative and quantitative measures. For each of the selected performance objectives, an analysis of the building is performed using the seismic hazard and the building response is compared to the acceptance criteria for the specified performance level. It is during this phase of the PBD procedure that the importance of a proper analytical model of the building is realized.

In this research, the response of an instrumented RCMRF building, located in Southern California, was studied and compared to the response of linear elastic analytical models of the

building. RCMRF buildings are particularly difficult to model when the objective is to predict the performance of the building. It is difficult to quantify the stiffness of the beams and columns in a linear elastic computer model primarily because the stiffness of each element is highly dependant on the level of strain induced by flexural and axial loads. Furthermore, the contribution of the floor slab to the stiffness of the beams, the effect of confinement on the behavior of the columns, and the stiffness of the beam-column joints, further increases the complexity of the modeling decisions.

### BUILDING DESCRIPTION

The focus of this study is a 20-story reinforced concrete frame hotel (Figure 1) located in North Hollywood, California, approximately 19 km from the epicenter of the 1994 Northridge Earthquake. Constructed in 1968, this building was the first to be designed using the 1966 Los Angeles building code that prescribed ductility requirements for reinforced concrete moment resisting frames (Wayman, 1968; Steinmann, 1998). As a result, the design features a strong column-weak beam concept, under-reinforced beams to assure steel yielding prior to concrete crushing, full hoop ties in the beam-column joints, continuous top and bottom beam bars through the joints, and column bar splices at the mid-height (Wayman, 1968).

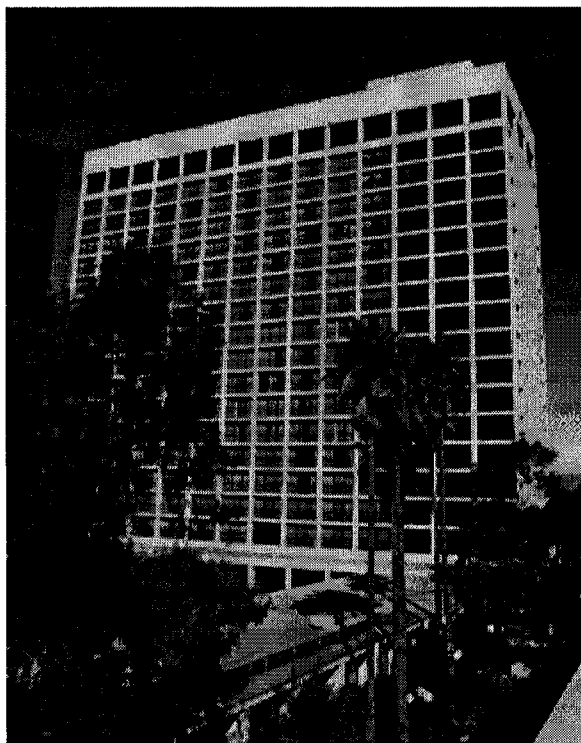


Figure 1 20-story North Hollywood building

All concrete is composed of lightweight aggregate with 3,000 psi and 4,000 psi compressive strength at 28 days. The reinforcing steel was specified to be both high-strength ASTM 432 grade with 60,000 psi yield strength and ASTM A-15 grade with 40,000 psi yield strength. The typical floor elevation is 8'-9" and a typical bedroom floor plan is shown in Figure 2. Below grade, perimeter concrete shear walls and spread footings support the 210-ft structure.

### SEISMIC BUILDING RESPONSE

The 20-story North Hollywood building is instrumented with strong motion sensors by the California Strong Motion Instrumentation Program (CSMIP). Sixteen strong motion sensors, as shown in Figure 3, are located over the height of the building, with three sensors placed at each of four floors (3rd, 9th, 16th, and Roof) and four sensors located at the basement level. Strong motion records are available from five major earthquakes over the past 30 years including: 1971 San Fernando, 1987 Whittier, 1992 Landers, 1992 Big Bear, and 1994 Northridge.

Only the records from the 1987 Whittier and the 1994 Northridge earthquakes are addressed in this research. The ground acceleration time histories in the North-South and East-West directions are shown for the Northridge and Whittier earthquakes in Figures 4 and 5, respectively. Note that for both events, the East-West direction peak ground acceleration (PGA) is the larger of the two components, and in the case Northridge, the East-West PGA is approximately three times larger. In terms of PGA, it is also observed that Northridge was clearly stronger than the Whittier event.

During the Northridge earthquake, the case study building suffered heavy non-structural and content damage, with no signs of significant structural damage. The non-structural damage was limited to partitions, door openings, floor tiles, chandeliers, and broken glass. Sidewalk slabs on grade were cracked, some oil spillage occurred in the basement, and damage to mechanical equipment was minimal (Naeim, 1997).

In order to compare the observed damage and the performance level guidelines provided in the Vision 2000 report, the recorded displacement response from the Northridge earthquake was studied. Figure 6 shows the roof relative displacement ratio history at the center-of-mass location. The center-of-mass displacement history was calculated by transforming the displacement history from the three roof sensors using the methodology outlined by Naeim (1997). Figure 6 also indicates the displacement ratio suggested by the Vision 2000 report for the Fully Operational and Operational performance levels. In general, the displacement ratios fall within the definition of the Fully Operational performance level, however, one strong pulse in the North-South direction displaces the building to a 0.4% displacement ratio. This is near the displacement ratio used to define the Operational performance level. According to the Vision 2000 report, the damage expected at the Operational performance level consists of minor structural damage, light to moderate non-structural damage including broken glass, cracked partitions, minor damage to light fixtures, and minor content damage. In general, this is very consistent with the observed damage.

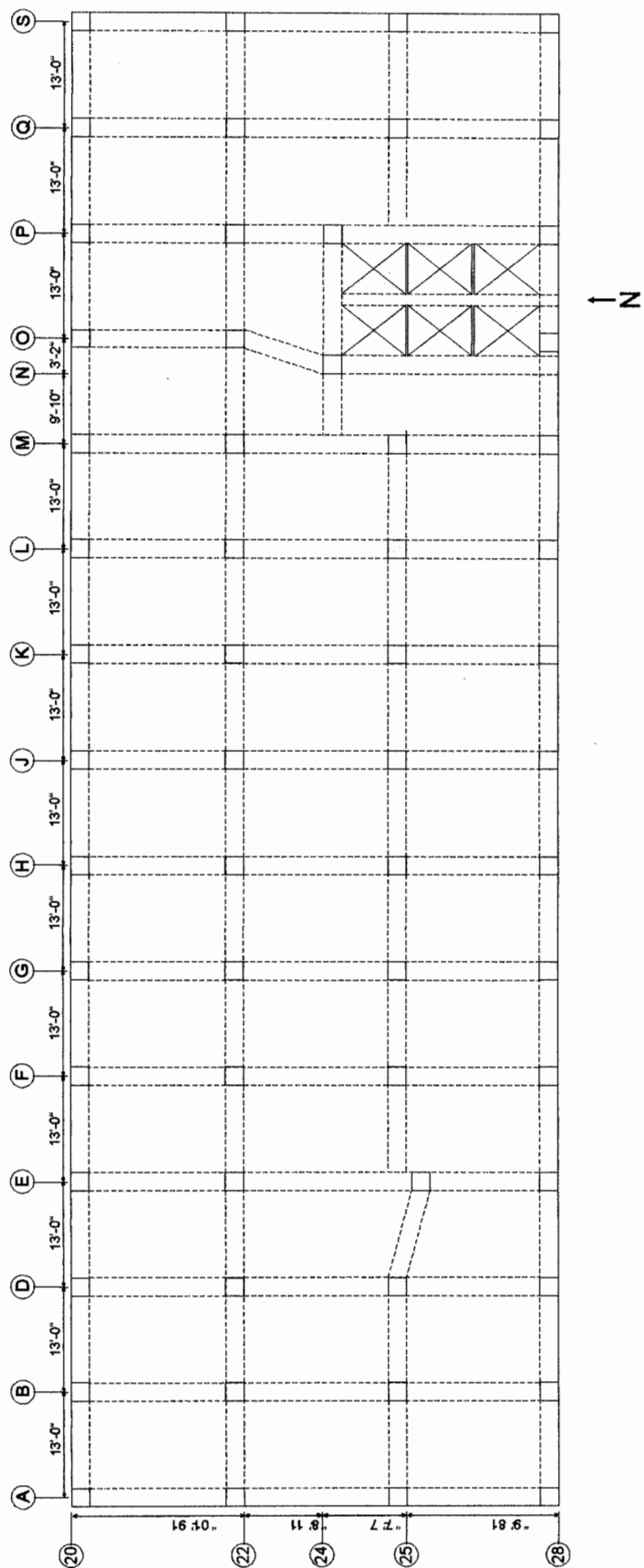


Figure 2 Typical bedroom floor plan

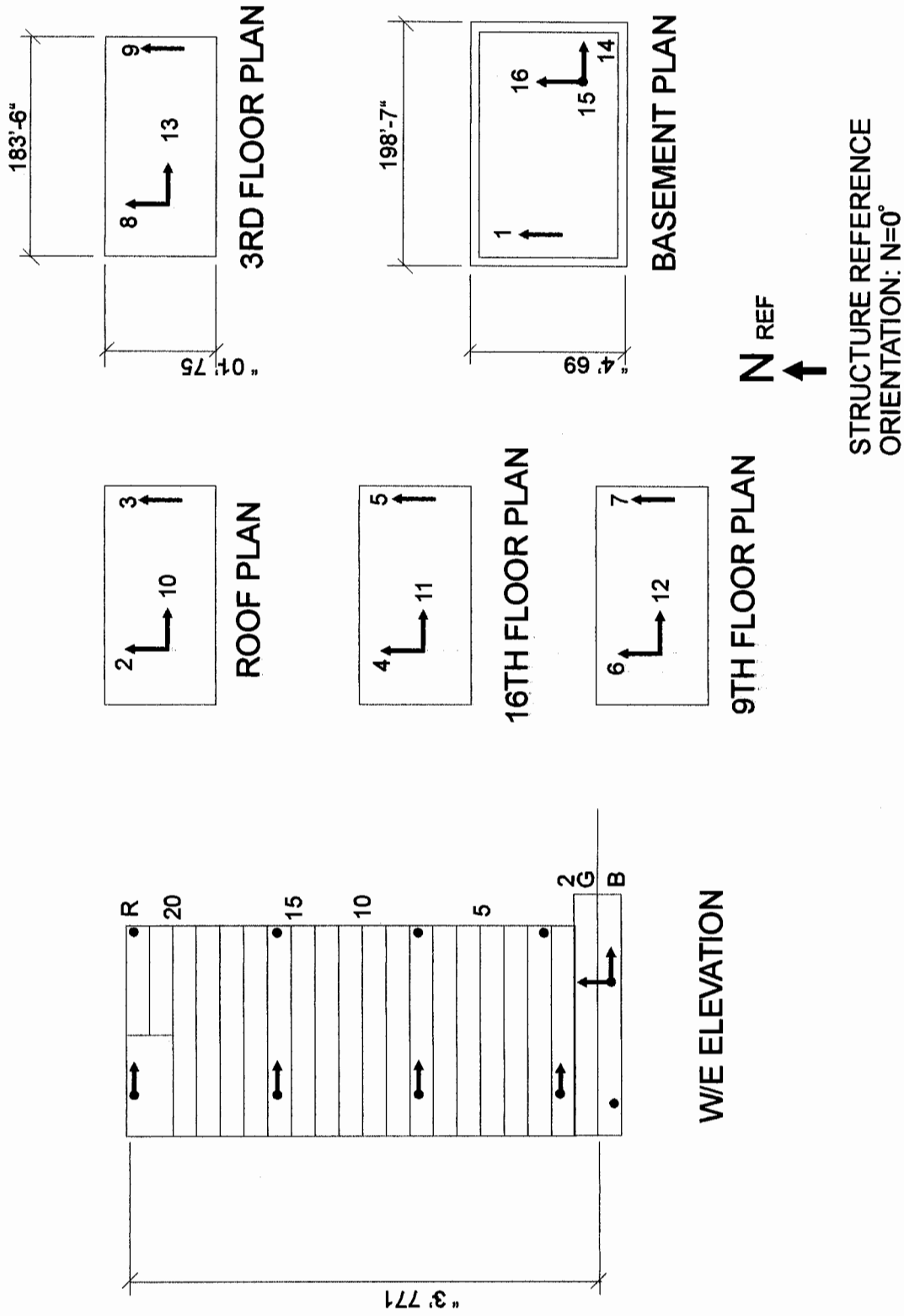
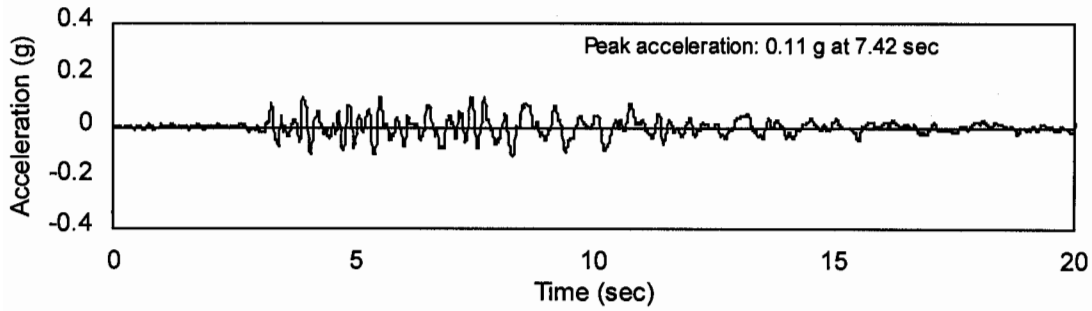
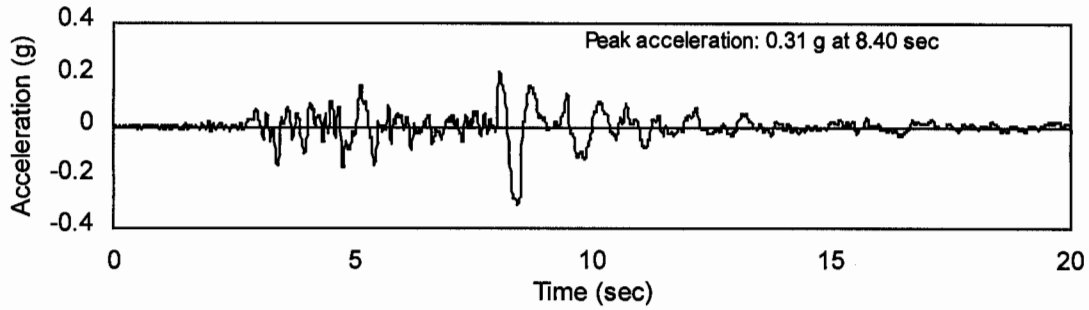


Figure 3 Sensor locations

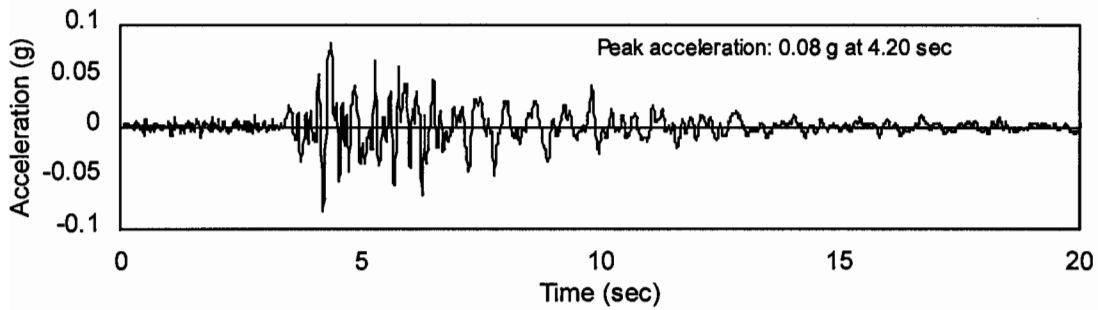


(a) North-South (Longitudinal) direction (Channel 16)

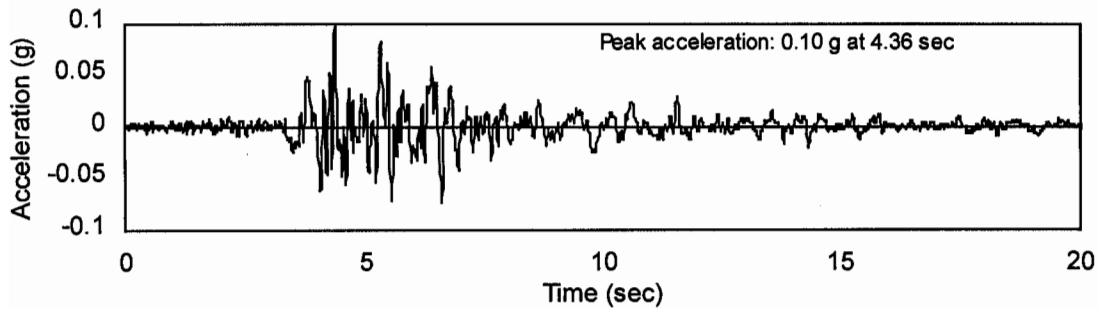


(b) East-West (Transverse) direction (Channel 14)

Figure 4 1994 Northridge earthquake acceleration time histories at ground level



(a) North-South (Longitudinal) direction (Channel 16)



(b) East-West (Transverse) direction (Channel 14)

Figure 5 1987 Whittier Earthquake acceleration time histories at ground level



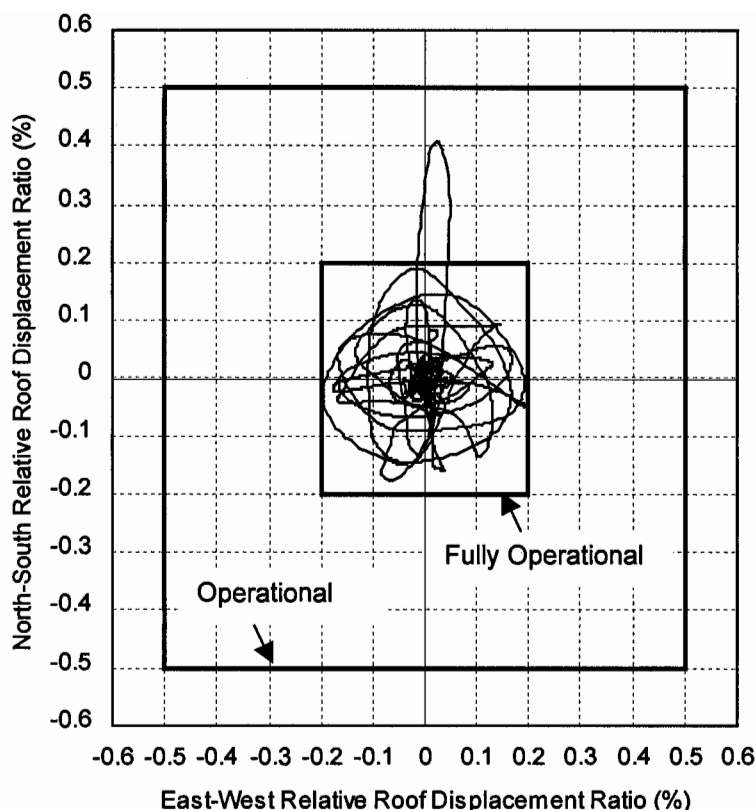


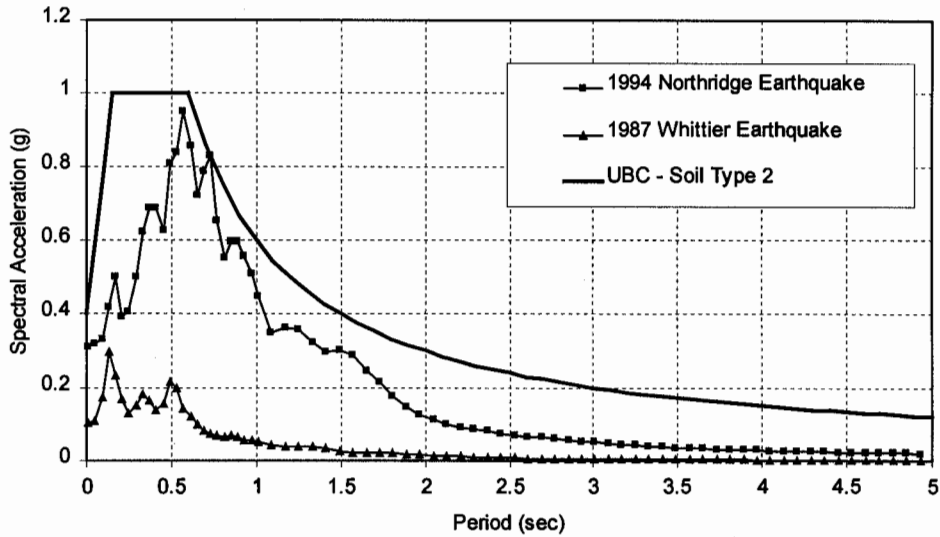
Figure 6 Northridge earthquake relative roof displacement ratio history with Vision 2000 (OES, 1995) performance level drift ratios

Studies of the instrumented response of the case study building (Goel, et. al, 1997; Naeim, 1997) have yielded estimates of the fundamental translational periods of vibration for the building. In addition, the studies by Goel, et. al. have resulted in estimates of the percentage of critical damping for these fundamental periods. The results of the work by Goel, et. al. are provided in Table 1. The results show that the periods of vibration in the transverse and longitudinal building directions are approximately equal. Note also that the fundamental periods estimated for the Northridge earthquake are approximately 18% larger than for the Whittier earthquake. This is most likely due to the fact that the displacement demands from the Northridge earthquake were significantly greater than during the Whittier earthquake.

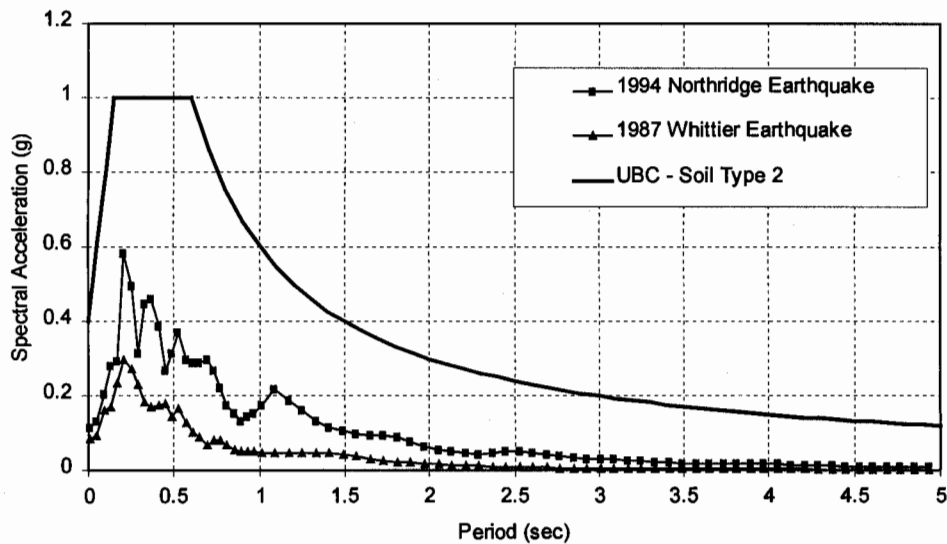
Table 1 Translational periods of vibration and percentage of critical damping (Goel, et. al, 1997)

| Earthquake Record | North-South (Longitudinal) |             | East-West (Transverse) |             |
|-------------------|----------------------------|-------------|------------------------|-------------|
|                   | Period (sec)               | Damping (%) | Period (sec)           | Damping (%) |
| 1987 Whittier     | 2.15                       | ---         | 2.21                   | ---         |
| 1994 Northridge   | 2.6                        | 5.9         | 2.62                   | 6.5         |

Using the ground acceleration records for the Whittier and Northridge earthquakes, the 5% damped response spectra were calculated and are given in Figure 7 along with the UBC design spectrum for soil type 2. For the fundamental periods estimated by Goel, et. al., notice that the spectral accelerations are well below the values that given by the UBC design spectrum.



(a) North-South (Transverse) direction



(b) East-West (Longitudinal) direction

Figure 7 5% damped response spectra at ground level

## ANALYTICAL COMPUTER MODELS

The case study building was analyzed using the three-dimensional linear elastic computer program ETABS (CSI, 1997). All of the beams and columns of the moment resisting frames were included in the model along with the walls at the basement level. A three-dimensional illustration of the computer model is provided in Figure 8.

The floor diaphragms were assumed to be rigid and assigned a mass, center-of-mass location, and mass moment of inertia based on detailed calculations assuming point masses at the column locations. Since the structural elements are composed of lightweight concrete, 105 pcf was assumed for the unit weight of all concrete. In addition, the weight of partitions, exterior cladding, and specific mechanical equipment was included along with 15 psf to account for mechanical, electrical, ceiling and floor finishes, and other miscellaneous items.

Nine models of the case study building were created by making three assumptions for the stiffness of the beams and columns and three assumptions for the stiffness of the beam-column joints.

For the *Gross Stiffness* model, all of the beams and columns were assigned a gross moment of inertia for flexure, representing the stiffness of the elements prior to cracking. This type of model would be applicable for buildings that are subjected to minor ground shaking inducing low levels of stresses in the structural elements.

In the *FEMA 273 Stiffness* model, the beams and columns were assigned an effective moment of inertia based on a percentage of the gross moment of inertia suggested by the *NEHRP Guidelines for the Seismic Rehabilitation of Buildings - FEMA 273* (ATC, 1997). FEMA 273 suggests the use of 50% of gross for beams, 70% of gross for columns in axial compression, and 50% of gross for columns in axial tension. Since the axial load in the columns will vary throughout the analysis, 60% of gross was assumed for the column stiffness in this model. These percentages are general guidelines intended to estimate the effective (or secant) stiffness of the elements at the first yield of the reinforcement.

The *Yield Stiffness* model is similar in concept to the FEMA 273 Stiffness model, except that the effective flexural stiffness at first yield of the reinforcement is determined from a moment-curvature analysis of the section. The reinforced concrete strength analysis computer program BIAx (Wallace, 1992) was used to calculate the moment-curvature relations. The analysis included the concrete stress-strain model developed by Saatcioglu, et. al. (1992) and strain hardening of reinforcing steel. Expected values were assumed for the concrete and steel strengths. For each beam, both a bare and flanged beam section were analyzed and the resulting stiffness values averaged based on the assumption that the beams will bend in double curvature. The effective slab width included in the flanged beam analyses was based on the recommendations by Paulay and Priestley (1992). For the columns, the axial load was varied in the analyses and the stiffness assigned to the column elements was based on an estimate of the axial load in the element due to gravity load. The results of the moment-curvature analyses showed that the effective stiffness typically ranges between 30-50% of gross for the beams and 30-60% of gross for the columns depending on the level of axial load.

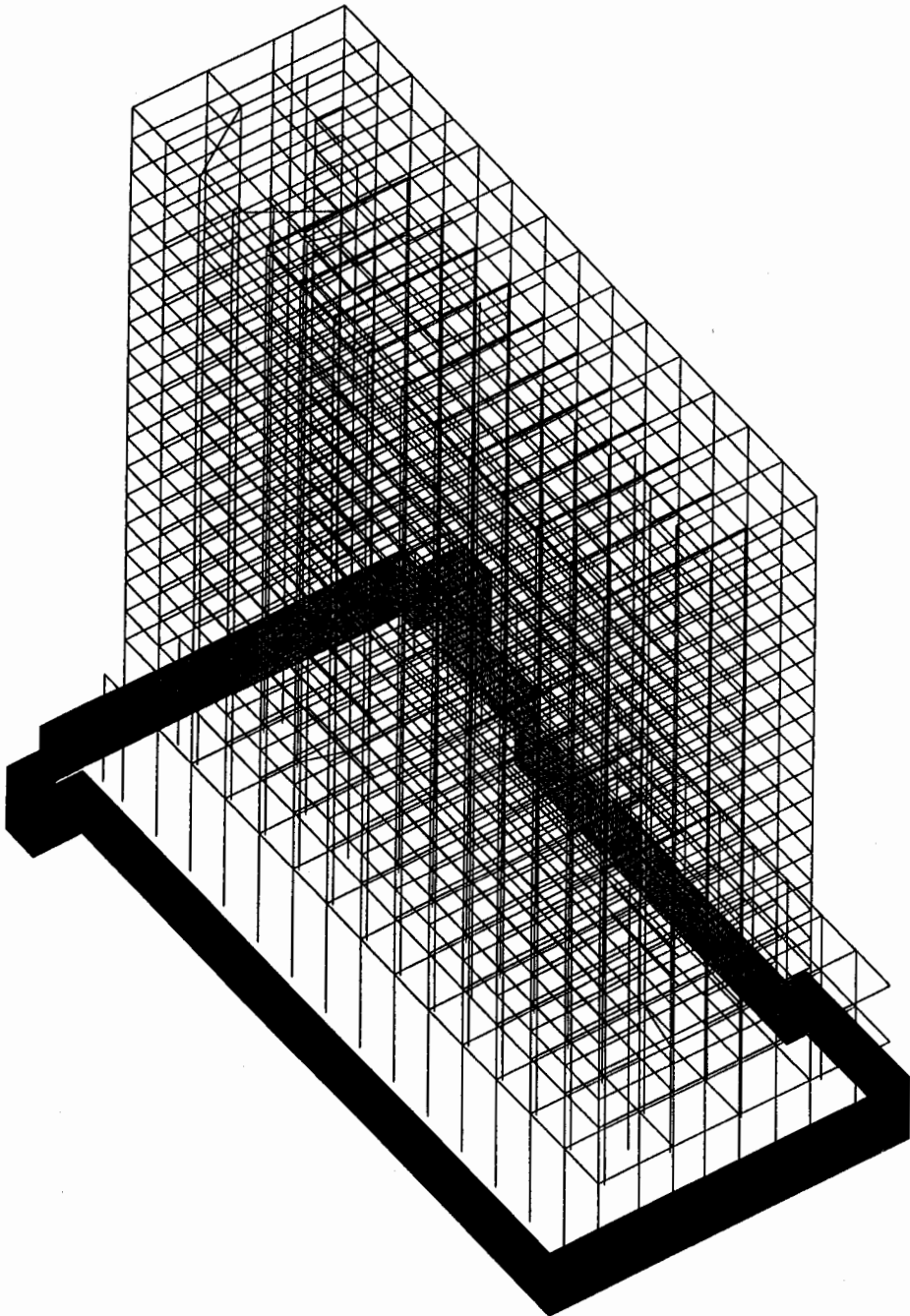


Figure 8 ETABS computer model

Both the FEMA 273 and Yield Stiffness models would be appropriate for a building subjected to a moderate level of ground shaking that induces sufficiently high stresses in the elements to cause cracking but not yield of the steel reinforcement.

The stiffness of the beam-column joints was varied to reflect a range of behavior. This was accomplished by varying the length of the rigid end zone (REZ) at the beam-column intersections. In the 100% REZ model, the entire beam-column intersection was assumed to rigid, the 50% REZ model assumes that only one-half of the beam-column intersection is rigid, and the *Centerline* model assumes no rigidity of the beam-column intersection.

### PREDICTED BUILDING RESPONSE

Using the nine ETABS models described in the previous section, eigenvalue analyses were performed to determine the natural frequencies and mode shapes for the models. Table 2 gives the periods of vibration and the percentage of participating mass in each direction for the first six modes of each model. As one would expect, as the stiffness of the beams, columns, and REZ's decrease, the periods of vibration tend to increase. Examination of these results also shows that there is a coupling between the fundamental North-South and Torsional modes of vibration. Figure 9 illustrates this coupling effect and the relatively uncoupled behavior of the East-West mode of vibration for the Gross Stiffness model with 50% REZ.

For the first three modes of vibration in the Gross Stiffness model with 50% REZ, the periods range between 2.27 and 2.08 seconds compared to the 2.15 and 2.21 second periods shown in Table 1 for the building response during the Whittier earthquake. Overall, the periods of vibration for the Gross Stiffness models fall within 15% of the periods shown in Table 1 for the Whittier earthquake. Comparison of the periods of vibration predicted by the analytical models and those given in Table 1 show that for the Northridge earthquake, the FEMA 273 Stiffness model with 100% REZ gives a good correlation, although the other FEMA 273 Stiffness models vary by only 25%. The Yield Stiffness models predict periods of vibration ranging between 25% and 40% of the values given in Table 1. Therefore, it can be said that the stiffness of the beams and columns during the Northridge earthquake is somewhere between the gross stiffness and the stiffness at first yield calculated from a moment-curvature analysis.

The nine ETABS models were subjected to the two components of ground acceleration (Channel 14 & 16) for the Northridge and Whittier earthquakes in a time history analysis. A sufficient number of modes were included in the analyses such that they account for at least 90% of the participating mass. As a benchmark consideration, 5% damping was assumed in the analyses for all modes, which is consistent with the damping estimated by Goel, et. al. for the fundamental modes of vibration during the Northridge earthquake.

Table 2 Periods of vibration and participating mass from ETABS models

(a) Gross Stiffness building model

| Mode # | 100% REZ Model |                      |      |          | 50% REZ Model |                      |      |          | Centerline Model |                      |      |          |
|--------|----------------|----------------------|------|----------|---------------|----------------------|------|----------|------------------|----------------------|------|----------|
|        | Period         | % Participating Mass |      |          | Period        | % Participating Mass |      |          | Period           | % Participating Mass |      |          |
|        |                | N-S                  | E-W  | Rotation |               | N-S                  | E-W  | Rotation |                  | N-S                  | E-W  | Rotation |
| 1      | 2.11           | 48.6                 | 0.3  | 19.3     | 2.27          | 44.7                 | 0.6  | 22.9     | 2.43             | 40.9                 | 1.2  | 26.0     |
| 2      | 1.98           | 21.3                 | 2.4  | 45.4     | 2.13          | 24.3                 | 7.5  | 37.8     | 2.30             | 19.8                 | 32.8 | 18.0     |
| 3      | 1.90           | 0.1                  | 67.8 | 2.3      | 2.08          | 1.1                  | 62.6 | 6.4      | 2.26             | 9.4                  | 36.9 | 23.1     |
| 4      | 0.71           | 10.5                 | 0.0  | 2.2      | 0.77          | 10.1                 | 0.0  | 2.4      | 0.83             | 9.7                  | 0.0  | 2.6      |
| 5      | 0.65           | 1.2                  | 1.6  | 8.2      | 0.71          | 1.1                  | 4.0  | 5.5      | 0.77             | 0.8                  | 7.2  | 2.5      |
| 6      | 0.63           | 0.1                  | 9.2  | 1.8      | 0.69          | 0.4                  | 6.7  | 4.1      | 0.75             | 0.9                  | 3.5  | 6.8      |

\* REZ = Rigid End Zones

(b) FEMA 273 Stiffness building model

| Mode # | 100% REZ Model |                      |      |          | 50% REZ Model |                      |      |          | Centerline Model |                      |      |          |
|--------|----------------|----------------------|------|----------|---------------|----------------------|------|----------|------------------|----------------------|------|----------|
|        | Period         | % Participating Mass |      |          | Period        | % Participating Mass |      |          | Period           | % Participating Mass |      |          |
|        |                | N-S                  | E-W  | Rotation |               | N-S                  | E-W  | Rotation |                  | N-S                  | E-W  | Rotation |
| 1      | 2.81           | 40.3                 | 0.6  | 27.2     | 3.03          | 36.5                 | 1.1  | 30.4     | 3.25             | 33.0                 | 2.3  | 32.7     |
| 2      | 2.64           | 29.4                 | 4.5  | 35.8     | 2.86          | 24.1                 | 28.5 | 17.8     | 3.11             | 8.9                  | 60.6 | 1.0      |
| 3      | 2.57           | 0.7                  | 64.9 | 3.9      | 2.82          | 9.8                  | 40.6 | 18.9     | 3.04             | 28.5                 | 7.5  | 33.3     |
| 4      | 0.95           | 9.3                  | 0.0  | 2.7      | 1.03          | 9.0                  | 0.0  | 3.0      | 1.11             | 8.7                  | 0.1  | 3.2      |
| 5      | 0.87           | 1.5                  | 2.4  | 6.6      | 0.95          | 1.1                  | 6.0  | 3.3      | 1.04             | 0.7                  | 8.5  | 1.2      |
| 6      | 0.85           | 0.3                  | 8.3  | 2.4      | 0.93          | 0.9                  | 4.6  | 5.5      | 1.01             | 1.4                  | 2.0  | 7.3      |

\* REZ = Rigid End Zones

(c) Yield Stiffness building model

| Mode # | 100% REZ Model |                      |      |          | 50% REZ Model |                      |      |          | Centerline Model |                      |      |          |
|--------|----------------|----------------------|------|----------|---------------|----------------------|------|----------|------------------|----------------------|------|----------|
|        | Period         | % Participating Mass |      |          | Period        | % Participating Mass |      |          | Period           | % Participating Mass |      |          |
|        |                | N-S                  | E-W  | Rotation |               | N-S                  | E-W  | Rotation |                  | N-S                  | E-W  | Rotation |
| 1      | 3.12           | 28.7                 | 4.8  | 35.5     | 3.38          | 14.1                 | 23.1 | 31.8     | 3.67             | 2.4                  | 55.5 | 11.4     |
| 2      | 3.04           | 34.1                 | 26.9 | 10.1     | 3.33          | 19.0                 | 43.2 | 7.1      | 3.60             | 22.5                 | 13.1 | 33.0     |
| 3      | 3.01           | 9.2                  | 37.4 | 22.7     | 3.27          | 38.8                 | 2.9  | 29.6     | 3.52             | 46.9                 | 0.7  | 24.0     |
| 4      | 1.10           | 9.9                  | 0.1  | 1.3      | 1.19          | 9.6                  | 0.2  | 1.5      | 1.29             | 8.3                  | 1.3  | 1.6      |
| 5      | 1.06           | 0.3                  | 8.8  | 1.9      | 1.17          | 0.4                  | 10.1 | 0.6      | 1.28             | 1.5                  | 9.4  | 0.0      |
| 6      | 1.03           | 0.4                  | 2.5  | 8.5      | 1.13          | 0.5                  | 1.1  | 9.6      | 1.23             | 0.5                  | 0.6  | 9.8      |

\* REZ = Rigid End Zones

The maximum displacement predicted by the analyses was compared to the maximum recorded displacements at each instrumented floor. The results of this comparison are shown in Table 3 and displayed graphically for the Northridge earthquake in Figure 10. The results from the FEMA 273 Stiffness model show that maximum displacement is predicted within 20% of the recorded displacement at each floor for the Northridge earthquake. Increased dispersion in the ratio between recorded and predicted maximum displacement is observed for the Gross Stiffness and Yield Stiffness models.

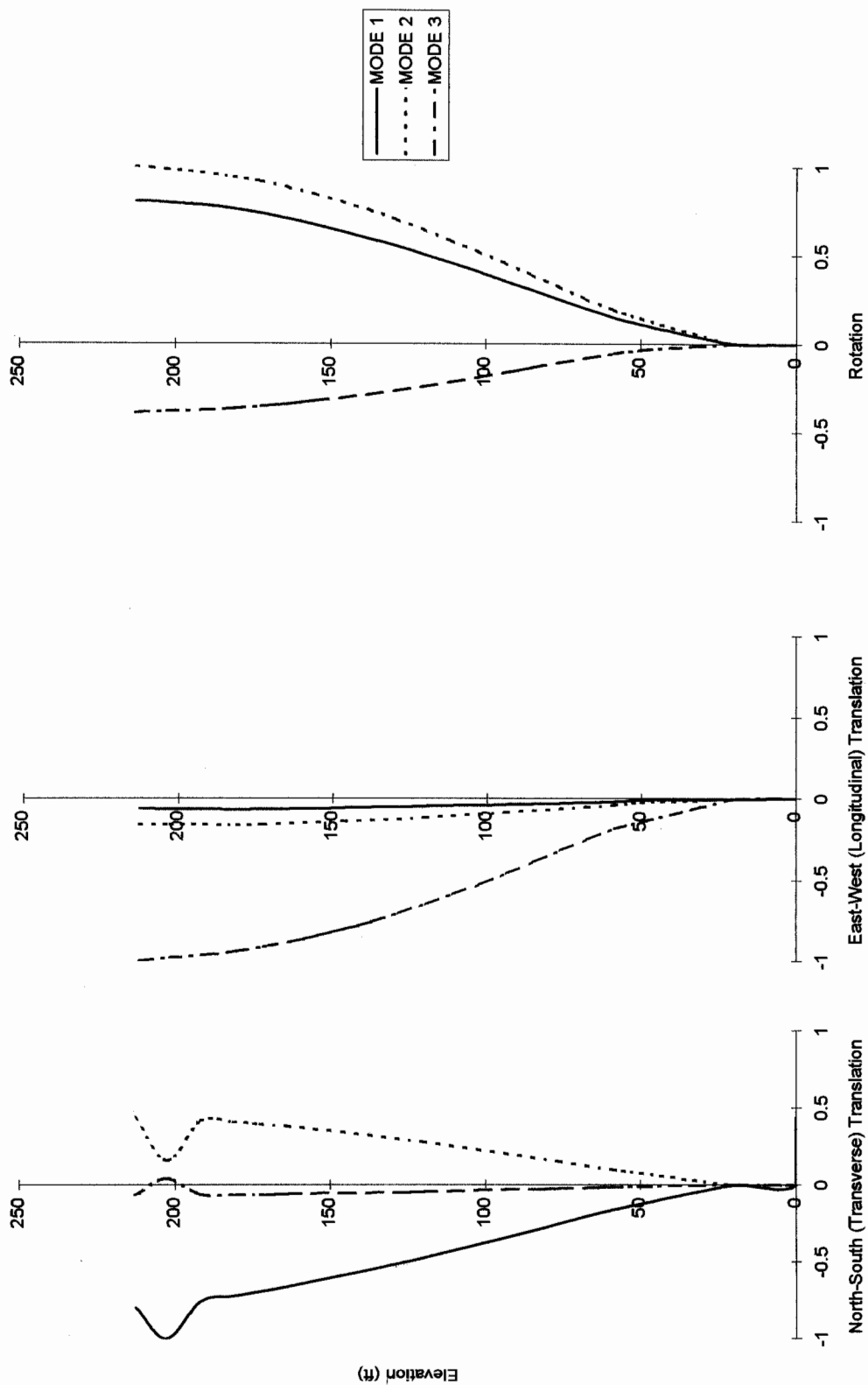


Figure 9 Normalized mode shapes for the Gross Stiffness model with 50% REZ

Table 3 Maximum recorded/maximum predicted floor displacement ratios

(a) 1994 Northridge earthquake North-South (Longitudinal) direction response

| Floor | Recorded (in) | Gross Stiffness Model |         |            | NEHRP Stiffness Model |         |            | Yield Stiffness Model |         |            |
|-------|---------------|-----------------------|---------|------------|-----------------------|---------|------------|-----------------------|---------|------------|
|       |               | 100% REZ              | 50% REZ | Centerline | 100% REZ              | 50% REZ | Centerline | 100% REZ              | 50% REZ | Centerline |
| Roof  | 8.67          | 1.00                  | 0.99    | 0.94       | 1.03                  | 1.15    | 1.29       | 1.25                  | 1.20    | 1.33       |
| 16th  | 4.48          | 0.84                  | 0.89    | 0.93       | 0.89                  | 0.91    | 0.92       | 0.91                  | 0.96    | 1.02       |
| 9th   | 3.13          | 0.74                  | 0.79    | 0.90       | 0.85                  | 0.82    | 0.91       | 0.89                  | 0.92    | 0.86       |
| 3rd   | 1.52          | 0.92                  | 1.01    | 1.12       | 1.04                  | 1.01    | 1.10       | 1.06                  | 0.72    | 0.68       |
| Mean  |               | 0.87                  | 0.92    | 0.97       | 0.95                  | 0.97    | 1.05       | 1.03                  | 0.95    | 0.97       |

\* REZ = Rigid End Zones

(b) 1994 Northridge earthquake East-West (Transverse) direction response

| Floor | Recorded (in) | Gross Stiffness Model |         |            | NEHRP Stiffness Model |         |            | Yield Stiffness Model |         |            |
|-------|---------------|-----------------------|---------|------------|-----------------------|---------|------------|-----------------------|---------|------------|
|       |               | 100% REZ              | 50% REZ | Centerline | 100% REZ              | 50% REZ | Centerline | 100% REZ              | 50% REZ | Centerline |
| Roof  | 4.18          | 1.24                  | 1.22    | 1.23       | 0.99                  | 1.12    | 1.09       | 1.03                  | 0.97    | 1.28       |
| 16th  | 3.35          | 1.20                  | 1.26    | 1.39       | 0.93                  | 1.09    | 1.08       | 1.16                  | 1.13    | 1.42       |
| 9th   | 1.93          | 0.99                  | 1.18    | 1.27       | 0.85                  | 1.07    | 1.16       | 1.10                  | 0.81    | 1.19       |
| 3rd   | 0.48          | 0.83                  | 0.96    | 0.92       | 0.83                  | 1.00    | 0.76       | 0.70                  | 0.59    | 0.71       |
| Mean  |               | 1.06                  | 1.16    | 1.20       | 0.90                  | 1.07    | 1.02       | 1.00                  | 0.87    | 1.15       |

\* REZ = Rigid End Zones

(c) 1987 Whittier earthquake North-South (Longitudinal) direction response

| Floor | Recorded (in) | Gross Stiffness Model |         |            | NEHRP Stiffness Model |         |            | Yield Stiffness Model |         |            |
|-------|---------------|-----------------------|---------|------------|-----------------------|---------|------------|-----------------------|---------|------------|
|       |               | 100% REZ              | 50% REZ | Centerline | 100% REZ              | 50% REZ | Centerline | 100% REZ              | 50% REZ | Centerline |
| Roof  | 0.65          | 0.78                  | 0.84    | 0.71       | 0.92                  | 1.10    | 1.03       | 0.98                  | 1.03    | 1.18       |
| 16th  | 0.61          | 1.03                  | 1.05    | 1.20       | 1.45                  | 1.65    | 1.79       | 1.74                  | 1.91    | 1.56       |
| 9th   | 0.46          | 1.00                  | 1.07    | 1.35       | 1.39                  | 1.21    | 1.39       | 1.35                  | 1.18    | 1.00       |
| 3rd   | 0.08          | 0.57                  | 0.50    | 0.47       | 0.38                  | 0.53    | 0.44       | 0.42                  | 0.38    | 0.40       |
| Mean  |               | 0.85                  | 0.87    | 0.93       | 1.04                  | 1.12    | 1.17       | 1.13                  | 1.12    | 1.04       |

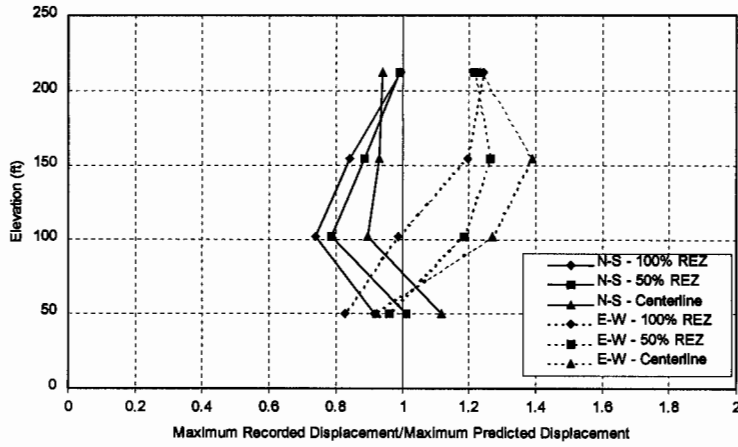
\* REZ = Rigid End Zones

(d) 1987 Whittier earthquake East-West (Transverse) direction response

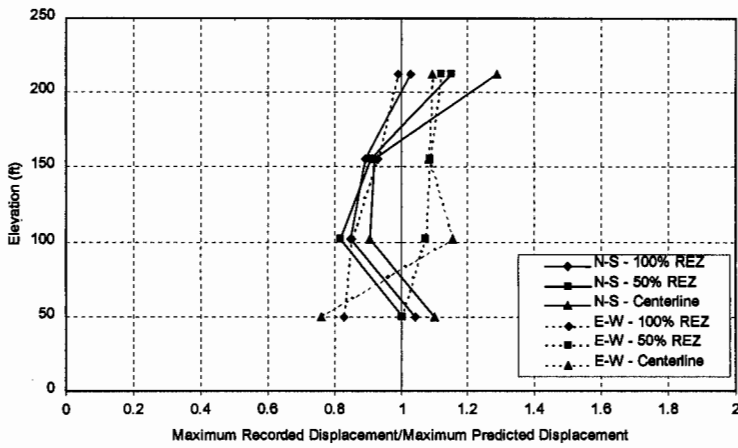
| Floor | Recorded (in) | Gross Stiffness Model |         |            | NEHRP Stiffness Model |         |            | Yield Stiffness Model |         |            |
|-------|---------------|-----------------------|---------|------------|-----------------------|---------|------------|-----------------------|---------|------------|
|       |               | 100% REZ              | 50% REZ | Centerline | 100% REZ              | 50% REZ | Centerline | 100% REZ              | 50% REZ | Centerline |
| Roof  | 0.85          | 0.91                  | 0.94    | 1.01       | 1.04                  | 1.16    | 1.33       | 1.20                  | 1.25    | 1.20       |
| 16th  | 0.64          | 0.83                  | 0.82    | 0.86       | 1.23                  | 1.39    | 1.45       | 1.39                  | 1.49    | 1.60       |
| 9th   | 0.38          | 0.78                  | 0.78    | 0.83       | 0.93                  | 1.06    | 1.06       | 1.06                  | 1.06    | 0.95       |
| 3rd   | 0.14          | 0.88                  | 0.74    | 0.82       | 0.82                  | 0.93    | 0.93       | 1.00                  | 0.78    | 0.54       |
| Mean  |               | 0.85                  | 0.82    | 0.88       | 1.00                  | 1.14    | 1.19       | 1.16                  | 1.14    | 1.07       |

\* REZ = Rigid End Zones

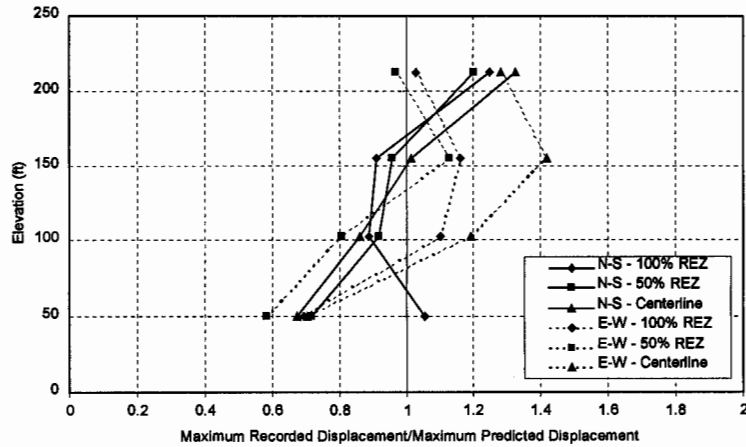




(a) Gross Stiffness building model



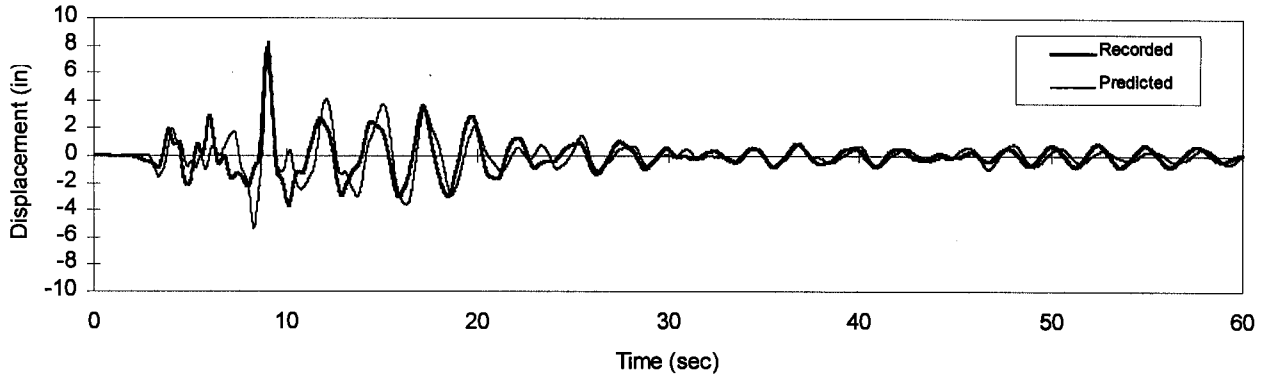
(b) FEMA 273 Stiffness building model



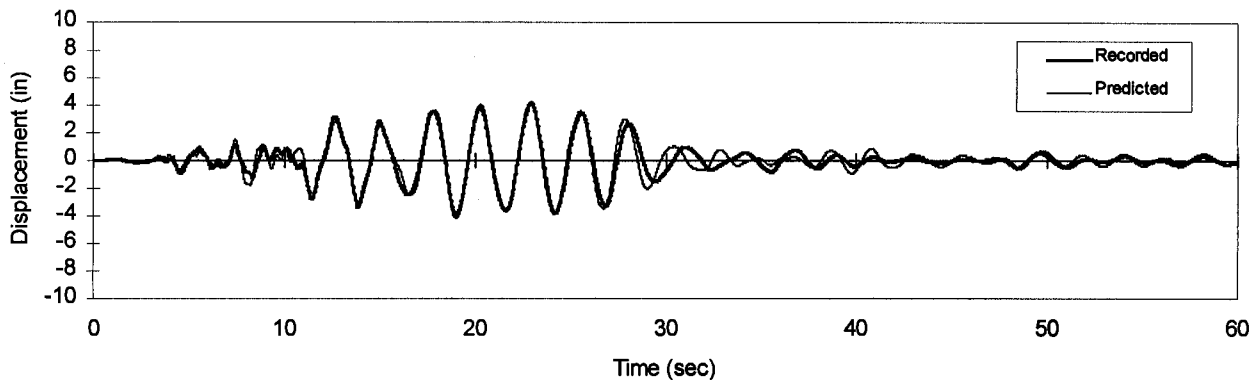
(c) Yield Stiffness building model

Figure 10 Maximum recorded/maximum predicted floor displacement ratios

The time history of relative roof displacement predicted by the FEMA 273 Stiffness model with 100% REZ is compared to the recorded relative displacement at the roof in Figure 11. Note that the peak displacement is accurately predicted and the predicted motion generally captures the frequency content of the recorded motion.



(a) North-South (Transverse)



(b) East-West (Longitudinal)

Figure 11 Relative roof displacement time history comparisons for the Northridge earthquake and the FEMA 273 Stiffness model with 100% REZ

### CONCLUSIONS

The following conclusions can be drawn from the research reported in this paper:

1. The displacement response of the building and the damage observed following the Northridge earthquake is consistent with the Vision 2000 definition of the Operational performance level.

2. The FEMA 273 Stiffness model with 100% REZ gives a good correlation with the period of vibration and the maximum displacement response for the Northridge earthquake. In addition, the time history of displacement predicted by this model matches the peak displacement at the roof and the overall frequency characteristics of the motion.
3. The periods of vibration calculated using the Gross Stiffness model with 50% REZ are consistent with the building periods during the Whittier earthquake. The predicted maximum displacement response was within 5% of the recorded displacements at the 16th and 9th floor, but fails to accurately predict the displacement response at the Roof and the 3rd floor.

### ACKNOWLEDGEMENTS

Funding for this research was provided by the State of California, Department of Conservation, Division of Mines and Geology, Strong Motion Instrumentation Program (SMIP). The authors wish to acknowledge the assistance and commitment of Dr. Marshall Lew, Dr. Farzad Naeim, Prof. Gerard Pardoen, Dr. Tom Sabol, Dr. Roger Li, Dr. Roy Lobo, Ms. Julia Li, Ms. Mary Elise Richter, and Mr. Insuck Song through the course of this research. Dr. Moh Huang of SMIP was essential in obtaining the recorded motions and the structural/architectural plans for this building. The additional efforts of Ms. Mary Elise Richter in the preparation of this paper are greatly appreciated.

### REFERENCES

- ATC. (1997). *NEHRP Guidelines for the Seismic Rehabilitation of Buildings, Volume I, Guidelines*. FEMA 273. Federal Emergency Management Agency.
- CSI (1997) "ETABS – Extended Three Dimensional Analysis of Building Systems – Nonlinear Version 6.21," Computers & Structures, Inc.
- Goel, R.K. and Chopra, A.K. (1997). "Vibration Properties of Buildings Determined From Recorded Earthquake Motions," *Report No. EERC/UCB-72/22*, Earthquake Engineering Research Center, University of California, Berkeley, California.
- Naeim, F. (1997). "Instrumented Buildings Information System, January 14, 1994, Northridge, California Earthquake, Version 1.0," John A. Martin & Associates.
- Paulay, T. and Priestley, M.J.N. (1992). *Seismic Design of Reinforced Concrete and Masonry Buildings*, Wiley Interscience, 744 pp.
- OES. (1995). California Office of Emergency Services, *Vision 2000: Performance Based Seismic Engineering of Buildings*. Prepared by Structural Engineers Association of California, Sacramento, California.

## SMIP98 Seminar Proceedings

Saatcioglu, M. and Razvi, S.R. (1992). "Strength and Ductility of Reinforced Concrete," *Journal of Structural Engineering*, Vol. 118, No. 6, pp. 1590-1607.

Steinmann, H.G. (1998). Personal Communication.

Wallace, J.W. (1992). "BIAX: Revision 1 – A Computer Program for the Analysis of Reinforced Concrete and Reinforced Masonry Sections," *Report No. CU/CEE-92/4*, Clarkson University, Potsdam, New York.

Wing, W.C. (1968). "Hotel Pioneers Earthquake Code," *Engineering News Record*, Feb. 22.

RESPONSE EVALUATION OF THREE CONCRETE FRAME BUILDINGS  
TO THE JANUARY 17, 1994 NORTHRIDGE EARTHQUAKE

Farzad Naeim and Roy Lobo

John A. Martin & Associates, Inc.  
1212 S. Flower Street, Los Angeles, CA 90015

Julia Li

Department of Civil and Environmental Engineering  
University of California at Los Angeles

Tom Sabol and Roger Li

Englekirk & Sabol, Inc.  
2116 Arlington Ave., Los Angeles, Ca 90180

ABSTRACT

As a part of a project sponsored by the Strong Motion Instrumentation Program of state of California (SIMP), responses of three concrete frame buildings during the 1994 Northridge earthquake are being evaluated. This investigation is at various stages of progress for the three buildings. For the 13 Story Sherman Oaks Building both linear and nonlinear analysis have been performed and nonstructural components response has been evaluated. For the 32 Story Burbank Building, linear analysis had been completed and nonlinear analysis is in progress. For the 7 Story Van Nuys Hotel construction of computer models are in progress. This paper serves as a status report on what has been learned so far from these investigations. Further details and refinements to observation presented in this paper will be forthcoming in a report to the SMIP.

13 STORY SHERMAN OAKS BUILDING

Description of the Building

A photo of the building retrieved from the SMIP Information System (Naeim,1997) is shown in Figure 1. This office building has 13 stories above and two floors below the ground. It was designed in 1964. The vertical load carrying system consists of 4.5 inches thick one-way concrete slabs supported by concrete beams, girders and columns. The lateral load resisting system consists of moment resisting concrete frames in the upper stories and concrete shear walls in the basements. The foundation system consists of concrete piles. The first floor spandrel girders were modified by post-tensioning after the 1971 San Fernando earthquake. Sketches of plan and elevation of the building showing the location of sensors are presented in Figure 2.

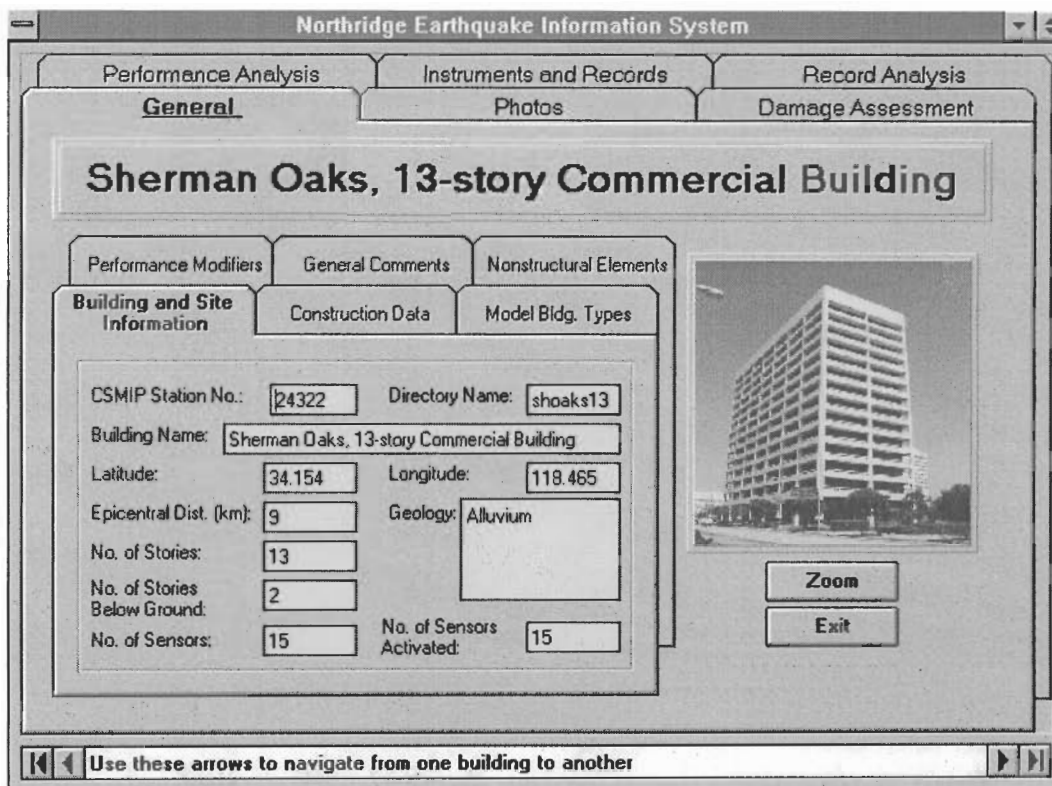


Figure 1. Three Dimensional View of the Building (from Naeim, 1997)

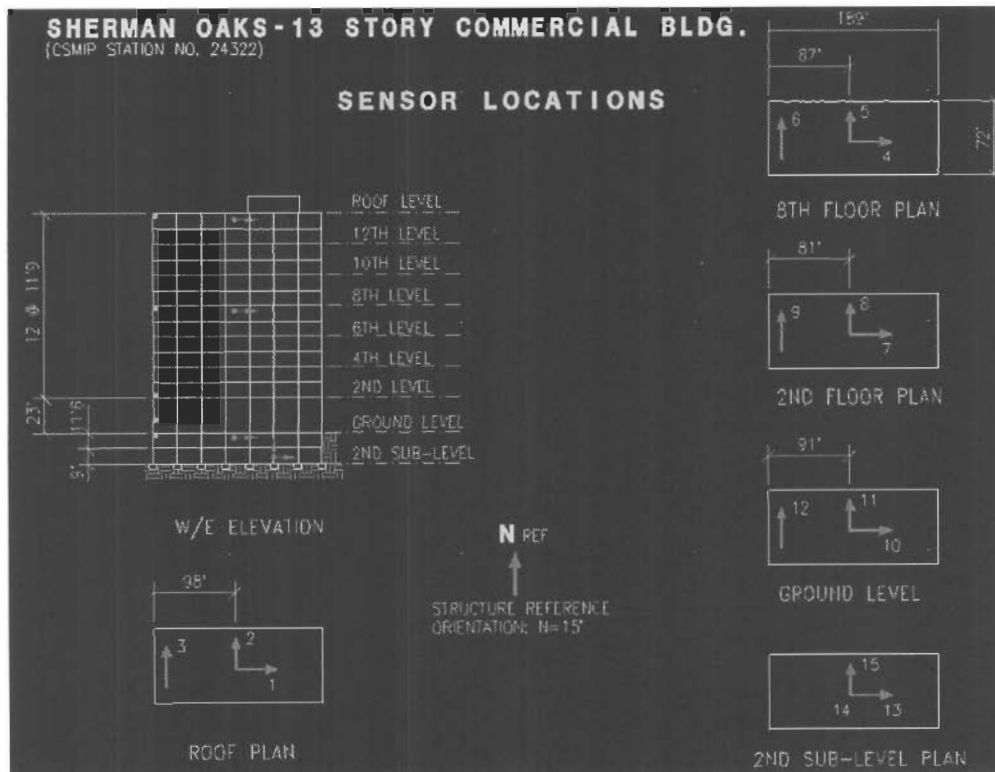


Figure 2. Location of Instruments (from Naeim, 1997)

### Building Performance

The largest peak horizontal accelerations recorded at the basement (Channel 15, N-S) and at the roof (Channel 3, N-S) are 0.46g and 0.65g, respectively. The middle experienced large acceleration in the neighborhood of 0.6g. The largest velocity recorded at the roof is about 68 cm/sec.

Performance analysis calculations for this building performed by Naeim (1997) are summarized in Table 1. The 0.19W maximum base shear apparently experienced by the building in the N-S direction is significantly larger than UBC strength design base shear of about  $1.4 \times 0.04W = 0.06W$  for a ductile moment resisting frame with this configuration. Notice that while the maximum base shear is experienced in the N-S direction, the maximum lateral displacement and an overall drift index of 0.0067 occurs in the E-W direction.

TABLE 1. Response Summary for Sherman Oaks 13-Story Office Building (from Naeim, 1997).

| Response Parameter                                     | Direction | Time of Maxima (seconds) | Maximum Value   |
|--|-----------|--------------------------|-----------------|
| Base Shear<br>(% Total Weight)                         | N-S       | 5.14                     | 18.70           |
|  | E-W       | 12.72                    | 7.57            |
|  | DIFF      | 3.24                     | 6.69            |
| Overturning Moment<br>(% Total Weight x feet)          | N-S       | 3.22                     | 1304            |
|  | E-W       | 11.52                    | 771             |
|  | DIFF      | 3.22                     | 615             |
| Roof Lateral Displacement<br>Relative to the Base (cm) | N-S       | 10.86                    | 24.10 (0.0048)* |
|  | E-W       | 37.98                    | 33.42 (0.0067)* |
|  | DIFF      | 11.00                    | 4.30 (0.0009)*  |

\* Overall drift index values are shown in brackets.

As documented by the SMIP Information System photos the building experienced noticeable but repairable structural damage in the form of cracks in the beams, slabs, girders, and walls. According to one source the repair costs exceeded several million dollars. In contrast, no mechanical equipment damage was observed either at the roof or the basement. Thanks to proper mounting and anchorage details.

As can be seen in Figure 3, participation of higher modes were particularly significant in the response of this building to Northridge earthquake. The N-S period of about 2.6 seconds is significantly larger than code estimated periods of 1.27 per UBC-67 and 1.60 seconds per UBC-94. In the E-W direction, a fundamental period of about 2.9 seconds is implied by FFT analysis (Figure 4). Our moving windows FFT analysis points to a softening of the structure which may be attributed to the concrete cracking (Figure 5).

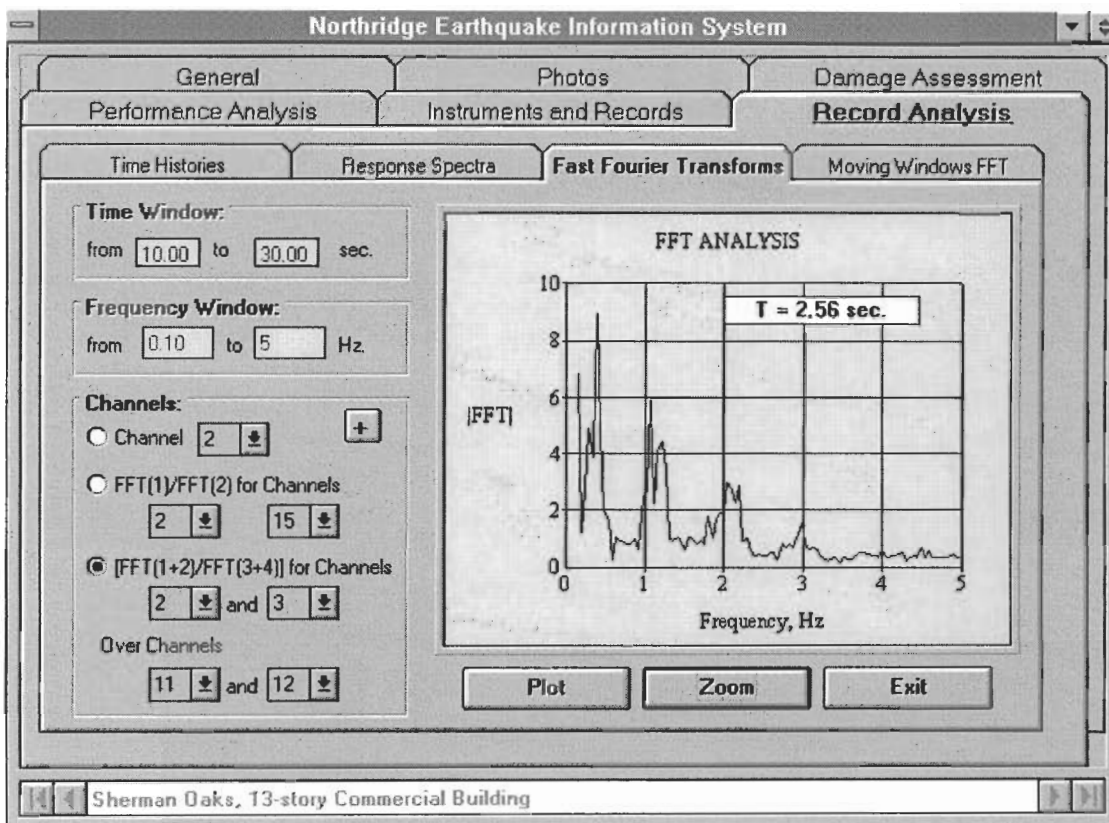


Figure 3. An FFT analysis for the N-S response (from Naeim, 1997).

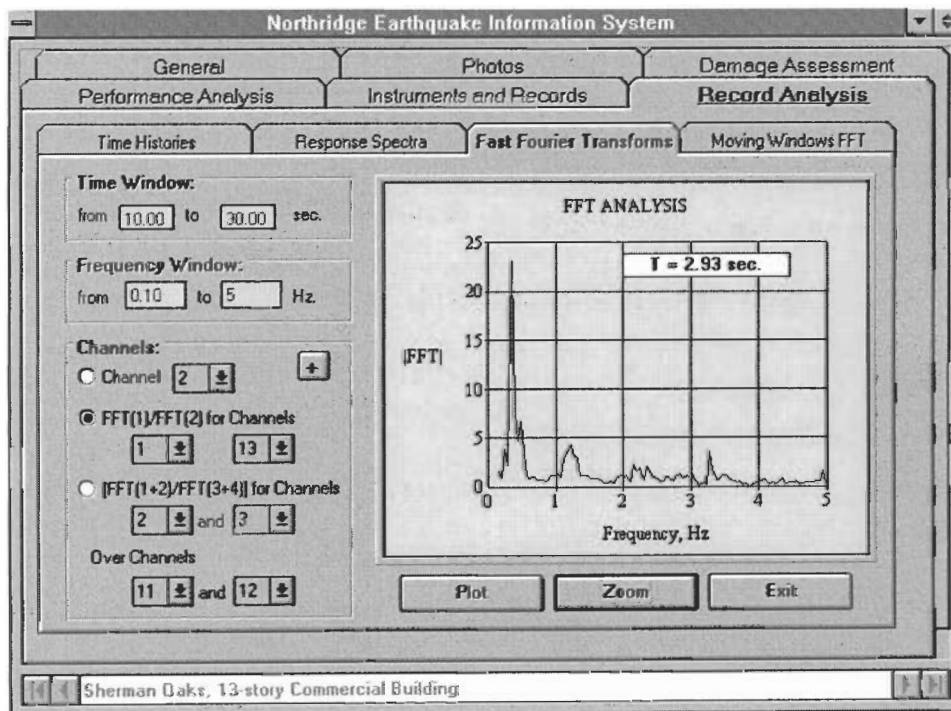


Figure 4. An FFT analysis for the E-W response (from Naeim, 1997).



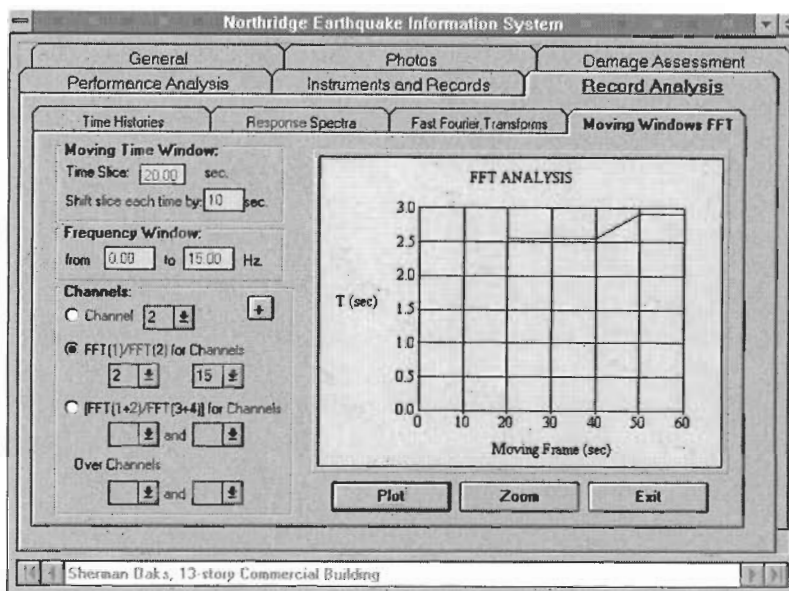


Figure 5. Moving windows FFT analysis indicates period elongation (from Naeim, 1997).

Performance of Non-Structural Systems and Components

The damage to non structural components and equipment for the building have been documented in the SMIP Interactive Information System (Naeim,1997). This building experienced noticeable but repairable structural damage in the form of cracks in the beams, slabs, girders, and walls (Figure 6a). In contrast, no mechanical equipment damage was observed either at the roof or the basement (Figures 6b, 6c, and 6d). This was due to proper mounting and anchorage details.

A summary of the damage to the nonstructural components are given in Table 2. This table also gives the corresponding  $a_p$  and  $R_p$  factors for the considered codes and guidelines.

TABLE 2. Summary of observed nonstructural damage and design coefficients

| Building                          | Component Description            | Observed Damage     | Design Coefficients |                   |                   |
|-----------------------------------|----------------------------------|---------------------|---------------------|-------------------|-------------------|
|                                   |                                  |                     | UBC-97              | NEHRP-97          | FEMA-273          |
|                                   |                                  |                     | $\frac{a_p}{R_p}$   | $\frac{a_p}{R_p}$ | $\frac{a_p}{R_p}$ |
| Sherman Oaks, 13 Story Commercial | Mechanical Equipment at basement | No damage           | 2.5/3               | 1/2.5             | 1/3               |
|                                   | Piping                           | No damage           | 1/3                 | 1/2.5             | 2.5/4             |
|                                   | Roof installed equipment         | Little or no damage | 2.5/3               | 1/2.5             | 1/3               |

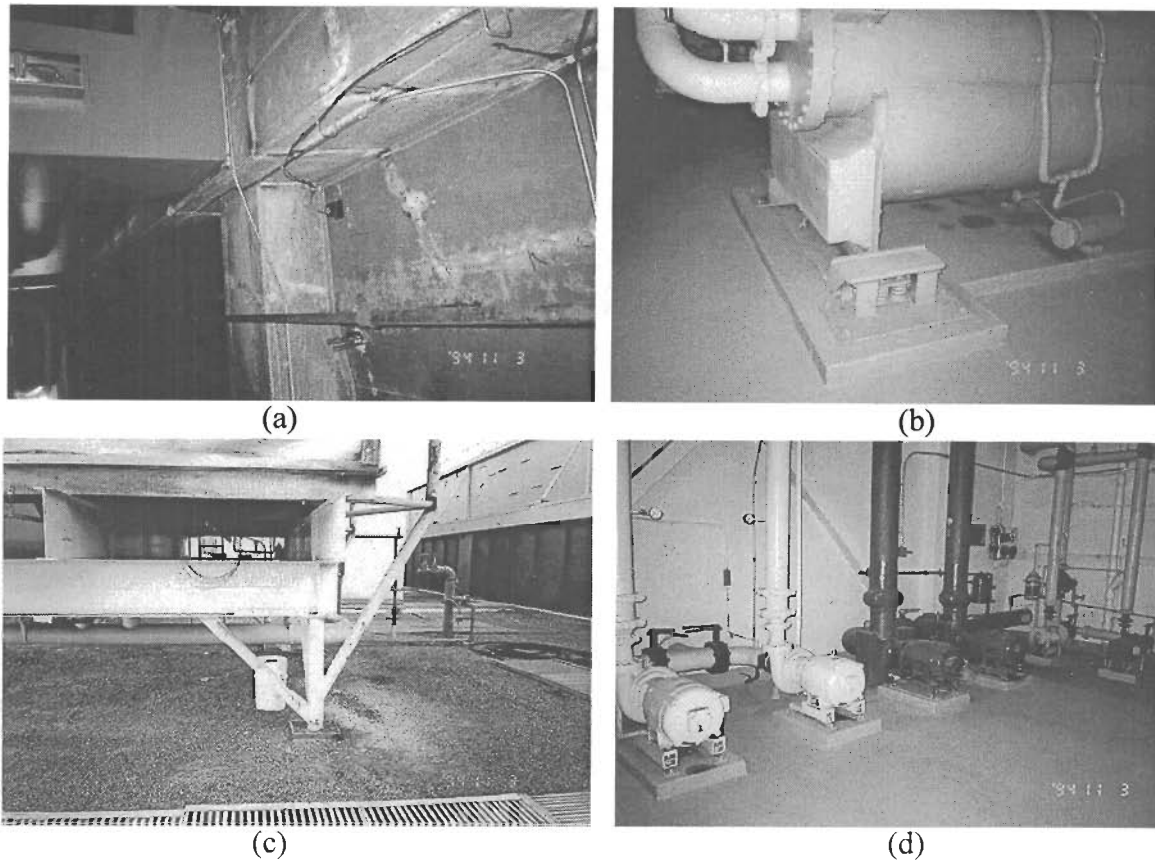


Figure 6. Contrasting Structural and nonstructural performance (13 Story Sherman Oaks Bldg).

Three different computer models were developed to analyze the 13 Story Sherman Oaks Building. The first is a three-dimensional linear elastic SAP-2000 model referred to as the *Elastic* model. The second and third are two-dimensional IDARC inelastic models referred to as the *Inelastic-EW* model and the *Inelastic-NS* model, respectively. The two sublevels below the ground floor were considered restrained because of the presence of perimeter shear walls limiting the motion at the basement levels. These levels were therefore ignored in the analysis, and the columns were considered fixed at the ground level.

For the *Elastic* model, the section properties are based on the gross section dimensions of the elements with a reduced modulus of elasticity. The modulus of elasticity for the beams was taken as  $0.4E_g$ , and for the columns as  $0.5E_g$ . The disadvantage of this model is that it not only reduces the flexural stiffness, but also the axial stiffness of the columns. The floor slabs are modeled as rigid diaphragms, therefore the axial stiffness of the beams do not play a part in the performance of the structure. The other obvious disadvantage of this model is that it does not capture any inelastic behavior that could occur.

The choice of the computational platforms available to analyze the *Inelastic-EW* and *Inelastic-NS* models were carefully selected in view of the following considerations. Firstly the very fact that these models are inelastic in nature, require additional data to be processed before the building can be analyzed. This includes the development of the moment curvature envelopes for each

member type. Column elements having different axial loads have to be treated as separate element types, even though they may have the same dimensions and reinforcement. Beam elements require a moment curvature analysis to be performed on the top and bottom face at each end of the beam. Additionally due consideration needs to be given to the development length of the reinforcement. While full capacity may not be developed with inadequate development lengths, there is definitely some contribution to the flexural capacity, at least for short-term dynamic loading. This could also include increased capacity by dynamic strain rate effects on the properties of the concrete. Gravity loading also needs to be considered to account for the initial state of stress in beams and columns (see Naeim et. al., 1998).

In light of the above considerations, the computer program IDARC4.0 was chosen as the computational platform to perform the analysis. This program was modified from its original form to include the effects of shear deformation. As this computational platform can only analyze buildings in two dimensions, the individual frames were modeled as duplicate frames in parallel to include the entire stiffness of the structure.

The dynamic characteristics of the building for the three models are compared with the interpreted characteristics in Table 3.

TABLE 3. Response Summary.

| Response parameter                               | Dir. | Observed | Elastic | Elastic -<br>E=0.7E <sub>gross</sub> | Inelastic-NS | Inelastic-EW |
|--|------|----------|---------|--------------------------------------|--------------|--------------|
| Period   | N-S  | 2.56     | 2.74    | 2.15                                 | 2.03         |              |
|  | E-W  | 2.93     | 2.40    | 1.91                                 |              | 1.84         |
| Roof Lateral Displacement Relative to the Ground | N-S  | 9.26     | 11.86   | 13.40                                | 8.67         |              |
|  | E-W  | 13.16    | 13.27   | 6.86                                 |              | 10.91        |

Time history analyses were performed on the three models using the actual recorded response at the ground floor. Figures 7 through 14 show the comparison of the responses for the various models, at the levels at which the instruments were located. The comparison of displacements at the second floor for both the Inelastic models causes a bit of concern. Probably indicating that the assumption that the boundary conditions are fully restrained is not entirely valid. In addition, there is an additional low roof structure at this level which is not modeled. The forces from this structure could be responsible for the differences between analysis and recorded responses. If the differences at this floor are reconciled, the comparison of responses for other floors become much better. We need to re-evaluate further our modeling assumptions with respect to the first floor low-rise area and boundary conditions.

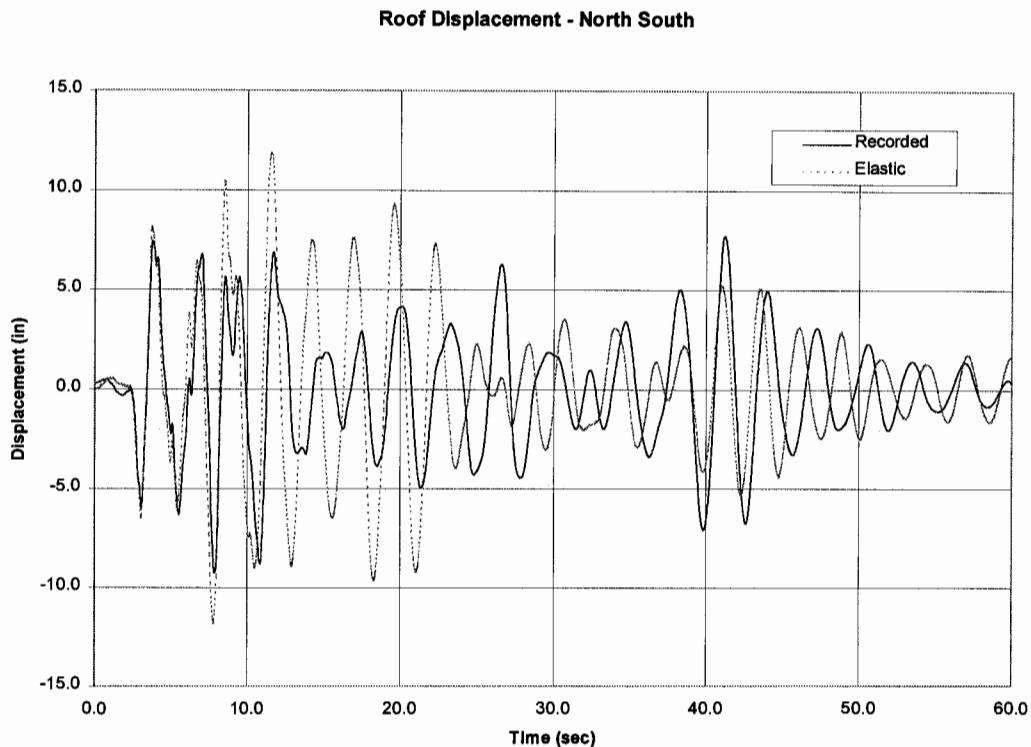


Figure 7. Comparison of Recorded Vs Elastic in North-South direction at Roof.

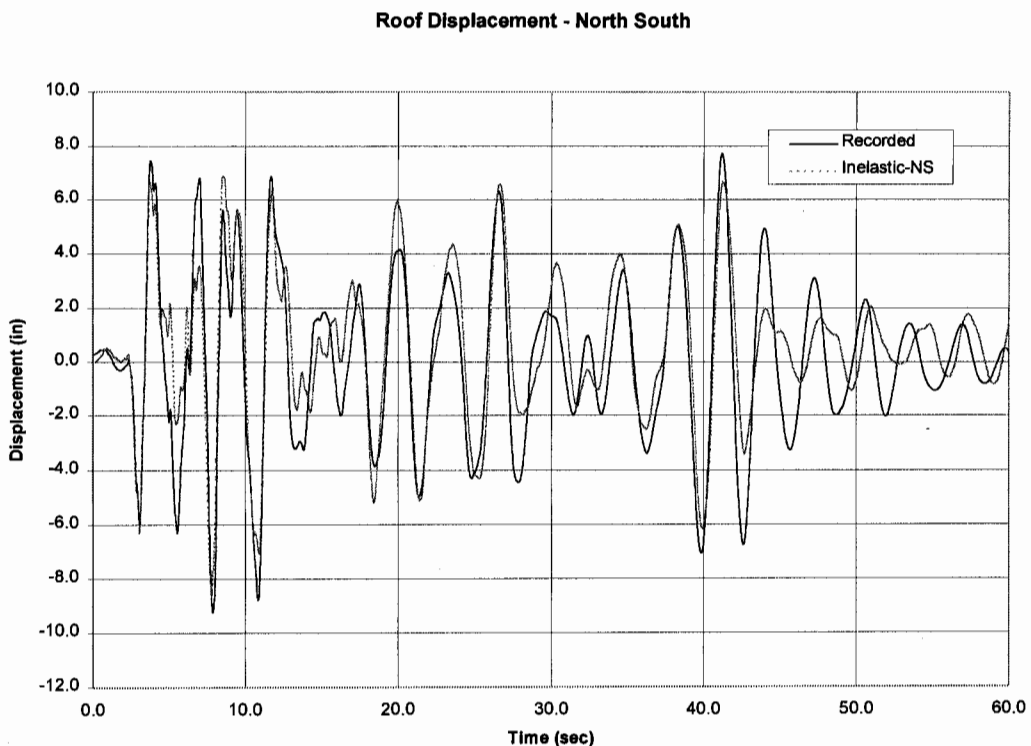


Figure 8. Comparison of Recorded Vs Inelastic-NS in North-South direction at Roof.

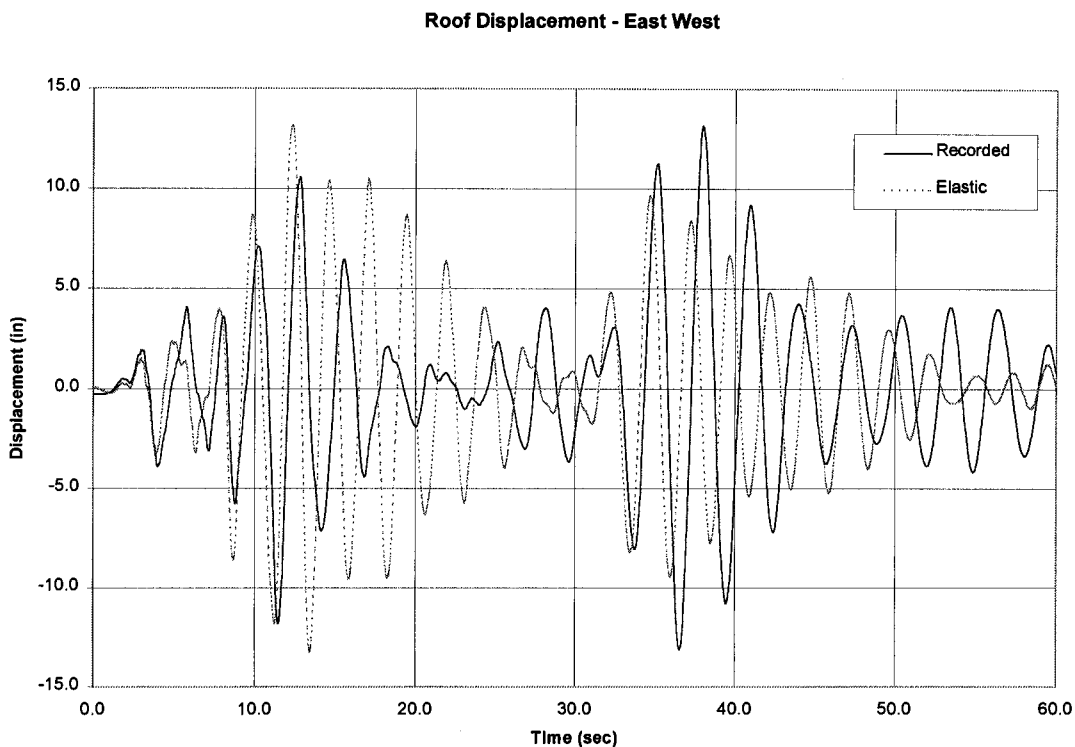


Figure 9. Comparison of Recorded Vs Elastic in East-West direction at Roof.

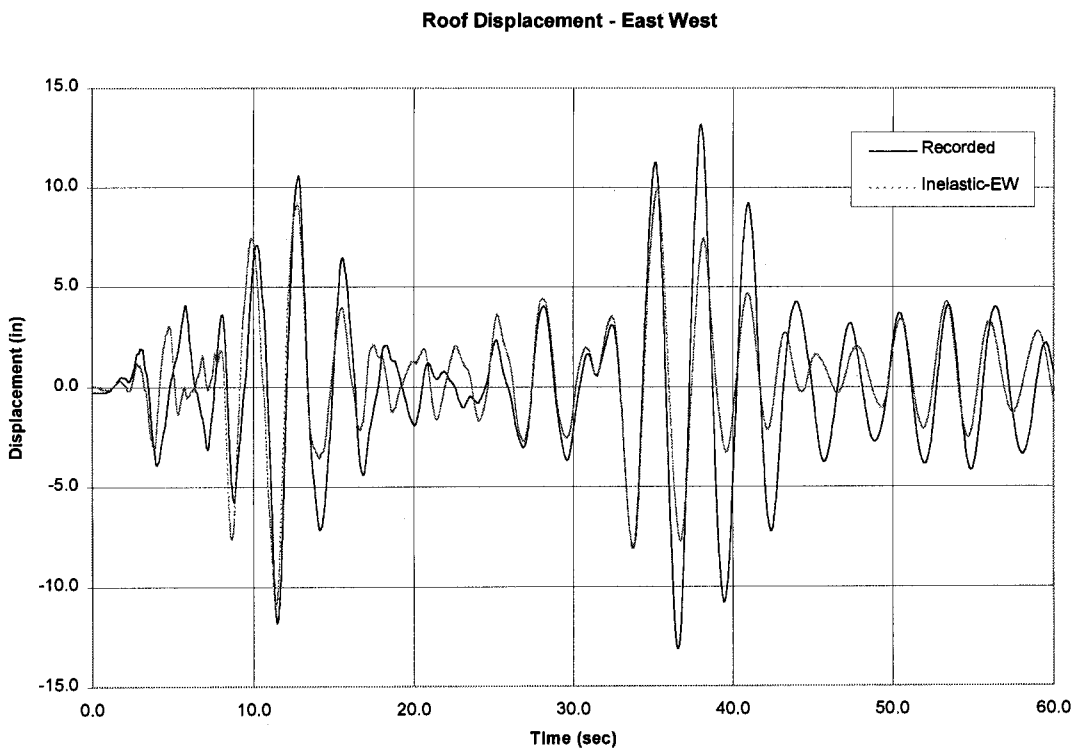


Figure 10. Comparison of Recorded Vs Inelastic-EW in East-West direction at Roof.

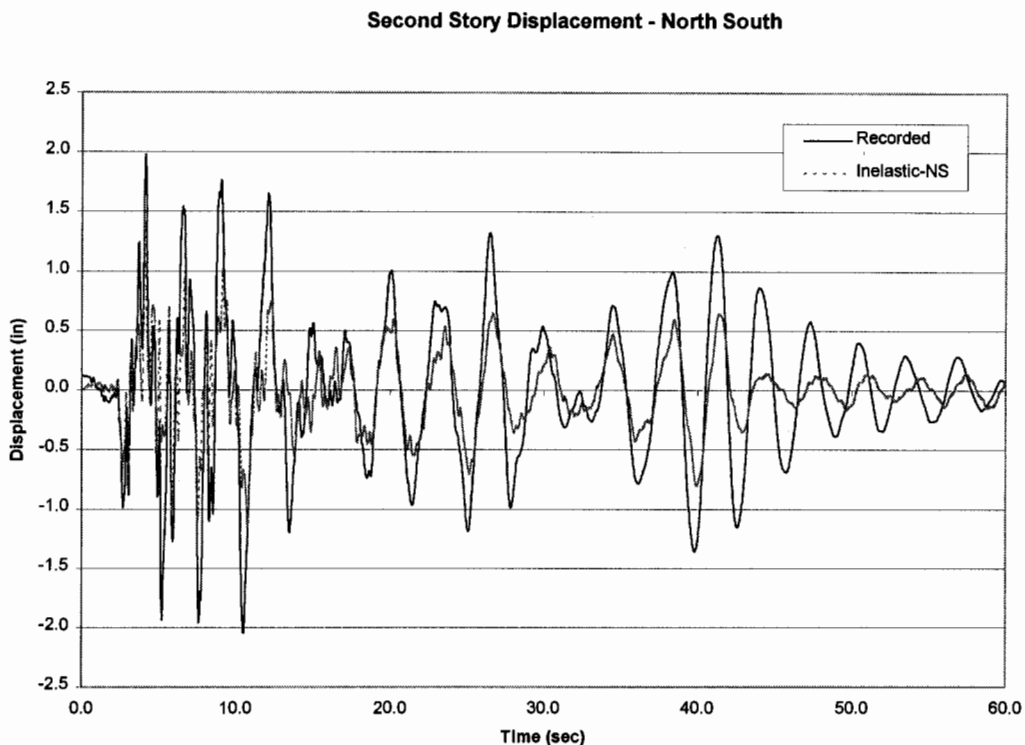


Figure 11. Comparison of Recorded Vs Inelastic-EW in North-South direction at 2nd.

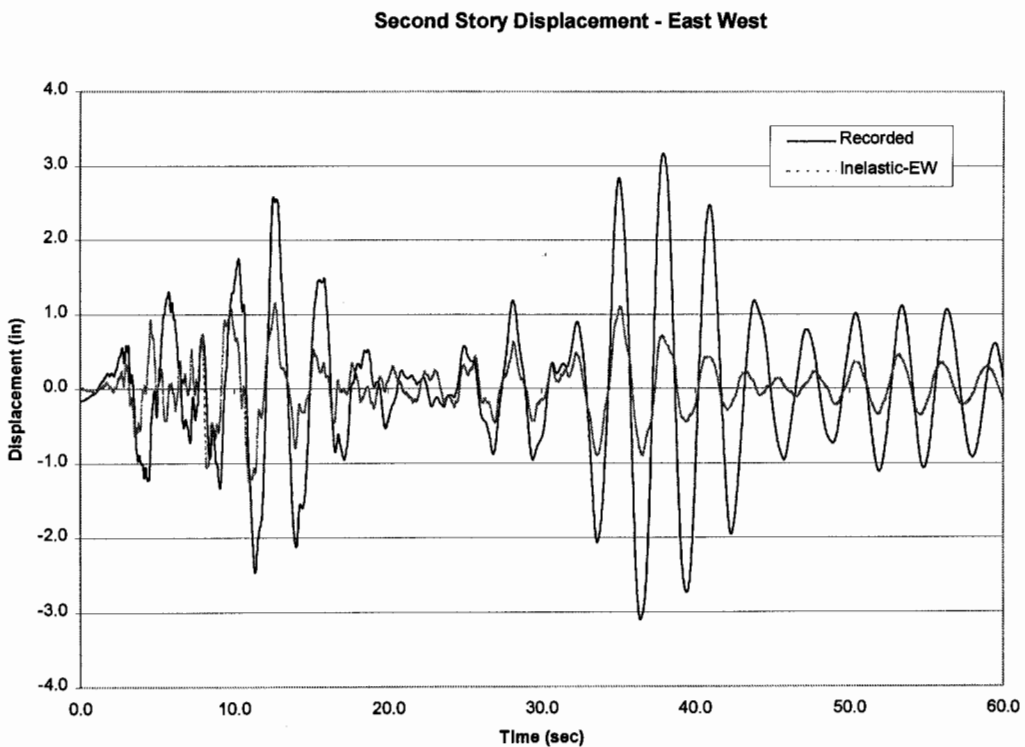


Figure 12. Comparison of Recorded Vs Inelastic-EW in East-West direction at 2nd.

Eight Story Displacement - North South

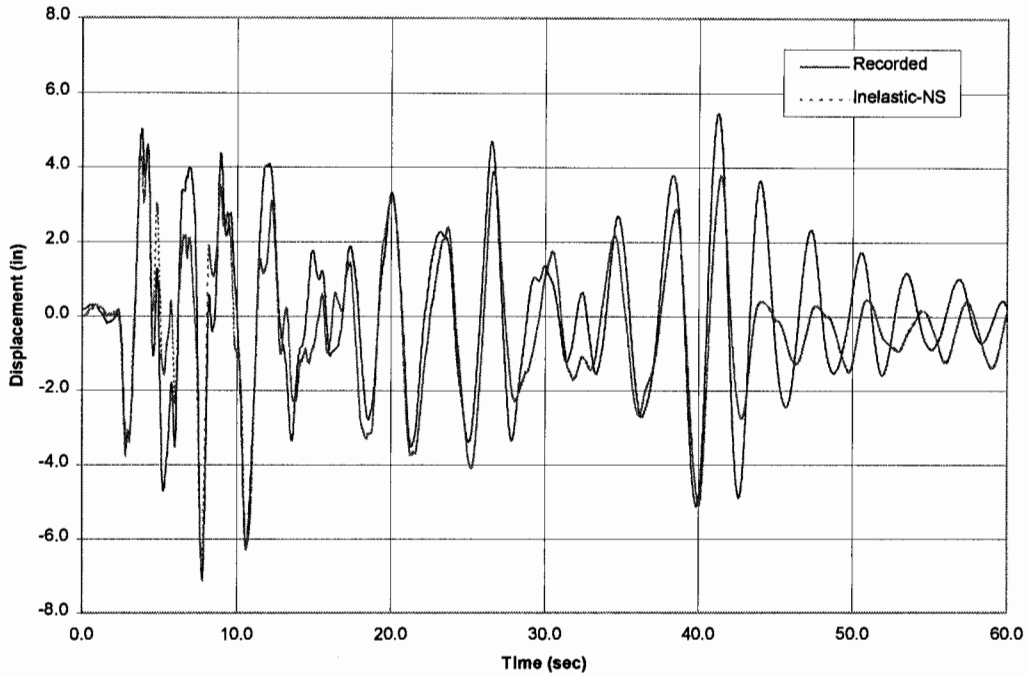


Figure 13. Comparison of Recorded Vs Inelastic-NS in North-South direction at 8th.

Eighth Story Displacement - East West

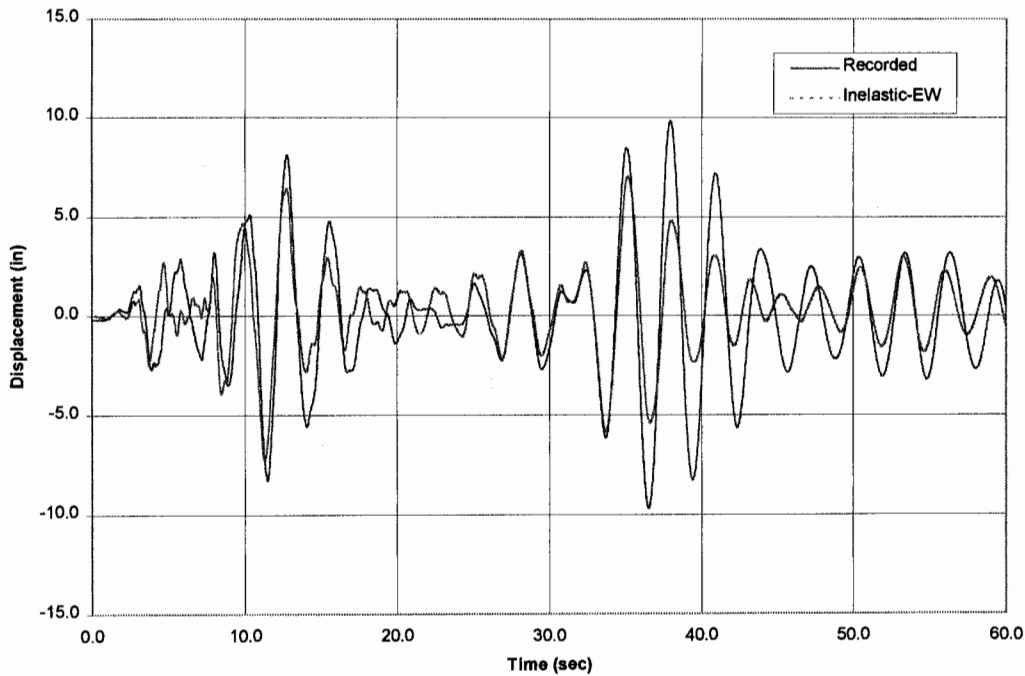


Figure 14. Comparison of Recorded Vs Inelastic-EW in East-West direction at 8th.

The *Elastic* model does not produce very different results in terms of peak displacements, but provides a very different time history response than the one actually observed. The lengthening of the period as the earthquake progressed is fairly well captured, however, with the inelastic models. An important point to note is that the initial gravity loading plays a significant role in the response of the inelastic models. A comparison was performed where the gravity loads were not included and the response was very different from the recorded. This is because the bottom reinforcement at the supports is much less than the top reinforcement and causes early cracking in positive bending, significantly altering the response.

### 32 STORY BURBANK BUILDING

#### Building Description

This building consists of a thirty-two story office building (referred to here as the “Tower Building”), and an eight-story parking structure (referred to here as the “Low-Rise Building”). Figure 15 shows a southeast elevation of the building. It was constructed in 1987 with a completed cost of \$42 million dollars.

The Tower Building has typical plan dimensions of approximately 269 feet in the northwest-southeast (longitudinal) direction and 81 feet in the southwest-northeast (transverse) direction. As shown in Figure 16, columns are typically placed at 26.87 feet on center in both longitudinal and transverse directions. The typical story height for the Tower Building is 12 feet. The Low-Rise parking structure has an eight story parking garage with four levels below grade and four levels above grade. The story height for the parking structure is typically 10 feet with an exception of 14 feet for the eighth level. According to the structural drawings, the reinforced concrete column strength varies from 4 ksi to 6 ksi. The reinforced concrete beam strength is 5 ksi. The floor system consists of 7 inch post-tensioned concrete flat plate slabs with a strength of 5 ksi. Reinforcement in frame ductile members complies with then UBC Standard No. 26-4 for low alloy A706.

The lateral resisting system of the Tower Building is comprised of reinforced concrete moment frames in both longitudinal and transverse directions. Frame column dimensions vary from 18 inches wide by 36 inches deep at higher levels to 48 inches wide by 44 inches deep at lower levels. The typical frame column size is 36 inches by 36 inches. Frame beam dimensions in the longitudinal direction vary from 18 inches wide by 38 inches deep to 20 inches wide by 38 inches deep. In the transverse direction, frame beams have dimensions of 30 inches wide by 33 inches deep to 36 inches wide by 33 inches deep. Ties for the frame column are typically #6 or #5 spaced at 3 or 3.5 inches on center throughout the full height of the column. Stirrups for the frame beams in the longitudinal direction typically consist of D31 wire fabric at 4 inches on center and in the transverse direction #5 rebars at 6 inches on center. The Low-Rise Building has four perimeter reinforced concrete shear walls up to 18 inches thick as its lateral resisting system.



## Instrumentation Information

The Tower Building is instrumented at the roof, 16<sup>th</sup>, and basement levels. Instrumentation data were retrieved and processed after the 1994 Northridge earthquake. Figures 17 through 25 illustrate the acceleration, velocity and displacement time histories at the roof, 16<sup>th</sup>, and basement levels in the longitudinal, transverse, and vertical directions. The epicenter of the Northridge earthquake is located about 12 miles northwest of the building. No damage to the building was reported after the earthquake. The ground shaking lasted about 20 seconds. The peak ground accelerations are estimated as 72.6 in/s/s (0.188g) in the longitudinal direction, 80.4 in/s/s (0.208g) in the transverse direction, and 78.8 in/s/s (0.204g) in the vertical direction. Estimated fundamental building periods from these time histories are 1.48 seconds for the longitudinal direction and 3.43 seconds for the transverse direction.

## Objectives of Evaluation

The objective of this study is to evaluate the response of the Tower Building to the 1994 Northridge earthquake and compare the recorded data with the results from elastic structural analysis (using ETABS) and inelastic structural analysis (using DRAIN2DX).

## Elastic Analysis

An elastic analysis was conducted using ETABS to obtain the building's mode shapes and natural periods and compare the natural periods with the estimated periods from the recorded building response data during the 1994 Northridge earthquake. A three-dimensional modal was established. The grid line of the ETABS model is shown in Figure 12 and a three-dimensional view of the model is shown in Figure 13. Only the Tower Building is included in the model. The shear walls in the Low-Rise Building are modeled as external spring restraints to the Tower Building. The model of the building is based on the existing structural plan. The post-tensioned concrete slabs are converted to equivalent concrete beams. The assumptions used in the model primarily follow the recommendations from ACI 318-95 (ACI, 1995) and ATC 40 (ATC, 1996). The following summarizes the most significant modeling assumptions used for the analysis.

### 1. Gross Section Stiffness Reduction Factors for Beams and Columns:

Concrete cracks when stressed beyond its tensile strength. Effective stiffness of a member represents an average stiffness after concrete cracks. The common approach for estimating an effective stiffness is to use gross section stiffness times a reduction factor. ACI 318-95 recommends using  $0.35I_g$  as effective stiffness for beams,  $0.70I_g$  for columns and  $0.35I_g$  for cracked walls. ATC-40 (1996) uses  $0.5I_g$  as effective stiffness for non-prestressed beams,  $1.0I_g$  for prestressed beams,  $0.7I_g$  for columns in compression and  $0.5I_g$  for cracked walls. Due to the moderate nature of the ground shaking that the building experienced during the 1994 Northridge earthquake, the stiffness reduction factors are assumed to be 0.6 for beams, 0.8 for columns, and 1.0 for equivalent post-tensioned slabs.

### 2. Rigid End Zone Reduction:

The rigid zone reduction was assumed to be 0 (no rigid end zone reduction). Since beam-to-column joints are well-confined, they are estimated to remain un-cracked under such a moderate ground shaking.

### 3. P-Delta Effect:

P-Delta effect is included in the analysis.

### 4. Effective Width of Post-Tensioned Slab as Equivalent Beam:

According to ATC-40, Hwang and Moehle (1993) recommend an effective beam width model having an effective width for interior framing lines equal to  $\beta(5c_1+0.25L_1)$ , where  $\beta$  represents cracking effects and ranges typically from one-third to one-half,  $c_1$  = column dimension in the direction of framing, and  $L_1$  = center-to-center span in the direction of framing. For exterior frame lines, use half this width. Use gross-section flexural stiffness properties for the effective width. In the case of prestressed slabs,  $\beta$  is taken as 1.0, since post-tensioned slabs are likely to have less cracking.

## Analytical Results

The first three mode shapes from the ETABS analysis are shown in Figures 26 through 29. The first, second, and third modes are in the transverse, longitudinal, and rotational directions, respectively. The corresponding natural periods are 3.27 seconds, 2.23 seconds and 1.71 seconds, respectively.

## Nonlinear Analysis

The nonlinear analysis of the building using DRAIN2DX is still on-going. A two-dimensional model will be established in the transverse direction to conduct a time history analysis using the recorded ground motion obtained at the basement of the building. The response of the building from nonlinear analysis will be compared with the recorded data at the roof and 16<sup>th</sup> floor. Conclusions regarding validity of modeling assumptions and nonlinear analysis will be drawn from this analysis.

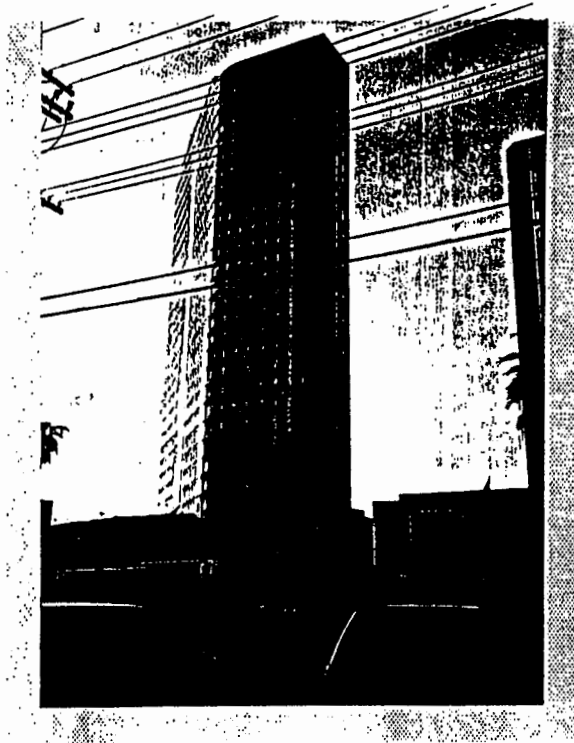


Figure 15. Southeast elevation

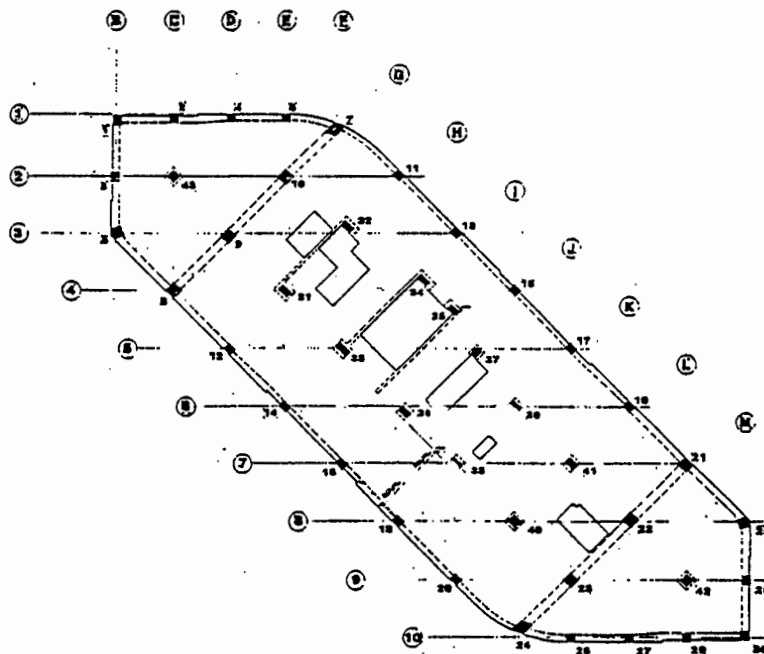


Figure 16. Typical framing plan of Tower Building

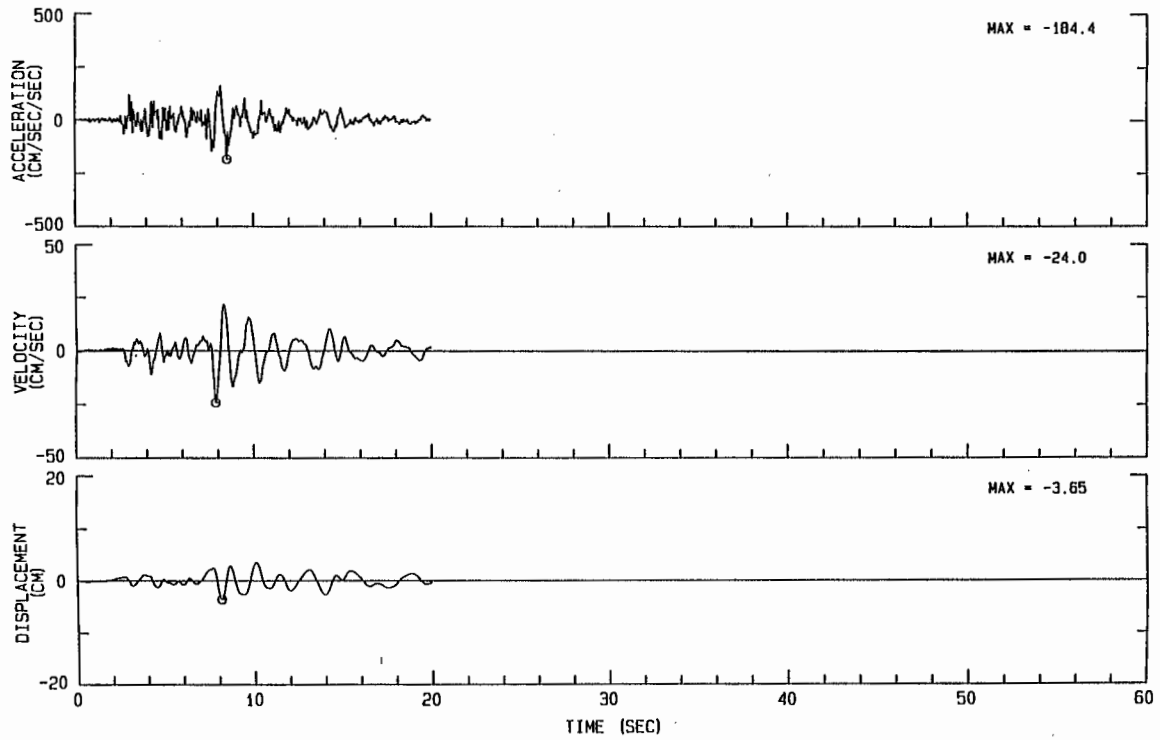


Figure 17. Response time histories in the longitudinal direction at the basement level. 1994 Northridge earthquake

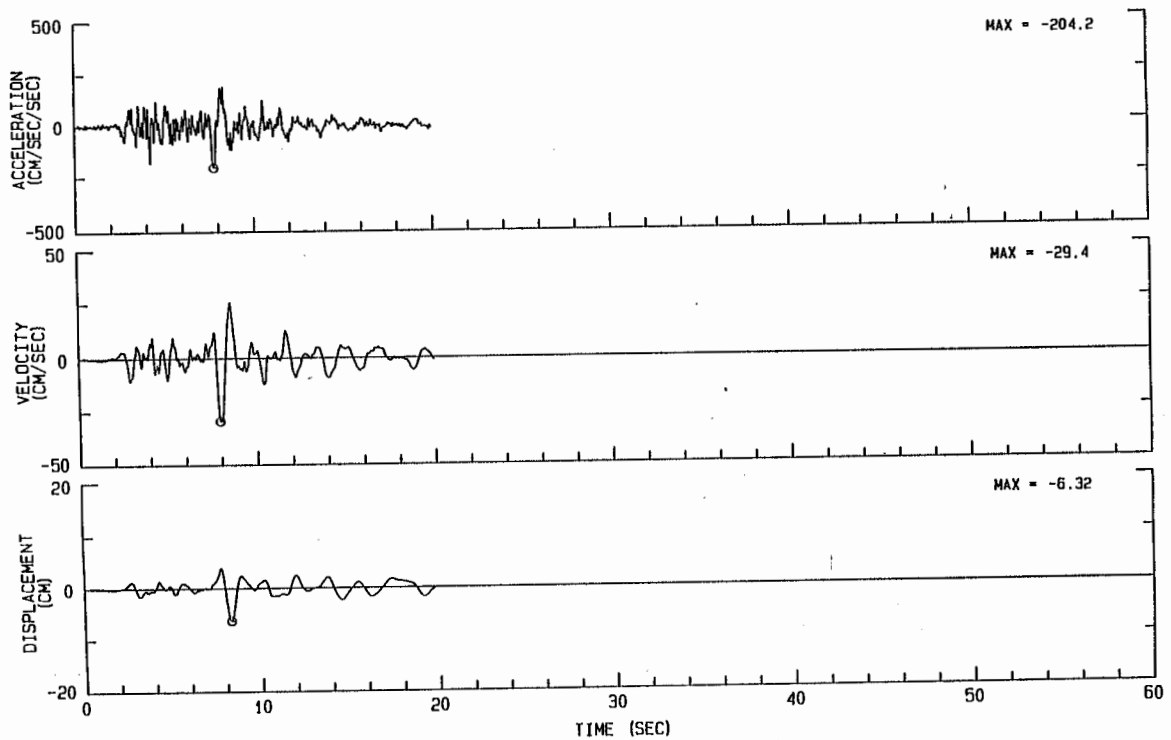


Figure 18. Response time histories in the transverse direction at the basement level. 1994 Northridge earthquake

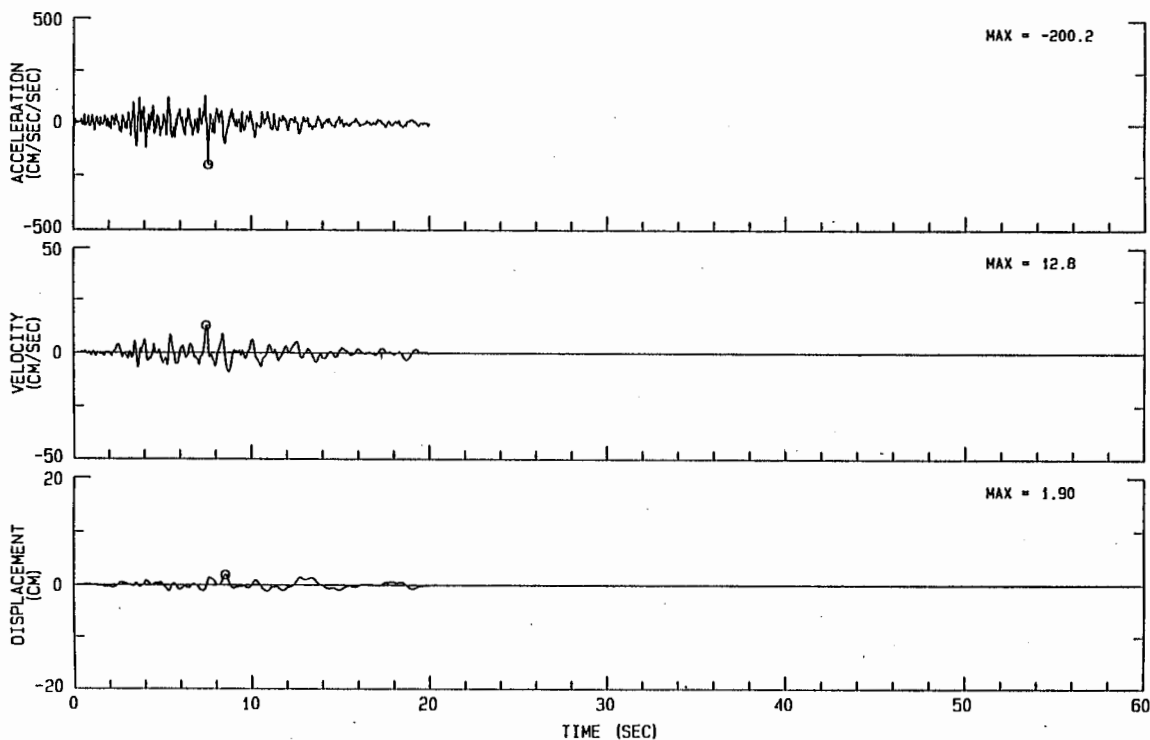


Figure 19. Response time histories in the vertical direction at the basement level. 1994 Northridge earthquake

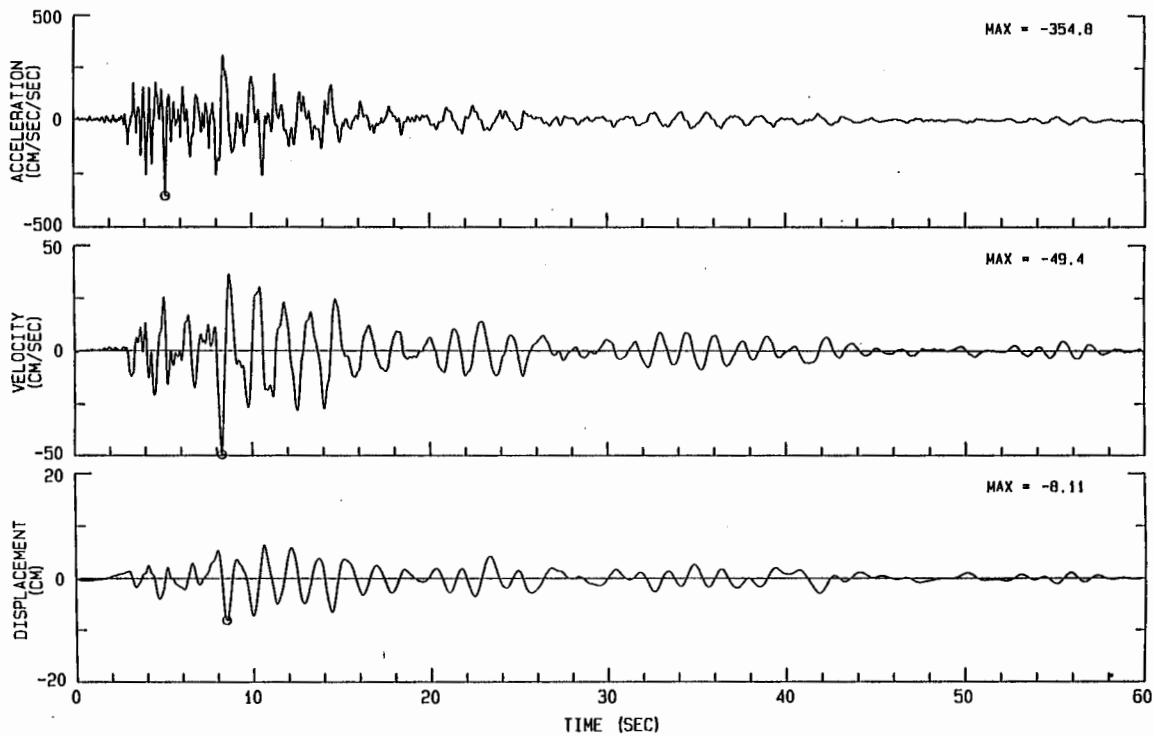


Figure 20. Response time histories in the longitudinal direction at the 16th level. 1994 Northridge earthquake

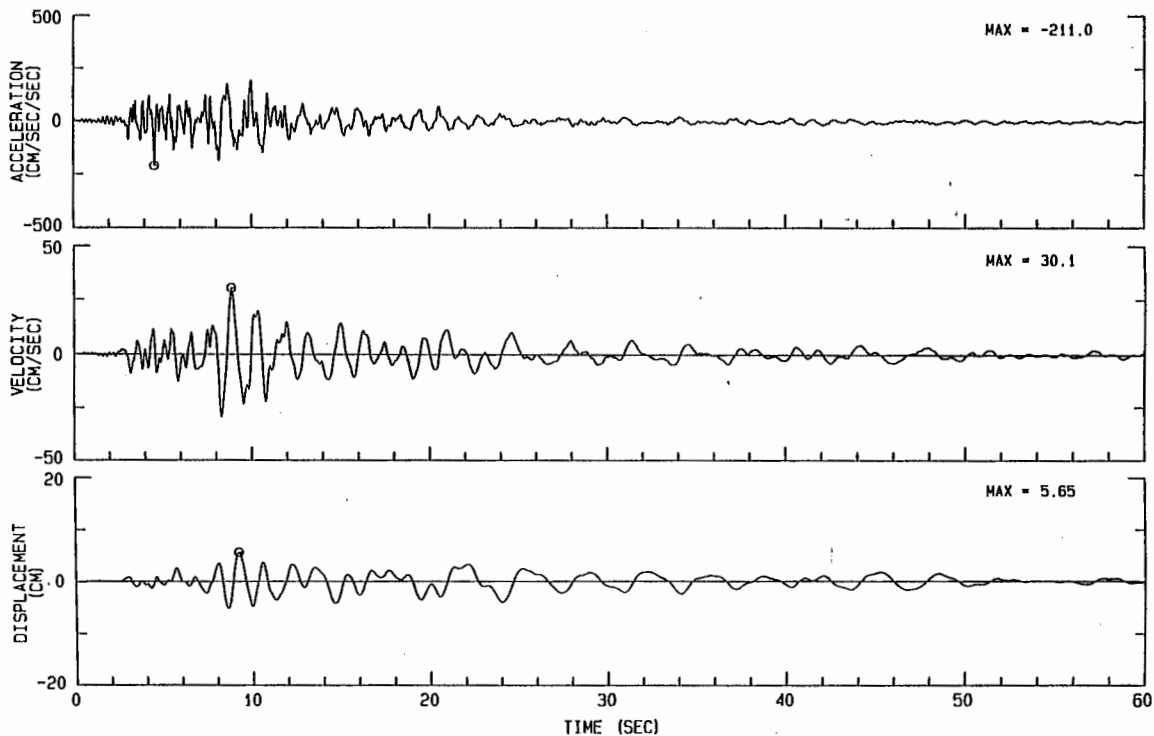


Figure 21. Response time histories in the transverse direction at the 16th level. 1994 Northridge earthquake

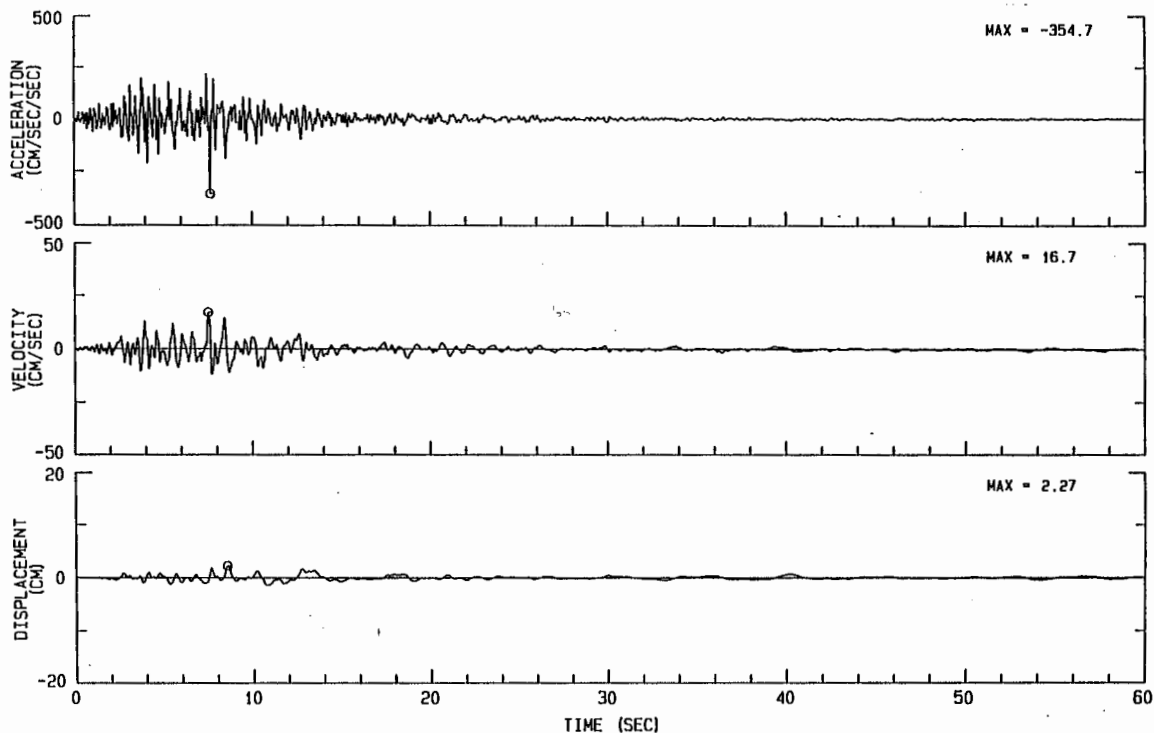


Figure 22. Response time histories in the vertical direction at the 16th level. 1994 Northridge earthquake

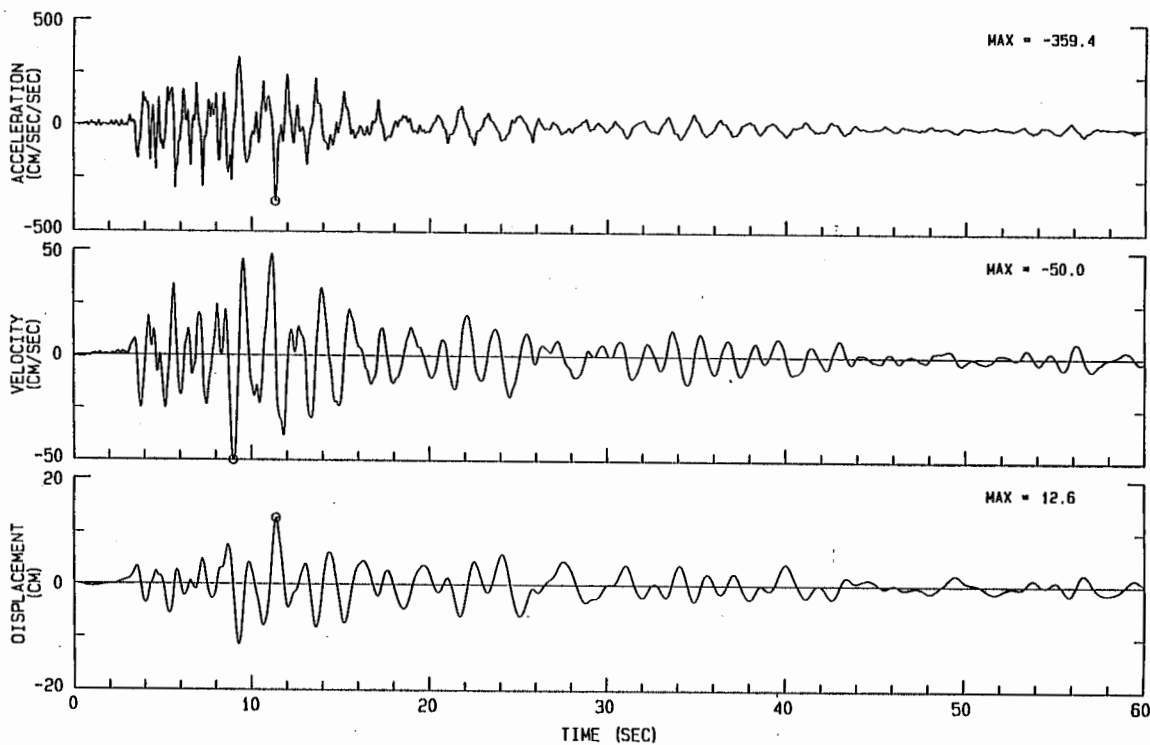


Figure 23. Response time histories in the longitudinal direction at the roof level. 1994 Northridge earthquake

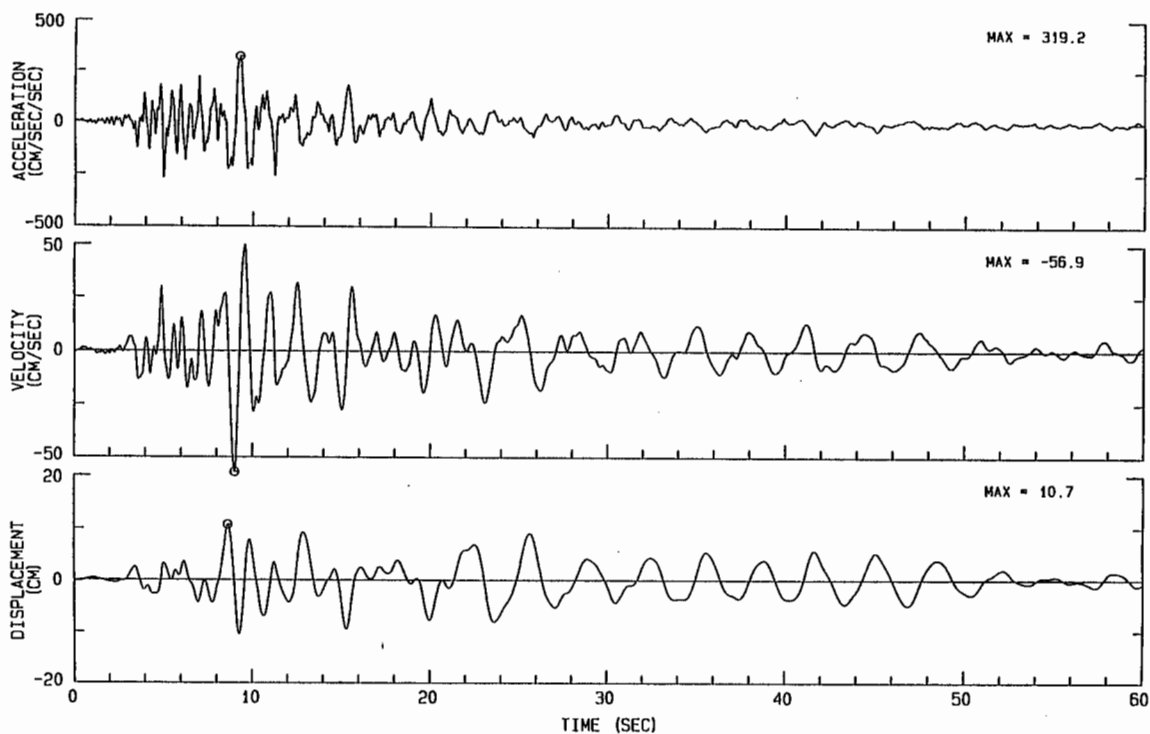


Figure 24. Response time histories in the transverse direction at the roof level. 1994 Northridge earthquake

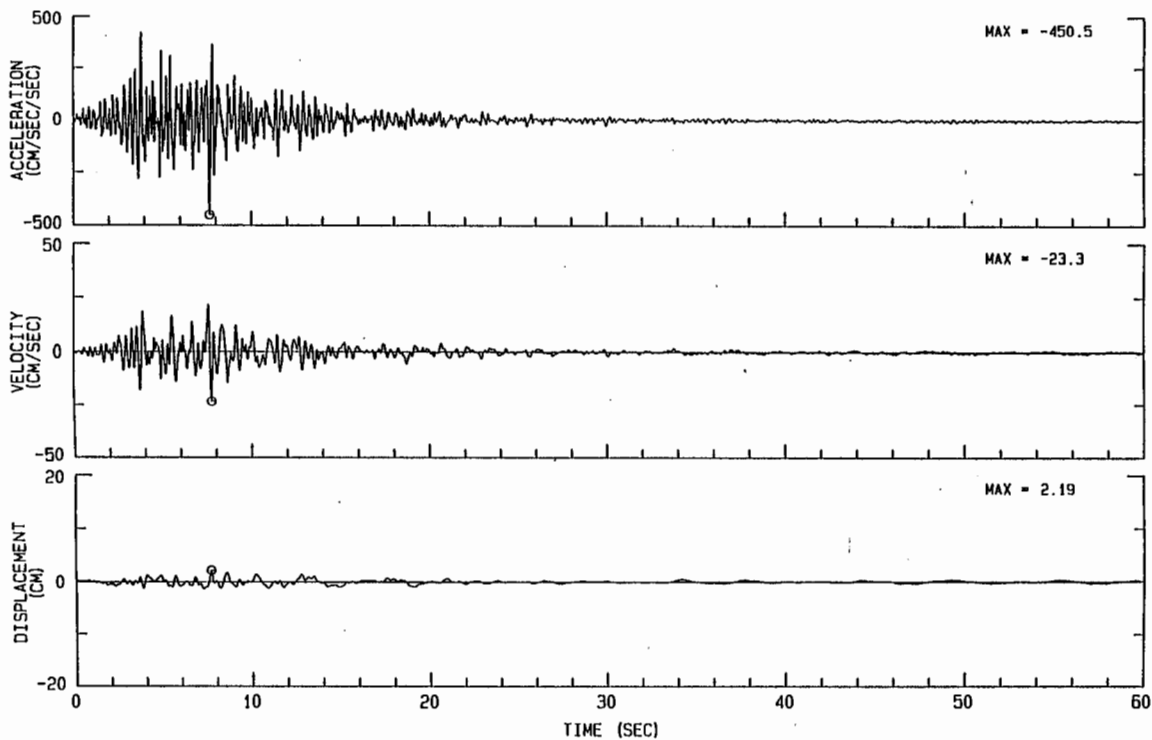


Figure 25. Response time histories in the vertical direction at the roof level. 1994 Northridge earthquake



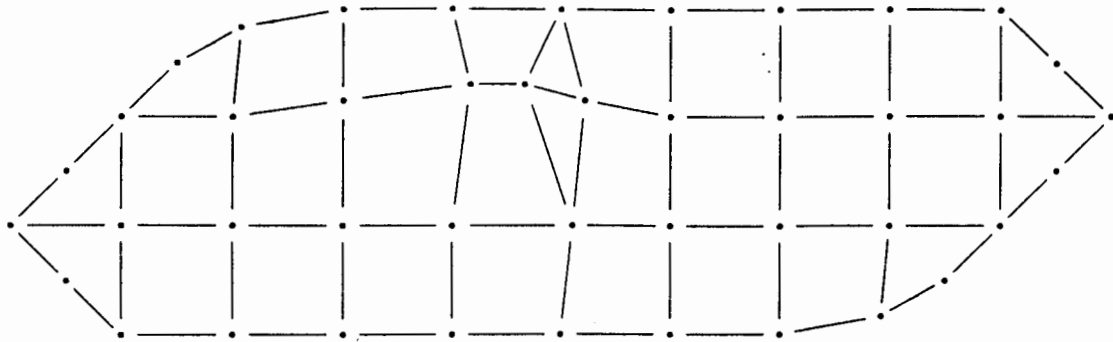


Figure 26. Frame grid line in the ETABS model

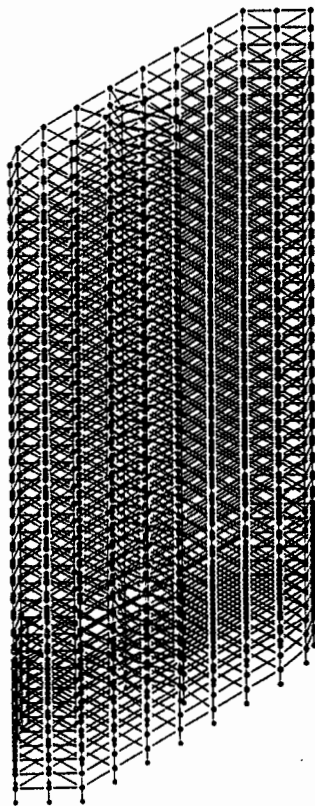


Figure 27. Three dimensional view of the ETABS model

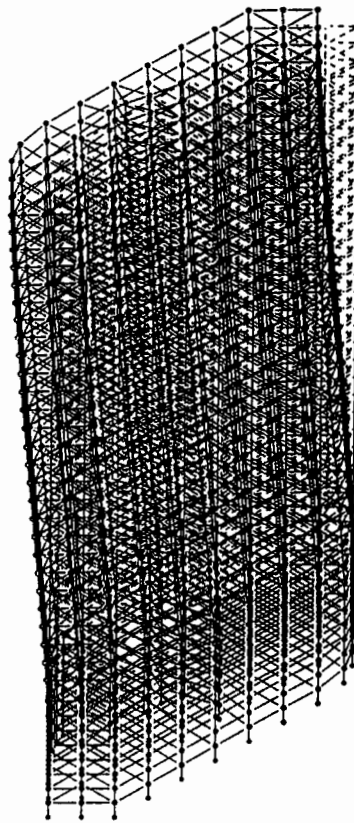


Figure 28. First mode shape from the ETABS analysis

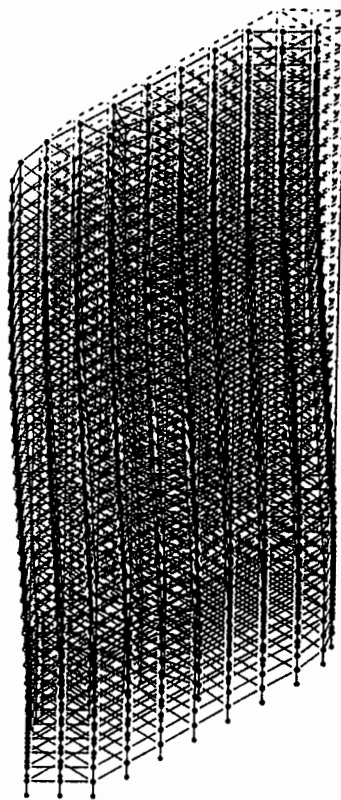


Figure 29. Second mode shape from the ETABS analysis

VAN NUYS, 7 STORY HOTEL

Evaluation of this building as a part of this project is in progress. The following information is based on the SMIP Information System (Naeim, 1997).

This 7 story reinforced concrete structure with no basements was designed in 1965 and constructed in 1966. Its vertical load carrying system consists of 8 in. and 10 in. concrete slabs supported by concrete columns, and spandrel beams at the perimeter. The lateral load resisting system consists of interior column-slab frames and exterior column-spandrel beam frames. The foundations consist of 38 inch deep pile caps, supported by groups of two to four poured-in-place 24 inch diameter reinforced concrete friction piles. Sketches of plan and elevation of the building showing the location of sensors are presented in Figure 31.

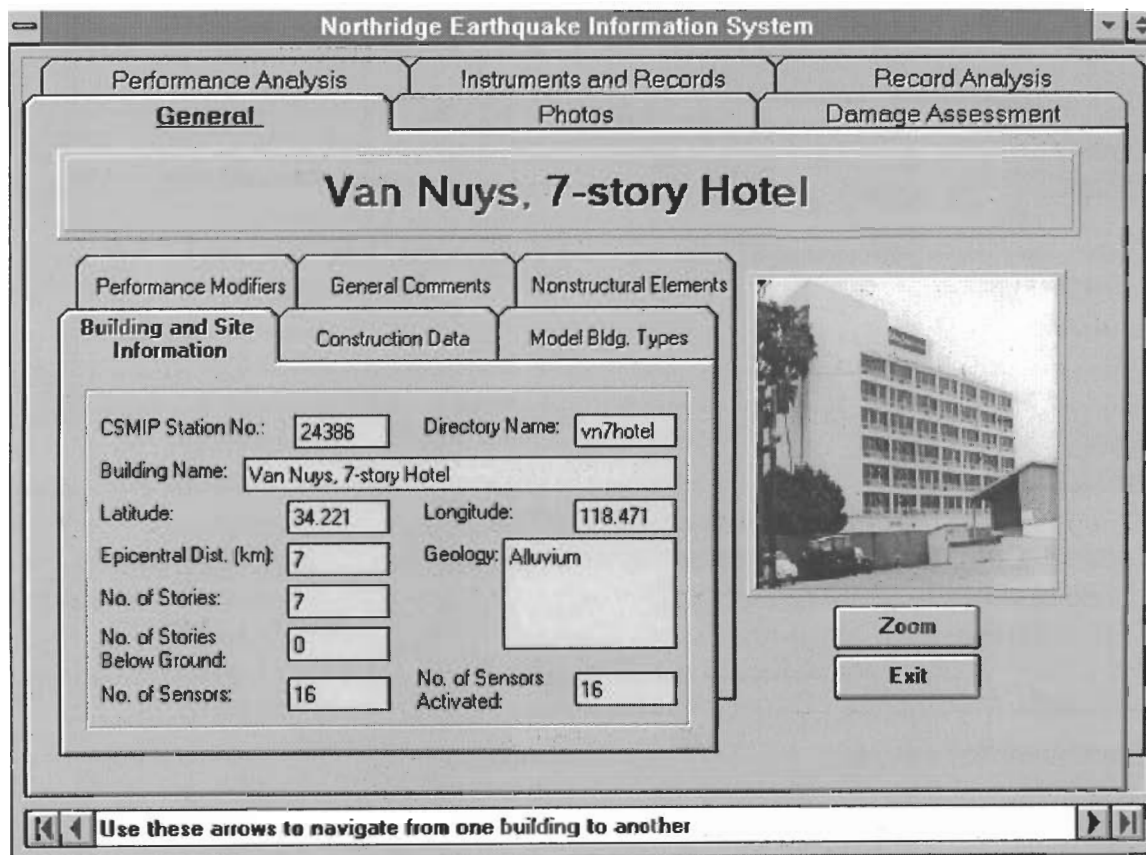


Figure 30. A view of the Van Nuys 7 Story Building (from Naeim, 1997)

The largest peak horizontal accelerations recorded at the basement (Channel 16, E-W) and at the roof (channels in both directions) are 0.45g and 0.58g, respectively. The largest velocity recorded at the roof is about 77 cm/sec.

Performance analysis calculations for this building are summarized in Table 4 where the significance of torsion (or differential response) to overall seismic behavior may be clearly seen.

The 0.33W maximum base shear apparently experienced by the building in the E-W direction is significantly larger than the 1964 UBC strength design base shear of about  $1.4 \times 0.05W = 0.07W$  and somewhat larger than the UBC-94 value of about  $1.4 \times 0.15 = 0.21W$  for a non-ductile moment resisting frame system (see Appendix B for backup calculations). Notice that the building experienced significant deformation particularly in the E-W direction with an overall drift index exceeding one percent of the height.

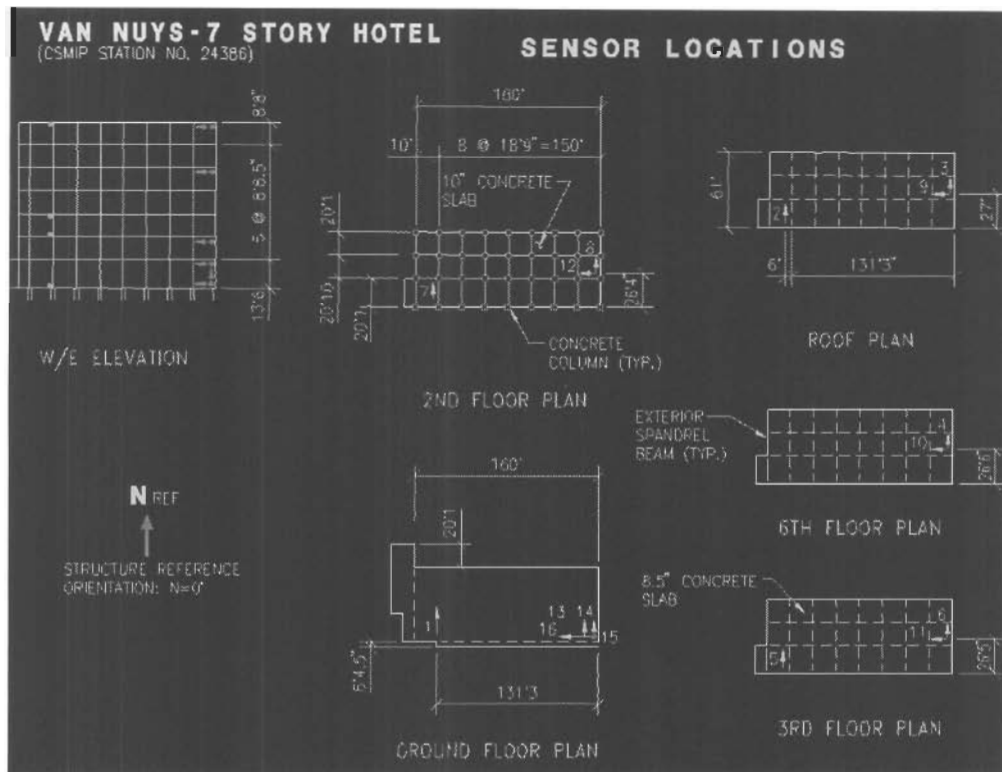


Figure 31. Instrumentation map for the Van Nuys 7 Story Building (from Naeim, 1997)

TABLE 4. Response Summary for Van Nuys 7-Story Hotel (from Naeim, 1997).

| Response Parameter                                  | Direction | Time of Maxima (seconds) | Maximum Value   |
|---|-----------|--------------------------|-----------------|
| Base Shear (% Total Weight)                         | N-S       | 8.38                     | 27.68           |
|   | E-W       | 9.24                     | 33.30           |
|   | DIFF      | 8.56                     | 40.46           |
| Overturning Moment (% Total Weight x feet)          | N-S       | 8.38                     | 830             |
|   | E-W       | 9.24                     | 1058            |
|   | DIFF      | 4.56                     | 1070            |
| Roof Lateral Displacement Relative to the Base (cm) | N-S       | 10.68                    | 19.82 (0.0099)* |
|   | E-W       | 9.36                     | 23.36 (0.0117)* |
|   | DIFF      | 8.74                     | 13.91 (0.0069)* |

\* Overall drift index values are shown in brackets.

The building had suffered minor structural damage and extensive nonstructural damage during the 1971 San Fernando earthquake and was subsequently repaired. The building experienced heavy damage during the Northridge earthquake where the South side exterior columns at fourth floor failed in shear (Figure 32). The building was repaired following the Northridge earthquake and the structural system in the E-W direction was changed to a shear-wall frame interaction system. The content damage was also heavy as documented in the information system. Surprisingly however, the mechanical equipment installed at the roof did not suffer any noticeable damage. The racking of the fourth floor was so significant that some of the hotel room doors needed to be opened using sledge hammers to get the occupants out (Figure 33).

A series of moving windows FFT analysis by Naeim, 1997 indicated an initial E-W fundamental period of about 1.4 seconds which elongates to about 2.2 seconds towards the end of the strong motion (Figure 34). Similar analysis shows a more moderate period elongation in the N-S direction from about 1.3 to 1.8 seconds, except when the kick from the E-W failure is captured (Figure 35). These periods are more than twice the code estimated periods of about 0.7 seconds.

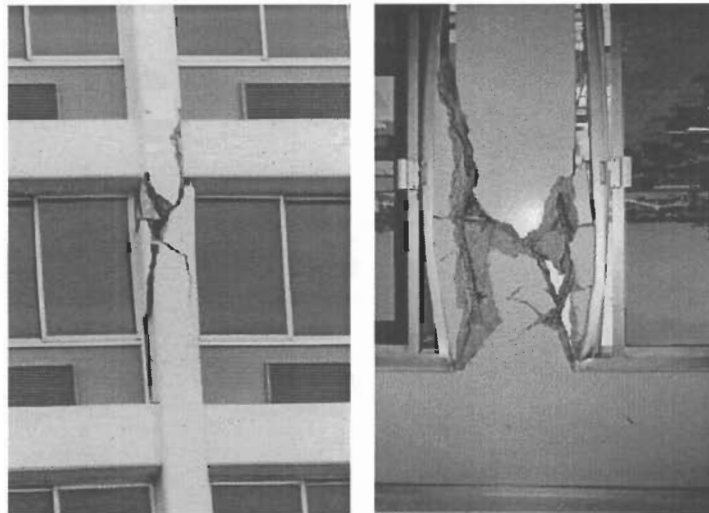


Figure 32. Shear failure of column at the fourth floor (Naeim, 1997).



Figure 33. Doors had to be opened with sledge hammers (Naeim, 1997).

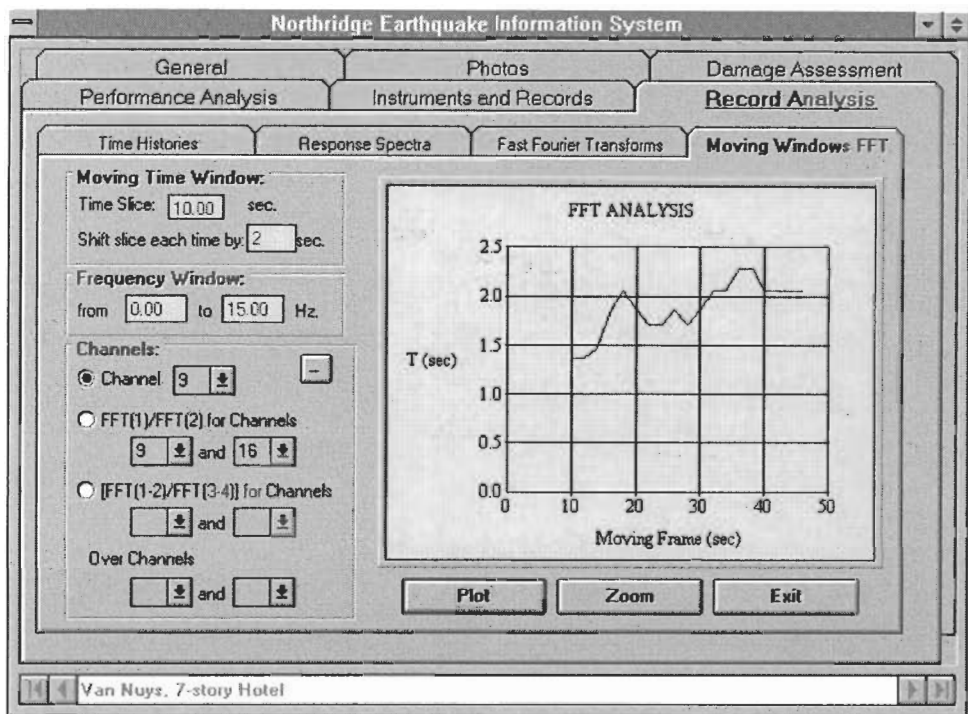


Figure 34. Moving windows FFT analysis for E-W response (Naeim, 1997).

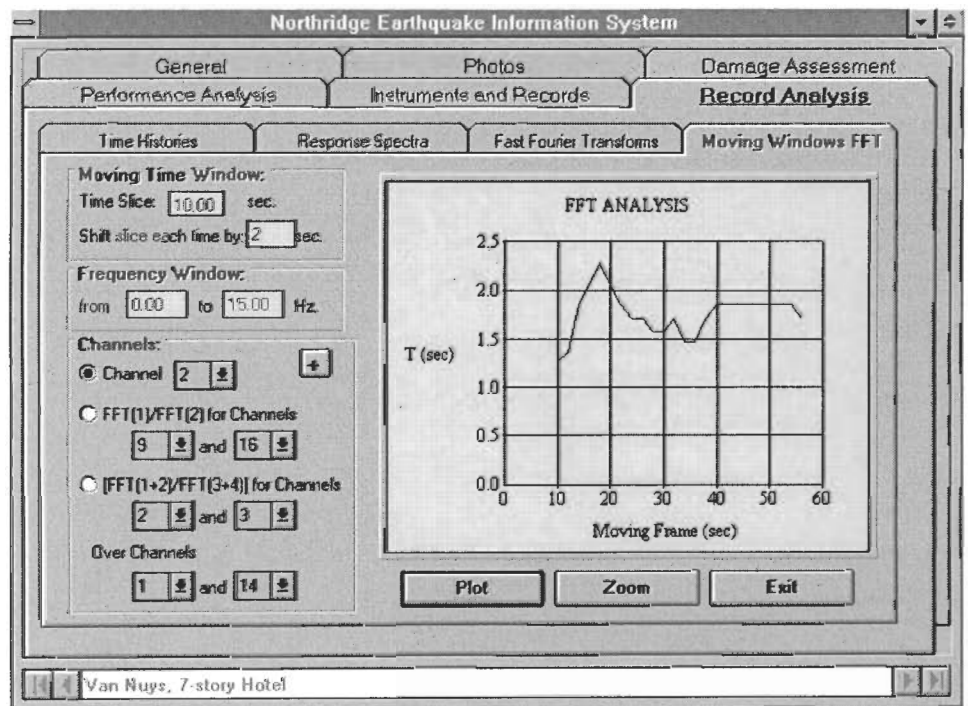


Figure 35. Moving windows FFT analysis for E-W response (Naeim, 1997).

REFERENCES

ACI 318-95, 1995, "Building Code Requirements for Structural Concrete (ACI 318-95) and Commentary (ACI 318R-95)", Farmington Hills, MI.

ATC-40, 1996, "Seismic Evaluation and Retrofit of Concrete Buildings", Vol. 1, Redwood City, California.

Federal Emergency Management Agency (1996), Ballot Version of NEHRP Guidelines for the Seismic Rehabilitation of Buildings, FEMA-273.

Federal Emergency Management Agency (1997), *NEHRP Recommended Provisions for the Development of Seismic Regulations for New Buildings*, 1997 Working Draft of Second Ballot Copy, June.

Hwang, S. -J., and Moehle, J. P., 1993, "An Experimental Study of Flat-Plate Structures Under Vertical and Lateral Loads," *UCB/EERC-93/03*, University of California, Earthquake Engineering Research Center, Berkeley, California.

International Conference of Building Officials (1997), *The Uniform Building Code - Volume 2*, Whittier, CA.

Naeim, Farzad (1997), '*Performance of Extensively Instrumented Buildings During the January 17, 1994 Northridge Earthquake - An Interactive Information System*', Report No. 7530-68, John A. Martin Associates, Inc., Los Angeles.

Naeim, Farzad and Lobo, Roy (1998), "The Ten Commandments of Push-Over Analysis," Proceedings of the Annual Meeting of the Los Angeles Tall Buildings Structural Design Council.

Workman, E. B., 1989, "The Tower at 3900 West Alameda A 32 Story Concrete Ductile Frame," *Proceedings for the 58<sup>th</sup> Annual Convention of SEAOC*, San Diego, California.





NEW TOOLS FOR PREDICTING AND  
MITIGATING EARTHQUAKE IMPACTS BASED ON  
GROUND MOTION DATA

Charles A. Kircher, Ph.D., P.E.

Kircher & Associates  
Mountain View, California

ABSTRACT

This paper describes the key features and components of the regional earthquake loss estimation methodology developed by the National Institute of Building Sciences (NIBS) with funding provided by the Federal Emergency Management Agency (FEMA). The FEMA/NIBS earthquake loss estimation methodology is intended primarily to assist emergency response planning and mitigation efforts of state, regional and local community governments. The FEMA/NIBS methodology incorporates state-of-the-art approaches for characterizing earthquake hazards, including ground shaking, liquefaction and land-sliding; estimating damage and losses to buildings and lifelines, estimating casualties, shelter needs and economic losses.

Of particular importance is the use of quantitative measures of ground shaking hazard (i.e., response spectra) in the estimation of building damage. Damage and loss are based on ground motion data, rather than on Modified Mercalli Intensity (MMI) commonly used by other earthquake loss estimation methods. While the FEMA/NIBS methodology was developed primarily for pre-earthquake planning purposes, the use of response spectra to predict damage makes the technology potentially valuable as a post-earthquake processor of near-real-time data from strong-motion networks such as the TriNet system. It is suggested that the FEMA/NIBS methodology be interfaced with strong-motion instrumentation networks to better assist post-earthquake response and recovery efforts. It is also suggested that predictions of earthquake damage and loss be used to assist locating strong-motion instruments in areas where buildings and other infrastructure are most at risk.

INTRODUCTION

With publication in 1972 of *A Study of Earthquake Losses in the San Francisco Bay Area* (Algermissen, et al., 1972), the federal government began to produce comprehensive estimates of the effects of major earthquakes on large urban regions. Direct economic losses, casualties, essential facilities' functionality, and some lifeline impacts were estimated. By the mid-1980's, similar studies had been produced for about dozen metropolitan areas in the United States, typically with more than one study for each area (FEMA, 1994). In general, these studies relied on predictions of Modified Mercalli Intensity (MMI) to estimate damage and loss.

The influential 1985 study, *Earthquake Damage Evaluation Data for California* (ATC, 1985), commonly referred to as ATC-13, used damage probability matrices based on expert opinion as its central framework. ATC-13 devised intensity-damage relationships for a large number of buildings and structure types, predicting a greater variety of losses than previous methods, and developed inventory relationships relating structure type and building occupancy. As in other methods, MMI remained the measure of ground shaking used to predict damage. However, in late 1980's the prestigious National Research Council's Panel on Earthquake Loss Estimation noted that,

*more complex representations of ground shaking, for example, through a filtered "effective" peak motion, a single-degree-of-freedom linear response spectrum, a nonlinear spectrum, a time history of motion, and the duration of strong shaking, have the ability to be more accurate predictors of damage and loss.* (NRC, 1989).

The FEMA/NIBS methodology has addressed the Panel's comment by use of response spectra (rather than MMI) to characterize ground shaking and by use of building damage functions that include pushover analyses that parallel procedures used in engineering design and evaluation of actual buildings.

### USERS OF EARTHQUAKE LOSS ESTIMATION

The FEMA/NIBS methodology "is intended primarily to provide local, state and regional officials with the tools necessary to plan and stimulate efforts to reduce risk from earthquakes and to prepare for emergency response and recovery from an earthquake" (NIBS, 1997). Different users will have different needs and the methodology has been programmed using GIS-based software (HAZUS) to be executed at different levels of analysis according to the user's ability to provide necessary data. At the lowest level, users rely on default databases supplied with HAZUS to make preliminary evaluations or crude comparisons among different study regions. More reliable results can be obtained when users have both the time and resources to develop additional data including such items as maps of site soil conditions or improved inventory data on building type, use and value.

Examples of pre-earthquake planning by local, state and regional government users includes development of earthquake hazard mitigation strategies (e.g., zoning or hazard abatement ordinances), development of preparedness (contingency) planning measures, and identification of response and recovery efforts. Federal government officials are now able to assess nationwide risk of loss from earthquakes. In the private sector, the methodology is available to building owners (e.g., large corporations) for identifying vulnerable structures and lifelines and to insurance and financial personnel for establishing appropriate premiums and loan criteria.

Example post-earthquake response and recovery applications include immediate economic impact assessments for state and federal resource allocation and immediate activation of emergency recovery efforts and long-term reconstruction plans. Immediate post-earthquake applications require that the study region to be developed prior to the event and that data be

available describing the ground shaking that has just occurred. While ground shaking can be estimated based on event magnitude and location (of epicenter), the most accurate predictions of damage and loss would come from a detailed map of ground shaking based on instrumental measurements. In this sense, strong-motion networks, such as the TriNet system (Shakal et al., 1997) may be able to provide the near-real-time strong-motion data necessary to make reliable post-earthquake estimates of damage and loss.

OVERVIEW OF THE FEMA/NIBS METHODOLOGY

The NIBS/FEMA earthquake loss estimation methodology is a complex collection of many components or modules (Whitman, et al., 1997). Modules are associated with either inventory, potential earth science hazards (PESH), damage (including both direct and induced damage) or loss (including both direct and or indirect economic impacts). Building-related modules (excluding inventory) of the FEMA/NIBS methodology and the flow of data between each is illustrated in Figure 1.

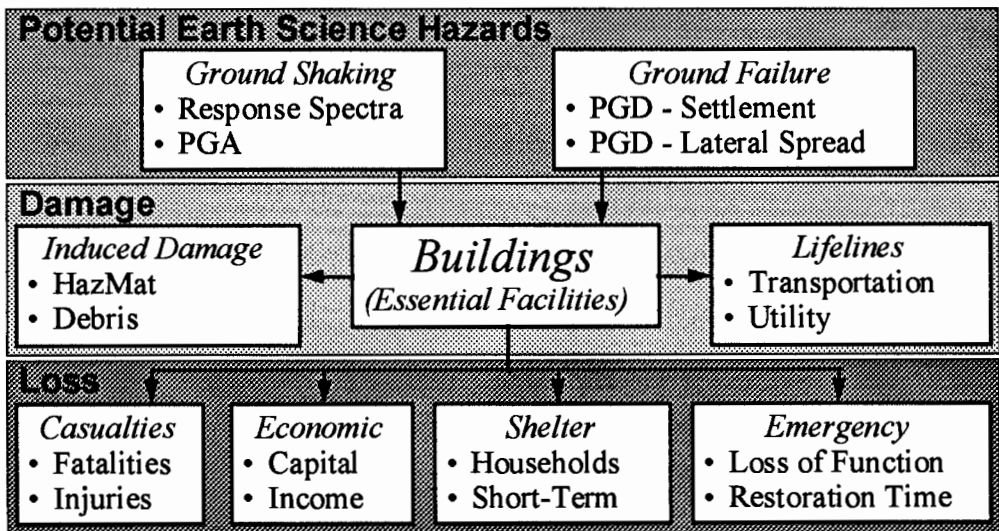


Figure 1. Building-related modules of the FEMA/NIBS methodology

Inputs to the estimation of building damage include ground failure, characterized by permanent ground deformation (PGD) due to settlement or lateral spreading, and ground shaking, typically characterized by response spectra, or, for those few buildings that are components of lifeline systems, by peak ground acceleration (PGA).

Estimates of building damage are used as inputs to other damage modules (e.g., debris generation), and as inputs to transportation and utility lifelines that have buildings as a part of the system (e.g., airport control tower). Most importantly, building damage is used as an input to a number of loss modules, including the estimation of casualties, direct economic losses, displaced households and short-term shelter needs, loss of emergency facility function and the time required to restore functionality.

The FEMA/NIBS building damage functions have two basic components: (1) capacity curves and (2) fragility curves. The capacity curves are based on engineering parameters (e.g., yield and ultimate levels of structural strength) that characterize the nonlinear (pushover) behavior of different model building types. For each building type, capacity parameters distinguish between different levels of seismic design and anticipated seismic performance. The fragility curves describe the probability of damage to a model building's (1) structural system, (2) nonstructural components sensitive to drift and (3) nonstructural components (and contents) sensitive to acceleration. For a given level of building response, fragility curves distribute damage between four physical damage states: Slight, Moderate, Extensive and Complete. A more thorough description of the FEMA/NIBS building damage functions is given below and in a recent *Earthquake Spectra* paper (Kircher, 1997a).

Earthquake loss due to building damage is based on the physical damage states that are the most appropriate and significant contributors to that particular type of loss. The number of buildings in the Complete damage state, which includes the kind of partial and complete collapse most likely to cause fatalities, heavily influences deaths. In contrast, direct economic loss (e.g., repair/replacement cost) is accumulated from significant loss contributions in all states of structural and nonstructural damage.

### BUILDING DAMAGE FUNCTIONS

Buildings are classified both in terms of their use, or occupancy class, and in terms of their structural system, or model building type. Damage is predicted based on model building type, since the structural system is considered the key factor in assessing overall building performance, loss of function and casualties. Occupancy class is important in determining economic loss, since building value is primarily a function of building use (e.g., hospitals are more valuable than most commercial buildings, primarily because of their expensive nonstructural systems and contents, not because of their structural systems).

Twenty-eight occupancy classes distinguish among residential, commercial, industrial or other buildings, and 36 model-building types classify buildings within the overall categories of wood, steel, concrete, masonry or mobile homes. Building inventory data relate model building type and occupancy class on the basis of floor area, so that for a given geographical area the distribution of the total floor area of model building types is known for each occupancy class.


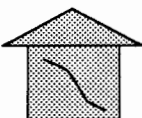
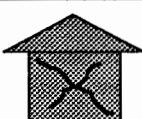

Model building types are derived from the classification system of the *NEHRP Handbook for the Seismic Evaluation of Existing Buildings* (FEMA, 1992), expanded to include mobile homes, and considering building height. Building damage functions distinguish among buildings that are designed to different seismic standards, or are otherwise expected to perform differently during an earthquake. These differences in expected building performance are determined on the basis of seismic zone location, design vintage and use (i.e., special seismic design of essential facilities).

Buildings are composed of both structural (load carrying) and nonstructural systems (e.g., architectural and mechanical components). While damage to the structural system is the most important measure of building damage affecting casualties and catastrophic loss of function (due

to unsafe conditions), damage to nonstructural systems and contents tends to dominate economic loss. Typically, the structural system represents about 25% of the building's worth. Building damage functions separately predict damage to: (1) the structural system, (2) drift-sensitive nonstructural components, such as partition walls that are primarily affected by building displacement, and (3) acceleration-sensitive nonstructural components, such as suspended ceilings, that are primarily affected by building shaking. Building contents are also considered to be acceleration sensitive.

Building damage is defined separately for structural and nonstructural systems of a building. Damage is described by one of four discrete damage states: Slight, Moderate, Extensive or Complete. Of course, actual building damage varies as a continuous function of earthquake demand. Ranges of damage are used to describe building damage, since it is not practical to have a continuous scale, and damage states provide the user with an understanding of the building's physical condition. The four damage states of the FEMA/NIBS methodology are similar to the damage states defined in *Expected Seismic Performance of Buildings* (EERI, 1994), except that damage descriptions vary for each model building type based on the type of structural system and material. Table 1 provides structural damage states for light-frame wood building typical of the conventional construction used for single-family homes.

Table 2. Example damage states - light-frame wood buildings

| Damage State  |                  | Description  |
|---|------------------|--|
|   | <b>Slight</b>    | Small plaster cracks at corners of door and window openings and wall-ceiling intersections; small cracks in masonry chimneys and masonry veneers. Small cracks are assumed to be visible with a maximum width of less than 1/8 inch (cracks wider than 1/8 inch are referred to as "large" cracks).  |
|  | <b>Moderate</b>  | Large plaster or gypsum-board cracks at corners of door and window openings; small diagonal cracks across shear wall panels exhibited by small cracks in stucco and gypsum wall panels; large cracks in brick chimneys; toppling of tall masonry chimneys.   |
|  | <b>Extensive</b> | Large diagonal cracks across shear wall panels or large cracks at plywood joints; permanent lateral movement of floors and roof; toppling of most brick chimneys; cracks in foundations; splitting of wood sill plates and/or slippage of structure over foundations.  |
|  | <b>Complete</b>  | Structure may have large permanent lateral displacement or be in imminent danger of collapse due to cripple wall failure or failure of the lateral load resisting system; some structures may slip and fall off the foundation; large foundation cracks. Five percent of the total area of buildings with Complete damage is expected to be collapsed. |

### BUILDING CAPACITY AND RESPONSE CALCULATION

A building capacity curve is a plot of a building's lateral load resistance as a function of a characteristic lateral displacement (i.e., a force-deflection plot). It is derived from a plot of static-equivalent base shear versus building displacement at the roof, known commonly as a

pushover curve. In order to facilitate direct comparison with spectral demand, base shear is converted to spectral acceleration and the roof displacement is converted to spectral displacement using modal properties that represent pushover response. Pushover curves and related-capacity curves, are derived from concepts similar to those of the *NEHRP Guidelines for the Seismic Rehabilitation of Buildings* (FEMA, 1997), and in *Seismic Evaluation and Retrofit of Concrete Buildings* (SSC, 1996), commonly referred to as ATC-40.

Building capacity curves are constructed for each model building type and represent different levels of lateral force design and building performance. Each curve is defined by two control points: (1) the “yield” capacity, and (2) the “ultimate” capacity. The yield capacity represents the lateral strength of the building and accounts for design strength, redundancies in design, conservatism in code requirements and expected (rather than nominal) strength of materials. Design strengths of model building types are based on the requirements of current model seismic code provisions (e.g., 1994 *UBC* or *NEHRP Provisions*) or on an estimate of lateral strength for buildings not designed for earthquake loads. Certain buildings designed for wind, such as taller buildings located in zones of low or moderate seismicity, may have a lateral design strength considerably greater than those based on seismic code provisions.

The ultimate capacity represents the maximum strength of the building when the global structural system has reached a full mechanism. Typically, a building is assumed capable of deforming beyond its ultimate point without loss of stability, but its structural system provides no additional resistance to lateral earthquake force. Up to yield, the building capacity curve is assumed to be linear with stiffness based on an estimate of the expected period of the building. From yield to the ultimate point, the capacity curve transitions in slope from an essentially elastic state to a fully plastic state. The capacity curve is assumed to remain plastic past the ultimate point. Examples of building capacity curves are shown in Figure 2.

Building response is determined by the intersection of the demand spectrum and the building capacity curve. Intersections are illustrated in Figure 2 for three example demand spectra representing what can be considered as weak, medium and strong ground shaking, and two building capacity curves representing weaker and stronger construction, respectively. The terms “weak,” “medium,” and “strong” and “weaker” and “stronger” are used here for simplicity; in the actual methodology, only quantitative values of spectral response and building capacity are used. As shown in Figure 2, stronger and stiffer construction displaces less than weaker and more flexible construction for the same level of spectral demand, and less damage is expected to the structural system and nonstructural components sensitive to drift. In contrast, stronger construction will shake at higher acceleration levels, and more damage is expected to nonstructural components and contents sensitive to acceleration.

The demand spectrum is based on the 5%-damped response spectrum at the building’s site (or centroid of a study area containing a group of buildings), reduced for effective damping when effective damping exceeds the 5% damping level of the input spectrum. Effective stiffness properties are based on secant stiffness, and effective damping is based on combined viscous and hysteretic measures of dissipated energy. Effective damping greater than 5% of critical is used to reduce spectral demand in a manner similar to the capacity-spectrum method of ATC-40.

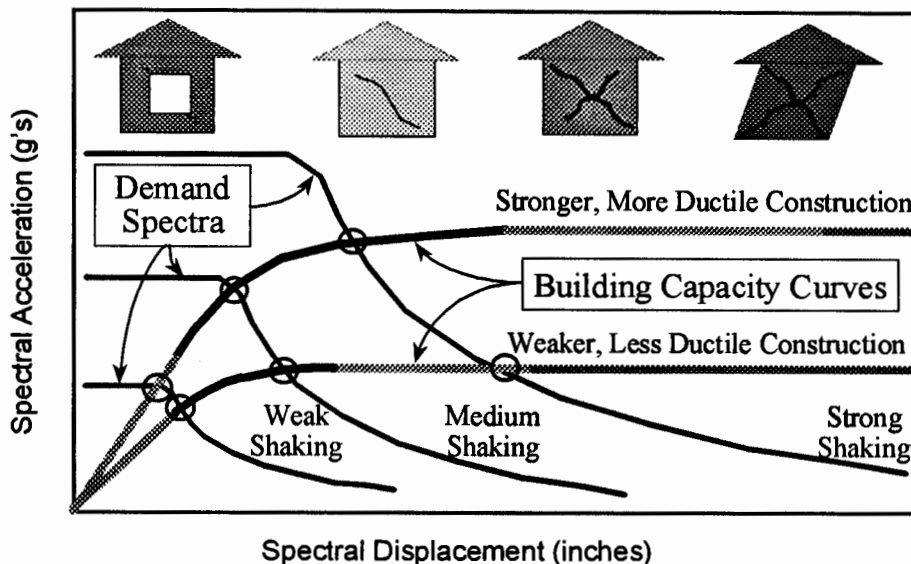


Figure 2. Example demand spectra and building capacity curves

The FEMA/NIBS methodology characterizes ground shaking using a standard response spectrum shape, as shown in Figure 3, for spectra representing rock, stiff soil and soft soil conditions, respectively. The standard shape consists of two primary parts: (1) a region of constant spectral acceleration at short periods and (2) a region of constant spectral velocity at long periods. Short-period spectral acceleration,  $S_s$ , is defined by 5%-damped spectral acceleration at a period of 0.3 seconds. The constant spectral velocity region has spectral acceleration proportional to  $1/T$  and is anchored to the 1-second, 5%-damped spectral acceleration,  $S_1$ . A region of constant spectral displacement exists at very long periods, although this region does not usually affect calculation of building damage and is not shown in Figure 3.

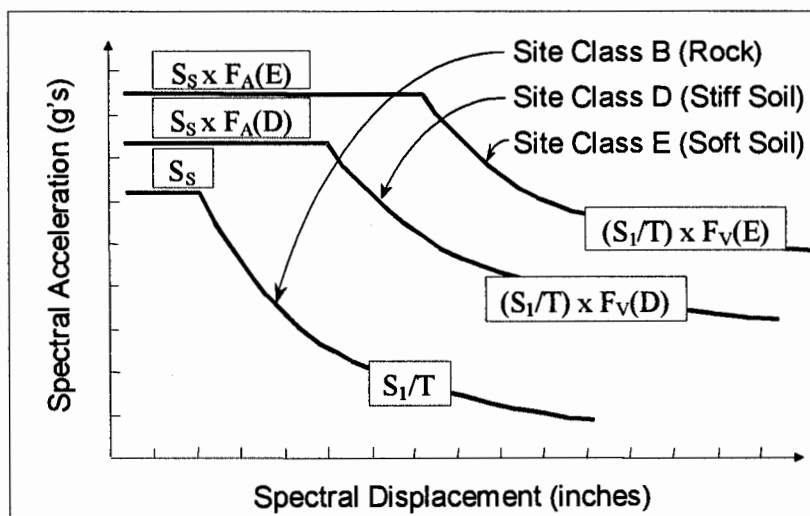


Figure 3. Example 5%-damped response spectra for three site classes

The FEMA/NIBS methodology predicts spectral response as a function of distance from scenario earthquake sources based on the same attenuation functions as those used by the United States Geological Survey to create national seismic hazard maps for *Project 97* (Frankel et al., 1996). These functions define ground shaking for rock (Site Class B) conditions based on earthquake magnitude and other source parameters (e.g., fault type).

Amplification of ground shaking to account for local site conditions is based on the soil factors of the *NEHRP Provisions*. The *NEHRP Provisions* define a standardized site geology classification scheme and specify soil amplification factors (i.e.,  $F_A$  for the acceleration domain and  $F_V$  for the velocity domain). Figure 3 shows construction of demand spectra for stiff soil sites (Site Class D) and soft soil sites (Site Class E). These spectra illustrate the importance of soil type on spectral demand (and building response), particularly in the velocity domain.

### BUILDING FRAGILITY AND LOSS CALCULATION

Building fragility curves are lognormal functions that describe the probability of reaching, or exceeding, structural and nonstructural damage states, given deterministic (median) estimates of spectral response, for example spectral displacement. These curves take into account the variability and uncertainty associated with capacity curve properties, damage states and ground shaking.

Figure 4 provides an example of fragility curves for the four damage states used in the FEMA/NIBS methodology and illustrates differences in damage-state probabilities for three levels of spectral response corresponding to weak, medium, and strong earthquake ground shaking, respectively. The terms “weak,” “medium,” and “strong” are used here for simplicity; in the actual methodology, only quantitative values of spectral response are used.

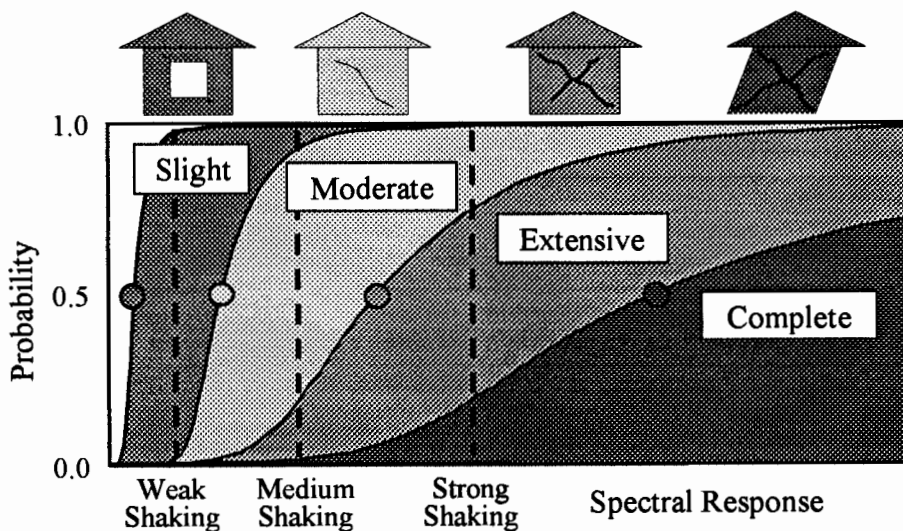


Figure 4. Example fragility curves for Slight, Moderate, Extensive and Complete damage



The fragility curves distribute damage among Slight, Moderate, Extensive and Complete damage states. For any given value of spectral response, discrete damage-state probabilities are calculated as the difference of the cumulative probabilities of reaching, or exceeding successive damage states. Discrete damage-state probabilities are used as inputs to the calculation of various types of building-related loss. Figure 5 provides an example of discrete damage state probabilities for the three levels of earthquake ground shaking.

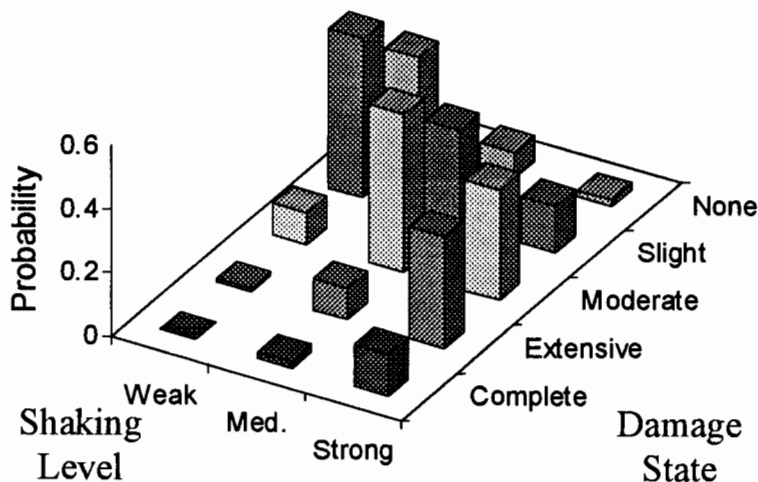


Figure 5. Example damage-state probabilities for weak, medium and strong shaking levels

Each fragility curve is defined by a median value of the demand parameter (e.g., spectral displacement) that corresponds to the threshold of that damage state and by the variability associated with that damage state. The total variability of each damage state is based on a complex combination of three primary sources of damage variability, namely the variability associated with the capacity curve, the variability associated with the demand spectrum and the variability associated with the discrete threshold of the damage state. While some fragility formulations have separated uncertainty from randomness, the FEMA/NIBS methodology does not and damage state variability represents composite "best-estimate" fragility. This approach is similar to that used to develop fragility curves for the FEMA-sponsored study of consequences of a large earthquake on six cities of the Mississippi Valley region (Kircher and McCann, 1983).

As mentioned previously, discrete probabilities of damage state are used as inputs to a variety of different building loss functions. In general, these functions return an estimate of the amount of loss for each building system (e.g., structural, nonstructural or contents) of each building type (e.g. light-frame wood) of each building occupancy (e.g., single-family residence). Estimated loss is based on the square footage of that particular combination of building type/occupancy in the area of interest (e.g., census tract or whole study region). Since the damage state probabilities are based on "best-estimate" fragility, loss estimates represent the center of the true distribution of actual loss that could occur.

## UTILIZATION OF STRONG-MOTION DATA IN LOSS ESTIMATION

By basing hazard on quantitative measures of ground shaking (e.g., response spectra), the FEMA/NIBS methodology utilizes strong-motion data in loss estimation, rather than relying on MMI to describe hazard. Strong-motion data are used indirectly in the form of various Western United States (WUS) attenuation relationships that are based on response spectra of actual earthquake records. Strong-motion data may also be input directly in the form of spectral contour maps of recorded ground shaking.

The methodology provides three approaches for characterizing ground shaking: the deterministic scenario event, the scenario event based on probabilistic seismic hazard maps, and the scenario event based on user-supplied ground shaking maps. In the first case, the user selects scenario-earthquake magnitude and identifies the source (fault) of interest. The HAZUS software provides a database of historical earthquakes and their epicenters, as well as databases (maps) of WUS faults (including fault type, location and orientation). Fault rupture length is determined based on the scenario-earthquake magnitude. Alternatively, users can specify all fault criteria for an "arbitrary" scenario-earthquake event.

After determination of scenario-earthquake magnitude and fault criteria, attenuation functions are used to calculate response spectra at various locations throughout the study region of interest. Response spectra are calculated at specific locations of special buildings (e.g., essential facilities) and at the centroid of census tracts for evaluation of general building stock (i.e., general building stock is grouped by census tract). For reference, there are about 1,650 census tracts in Los Angeles County, which has a population of about 9 million and a total building count of about 2.2 million (of which about 2 million buildings are residences).

Ground shaking is a function of the distance from the plane of fault rupture (which is defined by fault criteria). The location and geometry of the fault rupture plane are important to accurate estimation of damage and loss, particularly for thrust or reverse-slip faults that have a pronounced dip angle. The region of strongest ground shaking may not be well represented by the location of the earthquake's epicenter. For example, Figure 6 contrasts the location of the region of strongest ground shaking and the location of the epicenter of the 1994 Northridge earthquake (and the location of the region of densest residence value). In the Northridge earthquake, fault rupture occurred along a plane that dips at angle of about  $45^{\circ}$ . Fault rupture initiated at about 20 km below the epicenter and propagated up and to the north. The region of strongest ground shaking is located approximately over the plane of fault rupture.

In Figure 6, the region of strongest ground shaking is defined as ground shaking having a spectral acceleration of 0.75 g, or greater, at a period of 0.3 seconds. Spectral acceleration maps of the 1994 Northridge Earthquake were taken from the work of Somerville who developed smooth contour maps from ground shaking records for the SAC project (SAC Joint Venture, 1995). The spectral acceleration maps were also used to compare observed economic loss with that predicted by the FEMA/NIBS methodology (Kircher, 1997b). Predicted loss was found to compare favorably with observed loss when loss predictions were based on actual ground shaking data.

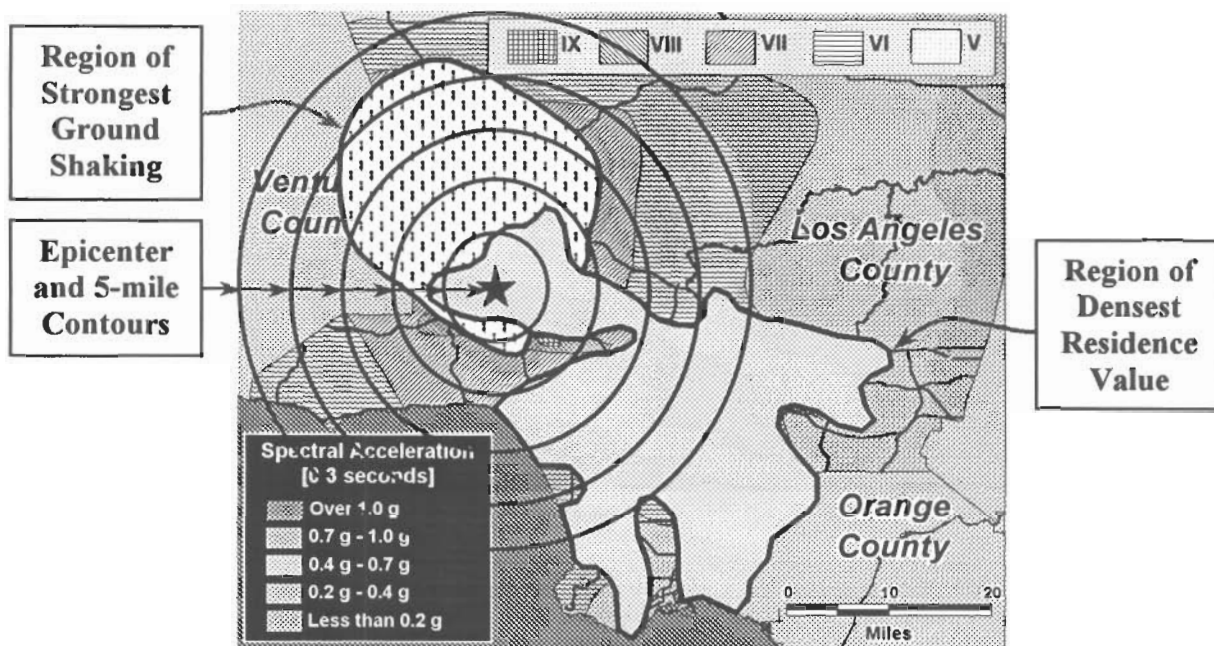


Figure 6. Map of Los Angeles County showing regions of densest residence value and strongest ground shaking of the 1994 Northridge Earthquake

In Figure 6, the region of densest residence value in Los Angeles County is defined approximately by those areas having a residential value density of more than 100 million dollars per square mile. While a portion of the region of strongest shaking overlaps with the region of densest residence value in the San Fernando Valley, most of the strong shaking occurred in the mountains and sparsely built areas to north and west of the valley. Only about 10% - 20% of Los Angeles County residences felt this level of strong ground shaking. A different location of the fault rupture plane would have created an entirely different region of strongest shaking, possibly closer to (or possibly farther from) the region of densest residence value, and the amount and spatial distribution of losses would likely have been quite different from those observed. Accurately relating the spatial distribution of strong ground shaking to the inventory of buildings (and other infrastructure) is a key factor in developing reliable estimates of earthquake loss.

The FEMA/NIBS methodology permits (and encourages) users to input detailed information on soil type. In lieu of such data, the methodology develops site or census-tract response spectra that include amplification factors for the default soil type (stiff soil). The use of true soil type (rather than default soil type) can significantly change the amount of damage and loss predicted for buildings, particularly for tall, flexible structures and/or for structures responding at or beyond yield. Likewise, post-earthquake damage and loss predictions based on instrumental records that explicitly include the effects of soil amplification would be expected to provide much better estimates of damage and loss.

To illustrate the importance of soil type on building response, and hence on damage and loss prediction, example response calculations are made for three soil profile types (rock, stiff soil and soft soil). Figure 7 illustrates the calculation of building response for strong ground

shaking at a stiff soil site. The building has an initial period of 0.6 seconds, representing a typical mid-rise building. The building yields at a spectral acceleration of about 0.2 g and reached full yield at a spectral acceleration of about 0.4 g. These strength properties represent a building that was designed to seismic-code requirements, but of an older design vintage (e.g., a typical older California commercial building).

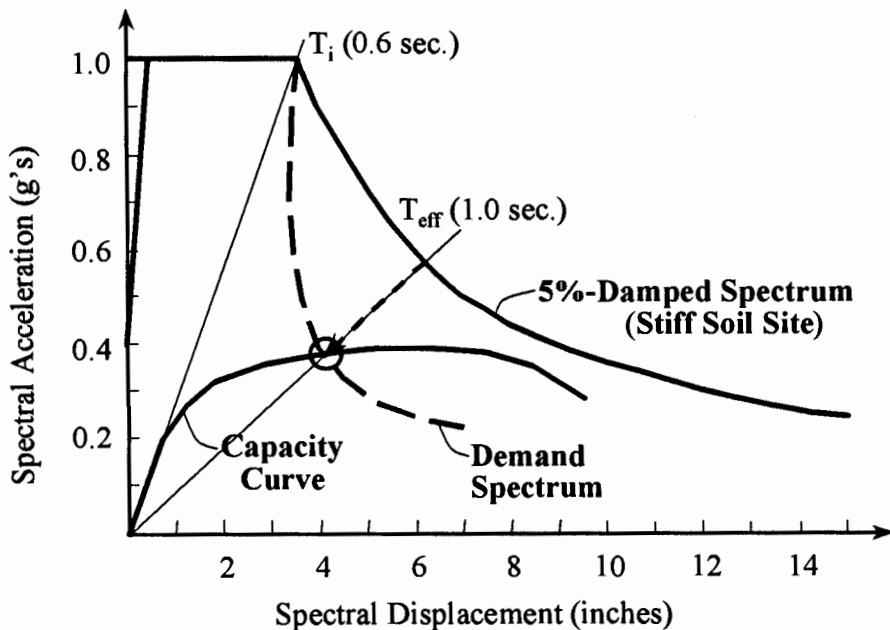


Figure 7. Example Response Calculation - Stiff Soil Site

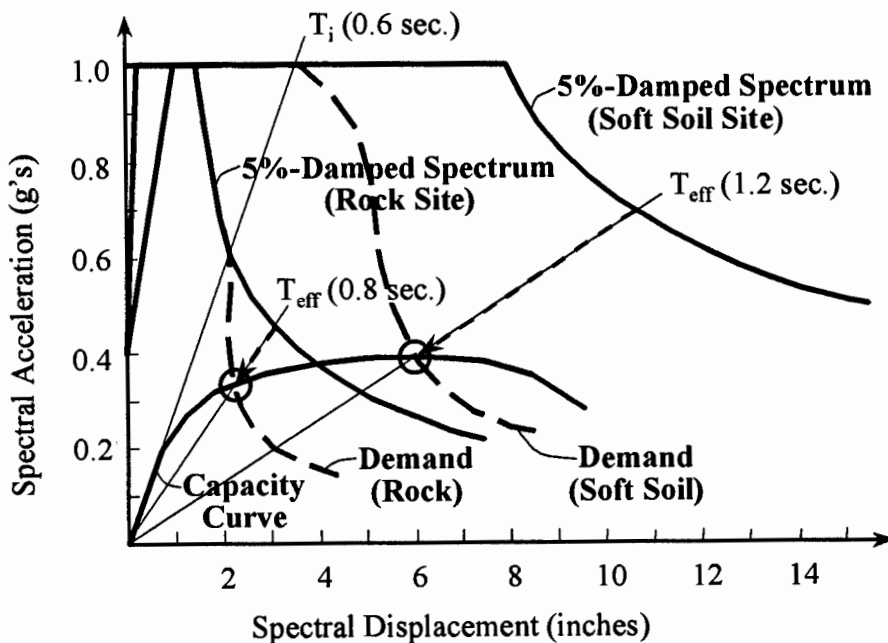


Figure 8. Example Response Calculation - Rock and Soft Soil Sites

Assuming the building to be a reinforced concrete, shear-wall structure, the FEMA/NIBS methodology specifies median spectral displacements (and corresponding inter-story drift values) for each structural damage state as given in Table 3. Median spectral displacements represent thresholds at which damage is expected to begin to occur for each damage state. For example, Moderate damage is not expected to begin to occur on average until spectral displacement reaches about 2.5 inches, or about 0.67 inch of inter-story drift.

Table 3. Example median spectral displacements and inter-story drifts corresponding to damage states of an older reinforced concrete mid-rise building

| Building Damage State | Spectral Displacement (inches) | Inter-Story Drift (inches) |
|-----------------------|--------------------------------|----------------------------|
| Slight                | 1.2                            | 0.33                       |
| Moderate              | 2.5                            | 0.67                       |
| Extensive             | 7.0                            | 1.9                        |
| Complete              | 18.0                           | 4.8                        |

Figure 7 shows a 5%-damped response spectrum that represents ground shaking at a stiff soil site. A demand spectrum is constructed using procedures that parallel those of ATC-40. The building's capacity curve intersects the stiff soil demand spectrum at about 4 inches of spectral displacement. Based on Table 3, the building would most likely have Moderate structural damage (but could also have either Slight or Extensive damage due to the variability of the damage functions).

Figure 8 shows 5%-damped response spectra that represent rock and soft soil sites, respectively, and the demand spectra corresponding to these site conditions. The building's capacity curve intersects the rock demand spectrum at about 2 inches and intersects the soft soil spectrum at about 6 inches. For the rock site, the spectral displacement indicates that either Slight or Moderate structural damage is likely (i.e., 2 inches is near the threshold of Moderate damage), and the building has about the same probability of either Moderate or Extensive structural damage. For the soft soil site, the spectral displacement is close to the Extensive damage-state threshold and the building has about the same probability of either Moderate or Extensive structural damage.

In this example, structural damage varies approximately from Slight/Moderate for a rock site to Moderate for a stiff soil site to Moderate/Extensive for a soft soil site. In terms of loss, the direct economic loss ratios of the FEMA/NIBS methodology expect about 5 times more dollar loss with Extensive damage than with the Moderate damage. Thus, two similar reinforced concrete mid-rise buildings located the same distance from fault rupture, one on soft soil and the other on rock, are expected to have significantly different responses and losses. The building on soft soil is expected to displace laterally about 3 times farther during strong ground shaking and to cost about 5 times as much to repair the structural system than the building on rock.

## CONCLUSION

This paper has summarized the key features and components of the regional earthquake loss estimation methodology developed by the National Institute of Building Sciences (NIBS) with funding provided by the Federal Emergency Management Agency (FEMA). The FEMA/NIBS earthquake loss estimation methodology is intended primarily to assist emergency response planning and mitigation efforts of state, regional and local community governments. The FEMA/NIBS methodology incorporates state-of-the-art approaches for characterizing earthquake hazards, including ground shaking, liquefaction and land-sliding; estimating damage and losses to buildings and lifelines, estimating casualties, shelter needs and economic losses.

The paper has emphasized the importance of using quantitative measures of ground shaking hazard (i.e., response spectra) in the estimation of building damage. Damage and loss are based directly on ground motion data, rather than on Modified Mercalli Intensity (MMI) commonly used by other earthquake loss estimation methods. While the FEMA/NIBS methodology was developed primarily for pre-earthquake planning purposes, the use of response spectra to predict damage makes the technology potentially valuable as a post-earthquake processor of near-real-time data from strong-motion networks such as the TriNet system. It is suggested that the FEMA/NIBS methodology be interfaced with strong-motion instrumentation networks to better assist post-earthquake response and recovery efforts.

It is further suggested that predictions of earthquake damage and loss be used to assist locating strong-motion instruments in areas where buildings and other infrastructure are most at risk. Recognizing that public safety needs require instrumentation networks that can be used to effectively reduce earthquake risk (not just improve earth science), strong-motion instrumentation should be located where there is the greatest likelihood of experiencing damaging ground shaking. This objective is best summarized by two criteria: (1) high probability of strong shaking, (2) large quantity of infrastructure at risk. While seismic hazard maps alone could address the first criterion, the second criterion requires determining the relative risk to the infrastructure of different seismic regions. Some visionary applications have already been made and suggest that loss estimation can be a valuable tool in developing strong-motion instrumentation networks (Borcherdt, 1997).

## REFERENCES

- Algermissen, S. T. et al. *A Study of Earthquake Losses in the San Francisco Bay Area: Data and Analysis*. (Washington, DC: Office of Emergency Preparedness and National Oceanic and Atmospheric Administration).
- Applied Technology Council, 1985. *Earthquake Damage Evaluation Data for California* (ATC-13). (Redwood City, CA: Applied Technology Council).
- Borcherdt, R., (Chairman), The Committee for the Future of the U.S. National Strong-Motion Program, 1997. "Vision for the Future of the US National Strong-Motion Program," United States Geological Survey (USGS) Open-File Report Number 97-530B. (Menlo Park, CA: USGS).
- Earthquake Engineering Research Institute (EERI), 1994. *Expected Seismic Performance of Buildings*. (Oakland, CA: EERI).

- Federal Emergency Management Agency (FEMA), 1997. *NEHRP Guidelines for the Seismic Rehabilitation of Buildings*, (Washington, D.C.: FEMA 273).
- Federal Emergency Management Agency (FEMA), 1995. *NEHRP Recommended Provisions for the Seismic Regulations for New Buildings*. (Washington, D.C.: FEMA 222A).
- Federal Emergency Management Agency (FEMA), 1994. *Assessment of the State-of-the-Art Earthquake Loss Estimation Methodologies*. (Washington, DC: FEMA 249).
- Federal Emergency Management Agency (FEMA), 1992. *NEHRP Handbook for the Seismic Evaluation of Existing Buildings*. (Washington, D.C.: FEMA 178).
- Frankel, Arthur, Charles Mueller, Theodore Barnhard, David Perkins, E.V. Leyendecker, Nancy Dickman, Stanley Hanson and Margaret Hopper, 1997. "National Seismic-Hazard Maps," United States Geological Survey (USGS) Open-File Reports 96-532 and 96-706. (Denver, CO: USGS).
- International Conference of Building Officials (ICBO), 1994. *Uniform Building Code* (Whittier, CA: ICBO).
- Kircher, Charles A., Aladdin A. Nassar, Onder Kustu and William T. Holmes, 1997a. "Development of Building Damage Functions for Earthquake Loss Estimation," *Earthquake Spectra*, Vol. 13, No. 4, (Oakland, California: Earthquake Engineering Research Institute).
- Kircher, Charles A., Robert K. Reitherman, Robert V. Whitman and Christopher Arnold, 1997b. "Estimation of Earthquake Losses to Buildings," *Earthquake Spectra*, Vol. 13, No. 4, (Oakland, CA: Earthquake Engineering Research Institute).
- Kircher, Charles A. and Martin W. McCann, 1983. "Development of Fragility Curves for Estimation of Earthquake-Induced Damage." *Workshop on Continuing Actions to Reduce Losses from Earthquakes in Arkansas and Nearby States*. (Washington, DC: United States Geological Survey).
- National Institute of Building Science (NIBS), 1997. *Earthquake Loss Estimation Methodology, HAZUS97: Users Manual*. Report prepared for the Federal Emergency Management Agency. (Washington, D.C.: NIBS).
- National Research Council, 1989. *Estimating Losses from Future Earthquakes*. Report of the Panel on Earthquake Loss Estimation Methodology. (Washington, DC: National Academy Press).
- SAC Joint Venture, 1995. *Technical report: Characterization of Ground Motions during the Northridge Earthquake of January 17, 1994*. SAC 95-03 (Sacramento, CA: SAC Joint Venture).
- Seismic Safety Commission (SSC), 1996. *Seismic Evaluation and Retrofit of Concrete Buildings*, SSC Report No. 96-01 (Sacramento, CA: Seismic Safety Commission, State of California).
- Shakal, Anthony, V. Graizer, C. Petersen and R. Darragh, 1997. "Near-Real-Time Strong-Motion, TriNet Data and Data Dissemination," *SMIP97 Seminar on Utilization of Strong-Motion Data*. (Sacramento, CA: California Strong Motion Instrumentation Program, Division of Mines and Geology).
- Whitman, Robert V., Thalia Anagnos, Charles A. Kircher, Henry J. Lagorio, R. Scott Lawson, Philip Schneider, 1997. "Development of a National Earthquake Loss Estimation Methodology," *Earthquake Spectra*, Vol. 13, No. 4, (Oakland, CA: Earthquake Engineering Research Institute).





SEISMIC CODE IMPROVEMENTS BASED ON  
RECORDED MOTIONS OF BUILDINGS DURING EARTHQUAKES

Anil K. Chopra

Department of Civil and Environmental Engineering  
University of California, Berkeley, California

Rakesh K. Goel

Department of Civil and Environmental Engineering  
California Polytechnic State University  
San Luis Obispo, California

Juan Carlos De la Llera

Pontificia Universidad Catolica de Chile  
Santiago, Chile

ABSTRACT

Summarized in this paper are the results of two recent investigations utilizing recorded motions of buildings to develop improvements in two aspects of seismic code provisions for buildings: (1) fundamental vibration period formulas, and (2) accidental torsion.

INTRODUCTION

The recorded motions of buildings during earthquakes are the basic data against which methods of earthquake-resistant design and techniques for calculating earthquake response must be judged. Perhaps the most common research use of these data has been in refining and improving structural modelling and response analysis techniques to match the calculated responses with measured data. Our interest has been quite different in recent years. We have utilized measured responses to investigate issues in building design that are not amenable to traditional analytical approaches. In particular, we have investigated two aspects of seismic code provisions for buildings: (1) fundamental vibration period formulas, and (2) accidental torsion.

The code formulas for estimating building period must be related to the actual periods of buildings, not to calculated values. The actual periods of interest are those "measured" from recorded motions of buildings shaken strongly during earthquakes. We have developed a comprehensive database of "measured" periods of buildings and proposed new formulas suitable for code application to estimate building period.

The subject of accidental torsion is not amenable to investigations by traditional analytical approaches because standard dynamic analyses do not predict torsion in symmetric-plan buildings. Analysis of recorded motions of nominally-symmetric-plan buildings provides the most direct means of developing an understanding of the torsional response of such buildings and for evaluating building code provisions for accidental torsion. We have utilized recorded motions of seven nominally-symmetric-plan buildings to evaluate a recent procedure for considering accidental torsion in building design.

Comprehensive reports on these investigations have been published (Goel and Chopra, 1997a; De la Llera and Chopra, 1997). Summaries of relevant portions of these reports are presented in this paper.

### PART I: FUNDAMENTAL VIBRATION PERIOD FORMULAS

#### *Code Formulas*

The fundamental vibration period of a building appears in the equations specified in building codes to calculate the design base shear and lateral forces. Because this building property can not be computed for a structure that is yet to be designed, building codes provide empirical formulas that depend on the building material (steel, RC, etc.), building type (frame, shear wall etc.), and overall dimensions. These formulas should be consistent with periods of buildings "measured" from their motions recorded during earthquakes.

The measured data that are most useful but hard to come by are from structures shaken strongly but not deformed into the inelastic range. Such data are slow to accumulate because relatively few structures are installed with permanent accelerographs and earthquakes causing strong motions of these instrumented buildings are infrequent. Thus, it is very important to investigate comprehensively the recorded motions when they do become available, as during the 1994 Northridge earthquake. Unfortunately, this obviously important goal is not always accomplished, as indicated by the fact that the vibration properties of only a few of the buildings whose motions were recorded during post-1971 earthquakes have been determined.

#### *Period Database*

Supported by an NSF project, we have "measured" the natural vibration periods of twenty-one buildings by system identification methods applied to building motions recorded during the 1994 Northridge earthquake (Goel and Chopra, 1997a). These data have been combined with similar data from the motions of buildings recorded during the 1971 San Fernando, 1984 Morgan Hill, 1986 Mt. Lewis and Palm Spring, 1987 Whittier, 1989 Loma Prieta, 1990 Upland, and 1991 Sierra Madre earthquakes reported by several investigators (an exhaustive list of references is available in Goel and Chopra, 1997a). The resulting database, which contains data for a total of 106 buildings, is described in Goel and Chopra (1997a). It includes thirty-seven data points for twenty-seven RC moment-resisting frame (MRF) buildings, fifty-three data points for forty-two steel MRF buildings, and twenty-seven data points for sixteen concrete shear wall (SW) buildings. The number of data points exceeds the number of buildings because the period of some buildings was determined from their motions recorded during more than one earthquake, or was reported by more than one investigator for the same earthquake.

#### *Theoretical Formulas*

With the use of Rayleigh's method, the following relationships for fundamental period of multistory moment-resisting frames with equal floor masses and story heights have been determined (Goel and Chopra, 1997a: Appendix E):

$$T = C_1\sqrt{H} \text{ or } C_2H \quad (1)$$

The exponent of  $H$  and the numerical values of  $C_1$  and  $C_2$  depends on the stiffness properties, including their heightwise variation.

Another formula for the fundamental period has been derived by Rayleigh's method under the following assumptions: (1) lateral forces are distributed linearly (triangular variation of forces) over the building height; (2) base shear is proportional to  $1/T^\gamma$ ; (3) weight of the building is distributed uniformly over its height; and (4) deflected shape of the building, under application of the lateral forces, is linear over its height, which implies that the inter-story drift is the same for all stories. The result of this derivation (Goel and Chopra 1997a, Appendix D) is:

$$T = C_3H^{1/(2-\gamma)} \quad (2)$$

If the base shear is proportional to  $1/T^{2/3}$ , as in U.S. codes of the recent past,  $\gamma = 2/3$  and Eq. (2) gives

$$T = C_4H^{3/4} \quad (3)$$

which is in the ATC3-06 report (1978) and appears in current U.S. codes.

The formulas presented in Eqs. (1) to (3) are of the form:

$$T = \alpha H^\beta \quad (4)$$

in which constants  $\alpha$  and  $\beta$  depend on building properties, with  $\beta$  bounded between one-half and one. This form is adopted for moment-resisting frame buildings in the present investigation and constants  $\alpha$  and  $\beta$  are determined by regression analysis of the measured period data.

To develop an appropriate theoretical formula for shear wall buildings we use Dunkerley's method. Based on this method the fundamental period of a cantilever, considering flexural and shear deformations, is:

$$T = \sqrt{T_F^2 + T_S^2} \quad (5)$$

in which  $T_F$  and  $T_S$  are the fundamental periods of pure-flexural and pure-shear cantilevers, respectively. For uniform cantilevers  $T_F$  and  $T_S$  are given by:

$$T_F = \frac{2\pi}{3.516} \sqrt{\frac{m}{EI}} H^2 \quad (6)$$

$$T_S = 4 \sqrt{\frac{m}{\kappa G}} \frac{1}{\sqrt{A}} H \quad (7)$$

In Eqs. (6) and (7),  $m$  is the mass per unit height,  $E$  is the modulus of elasticity,  $G$  is the shear modulus,  $I$  is the section moment of inertia,  $A$  is the section area, and  $\kappa$  is the shape factor to account for nonuniform distribution of shear stresses ( $= 5/6$  for rectangular sections). Combining Eqs. (5) to (7) and recognizing that  $G = E / 2(1 + \mu)$ , where the Poisson's ratio  $\mu = 0.2$  for concrete, leads to:

$$T = 4 \sqrt{\frac{m}{\kappa G}} \frac{1}{\sqrt{A_e}} H \quad (8)$$

with

$$A_e = \frac{A}{\left[1 + 0.83 \left(\frac{H}{D}\right)^2\right]} \quad (9)$$

where  $D$  is the plan dimension of the cantilever in the direction under consideration. Comparing Eqs. (8) and (9) with Eq. (7) reveals that the fundamental period of a cantilever considering flexural and shear deformations may be computed by replacing the area  $A$  in Eq. (7) with the equivalent shear area  $A_e$  given by Eq. (9).

We next considered a class of a class of symmetric-plan buildings—symmetric in the lateral direction considered—with lateral-force resisting system comprised of a number of uncoupled (i.e., without coupling beams) shear walls connected through rigid floor diaphragms. Assuming that the stiffness properties of each wall are uniform over its height, the equivalent shear area,  $A_e$ , is given by a generalized version of Eq. (9) (details are available in Goel and Chopra 1997a, Appendix G):

$$A_e = \sum_{i=1}^{NW} \left(\frac{H}{H_i}\right)^2 \frac{A_i}{\left[1 + 0.83 \left(\frac{H_i}{D_i}\right)^2\right]} \quad (10)$$

where  $A_i$ ,  $H_i$ , and  $D_i$  are the area, height, and dimension in the direction under consideration of the  $i$ th shear wall, and  $NW$  is the number of shear walls. With  $A_e$  so defined, Eq. (8) is valid for a system of shear walls of different height.

Equation (8) was then expressed in a form convenient for buildings:

$$T = \bar{C} \frac{1}{\sqrt{\bar{A}_e}} H \quad (11)$$

where  $\bar{C} = 40\sqrt{\rho/\kappa G}$ ,  $\rho$  is the average mass density, defined as the total building mass ( $= mH$ ) divided by the total building volume ( $= A_B H$  --  $A_B$  is the building plan area), i.e.,  $\rho = m/A_B$ ; and  $\bar{A}_e$  is the equivalent shear area expressed as a percentage of  $A_B$ , i.e.,

$$\bar{A}_e = 100 \frac{A_e}{A_B} \quad (12)$$

### *Regression Analysis Method*

Regression analysis of the measured period data leads to values of  $\alpha_R$  and  $\beta$  for Eq. (4) and  $\bar{C}_R$  for Eq. (11) to represent the best fit, in the least-squared sense, to the data. However, for code applications the formula should provide lower values of the period in order not to underestimate the base shear, and this was obtained by defining  $\alpha_L$  and  $\bar{C}_L$  as the mean ( $\alpha_R$  and  $\bar{C}_R$ ) minus one standard deviation value;  $\alpha_L$  and  $\bar{C}_L$  are the 15.9 percentile values, implying that 15.9 percent of the measured periods would fall below the curves corresponding to  $\alpha_L$  and  $\bar{C}_L$  (subsequently referred to as the best-fit  $-1\sigma$  curve). If desired,  $\alpha_L$  and  $\bar{C}_L$  corresponding to other non-exceedance probabilities may be selected. Additional details of the regression analysis method and the procedure to estimate  $\alpha_L$  and  $\bar{C}_L$  are available elsewhere (Goel and Chopra 1997, Appendix F). Building codes also specify an upper limit on the period calculated by rational analysis. This limit is established in this investigation by defining  $\alpha_U$  and  $\bar{C}_U$  as the mean ( $\alpha_R$  and  $\bar{C}_R$ ) plus one standard deviation value to give the best-fit  $+1\sigma$  curves.

### *Recommended Formulas*

**MRF Buildings.** The formula for estimating the fundamental period of MRF buildings was obtained by calibrating the theoretical formula of Eq. (4) by regression analysis of the measured period data for twenty-seven RC MRF buildings (thirty-seven data points) and for forty-two steel MRF buildings (fifty-three data points); these buildings are listed in Tables 1 and 2 of Goel and Chopra (1997b).

Figures 1 and 2 give an impression of the scatter in the measured period data relative to the best-fit or  $T_R$  curve. The measured periods of a building in two orthogonal lateral directions are shown by circles connected by a vertical line. As expected, the data fall above and below the curve, more or less evenly, and most of the data are above the best-fit  $-1\sigma$  or  $T_L$  curve.

The best-fit  $-1\sigma$  and best-fit  $+1\sigma$  curves for steel buildings are presented in Fig. 3. The fundamental vibration period of steel MRF buildings should be estimated from

$$T_L = 0.028H^{0.80} \quad (13)$$

The  $T_U$  curve is suitable for limiting the period of a building calculated by any rational analysis. Thus, the period from rational analysis should not be allowed to exceed  $1.6T_L$ ; the factor 1.6 is determined as the ratio  $0.045 \div 0.028$ , rounded off to one digit after the decimal point.

In the best-fit  $-1\sigma$  and best-fit  $+1\sigma$  curves for RC buildings presented in Fig. 4, observe that the coefficient 0.016 in  $T_L$  is slightly larger than the 0.015 value in Fig. 2a to recognize that the period of an RC building lengthens at motions large enough to cause cracking of concrete;  $\alpha_L = 0.016$  was obtained from regression analysis of period data for buildings that experienced peak ground acceleration  $\ddot{u}_{go} > 0.15g$ . Thus, the fundamental vibration period of RC MRF buildings should be estimated from

$$T_L = 0.016H^{0.80} \quad (14)$$

and the building period calculated by any rational analysis should not be allowed to exceed  $1.4T_L$ ; the factor 1.4 is determined as the ratio  $0.023 \div 0.016$ .

#### *RC Shear Wall Buildings*

The formula for estimating the fundamental period of concrete SW buildings was obtained by calibrating the theoretical formula of Eq. (11) by regression analysis of the measured period data for nine concrete SW buildings (17 data points) listed in Table 2 of Goel and Chopra (1998). For each building  $\bar{A}_e$  was calculated from Eqs. (10) and (12) using dimensions from structural plans (Goel and Chopra 1997a, Appendix H); for shear walls with dimensions varying over height,  $A_i$  and  $D_i$  were taken as the values at the base. Regression analysis gives  $\bar{C}_R = 0.0023$  and  $\bar{C}_L = 0.0018$ . Using these values for  $\bar{C}$  in Eq. (11) give  $T_R$  and  $T_L$ , the best-fit and best-fit  $-1\sigma$  values of the period, respectively.

These period values are plotted against  $H \div \sqrt{\bar{A}_e}$  in Fig. 5, together with the measured periods shown in circles; the measured periods of a building in the two orthogonal directions are not joined by a vertical line because the ratio  $H \div \sqrt{\bar{A}_e}$  is different if the shear wall areas are not the same in the two directions. As expected, the measured period data falls above and below (more or less evenly) the best-fit curve.

The best-fit  $-1\sigma$  and best-fit  $+1\sigma$  curves are presented in Fig. 6 wherein  $\bar{C}_L = 0.0019$  is slightly larger than the 0.0018 value in Fig. 5 for reasons mentioned earlier in the context of the RC MRF buildings. Thus, the fundamental vibration period of RC shear wall buildings should be estimated from

$$T_L = 0.0019 \frac{1}{\sqrt{A_e}} H \quad (15)$$

and the building period calculated by any rational analysis should not be allowed to exceed  $1.4T_L$ ; the factor 1.4 is determined as the ratio  $0.0026 \div 0.0019$  rounded off to one digit after the decimal point.

## ACCIDENTAL TORSION

### *Code Estimates of Accidental Torsion*

Building codes require consideration of accidental torsion in one of two ways: (1) apply the equivalent static lateral forces at eccentricity  $e_a$  from the center of stiffness (CS), which includes the accidental eccentricity  $e_a = \pm\beta b$ ; and (2) perform dynamic analyses with the center of mass (CM) of each floor shifted a distance equal to the accidental eccentricity  $e_a = \pm\beta b$  from its nominal position, where  $b$  is the plan dimension of the building perpendicular to the direction of ground motion. For each structural element the algebraic sign in  $e_a$  that leads to the larger design force is to be used. Implementation of these code provisions requires two three-dimensional (3-D) static or dynamic analyses of the building for each lateral direction. The two types--static and dynamic--of analyses predict significantly different increases in design forces resulting from accidental eccentricity; the code-static analyses are not consistent with the analytical results (De la Llera and Chopra, 1994d).

### *Analytical Estimates of Accidental Torsion*

Determined in earlier investigations (De la Llera and Chopra, 1994b,e) is the increase in response due to the following sources of accidental torsion: (1) rotational motion of the building foundation, (2) uncertainty in the stiffness of structural elements in both principal directions of analysis, (3) uncertainty in the location of the CM, and (4) uncertainty in stiffness and mass distributions in stories of a building other than the story analyzed.

Shown in Fig. 7 are the mean and mean-plus-one standard deviation of  $\hat{u}_{b/2}$ , the normalized edge ( $x = b/2$ ) displacement, considering all sources of accidental torsion plotted against  $\Omega = \omega_\theta / \omega_y$ , the ratio between the natural vibration frequencies of the uncoupled torsional and lateral motions of the building (De la Llera and Chopra, 1995a). The normalized response in Fig. 7 and subsequent figures refers to the ratio of responses computed on two bases: considering accidental torsion and neglecting accidental torsion. The mean value of the increase in response,  $\hat{u}_{b/2} - 1$ , is usually less than 3%. Furthermore, with the exception of systems with  $T_y < 0.5$  sec. and  $\Omega < 1$ , this mean increase in response is insensitive to  $\Omega$ . The mean-plus-one standard deviation value of the response increase reaches a peak value of 45% for systems with  $\Omega = 0.85$  or  $\Omega = 1.1$ ; it decreases steadily

for values of  $\Omega$  larger and smaller than these two values; and it varies rapidly between its peaks at  $\Omega \approx 0.85$  and 1.1 to a minimum at  $\Omega \approx 1$ .

*Design Procedure*

Compared in Fig. 7 is  $\hat{u}_{b/2}$  predicted by code-dynamic analysis with  $e_a = \pm 0.05b$  and the analytical result. The code increase in edge displacements is much larger than the mean value of the analytical estimate, but is about one-half of the mean-plus-one standard deviation value. The code value corresponds to an exceedance probability of about 30%.

The discrepancy in the design forces due to accidental torsion, as predicted by code-specified static and dynamic analysis procedures, can be overcome by defining a unique design envelope for the edge displacements:

$$\hat{u}_{b/2} = \begin{cases} A & 0 \leq \Omega \leq 1 \\ A - \frac{A-1}{\Omega_c-1} (\Omega-1) & 1 < \Omega \leq \Omega_c \\ 1 & \Omega > \Omega_c \end{cases} \quad (16)$$

where  $\Omega_c = 1.8$  and

$$A = 1 + 0.0475(b/r)^2 \quad (17)$$

where  $r$  = radius of gyration of the floor diaphragm about the center of mass.

Equation (17) is a good approximation to the maximum value of  $\hat{u}_{b/2}$  over all  $\Omega$  (Fig. 8a) determined by code-specified dynamic analysis (Fig. 8b). Furthermore, Eqs. (16) and (17) have been intentionally calibrated to produce values that are conservative, especially for the range  $0.9 \leq \Omega \leq 1.1$ . There are three reasons for this. First, the estimation of  $\Omega$  is obviously subject to error; therefore, taking advantage of the sharp dip in the analytical response curve near  $\Omega = 1$  is not appropriate for design. Second, this conservatism proves to be useful in preventing resisting planes in the interior of the building plan to be underdesigned by the procedure developed. Third, the "recorded" increase in response for a system with  $\Omega \approx 1$  can be larger than predicted by code-specified dynamic analysis for accidental torsion (De la Llera and Chopra, 1995).

In order to overcome the limitations of the present code procedures, the design envelope of Eqs. (16) and (17) forms the basis for a design procedure to include accidental torsion in the seismic design of buildings. This procedure is "exact" for single-story systems and for multistory buildings belonging to the special class defined in Hejal and Chopra, (1989); it is also a good approximation



for other multistory systems. It has several important advantages over the current seismic code procedures. First, it avoids the two additional 3-D static or dynamic analyses of the building in each lateral direction. Second, it includes the effects of all sources of accidental torsion whereas codes include only those that can be represented by a constant accidental eccentricity. Third, it gives a unique value for the increase in a design force due to accidental torsion, whereas current codes give very different results depending on whether the analysis is static or dynamic. Fourth, the procedure defines explicitly the expected increase in design forces due to accidental torsion, in contrast to the use of accidental eccentricity in codes implying an indirect increase in member forces. Fifth, the increase in design forces specified by the new procedure has a well-established probability of exceedance.

### *"Measured" Accidental Torsion*

In this section a procedure is described to determine the torsion in nominally symmetric buildings from their motions recorded during earthquakes; three channels of horizontal acceleration are necessary at each instrumented floor of a building. First, the motions of uninstrumented floors are inferred from the motions of instrumented floors by a cubic spline interpolation procedure (Figure 9) without modelling or structural analysis of the building. In this procedure interpolation is performed on floor displacements (relative to the base) instead of the common choice of floor accelerations. Cubic spline functions satisfy conditions of continuity and differentiability of second-order at the interpolation points (i.e., instrumented floors) and, hence, provide smooth shapes for the heightwise distribution of displacements.

Next, floor accelerations are computed from the inferred or "measured" displacements at uninstrumented floors. The total displacement-time function for such a floor is obtained by adding the ground displacements to the floor displacement relative to the base determined by the cubic spline interpolation procedure. Floor velocity-time and acceleration-time functions are computed by time differentiation of the displacement-time function. Since differentiation emphasizes the high frequency components, these velocity and acceleration traces are low-pass filtered. The filter parameters are chosen so that the resulting accelerations match closely the recorded acceleration at an instrumented floor. A ninth-order Butterworth low-pass filter was selected with the cut-off frequency chosen to ensure a close match. Furthermore, the predicted velocity- and acceleration-time functions are filtered in both forward and reverse directions to eliminate any phase distortion (MATLAB, 1994).

Presented in Fig. 10 is an example of the low-pass filtering procedure and the results obtained by the interpolation procedure applied to the motions of a seven-story R/C-frame building recorded during the 1994 Northridge earthquake. The predicted motions of the building at the locations of the instruments on the sixth floor are compared with the actual recorded motions; the latter are not used in the interpolation process and hence provide a benchmark for evaluating the accuracy of the procedure. The predicted displacement-time and acceleration-time functions are seen to be accurate.

At the end of this interpolation and filtering procedure, the displacement-, velocity-, and acceleration-time functions are known for all floors; these will be referred to as the "recorded" motions. The "recorded" motions at the center of mass in the  $x$ -,  $y$ -, and  $\theta$ -directions are then calculated assuming a rigid floor diaphragm.

This procedure was implemented for the nominally-symmetric buildings listed in Table 1. The influence of accidental torsion on response of selected buildings is shown in Fig. 11 by superimposing the time variation of the deformation (displacement relative to the base) at the edge of the roof plan due to building translation only (dashed line) and due to building rotation and translation simultaneously (solid line). The difference between these two functions is due to accidental torsion induced in these nominally-symmetric buildings. The normalized edge displacement, defined as the peak (maximum absolute) value of the displacement including torsion divided by the corresponding value excluding torsion is computed for each building considered. This is the "measured" value of normalized edge displacement considering accidental torsion.

Table 1. Nominally Symmetric Buildings Considered

| Buildings    | CSMIP | PGA   | Material | $(b/r)_x$ | $(b/r)_y$ | $\Omega_x$ | $\Omega_y$ |
|--------------|-------|-------|----------|-----------|-----------|------------|------------|
| A: Richmond  | 58506 | 0.11g | Steel    | 3.12      | 1.49      | 1.36       | 1.52       |
| B: Pomona    | 23511 | 0.13g | RC       | 2.22      | 2.67      | 1.42       | 1.34       |
| C: San Jose  | 57562 | 0.20g | Steel    | 3.22      | 1.28      | 1.00       | 1.03       |
| D: Sylmar    | 24514 | 0.67g | Steel    | 3.06      | 3.04      | 0.75       | 0.82       |
| E: Burbank   | 24370 | 0.30g | Steel    | 2.45      | 2.45      | 1.72       | 1.72       |
| F: Burbank   | 24385 | 0.29g | RC       | 1.11      | 3.28      | 1.14       | 1.10       |
| G: Warehouse | 24463 | 0.26g | RC       | 2.13      | 2.74      | 1.54       | 1.40       |

### *Evaluation of Design Procedure*

The normalized edge displacement is plotted as a function of  $\Omega$  in Fig. 12. The "measured" values are plotted for each building at its  $\Omega$  value in Table 1. For buildings D, E, F and G the vertical bar gives the range of values for the different floors and the star denotes the mean value. For buildings A, B and C the open circles denote the value for the roof only from an earlier investigation (De la Llera and Chopra, 1994a). Superimposed on these data are the design curves (Eqs. 16 and 17) for  $b/r = 1, 2, \text{ and } 3$ .

Figure 12 shows that the increase in response due to accidental torsion of buildings with  $\Omega$  close to one varies from essentially zero for building F to about 40% for building C. The implied sensitivity of this increase to small changes in  $\Omega$  is consistent with theoretical predictions (mean-plus-one standard deviation curve in Fig. 7). It is for this reason that the dip in the theoretical curve at  $\Omega = 1$  has been ignored in the design envelopes (Fig. 8). Obviously, Fig. 12 must be interpreted carefully since for each value of  $\Omega$ , the displacement increase due to accidental torsion is a random variable, and the data points are just a very few outcomes of this random variable.

Figure 12 also indicates that the measured accidental torsion is smaller for buildings with larger  $\Omega$ , i.e., torsionally-stiff buildings. The design curves are consistent with this trend and neglect accidental torsion for buildings with  $\Omega > 1.8$ .

CONCLUDING COMMENTS

Earthquake-resistant design must be based upon recorded motions of buildings during earthquakes. In this paper we have utilized these records to develop improvements in two aspects of seismic code provisions for buildings—fundamental vibration period formulas and accidental torsion—that are not amenable to traditional analytical approaches. We hope that these proposals would receive the attention of code-writing committees.

ACKNOWLEDGEMENTS

The investigation on fundamental vibration period formulas was supported during 1994-1995 by the National Science Foundation under Grant No. CMS-9416265 from the 1994 Northridge Earthquake Research Program. The work on accidental torsion was part of a comprehensive investigation funded by CSMIP to utilize building motions recorded during the 1994 Northridge earthquake.

REFERENCES

Applied Technological Council (1978). *Tentative provisions for the development of seismic-regulations for buildings*, Report No. ATC3-06, Applied Technological Council, Palo Alto, California.

De la Llera, J.C. and A.K. Chopra (1994a). Evaluation of code accidental-torsion provisions from building records. *Journal of Structural Engineering*, ASCE, **120**, 597-616.

De la Llera, J.C. and A.K. Chopra (1994b). Accidental torsion in buildings due to stiffness uncertainty. *Earthquake Engineering and Structural Dynamics*, **23**, 117-136.

De la Llera, J.C. and A.K. Chopra (1994c). *Accidental and Natural Torsion in Earthquake Response and Design of Buildings*, Report No. UCB/EERC-94/07, Earthquake Engineering Research Center, University of California, Berkeley.

De la Llera, J.C. and A.K. Chopra (1994d). Using accidental eccentricity in code-specified static and dynamic analyses of buildings. *Earthquake Engineering and Structural Dynamics*, **23**, 947-967.

De la Llera, J.C. and A.K. Chopra (1994e). Accidental torsion in buildings due to base rotational excitation. *Earthquake Engineering and Structural Dynamics*, **23**, 1003-1021.

De la Llera, J.C. and A.K. Chopra (1995). Estimation of accidental torsion effects for seismic design of buildings. *Journal of Structural Engineering*, ASCE, **121**, 102-114.

De la Llera, J. C. and A. K. Chopra (1997). *Evaluation of seismic code provisions using strong-motion building records from the 1994 Northridge earthquake*, Report No. UCB/EERC-97/16, Earthquake Engineering Research Center, December, 1997, 308 pp.

Goel, R. K. and A. K. Chopra (1997a). *Vibration Properties of Buildings Determined from Recorded Earthquake Motions*, Report No. UCB/EERC-97/14, Earthquake Engineering Research Center, December, 1997, 271 pp.

Goel, R. K. and A. K. Chopra (1997b). Period formulas for moment-resisting frame buildings. *Journal of Structural Engineering*, ASCE, **123**, 1454-1461.

Goel, R. K. and A. K. Chopra (1998). Period Formulas for Concrete Shear Wall Buildings. *Journal of Structural Engineering*, ASCE, **124**, 426-433.

Hejal, R. and A. K. Chopra (1989). Response spectrum analysis of a class of torsionally coupled buildings, *Journal of Engineering Mechanics*, ASCE, **115**, 1761-1781.

MATLAB (1994). *Reference Guide*, the Mathworks, Inc., Natick, Massachusetts.

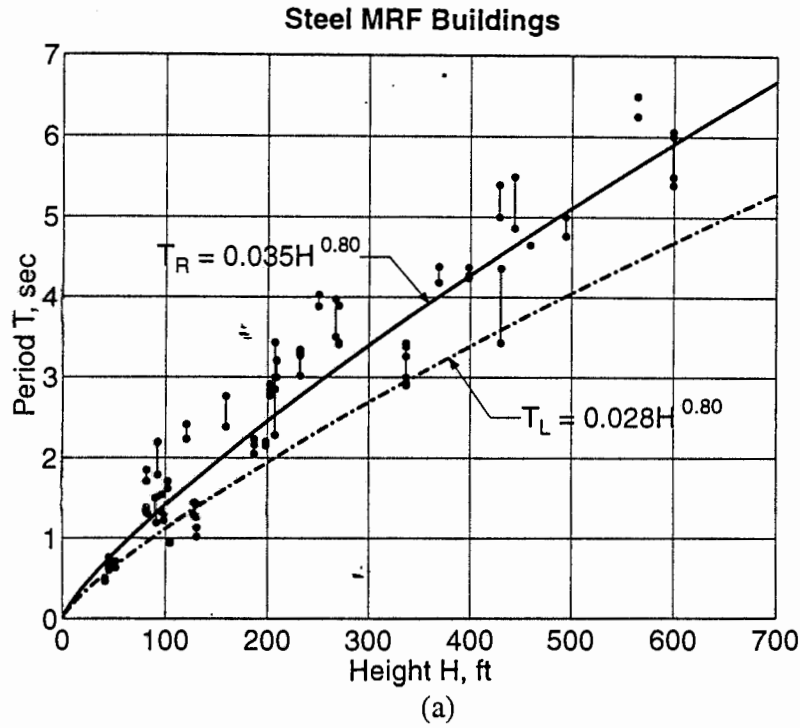


Figure 1: Regression analysis of measured period data for steel MRF buildings.

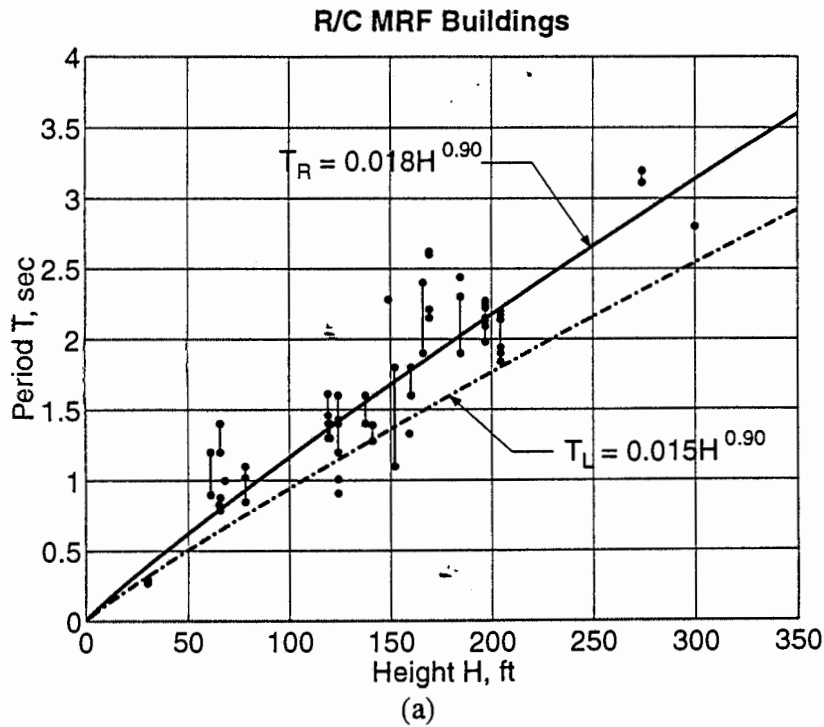


Figure 2: Regression analysis of measured period data for RC MRF buildings.

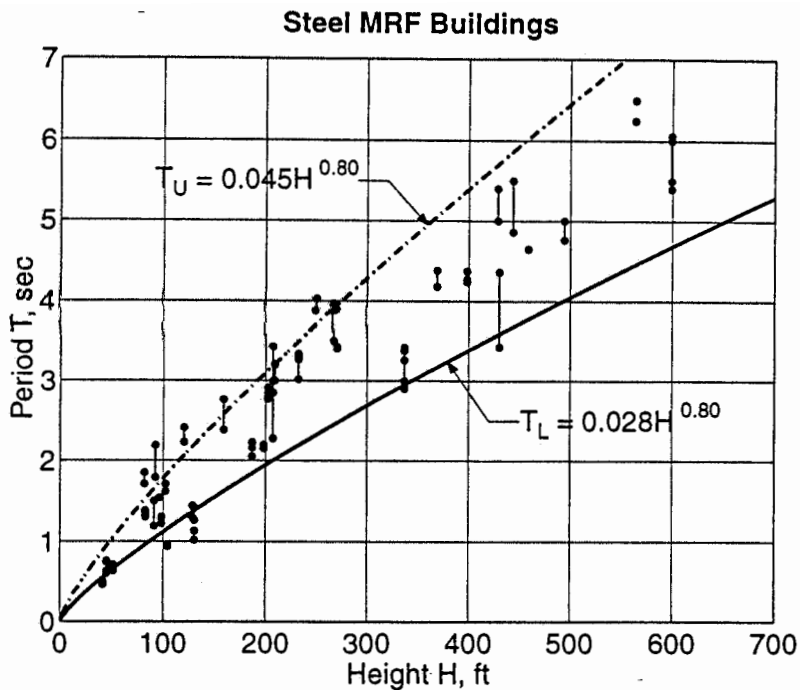


Figure 3: Recommended period formula and upper limit for fundamental period of steel MRF buildings.

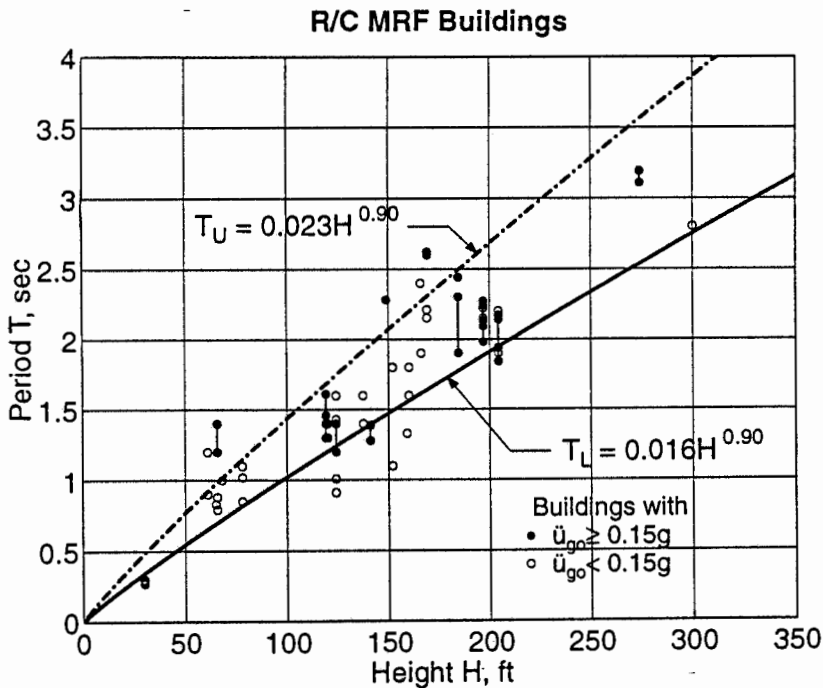


Figure 4: Recommended period formula and upper limit for fundamental period of RC MRF buildings.

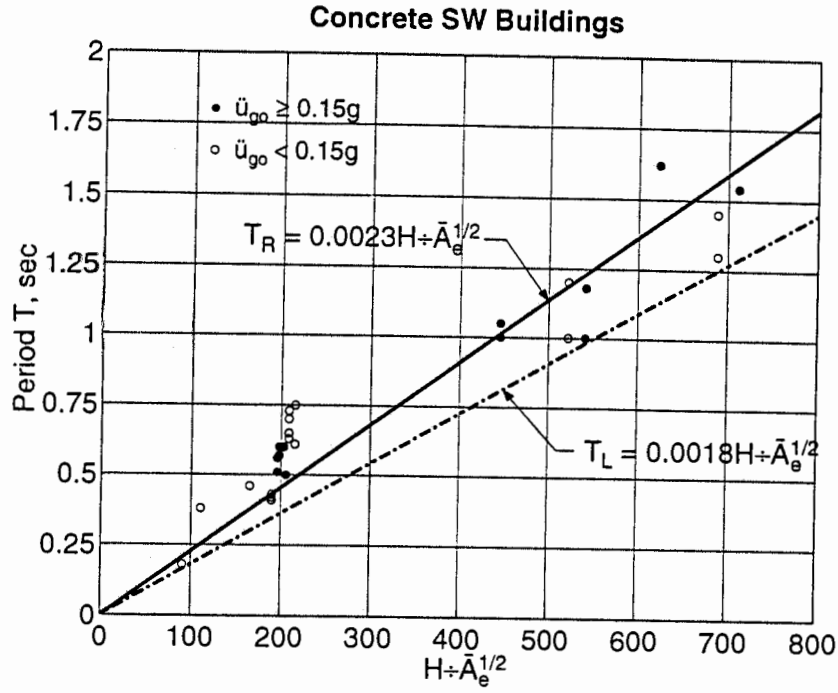


Figure 5: Regression analysis of measured period data for shear wall buildings.

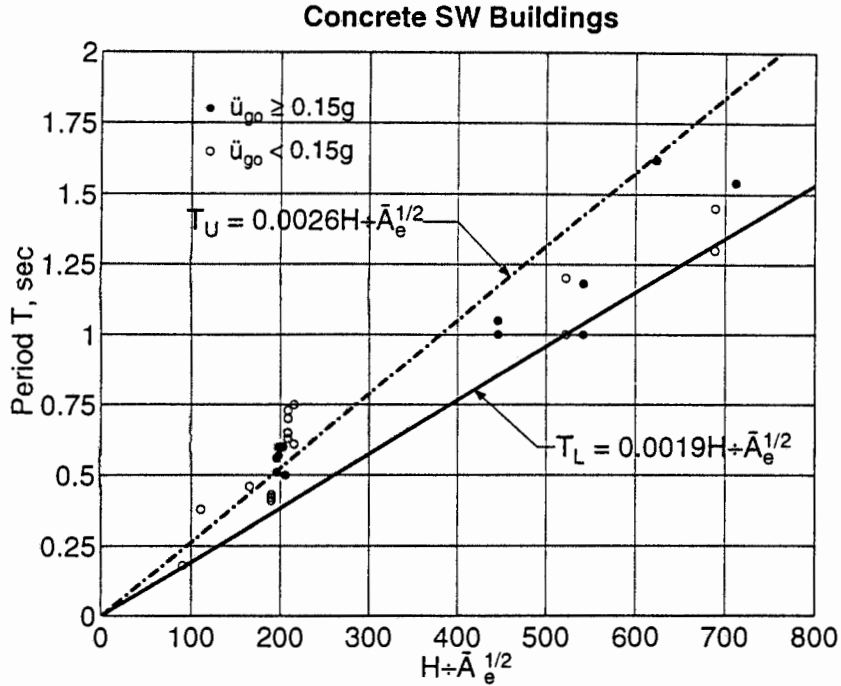


Figure 6: Recommended period formula and upper limit for fundamental period of shear wall buildings.

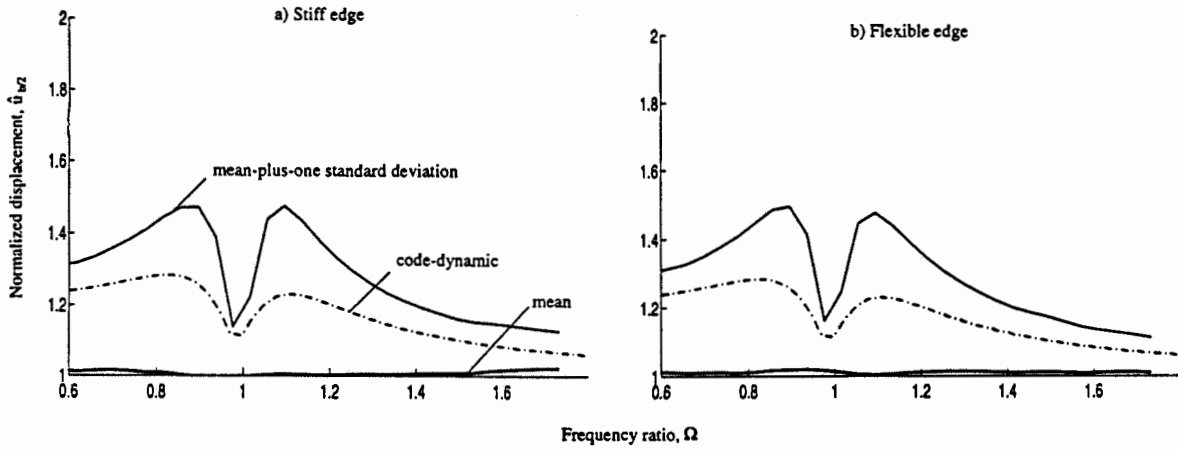


Figure 7: Comparison between  $\hat{u}_{b/2}$  computed from code-dynamic analysis and from statistical analysis of different sources of accidental torsion.

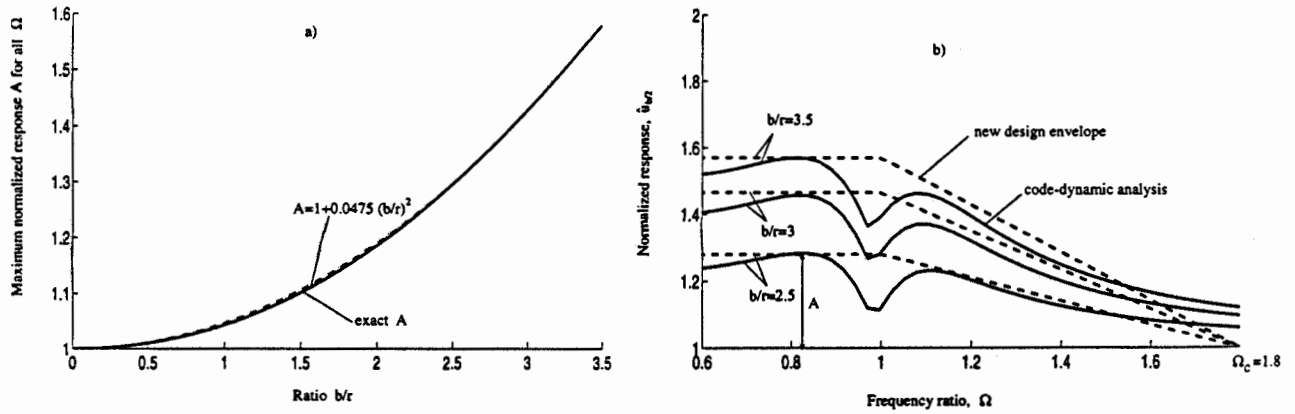


Figure 8: Design envelopes for normalized edge displacement  $\hat{u}_{b/2}$ : (a) variation of  $A$  as function of  $b/r$ ; and (b) design envelopes for  $b/r = 2.5, 3,$  and  $3.5$ .



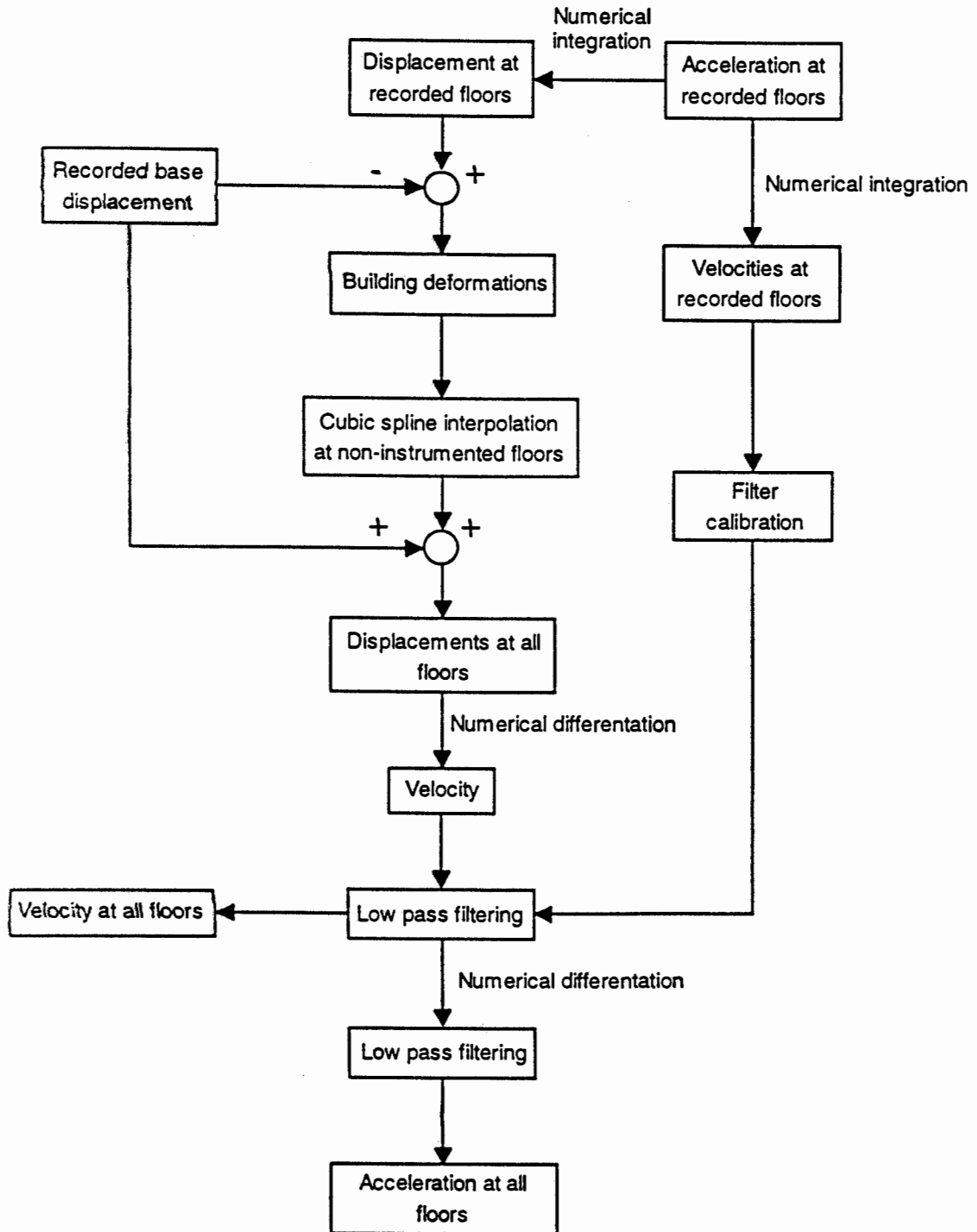


Figure 9: Heightwise interpolation of recorded floor motions of buildings.

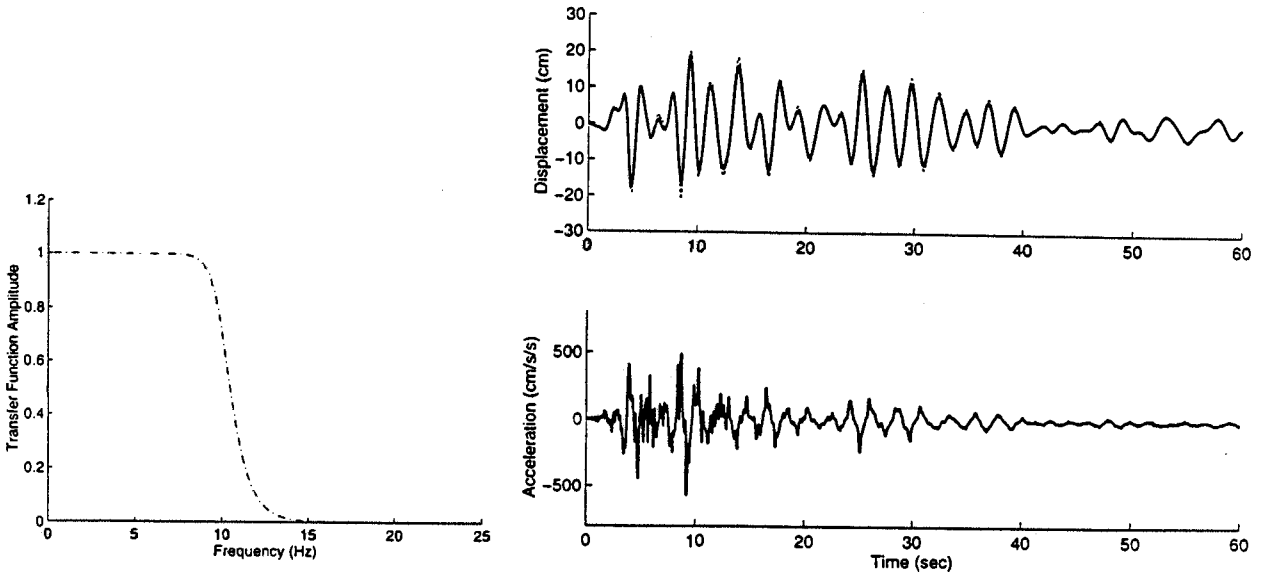


Figure 10: Example of heightwise interpolation of floor motions; recorded motions are shown by a solid curve and predicted motions by a dashed curve.

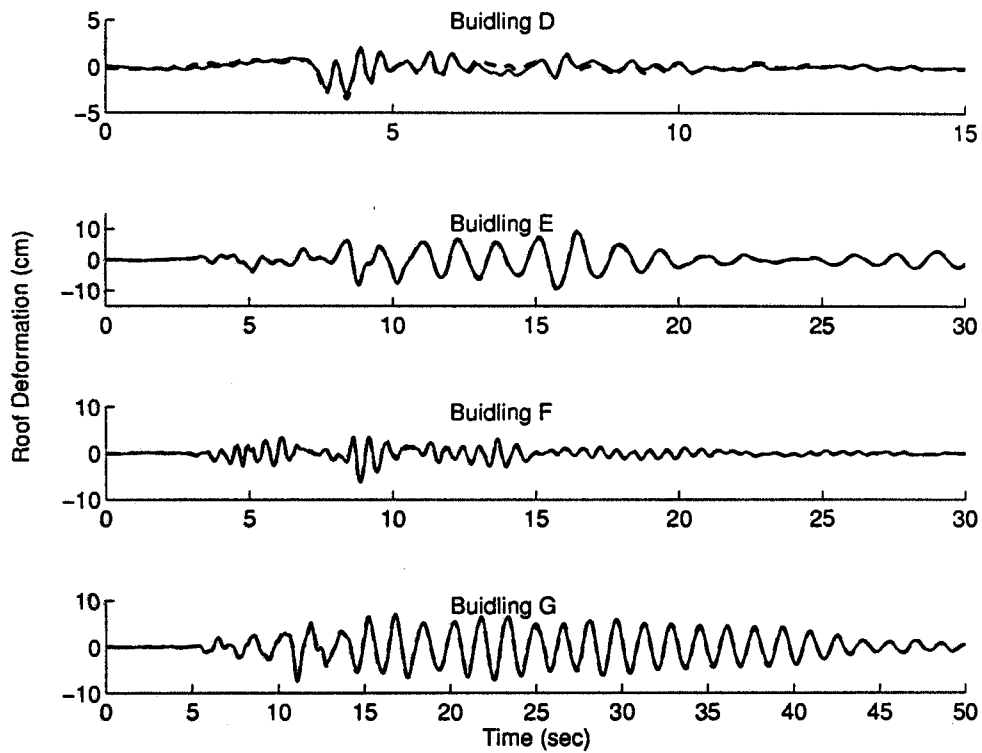


Figure 11: Accidental torsion effects in roof displacements of buildings D, E, F, and G.

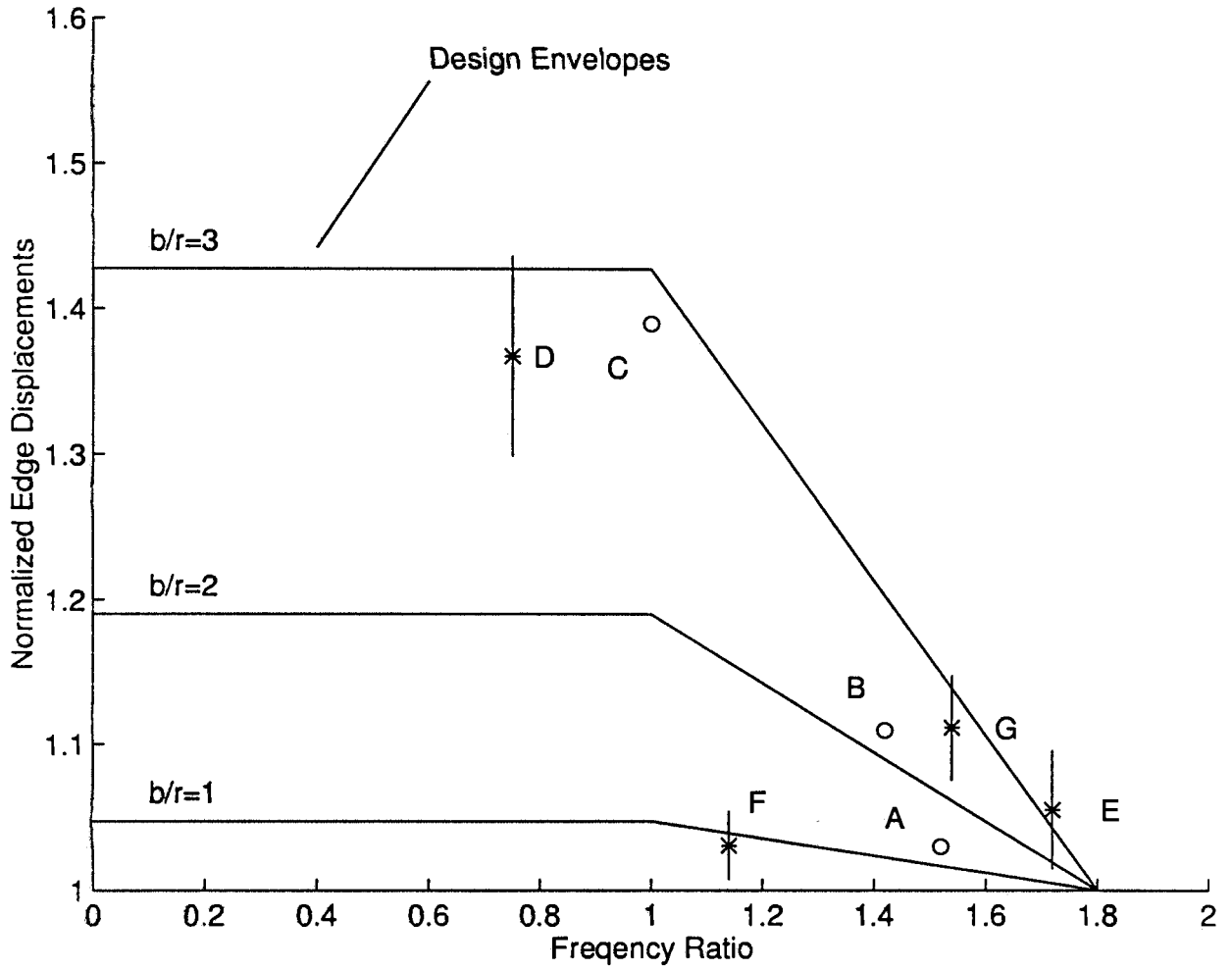


Figure 12: Comparison of design envelopes with “measured” increase in edge displacements of seven buildings due to accidental torsion.



TRINET "SHAKEMAPS": RAPID GENERATION OF PEAK GROUND MOTION  
AND INTENSITY MAPS FOR EARTHQUAKES IN SOUTHERN CALIFORNIA

David J. Wald

U.S. Geological Survey, Pasadena

V. Quitoriano, T. H. Heaton, H. Kanamori

Seismological Laboratory, Caltech, Pasadena

C. W. Scrivner

California Dept. of Conservation, Div. Mines and Geology, Sacramento

ABSTRACT

Rapid (3-5 minutes) generation of maps of ground motion shaking and intensity is accomplished with advances in real-time seismographic data acquisition combined with newly-developed relationships between recorded ground motion parameters and expected shaking intensity values. Estimation of shaking over the entire regional extent of southern California is accomplished by spatial interpolation of the measured ground motions with geologically-based, frequency and amplitude-dependent site corrections. Production of the maps is automatic, triggered by any significant earthquake in southern California. Maps are now made available within several minutes of the earthquake for public and scientific consumption via the World-Wide-Web; they will be made available with dedicated communications for emergency response agencies and critical users.

INTRODUCTION

The most common information available immediately following a damaging earthquake is its magnitude and the epicentral location. However, the damage pattern is not a simple function of these two parameters alone, and more detailed information must be provided to properly ascertain the situation. For example, for the February 9, 1971 earthquake, the northern San Fernando valley was the region with the most damage, even though it was more than 15 km from the epicenter. Likewise, areas strongly affected by the Loma Prieta and Northridge, California, earthquakes that were either distant from the epicentral region or out of the immediate media limelight, were not fully appreciated until long after the initial reports of damage. Most recently, the full extent of damage from the 1995 Kobe, Japan, earthquake was not recognized by the central government in Tokyo until many hours later (e.g., Yamakawa, 1997), delaying rescue and recovery efforts.

As part of the research and development efforts of the TriNet (California Institute of Technology, the California Division of Mines and Geology, and the U. S. Geological Survey) project (see Mori *et al.*, 1998), we have been creating ShakeMap<sup>TM</sup> for earthquakes (magnitude greater than 3.0) in southern California for the last year (Wald *et al.*, 1997). We currently generate separate maps of the spatial distribution of peak ground motions (acceleration and velocity) as well as a map of instrumentally-derived seismic intensities. These maps provide a rapid portrayal of the extent of potentially damaging shaking following an earthquake and can be used for emergency response, loss estimation, and for public information through the media. Generation of the maps is fully automatic, triggered by any significant earthquake in southern California and made available within

several minutes of the earthquake for public and scientific consumption via the World-Wide-Web; they will be made available with more reliable, dedicated communications for emergency response agencies in the near-future. For example, maps of shaking intensity can be combined with databases of inventories of buildings and lifelines to rapidly produce maps of estimated damage (e.g., Eguchi *et al.*, 1997).

Such maps have traditionally been difficult to produce rapidly and reliably due to limitations of seismic network instrumentation and data telemetry. In addition, adequate relationships between recorded ground motions and damage intensities have only recently been developed, for example, the JMA seismic intensity scale in Japan (Japan Meteorological Agency, 1996). However, with recent advances in digital communication and computation, it is now technically feasible to develop systems to display ground motions in an informative manner almost instantly. A detailed description of the shaking over the entire regional extent of southern California requires interpolation of the measured ground motions. In addition, simple geologically-based, frequency- and amplitude-dependent site corrections factors, currently under development, provide a useful first-order correction for local amplification in areas that are not instrumented. In this report we present ongoing efforts addressing the issues pertinent to rapid ground-motion map-making.

### PEAK GROUND MOTION MAPS

The current TriNet seismic station distribution in southern California is shown in Figure 1. The USGS/Caltech stations (triangles) are acquired in real time using a variety of digital telemetry methods (see Mori *et al.*, 1998, for more details). The California Division of Mines and Geology, CDMG, stations (square) are near-real time, utilizing an automated dial-up procedure developed for use with telephone communications (see Shakal *et al.*, 1996, 1998). As of May, 1998, there are 80 USGS/Caltech real-time stations online and nearly 100 CDMG dialup stations; in all there will be approximately 670 TriNet strong-motion stations in the next 3 years. The generation of ShakeMaps is triggered automatically by the event associator for the Southern California Seismic Network (SCSN), operated by the USGS and Caltech. Within the first minute following the shaking, ground motion parameters are available from the USGS/Caltech component of the network and within several minutes most of the important near-source CDMG stations contribute. A more complete CDMG contribution is available approximately within the first half hour. Initial maps are made with just the real-time component of TriNet, but they are updated automatically as more data is acquired. Parametric data from the stations includes PGA and PGV as well as spectral amplitudes (at 3.0 Hz, 1 Hz, and 0.3 Hz).

Shaking maps are prepared by contouring shaking information estimated for every point in a 3-km square grid uniformly sampled throughout southern California. If there were stations at each of the 11,000 grid points, then the creation of shaking maps would be relatively simple. Of course stations are not available for all of these grid points, and in many cases grid points may be tens of kilometers from the nearest reporting station. The overall mapping philosophy is to combine information from individual stations, geology (e.g., soil versus rock), and the distance to the centroid to create the best composite map. The procedure must produce reasonable estimates at grid points located far from available data, while preserving the detailed shaking information available for regions where there are nearby stations. That is, we want the procedure to return the actual data values for stations where there is data.

To determine the strong motion "centroid" (Kanamori, 1993), we apply empirically-derived station site corrections and then fit the observed ground motions to find the best equivalent point-source latitude, longitude, and magnitude. We scan the parameter space to determine the global minimum solution for location and magnitude, and then refine the solution using the method of

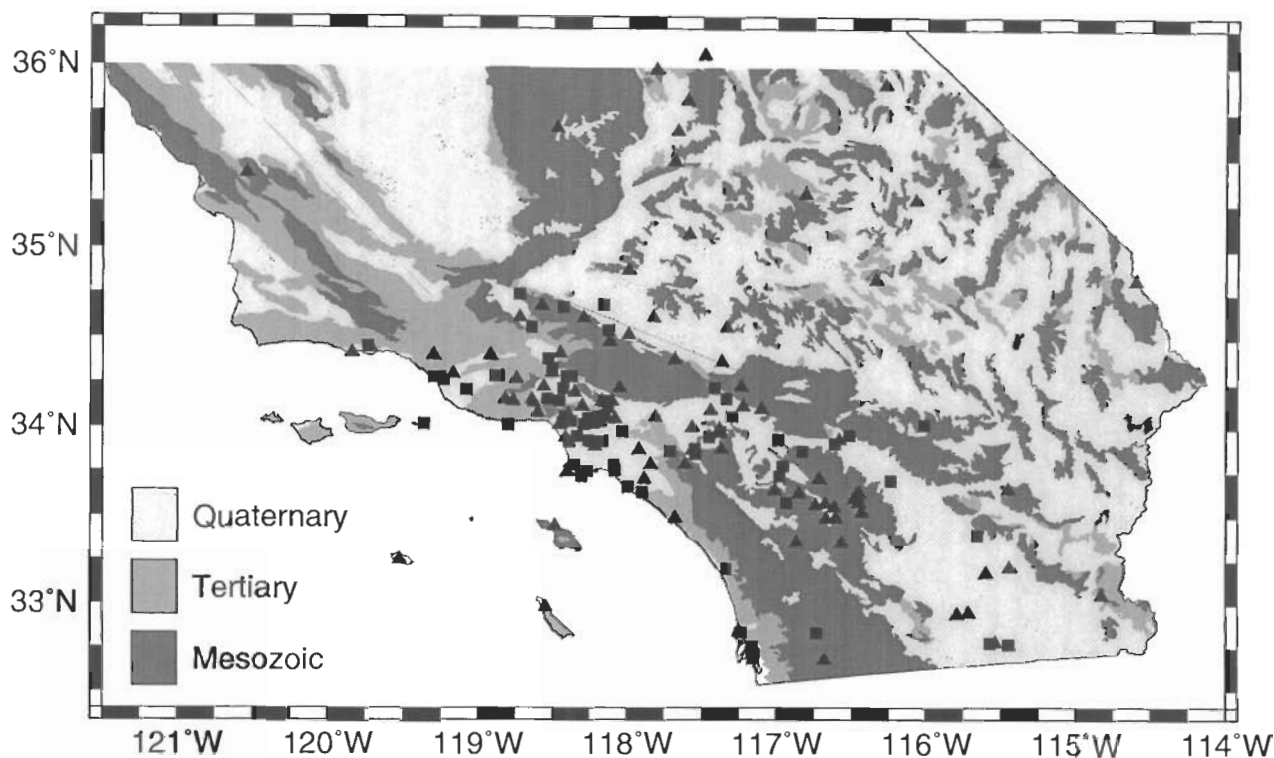


Figure 1: Map of southern California showing current TriNet station distribution. CDMG stations are shown as squares and USGS/Caltech stations are depicted with triangles. Shading indicates the Quaternary, Tertiary, and Mesozoic (QTM) geologic unit designations of Park and Ellrick (1998) as shown in the legend.

least squares. As the real-time TriNet station density increases, the importance of the centroid will diminish but currently it is imperative for the robust generation of ground motion maps. Fortunately, as planned, TriNet stations are more concentrated in heavily populated regions, so the most reliable recovery of the shaking distribution should be where potential losses and the need for concerted emergency response efforts could be the greatest.

We begin by creating a coarse “rock site” grid (30-km spacing); “phantom” ground motions are assigned to each point on the coarse grid using the Joyner and Boore (1981) distance attenuation relationship for “rock sites” and magnitude of the centroid and its distance to each grid point. These “phantom” ground motion estimates are used to assign shaking values to those points for which there are no nearby TriNet stations (within 30 km). Shaking data from reporting TriNet stations are corrected to “rock site” conditions using a procedure described later and this corrected data is then placed on the coarse “rock site” grid map. The coarse “rock site” grid is next interpolated to a fine “rock site” grid (3-km spacing) which is then corrected for geology. However, shaking at individual stations in this final grid map is the same as that which was actually recorded at the site.

In Figure 2 we show an example of a peak acceleration map for a magnitude 4.4 earthquake near Wrightwood, California (northeast of Los Angeles) which occurred on August 20, 1998. No site corrections have been applied to these maps; however, attenuation with distance and stability to the contour pattern has been assured by the ground motions assigned to the “phantom” stations

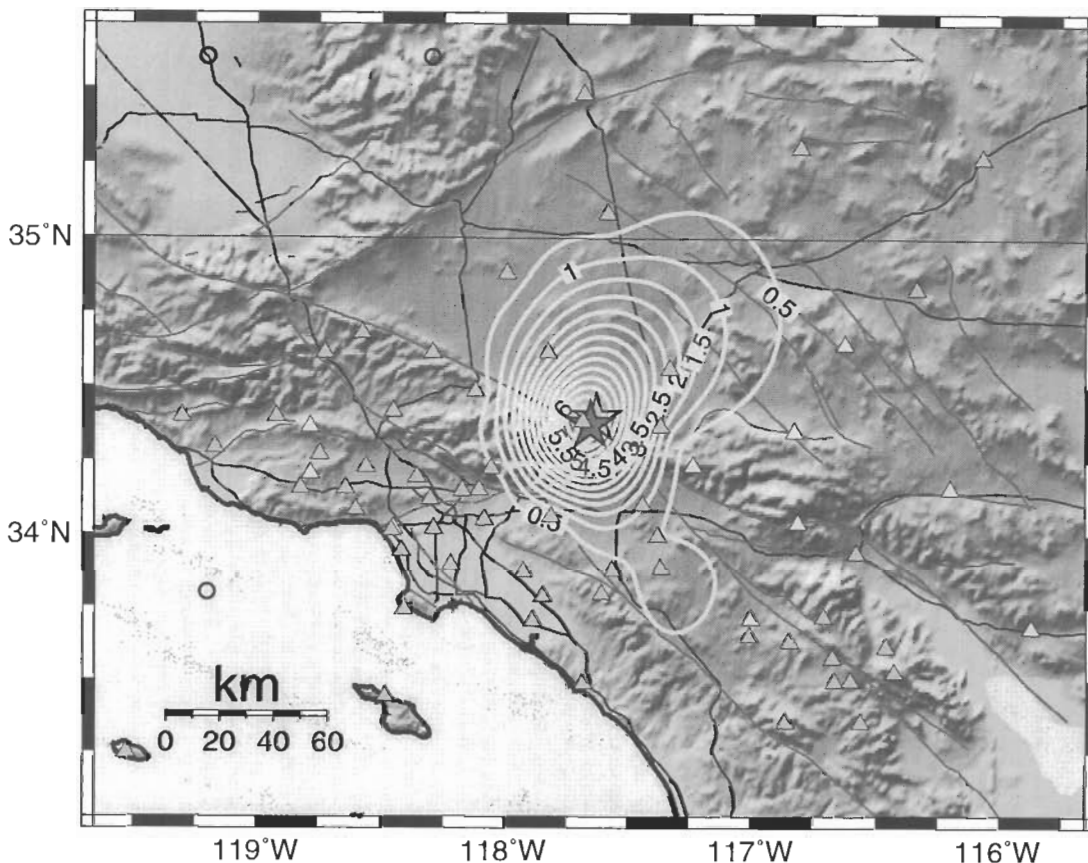


Figure 2: Shaded relief map showing peak accelerations for the August 20, 1998 magnitude 4.4 Wrightwood earthquake with contours of acceleration in percent “g”. Lightly shaded triangles represent USGS/Caltech stations; darker shaded triangles represent CDMG stations. Dark lines are freeways and lightly-shaded lines are mapped faults. The shaded star shows the epicenter and the open star represents the strong motion “centroid”. Open circles represent “phantom” grid stations (see text for details).

based on the strong motion centroid (M4.4 at location of the open star in Fig. 2) Since this area is fairly well instrumented, there are few “phantom” stations, and the only ones necessary within the map dimensions are depicted (as a open circles) near the eastern edge of the map and in the ocean. All other predicted values in this case are superseded by recorded amplitudes. Out at greater distances, however, more “phantom” stations do contribute and they insure that the contour maps remain well-behaved and bounded at the edges.

### SITE CORRECTIONS

In order to interpolate from ground motions recordings on a fairly coarse, non-uniformly spaced network of stations to maps showing continuous functions of ground motion, basic site corrections are useful. For example, direct interpolation between two rock sites surrounding a basin would inadequately represent the true motion within the basin. Hence, we interpolate the data, plus the coarse “grid” stations, onto a finely-spaced (3 km) uniform grid over the entire region. The finely-



interpolated grid has been predefined and so we can preassign a geologically-based site classification to each location.

The amplification correction we use is based on the Quaternary, Tertiary, Mesozoic (“QTM”) geological classification of Park and Ellrick (1998). These categories can be considered to represent soil, soft rock, and hard rock, respectively, and hence they provide a very simple but effective way to assign amplification on a regional scale. Based on the average velocities assigned to the QTM categories (Park and Ellrick, 1998), we applied the frequency-and amplitude-dependent amplification factors determined by Borchardt (1994). Table 1 shows the site amplifications factor for the QTM categories at periods of both 0.3 and 1.0 seconds for each of four input ground acceleration levels. At .3 sec, amplification for the soil (Quaternary Alluvium) sites is nearly a factor of 1.5 at low input motions and it decreases to slightly over 1.0 for strong motions; Tertiary and Mesozoic rock units have a less pronounced amplitude dependency (see Table 1).

Table 1: Site Amplification Factors

| Period (sec) | Input Rock Peak Ground Acceleration (gals) |             |              |           |
|--------------|--|-------------|--------------|-----------|
|              | <50 gals                                   | 50-100 gals | 100-200 gals | >200 gals |
| Mesozoic:    |  |             |              |           |
| 0.3          | 1.00                                       | 1.00        | 1.00         | 1.00      |
| 1.0          | 1.00                                       | 1.00        | 1.00         | 1.00      |
| Tertiary:    |  |             |              |           |
| 0.3          | 1.14                                       | 1.10        | 1.04         | 0.98      |
| 1.0          | 1.27                                       | 1.25        | 1.22         | 1.18      |
| Quaternary:  |  |             |              |           |
| 0.3          | 1.39                                       | 1.15        | 1.06         | 0.97      |
| 1.0          | 1.45                                       | 1.41        | 1.35         | 1.29      |

We correct the peak acceleration (PGA) amplitude with the 3 Hz amplification factors while the peak velocity (PGV) values are corrected with the 1 Hz factors. The site correction procedure is applied so that the original data values are used to construct the final contours. We then contour the interpolated, site-corrected peak ground acceleration and peak ground velocity values.

Since site amplification factors are considerable at low levels of shaking, applying the site corrections to small earthquakes shows quite noticeable effects. Figure 3 shows a map of the peak accelerations for a magnitude 3.9 earthquake the which occurred in the Imperial Valley on June 26, 1998. The overall pattern of shaking is not well-constrained by the data, in fact this event occurred very near the Mexican border and the edge of the TriNet station coverage. However, a relatively simple pattern of shaking emerges on the contour map. The strong motion centroid (open star) just southeast of the epicenter, is not well constrained in part due to the lack of data to south. Based on this data alone, there is some indication that shaking in the soft-sediment valley floor to the east was greater than to the west, in the mountains. Figure 4 shows the effect of our site correction on the same data set. Note that the shape of the valleys and mountains are clearly delineated, which was not the case with the limited data set alone.

Although only relatively small events have been recorded during the year or so that we have been making “ShakeMap”, we can apply the procedure in retrospect to larger earthquakes. In Figure 5 we show a map of the recorded peak velocity distribution (contoured in cm/sec) for the 1994 magnitude 6.7 Northridge earthquake to illustrate the nature of the information provided by

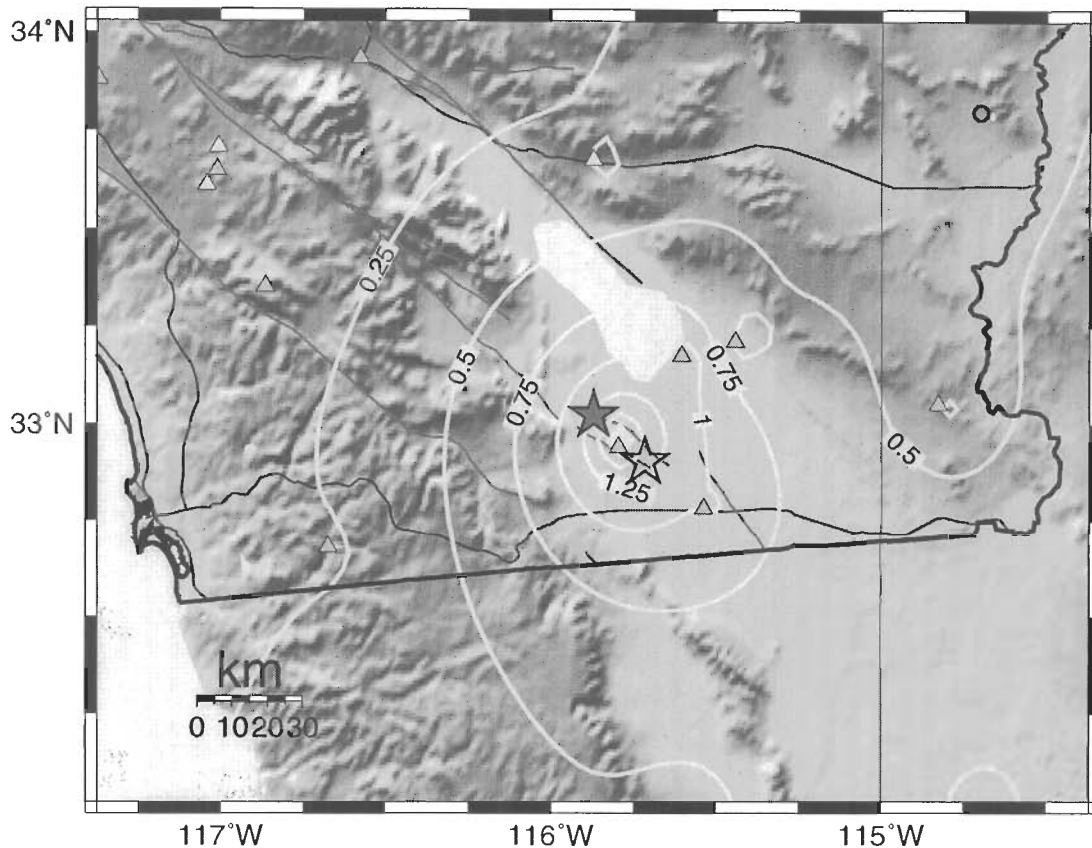


Figure 3: Shaded relief map showing peak acceleration contours for the June 26, 1998 magnitude 3.9 earthquake near Westmorland, California. Contours are in units %g. No site corrections have been applied. Triangles represent strong-motion stations. The shaded star shows the epicenter and the open star represents the strong motion “centroid”.

ShakeMap and the effects of applying the site correction for a larger earthquake. In this particular example, the ground motion data is from existing analog networks (CDMG, USGS, University of Southern California, Southern California Edison, the Los Angeles Department of Water and Power), not the current TriNet digital instrument deployment.

Typically, for moderate-to-large events, the pattern of peak ground velocity reflects the pattern of the earthquake faulting geometry, with largest amplitudes in the near-source region, and in the direction of rupture directivity (Fig. 5). Differences between rock and soil sites are apparent, but the overall pattern is more a reflection of the source proximity and rupture process. Nonetheless, the site effects are important. Based on the tabulated amplification factors (Table 1), we expect that for larger events which are dominated by strong shaking, the effect of site corrections, particularly at high frequencies, are less significant than for the lower shaking levels associated with smaller earthquakes.

The site-corrected peak velocity map for the Northridge earthquake is shown in Figure 6. The differences between the ground velocities within the valleys and surrounding mountains becomes more evident once the site corrections are applied. For example, the overall level of the ground velocities in the San Fernando valley (the “Northridge” label) is higher on the site corrected maps.

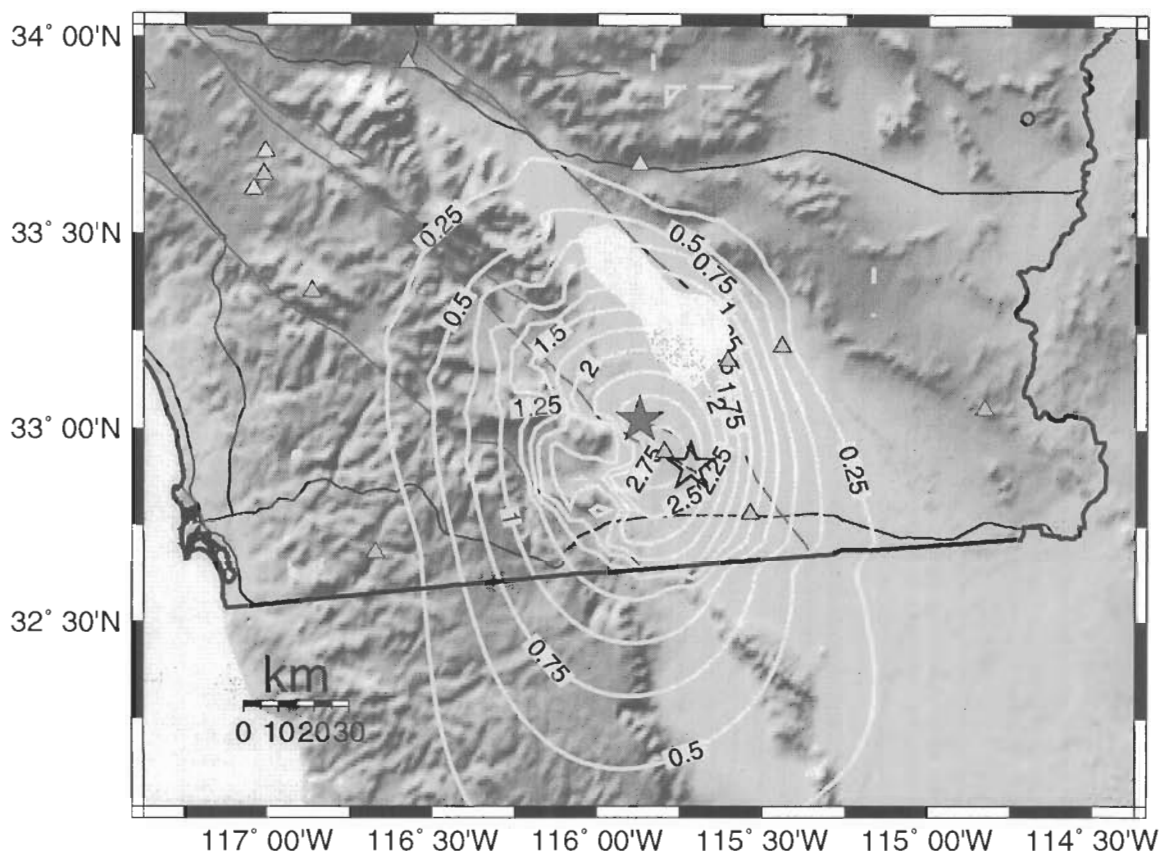


Figure 4: Shaded relief map showing site-corrected peak acceleration contours for the June 26, 1998 magnitude 3.9 earthquake near Westmorland, California. Contours are in units %g. Triangles represent strong-motion stations. The shaded star shows the epicenter and the open star represents the strong motion "centroid".

In addition, originally smooth contours which simply connected adjacent but distant stations, become more complex when intervening geologically-based site corrections play a role in determining the interpolated amplitudes.

#### INSTRUMENTAL SEISMIC INTENSITY MAPS

From the PGA and PGV maps, we would like to estimate the ground motion intensity as a simple visual and intuitive way to represent the overall nature of the shaking. Seismic intensity has been traditionally used worldwide as a method for quantifying the shaking pattern and the extent of damage for earthquakes. Though derived prior to the advent of today's modern seismometric instrumentation, seismic intensity nonetheless provides a useful means of describing, in a simplified fashion, the complexity of these same recordings. Such simplification is necessary to grasp the overall extent of the situation for those unfamiliar with the subtleties associated with relating the spatially complex ground motions, which vary as a function of frequency, duration and amplitude, to potential damage.

That is not to say that instrumental intensity alone is sufficient for loss estimation, and in fact, spectral response provides a better physical basis for such analyses. ShakeMap will also provide

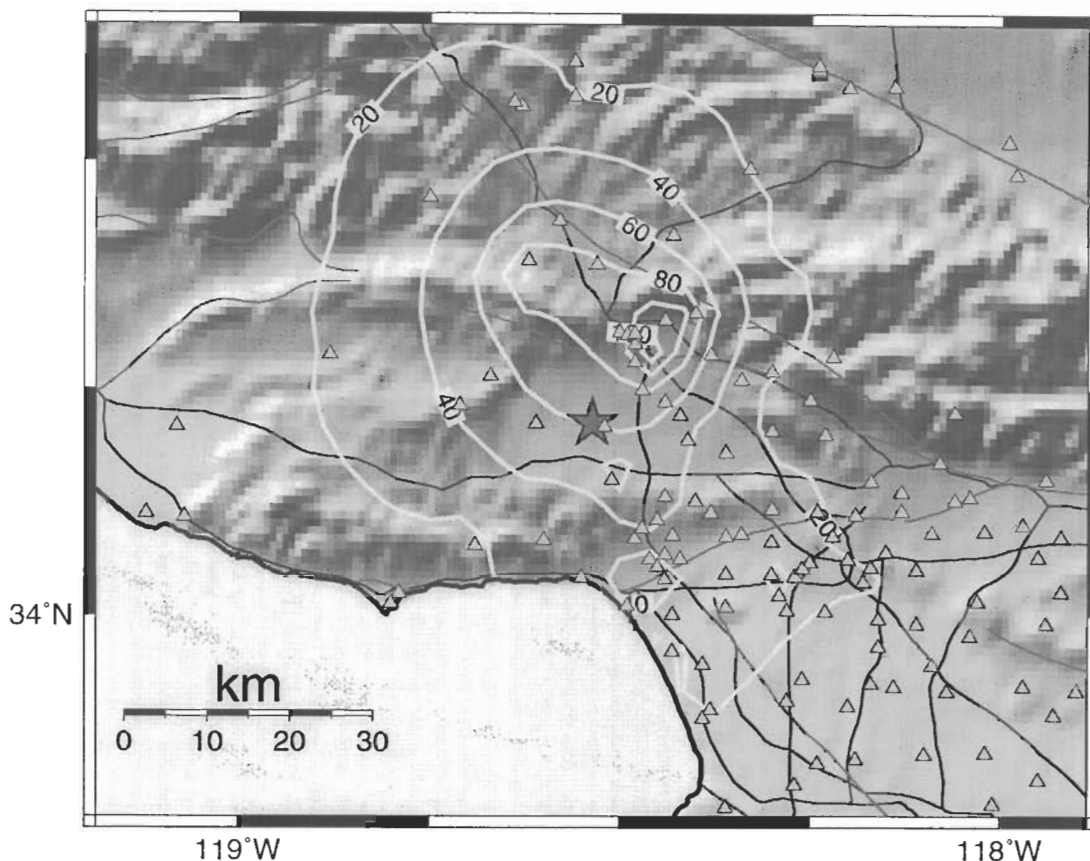


Figure 5: Shaded relief map showing recorded peak velocity contours for the magnitude 6.7 1994 Northridge earthquake. Contours of velocity are in cm/sec. The shaded star shows the epicenter and the open star represents the strong motion “centroid”. No site corrections have been applied.

spectral response maps (at 0.3, 1.0, and 3.0 sec), but for the overwhelming majority of users, we feel the intensity map will be more intuitive. Naturally, distilling the complex relationship between spatially highly variable strong ground motions and the potential damage to a wide variety of building construction types in regions of variable building exposure, into a simple-to-use map requires approximation, as does simplifying any complex scientific issue for general understanding. But it is desirable to convey the information in a generally acceptable form.

We have recently developed regression relationships between Modified Mercalli intensity ( $I_{mm}$ , Wood and Neumann, 1931, later revised by Richter, 1958) versus PGA and PGV by comparing the peak ground motions to observed intensities for eight significant California earthquakes. The eight events, the 1971 (M6.7) San Fernando, the 1979 (M6.6) Imperial Valley, the 1986 (M5.9) North Palm Springs, the 1987 (M5.9) Whittier Narrows, the 1989 (M6.9) Loma Prieta, the 1991 (M5.8) Sierra Madre, the 1992 (M7.3) Landers, and the 1994 (M6.7) Northridge earthquakes, were used since they were well recorded by regional strong motion networks in addition to having numerous intensity observations (Dewey, written communication, 1997).

Given these events, there is a reasonable overlap between recorded ground motions and the intensity measurements. In earlier studies (e.g., Trifunac and Brady, 1975), similar relations were derived based on taking the intensity value off a map at the location of the strong motion station

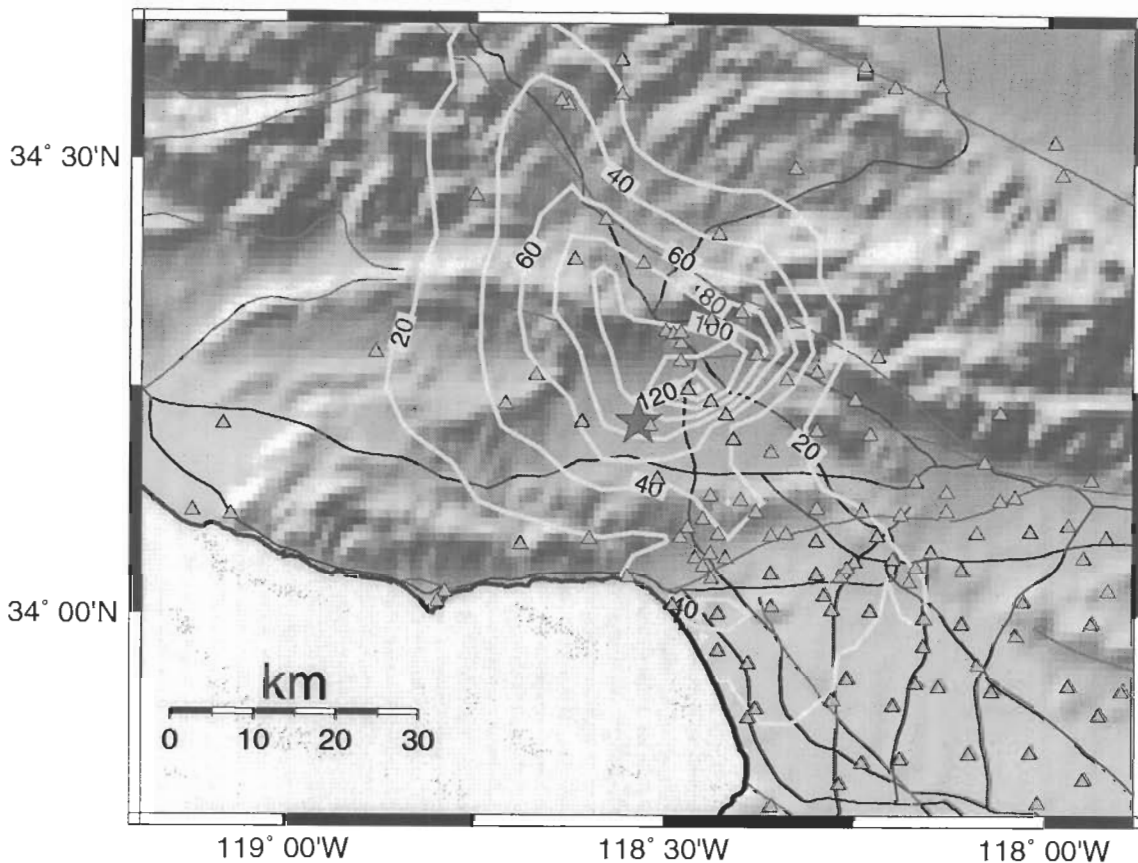


Figure 6: Shaded relief map showing recorded peak velocities, corrected for site amplification, for the magnitude 6.7 1994 Northridge earthquake. Velocity are units of cm/sec. The shaded star shows the epicenter.

when no observation was available near the strong motion site. Since the  $I_{mm}$  maps are typically simplified representations of a spatially variable field, the true  $I_{mm}$  value at the strong motion recording site is not usually known; there is no guarantee that the  $I_{mm}$  at the strong motion station location corresponds with the value  $I_{mm}$  value on the map. Here, we chose to correlate only those values where the strong motion station is near (within 3 km) a  $I_{mm}$  observation. For each station, the nearest intensity observation is chosen, if no intensity measurement is within 3 km then the strong motion data at that site is not used for correlation purposes. Although ground motions can vary significantly over this distance, requiring more nearly co-located observations reduces the available pairing of data. Since the earlier studies, there is now substantially more strong motion data available, particularly at larger amplitudes, for such a comparison.

Earlier comparisons of peak ground motions and intensities were also based primarily on regressions of intensity against peak acceleration, or in a few cases, against peak velocity. We differ from previous studies in that here we chose to use both peak acceleration and velocity jointly, recognizing the amplitude- and frequency-dependent nature of the intensity scale as manifested by both felt shaking descriptions and actual damage. Figure 7 shows the relationship of  $I_{mm}$  values and PGA for the individual events analyzed; Figure 8 shows the same for PGV. Figures 9 and 10 show the regressions of  $I_{mm}$  verses and PGA and PGV, respectively, for the data from all eight

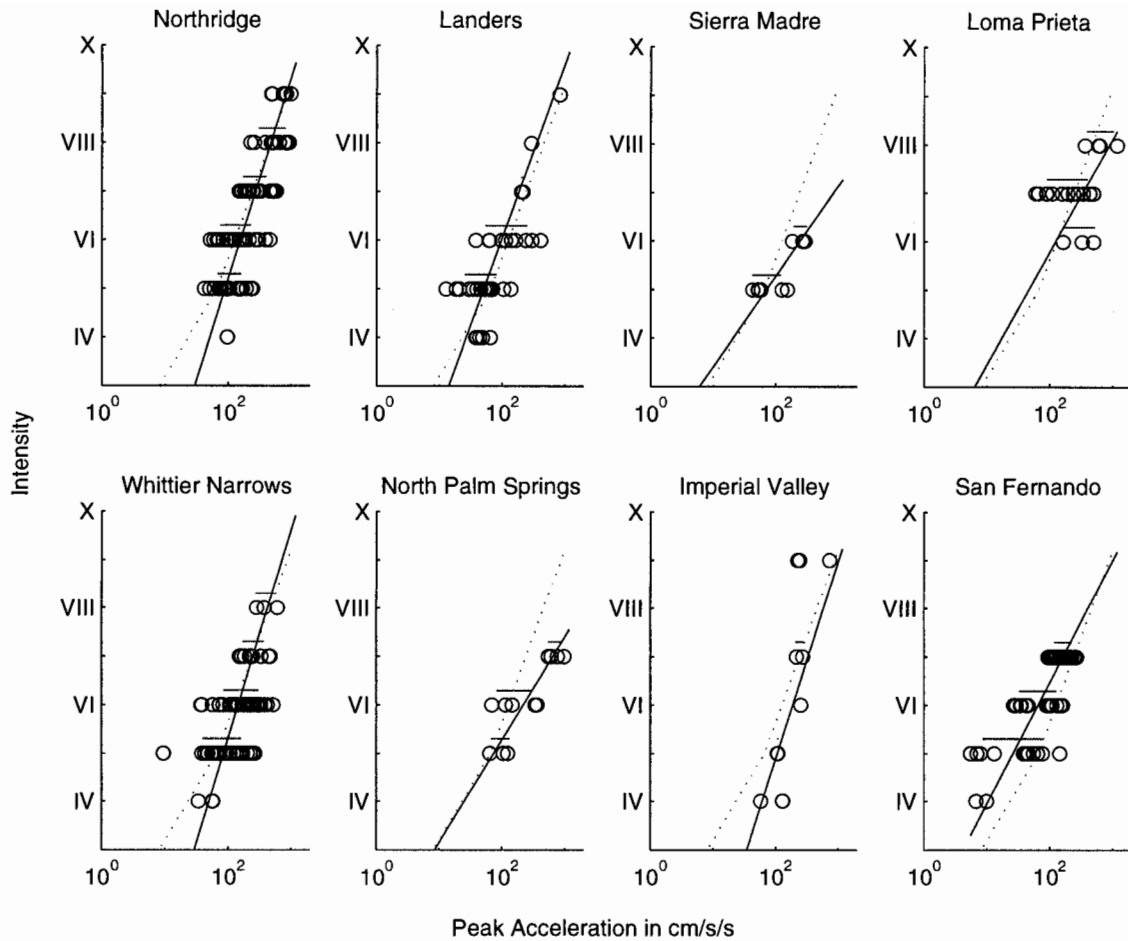


Figure 7: Modified Mercalli intensity plotted against peak ground acceleration for individual earthquakes. Circles denote data, horizontal lines above data depict the range of the geometric mean, plus and minus one standard deviation. Solid line is the regression for individual events; short-dashed line is regression for events combined.

earthquakes combined.

Requiring that the ground motion recording sites and  $I_{mm}$  observation points have the same QTM designation, in addition to the maximum distance requirement, did not significantly improve scatter shown in Figures 9 and 10. However, this may be a limitation of the map scale used in the geology classification (1:750,000), and a more detailed association of the geology at the strong motion sites and intensity observations may be useful. Naturally, though, the association of an instrumental, point measurement of ground motion with an intensity observation defined as an average over a designated areal extent would be expected to show substantial scatter, particularly if the area does not even contain the point measurement. This is a fundamental limitation originating from the definition of seismic intensity which requires an (unspecified) area be assigned an given intensity value based on the representative or average level of damage in the specified region. Any single point observation in that area is not sufficient to satisfy such a definition.

While there is no fundamental reason to expect a simple relationship between Modified Mercalli

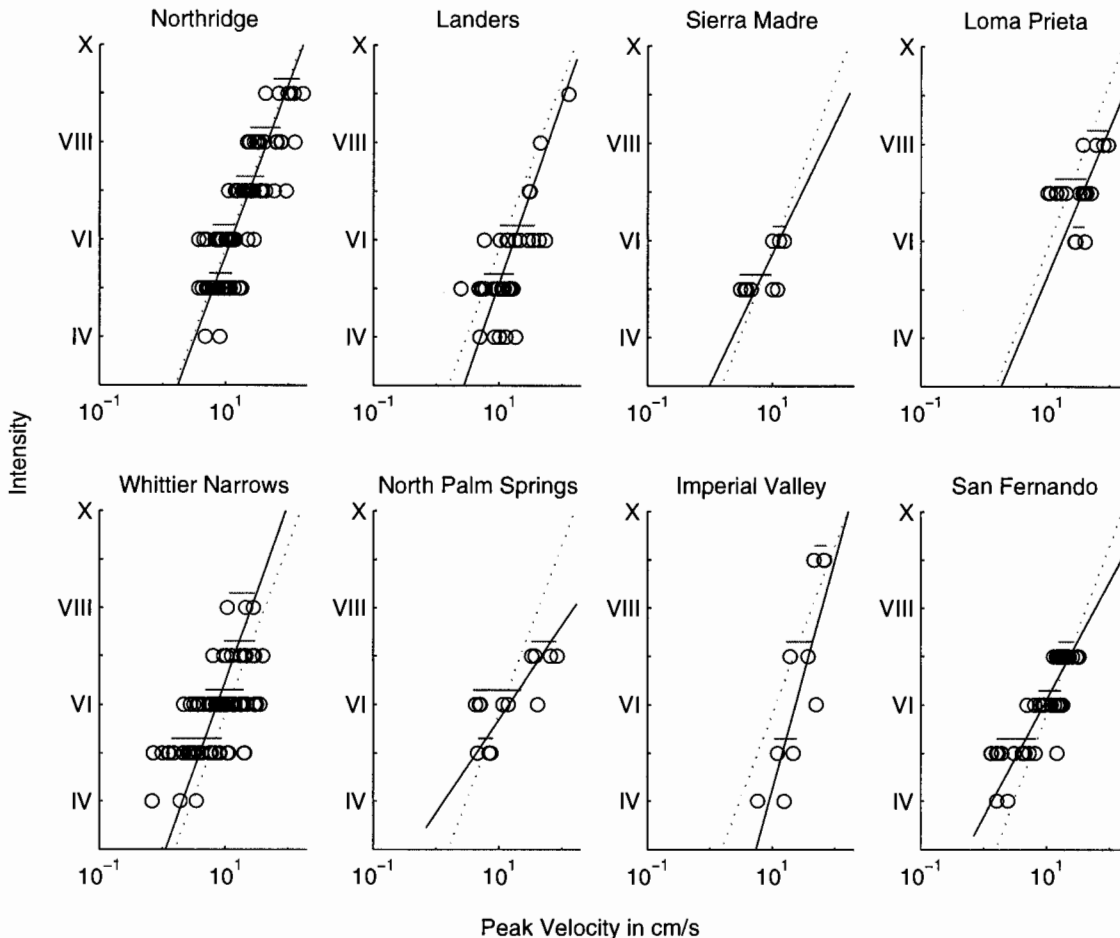


Figure 8: Modified Mercalli intensity plotted against peak ground velocity for individual earthquakes. Circles denote data, horizontal lines above data depict the range of the geometric mean, plus and minus one standard deviation. Solid line is the regression for individual events; short-dashed line is regression for events combined.

intensity and recorded ground motion parameters, over a range of accelerations and velocities a simple power-law representation is adequate and convenient. For the limited range of Modified Mercalli intensities ( $I_{mm}$ ), we find that for peak acceleration (PGA) with  $V \leq I_{mm} \leq VIII$ ,

$$I_{mm} = 3.56 \log(PGA) - 1.48 \tag{1}$$

and for peak velocity (PGV) with  $V \leq I_{mm} \leq IX$ ,

$$I_{mm} = 3.48 \log(PGV) + 2.32 \tag{2}$$

Here the regressions are made on the geometric mean of the peak ground motion values for a given intensity value. For acceleration,  $I_{mm}$  IX is not used in the regression since the peak acceleration values appear to be saturated, and as such a simple power-law relation will not suffice. Likewise at  $I_{mm}$  IV, peak accelerations may be biased high due to lack of digitization of data from

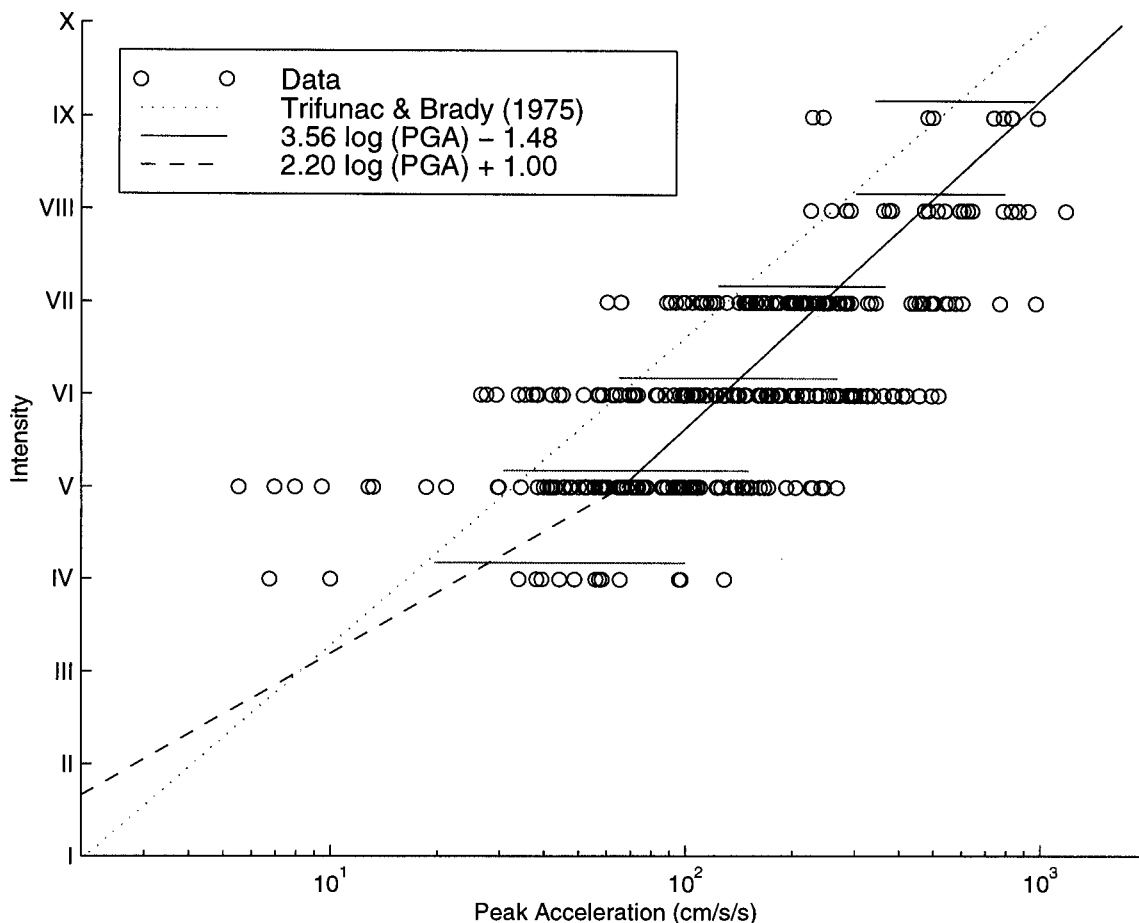


Figure 9: Modified Mercalli intensity plotted against peak ground acceleration for all events combined. Circles denote data; horizontal lines above data depict the range of the geometric mean, plus and minus one standard deviation. Solid line is regression from this study; short-dashed line is that of Trifunac and Brady (1975).

station with lower values and so they are not used in the regression. For  $I_{mm} \leq IV$ , peak velocities do not continue decreasing, suggesting perhaps not only the above-mentioned bias, but also a higher noise level (likely introduced in the integration of digitized recordings) may be controlling the peak values; hence, those values are not used in the regression.

Since we are defining intensity at lower values by the peak acceleration value, and our current collection of data from historical earthquakes does not provide constraints for lower intensity, we have imposed the following relationship between PGA and  $I_{mm}$ :

$$I_{mm} = 2.20 \log(PGA) + 1.00 \tag{3}$$

This basis for the above relationship comes from correlation of TriNet peak ground motions recordings for recent magnitude 3.5 to 5.0 earthquakes with intensities derived from voluntary response from Internet users (Quitoriano *et al.*, 1998) for the same events. We determined that the boundary between “not felt” and “felt” ( $I_{mm}$  I and II, respectively) regions corresponds to



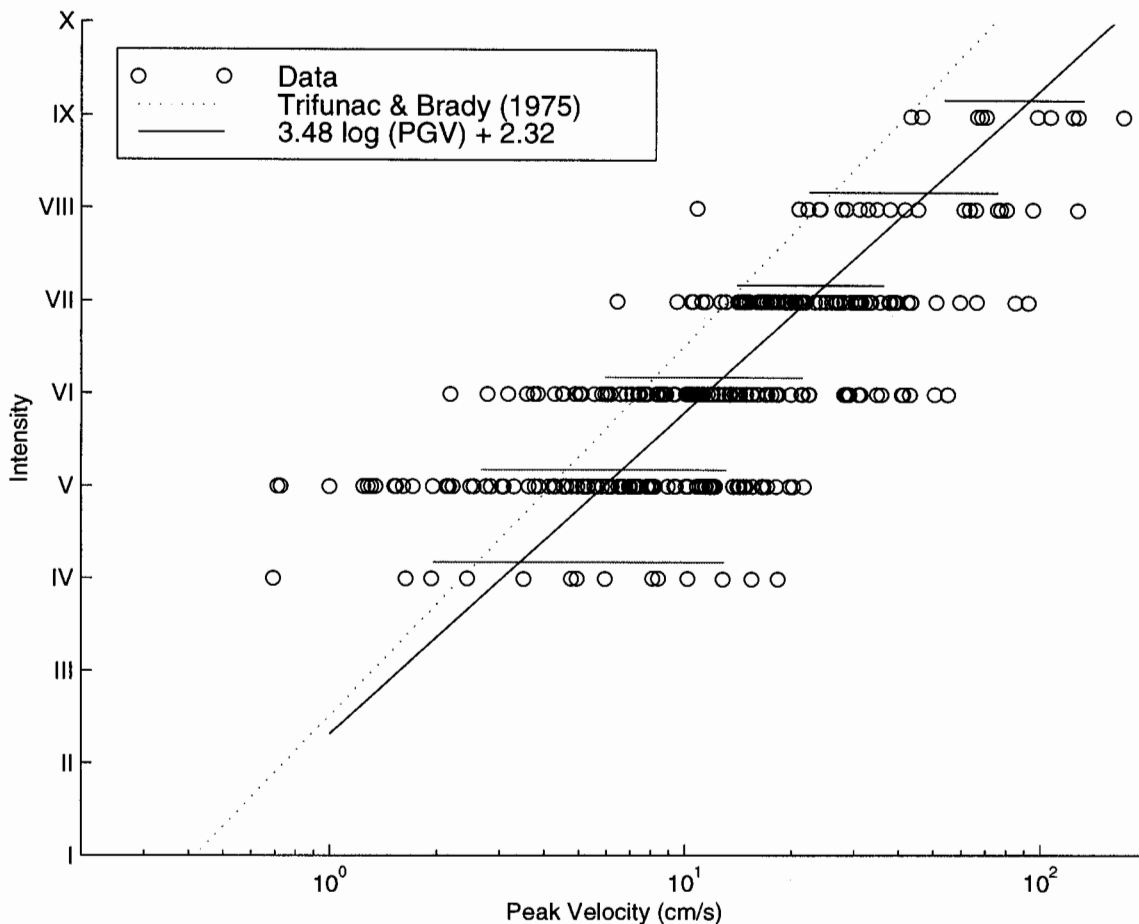


Figure 10: Modified Mercalli intensity plotted against peak ground velocity for all events combined. Circles denote data; horizontal lines above data depict the range of the geometric mean, plus and minus one standard deviation. Solid line is regression from this study; short-dashed line is that of Trifunac and Brady (1975).

approximately one to two cm/sec/sec, at least for this range of magnitudes. We then assigned the slope such that the curve would intersect the relationship in equation 1 at  $I_{mm}$  V. We plan to refine this as more digital data becomes available.

For a given ground motion level, our intensities are higher compared to the commonly used relationships of Trifunac and Brady (1975), which is also displayed on Figures 9 and 10. Only data from the 1971 San Fernando earthquake are common; our data is from 1971 forward, while that of Trifunac and Brady (1975) contains prior earthquakes. In general, the main differences are due to the addition of new data since the Trifunac and Brady (1975) study. However, for acceleration, part of the difference is that we do not include the intensity IX (or larger) values in the regression, due to the evidence of amplitude saturation, whereas Trifunac and Brady (1975) used an intensity X value. Likewise, for velocity, we did not use lower intensity values ( $I_{mm} \leq IV$ ) for the regression whereas Trifunac and Brady (1975) did so.

It is notable that relations of Trifunac and Brady (1975) were substantially higher (stronger motions required for a given intensity) than most earlier estimates (see Trifunac and Brady, 1975,

Figure 3), and now our relationship indicates yet higher ground motions associated with the same intensity levels. There are a number factors that may influence this trend, and certainly more densely spaced recordings in the near-fault region of the recent events, particularly for the Northridge earthquake, does presumably favor a more accurate portrayal of the relationship. However, building practices have certainly improved since the earlier events studied, altering the association of shaking and damage. There are fewer brittle structures that are easily damaged at moderate levels of ground acceleration. Hence, it may be natural that such empirical relationships change with time.

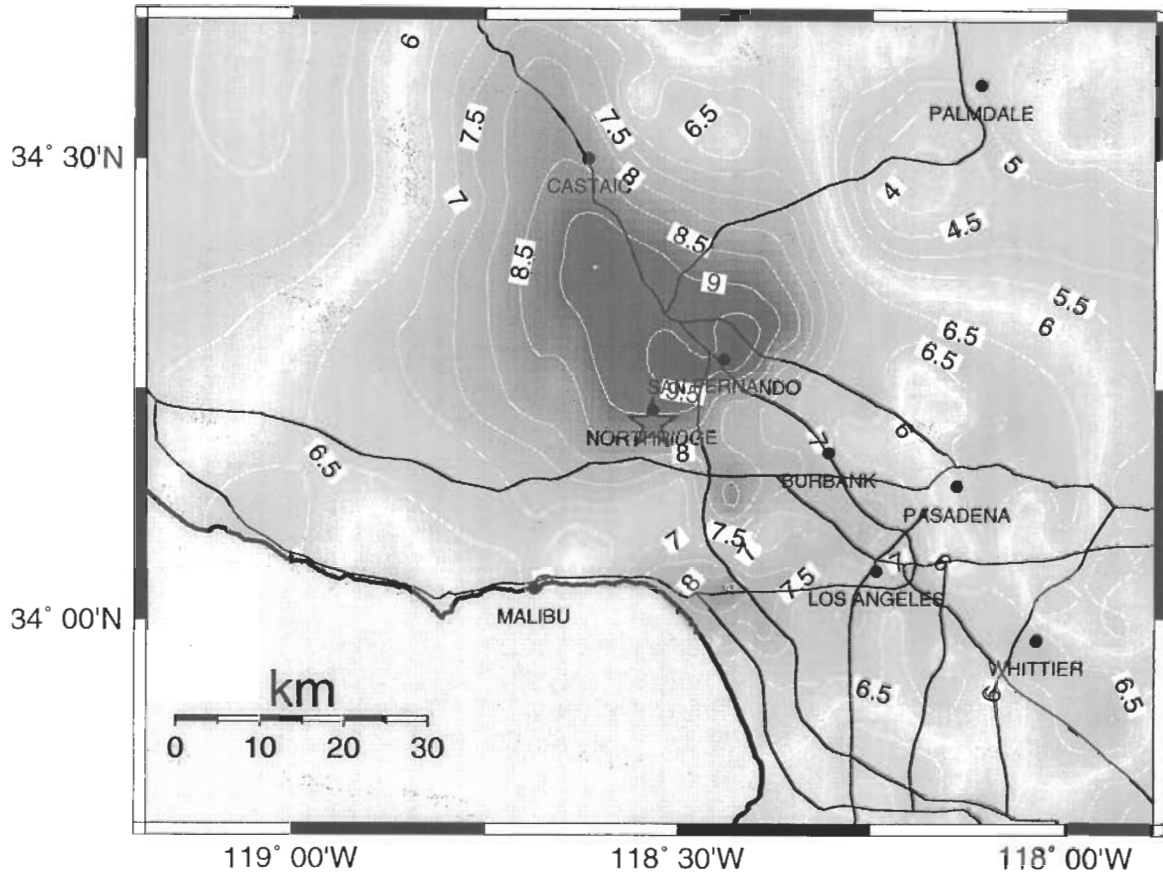
As seen in Figures 9 and 10, low levels of shaking intensity correlate best with peak acceleration, while high intensities correlate best with peak velocity. Basically, peak acceleration levels off at high intensity while peak velocity continues to grow. In contrast the ground velocities, derived by integration of digitized analog accelerograms, are noisy at low levels of motion so a meaningful correspondence is elusive. By comparing maps of instrumental intensities with  $I_{mm}$  for the eight above-mentioned earthquakes, we have found that a relationship that follows acceleration for  $I_{mm} < VII$  and follows velocity for  $I_{mm} > VII$  works fairly well. In practice, we compute the  $I_{mm}$  from the  $I_{mm}$  versus PGA relationship; if the intensity value determined from peak acceleration is  $\geq VII$ , we then use the value of  $I_{mm}$  derived from the  $I_{mm}$  versus PGV relationship.

This is intuitively consistent with the notion that lower (<VI) intensities are assigned based on felt accounts, and people are more sensitive to ground acceleration than velocity. Higher intensities are defined by the level of damage; the onset of damage at the intensity VI to VII range is usually characterized by brittle-type failures (masonry walls, chimneys, unreinforced masonry, etc.) which are sensitive to higher-frequency accelerations. With more substantial damage (VII and greater), failure begins in more flexible structures, for which peak velocity is more indicative of failure (e.g., Hall *et al.*, 1996).

Table 2 gives the peak ground motions that correspond to each unit Modified Mercalli intensity value according to our regression of the observed peak ground motions and intensities for California earthquakes. By relating recorded ground motions to Modified Mercalli intensities, we can now estimate shaking intensities within a few minutes of the event based on the recorded peak motions made at seismic stations. Note that the estimated intensity map is derived from ground motions recorded by seismographs and represents intensities that are likely to have been associated with the ground motions. However, unlike conventional intensities, the instrumental intensities are not based on observations of the earthquake effects on people or structures. Further, the range of peak values for a given intensity is likely to change as additional data sets are included.

Table 2: Relationship of Peak Ground Motions to Intensities

| Intensity         | I        | II-III   | IV      | V          | VI     | VII         | VIII              | IX      | X+         |
|-------------------|----------|----------|---------|------------|--------|-------------|-------------------|---------|------------|
| Perceived Shaking | Not Felt | Weak     | Light   | Moderate   | Strong | Very Strong | Severe            | Violent | Extreme    |
| Damage            | None     | None     | None    | Very Light | Light  | Moderate    | Moderate to Heavy | Heavy   | Very Heavy |
| Peak Acc. (% g)   | <0.17    | 0.17-1.4 | 1.4-4.0 | 4.0-9.3    | 9.3-18 | 18-34       | 34-65             | 65-124  | >124       |
| Peak Vel. (cm/s)  | <0.6     | 0.6-2.2  | 2.2-4.2 | 4.2-8.2    | 8.2-16 | 16-31       | 31-60             | 60-114  | >115       |



| INTENSITY         | I        | II-III   | IV      | V          | VI     | VII         | VIII           | IX      | X+         |
|-------------------|----------|----------|---------|------------|--------|-------------|----------------|---------|------------|
| Perceived Shaking | Not felt | Weak     | Light   | Moderate   | Strong | Very strong | Severe         | Violent | Extreme    |
| DAMAGE            | none     | none     | none    | Very light | Light  | Moderate    | Moderate/Heavy | Heavy   | Very Heavy |
| PEAK ACC. (%g)    | <0.17    | 0.17-1.4 | 1.4-4.0 | 4.0-9.3    | 9.3-18 | 18-34       | 34-65          | 65-124  | >124       |
| PEAK VEL. (cm/s)  | <0.6     | 0.6-2.2  | 2.2-4.2 | 4.2-8.2    | 8.2-16 | 16-31       | 31-60          | 60-115  | >115       |

Figure 11: Instrumental intensity map for the 1994 Northridge earthquake derived using the procedure outlined in the text. Shading corresponds to the intensity scale in the legend at the bottom of the figure. The epicenter is shown with a filled star, Black lines depict highways. Small circles show selected city locations as labeled. Also given in the scale bar are corresponding peak ground motion values, one- or two-word shaking and damage descriptors (See also Table 1).

Figure 11 shows the site-corrected, instrumental intensity map derived using the procedure outlined above using strong motion data recorded during the Northridge earthquake. The epicenter is shown with a solid star and black lines depict highways. The shading corresponds to the intensity scale shown below the figure, and two-word descriptions of both shaking and damage levels are provided (L. Dengler and J. Dewey, written communication, 1998). On the World Wide Web version of the maps, rather than contour lines, the shading is color-coded, with yellow, orange and red representing increasing levels of potential damage. Given the current station distribution, we can recover approximately the Northridge intensity map (Fig. 11) if the CDMG dialup data is included (1/2 hour). This map shares most of the notable features of the Modified Mercalli map prepared by Dewey *et al.* (1995). The area of  $I_{mm}$  IX on the instrumentally-derived intensity map is greater in comparison with the Dewey *et al.* (1995) map. This reflects the fact that although much of the regions in the Santa Susanna mountains, north and northwest of the epicenter, were very strongly shaken, the region is also sparsely populated. Hence the observed intensities were not represented. This is a fundamental difference between observed and instrumentally-derived intensities.

Though there is some degradation when the 5-minute map is made using only the USGS/Caltech real-time stations, it nonetheless provides for more information that was available in the early morning of January 17, 1994. In that case it took over one half an hour to provide just the epicenter and magnitude. Had this map been available in the minutes following the Northridge earthquake, much more would have been understood about the scope of the disaster and the variations in damage over the Los Angeles metropolis.

Initially, our use of PGA and PGV for estimating intensities was simply practical. We were only retrieving peak values from a large subset of the network, so it was impractical to compute more specific ground motion parameters, such as average response spectral values, kinetic energy, cumulative absolute velocities (CAV, EPRI, 1991), or the JMA algorithm (Japan Meteorological Agency, 1996). However, we find the use of PGA and PGV to be quite suitable, particularly since near-source ground motions recorded during these earthquakes are nearly always dominated by short-duration, pulse-like characteristics usually associated with source directivity, and these are by far the largest motions. In other words, for the many of the most damaging ground motions, the kinetic energy available for damage can be well characterized by the peak velocity value. The close correspondence of the JMA intensities and peak ground velocity (Kanezashi and Kaneko, 1997) indicates that our use of peak ground velocities for higher intensities is consistent with the algorithm used by JMA. Another consideration in the choice of peak ground motion values, rather than derived parameters, is the ease in then relating intensity directly to simple ground motion observables.

For large distant earthquakes, the peak values will be less informative, and duration and spectral content will become key parameters. While eventually we may adopt corrections for these situations, it is difficult to assign intensities in such cases. For instance, what is the intensity in the zone of Mexico City from the 1985 Michoacan earthquake, where numerous high-rises collapsed, but the overwhelming majority of smaller buildings were unaffected? While the peak ground velocities were moderate and would imply  $I_{mm}$  VIII, resonance and duration conspired to cause a more substantial disaster. Although this is, in part, a shortcoming of using peak parameters alone, it is more a limitation imposed by simplifying the complexity of ground motions into a single parameter. As such, in addition to providing peak ground motion values and intensities, we will be producing spectral response maps as well (for 0.3, 1.0, and 3.0 sec), and those users that can take advantage of this information for loss estimation will have a clearer picture than intensity and peak ground motion values alone can provide. However, as discussed earlier, a simple intensity map is extremely useful for the overwhelming majority of the users, which includes the general public and many

involved with the initial emergency response.

The use of PGV for higher intensities also proves important for several cases for which we have recorded a large, single-spike of high-frequency acceleration recorded for small earthquakes. With our procedure, while the large acceleration peak would provide an abnormally high intensity, the much smaller velocity amplitude provides a more appropriate, lower intensity. In contrast small earthquakes, which are nonetheless widely felt in many areas of southern California, generally provide rather noisy velocity recordings and hence the estimation of intensity from them alone is less reliable. For smaller events, acceleration amplitudes provide more reliable intensity estimates though there are currently few data constraining the lowest intensity levels.

### THE SHAKEMAP WEB PAGE

After triggering, events are automatically processed, added to the database and are made available through the World Wide Web online interface. The Web site provides access to not only maps of recent earthquakes (for instance, a mainshock and significant aftershocks), but also historical events processed to provide a basis for comparison with recent events. The actual processing of the peak acceleration, peak velocity, and intensity maps, including printing and complete Web page generation, takes less than one minute once triggered for the uncorrected maps; site corrections take an additional minute.

The maps as viewed on the Web are interactive imagemaps. Selection of individual stations on the map initializes a lookup table that provides station information, including station names, coordinates, and the peak ground motions values recorded on each component. Such information has been greatly sought following major earthquakes but only now can it be provided in a rapid fashion.

For significant events (e.g., magnitude greater than 5.0), full-color, poster-sized maps are also generated automatically. In addition, a first motion mechanism (e.g., Reasenber and Oppenheimer, 1975) and rapid moment tensor solution (Thio and Kanamori, 1995), both automatically generated, are added to the ShakeMap Web page as they are received to provide additional information about the nature of the earthquake source. Summary files are also generated for each data set to be used for distribution. These files include the raw data, interpolated and site-corrected grid files and the values of the contour lines used on the maps.

### DISCUSSION

With the QTM designation, we can get a large component of the total amplification effect with a small number of parameters. More importantly, these simple, geological classifications are available over the whole of southern California. A compilation of more localized (and better constrained) site corrections based on either shallow soil velocity profiles or mainshock/aftershock studies (e.g., Hartzell *et al.*, 1998) may improve the interpolation technique that we currently use. However, such data is not uniformly available and a new technique would have to be developed to incorporate such subsets into the interpolation scheme. Further, the effects of soil nonlinearity are not quantified in such site response maps since a majority of the ground motions are at low levels of input motion, and these effects could be important at the strong motion levels for which we anticipate ShakeMap will be most useful.

One implication of using site-corrections that depend on frequency and amplitude, which clearly reflect nonlinearity at large motions, is that the site corrections become smaller as amplitudes increase into the nonlinear range. Arguably, this range is for peak accelerations above 15-20% "g" (e.g., Beresnev and Wen, 1996; Field *et al.*, 1997). As seen in Table 1, both the 1 and 3 Hz site

corrections are rather small above 200 gals, so the site correction has only a minor effect for intensity VII or greater (which are based on the peak velocity, or 1 Hz, correction factors). However, with any moderate-to-large earthquake, it will be important to delineate the boundaries of potentially damaging strong motions and those regions moderately shaken at greater distances from the source.

The current site corrections being used are clearly only first order corrections. The QTM geology is highly simplified; shallow Quaternary alluvium sites can behave as bedrock; likewise, some digital stations mapped on rock indicate substantial observed site amplifications. We have not yet addressed the potential for severe site effects and liquefaction in areas of southern California with extremely slow surface shear wave velocities (NEHRP category D) such as in the Los Angeles Harbor region and along former and current river channels. Not only are we limited by the lack of sufficiently detailed geologic maps of such areas, but the connection between the surface geology and the site amplification is not fully established for strong motions. Similarly, basin edge effects are not included, and differences between very deep basin and shallow basin sites are not yet distinguished. In addition, only peak values have been considered here; site resonance is not yet considered. Shaking duration has also not yet been included, though it may be an important under certain circumstances. For instance, at this point we would likely underestimate the extent of damage (intensity) in Los Angeles for a great San Andreas event since only peak amplitude is considered, but currently there is little empirical constraint upon which to base a modification to the instrumental intensity computation for such an event. For such an earthquake, evaluation of the response spectral map would be crucial.

## CONCLUSIONS

The peak ground motion versus intensity correlation is based on observations collected from recent California earthquakes. Hence, although intended to correspond with observations, as more data become available, this parameterization is subject to revision as necessary to accommodate additional observations as well as changes in building practice. The seismic intensities we produce immediately following damaging earthquakes are based on recorded ground motions; they are not based on observed phenomena usually associated with seismic intensities. Although intended to correspond, locations of equal instrumental intensity may suffer different degrees of damage based on both the density and type of structures and the exact nature of the ground motions.

At present, there is little data to correlate lower intensity values and recorded ground motions since most of the ground motion data is for larger earthquakes, and intensity data is not typically collected for smaller events. In addition, the calibration we have is primarily for analog recordings, so the noise level is high, especially for low amplitude (once-integrated) velocity seismograms. The digital data now being collected with TriNet will be more useful in calibrating against intensity at lower amplitudes. TriNet will provide low amplitude ground motion recordings, previously unavailable with triggered, analog stations. In addition, we are also collecting intensity measurements at near-station locations through voluntary response on the Internet (Quitoriano *et al.*, 1998) ([URLhttp://www-socal.wr.usgs.gov/ciim.html](http://www-socal.wr.usgs.gov/ciim.html)). The combination of assigning intensities for low shaking levels with digital recordings will help constrain the relationship between acceleration and intensity at the lowest values.

Naturally, we are most concerned about accurately portraying the highest intensities. For example, due to the Northridge earthquake, approximately 86% of the residential losses occurred in the intensity VII-IX region (Kircher *et al.*, 1997, p 714). Intensity IX was the largest mapped value for that event. Interestingly, though, while the main emphasis of "ShakeMap" is to provide information about shaking for damaging earthquakes where the pattern of shaking can be quite complex, there has been widespread interest in viewing maps for smaller earthquakes which are,

nonetheless, widely felt. We generate "ShakeMap" for all earthquakes in southern California above magnitude 3.0, but we only update the Web pages for magnitude 3.9 and greater, since the felt area for the smaller events is usually nominal. However, for several notable earthquakes in the 3.0 to 3.9 range, there has been a substantial demand for rapid display of the shaking pattern and so we have provided maps for these events as well. The advantage in providing ShakeMap for non-damaging earthquakes is twofold. First, we gain experience processing, calibrating, and checking our system by responding to small events daily to weekly, rather than on the very infrequent basis allowed by the occurrence of moderate to large earthquakes. Second, the user groups (which includes emergency response agencies, utilities, the media, scientists, and the general public) are afforded the opportunity to become familiar with the maps and to test their response on a more regular basis.

A critical component in successfully generating "ShakeMap" is a system that is robust; that is, it must function under the adverse conditions present during a damaging earthquake including strong shaking of computer equipment, power failures, communication problems, Internet bottlenecks, etc. Efforts have been ongoing to address these concerns. The generation of ShakeMap will provide a much clearer picture of the nature and extent of ground movement following the next significant southern California earthquake and will provide a sound starting point for immediate loss estimation. The World Wide Web uniform resource locator for the "ShakeMap" is

*<http://www.trinet.org/shake.html>*

### ACKNOWLEDGMENTS

Conversations with J. Boatwright, R. Borchardt, L. Dengler, J. Dewey, J. Goltz, K. Campbell, R. Nigbor, and M. Petersen were very helpful. Jim Dewey provided the intensity data in digital form. S. Park provided his QTM geology maps in digital form. All the participants in TriNet played a critical role in making this happen, most notably D. Given, E. Hauksson, P. Maechling, and A. Shakal. Maps and significant portions of the interpolation processing is done with Generic Mapping Tools (GMT, Wessel and Smith, 1991).

### REFERENCES

- Beresnev, I. A., and K.-L. Wen (1996). Nonlinear soil response - a reality? (A review), *Bull. Seism. Soc. Am.*, **86**, 1964-1978.
- Borchardt, R. D. (1994). Estimates of site-dependent response spectra for design (methodology and justification), *Earthquake Spectra*, **10**, 617-654.
- Dewey J. W., B. Glen Reagor, L. Dengler, and K. Moley (1995). Intensity distribution and isoseismal maps for the Northridge, California, earthquake of January 17, 1994, *U. S. Geological Survey Open-File Report 95-92*, 35 pp.
- Eguchi, R. T., J. D. Goltz, H. A. Seligson, P. J. Flores, T. H. Heaton, and E. Bortugno (1997). Real-time loss estimation as an emergency response decision support system: The Early Post-Earthquake Damage Assessment Tool (EPEDAT), *Earthquake Spectra*, **13**, 815-832.
- EPRI (1991). Standardization of cumulative absolute velocity, EPRI TR100082 (Tier 1), Palo Alto, California, Electric Power Research Institute, prepared by Yankee Atomic Electric Company.
- Field, E. H. P. A. Johnson, I. A. Beresnev, and Y. Zheng (1997). Nonlinear sediment amplification during the 1994 Northridge earthquake, *Nature*, **390**, 599-602.

## SMIP98 Seminar Proceedings

- Hall, J. F., T. H. Heaton, M. W. Halling, and D. J. Wald (1996). Near-source ground motions and its effects on flexible buildings, *Earthquake Spectra*, **11**, 569-606.
- Hartzell, S. H., S Harsen, A. Frankel, D. Carver, E. Cranswick, M. Meremonte, and J. Michael (1998) First-generation site response maps for the Los Angeles region based on earthquake ground motions, *Bull. Seism. Soc. Am.*, **88**, 463-472.
- Japan Meteorological Agency (1996). Note on the JMA seismic intensity, JMA report 1996, *Gyosei* (in Japanese).
- Joyner, W. B. and Boore, D. M. (1981). Peak horizontal accelerations and velocity from strong-motion records including records from the 1979 Imperial Valley, California, earthquake, *Bull. Seism. Soc. Am.* **71**, 2011-2038.
- Kanamori, H. (1993). Locating earthquakes with amplitude: Application to real-time seismology, *Bull. Seism. Soc. Am.* **83**, 264-268.
- Kanezashi, S., and F. Kaneko, (1997). Relations between JMA's measuring seismic intensity (MI) and physical parameters of earthquake ground motion, *OYO Tenical Report*, 1997, 85-96.
- Kircher, C. A., R. K. Reitherman, R. V. Whitman, and C. Arnold, 1997. Estimation of earthquake losses to buildings, *Earthquake Spectra*, bf 13, 703-720.
- Mori, J., H. Kanamori, J. Davis, E. Hauksson, R. Clayton, T. Heaton, L. Jones, and A. Shakal (1998). Major improvements in progress for southern California earthquake monitoring, *Eos Trans. AGU*, **79**, p. 217,221.
- Park, S. and S. Ellrick (1998). Predictions of shear wave velocities in southern California using surface geology, *Bull. Seism. Soc. Am.*, **88**, 677-685.
- Quitoriano, V., D. J. Wald, L. Dengler, and J. W. Dewey (1998). Utilization of the Internet for Rapid Community Seismic Intensity Maps, *Eos Trans. AGU*, **79**, in press.
- Reasenber, P., and D. Oppenheimer (1975). FPFIT, FPLOT, and FPPAGE: Fortran programs for calculating and displaying earthquake fault plane solutions, *U. S. Geological Survey Open-File Report 75-739*, 109 pp.
- Richter, C.F. (1958). Elementary Seismology. W. H. Freeman and Company, San Francisco, pp. 135-149, 650-653.
- Shakal, A., C. Peterson, A. Cramlet, and R. Darragh (1996). Near-real-time CSMIP strong motion monitoring and reporting for guiding event response, in *Proceedings of the 11th World Conference on Earth. Eng.*, Acapulco, Mexico.
- Shakal, A., C. Peterson, and V. Grazier (1998). Near-real-time strong motion data recovery and automated processing for post-earthquake utilization, *Sixth Nat'l Conference on Earth. Eng.*, Seattle.
- Thio, H. K., and H. Kanamori (1995). Moment tensor inversion for local earthquakes using surface waves recorded at TERRAscope, *Bull. Seism. Soc. Am.* **85**, 1021-1038.
- Trifunac, M. D., and A. G. Brady (1975). On the correlation of seismic intensity scales with the peaks of recorded ground motion, *Bull. Seism. Soc. Am.* **65**, 139-162.



- Wald, D. J., T. Heaton, H. Kanamori, P. Maechling, and V. Quitoriano (1997). Research and Development of TriNet "Shake" Maps, *Eos Trans. AGU*, **78**, No. 46, p F45.
- Wessel, P. and Smith, (1991). Generic Mapping Tools, *Eos Trans. AGU* **72**, 441.
- Wood, H. O. and Neumann (1931). Modified Mercalli intensity scale of 1931, *Bull. Seism. Soc. Am.* **21**, 277-283.
- Yamakawa, K. (1998). The Prime Minister and the earthquake: Emergency Management Leadership of Prime Minister Marayama on the occasion of the Great Hanshin-Awaji earthquake disaster, *Kansai Univ. Rev. Law and Politics*, **No. 19**, 13-55.